

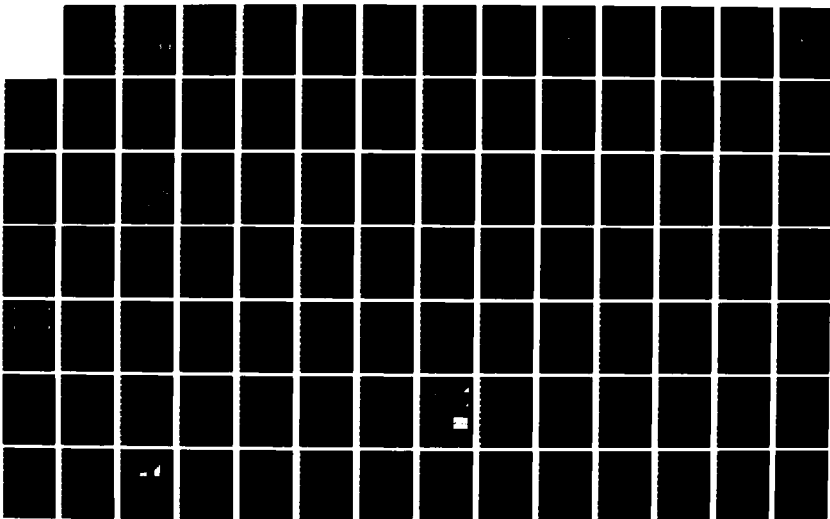
AD-A175 472

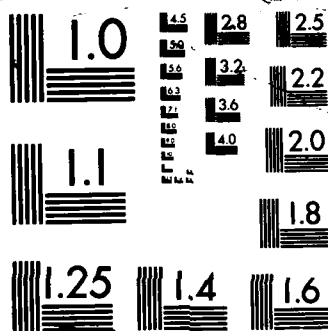
TUNABLE MICROWAVE TRANSVERSAL FILTERS AND DISPERSIVE  
DELAY LINES BASED ON (U) TEXAS UNIV AT ARLINGTON DEPT  
OF ELECTRICAL ENGINEERING J M OWENS ET AL 30 SEP 86  
ARO-17685 1-EL DARG29-82-K-0073 F/G 9/5

1/3

UNCLASSIFIED

NL





XEROCOPY RESOLUTION TEST CHART

AD-A175 472

ARO 17685.1-EL

2

Report CAEDS 1986-ARO-1

TUNABLE MICROWAVE TRANSVERSAL FILTERS AND  
DISPERSIVE DELAY LINES BASED ON OBLIQUE  
INCIDENCE REFLECTION OF MAGNETOSTATIC WAVE  
PROPAGATING IN EPITAXIAL GARNETS

J.M. Owens  
R.L. Carter  
Department of Electrical Engineering  
College of Engineering  
The University of Texas at Arlington

30 September 1986

Final Report for Period I June 1982 - 31 July 1986  
ARO Grant No. DAAG 29-82-K-0073

Prepared for

U.S. Army Research Office  
P.O. Box 1221  
Research Triangle Park  
N.C. 27709  
Attn Dr. J. Mink

DTIC  
ELECTE  
S DEC 31 1986 D  
D

DTIC FILE COPY

DISTRIBUTION STATEMENT A

Approved for public release;  
Distribution Unlimited

UNCLASSIFIED

SECURITY CLASSIFICATION OF THIS PAGE

ADA175472

## REPORT DOCUMENTATION PAGE

|  |  |   |                                  |
|--|--|---|----------------------------------|
| 1a. REPORT SECURITY CLASSIFICATION<br>Unclassified   |  | 1b. RESTRICTIVE MARKINGS  |                                  |
| 2a. SECURITY CLASSIFICATION AUTHORITY  |  | 3. DISTRIBUTION/AVAILABILITY OF REPORT<br>Approved for public release;<br>distribution unlimited.   |                                  |
| 2b. DECLASSIFICATION/DOWNGRADING SCHEDULE  |  | 5. MONITORING ORGANIZATION REPORT NUMBER(S)<br>ARO 17685-1-EL                                       |                                  |
| 4. PERFORMING ORGANIZATION REPORT NUMBER(S)  |  | 7a. NAME OF MONITORING ORGANIZATION<br>U. S. Army Research Office                                   |                                  |
| 6a. NAME OF PERFORMING ORGANIZATION<br>Dept of Electrical Engineering  | 6b. OFFICE SYMBOL<br>(if applicable)<br>CAEDS                        | 7b. ADDRESS (City, State, and ZIP Code)<br>P. O. Box 12211<br>Research Triangle Park, NC 27709-2211 |                                  |
| 6c. ADDRESS (City, State, and ZIP Code)<br>P.O.Box 19016-UTA<br>Arlington, Tx 76019  | 9. PROCUREMENT INSTRUMENT IDENTIFICATION NUMBER<br>DAAG-29-82-K-0073 |   |                                  |
| 8a. NAME OF FUNDING/SPONSORING ORGANIZATION<br>U. S. Army Research Office  | 8b. OFFICE SYMBOL<br>(if applicable)                                 | 10. SOURCE OF FUNDING NUMBERS   |                                  |
| 8c. ADDRESS (City, State, and ZIP Code)<br>P. O. Box 12211<br>Research Triangle Park, NC 27709-2211  |  | PROGRAM<br>ELEMENT NO.  | PROJECT<br>NO.                   |
|  |  | TASK<br>NO.   | WORK UNIT<br>ACCESSION NO.       |
| 11. TITLE (Include Security Classification)<br>TUNABLE MICROWAVE TRANSVERSAL FILTERS AND DISPERSIVE DELAY LINES BASED ON OBLIQUE INCIDENCE<br>REFLECTION OF MAGNETOSTATIC WAVE PROPAGATING IN EPITAXIAL GARNETS  |  |   |                                  |
| 12. PERSONAL AUTHOR(S)<br>J.M. Owens, R.L. Carter  |  |   |                                  |
| 13a. TYPE OF REPORT<br>Final Technical Report  | 13b. TIME COVERED<br>FROM 6-1-82 TO 7-31-86                          | 14. DATE OF REPORT (Year, Month, Day)<br>1986 September 30  | 15. PAGE COUNT<br>255            |
| 16. SUPPLEMENTARY NOTATION<br>The view, opinions and/or findings contained in this report are those of the author(s) and should not be construed as an official Department of the Army position, policy, or decision, unless so designated by other documentation.   |  |   |                                  |
| 17. COSATI CODES   |  | 18. SUBJECT TERMS (Continue on reverse if necessary and identify by block number)                   |                                  |
| FIELD  | GROUP  | SUB-GROUP   |                                  |
|  |  | Magnetostatic Waves, Millimeter Wave Isolators, Microwave Analog Signal Processing                  |                                  |
| 19. ABSTRACT (Continue on reverse if necessary and identify by block number)<br>The report summarizes work to date toward a goal of establishing novel microwave analog signal processing using oblique reflection of magnetostatic waves propagating in epitaxial YIG. Also, investigation has been carried out on the realization of MM wave isolators based on field displacement in dielectric waveguides formed from an epitaxial YIG system. |  |   |                                  |
| 20. DISTRIBUTION/AVAILABILITY OF ABSTRACT<br><input type="checkbox"/> UNCLASSIFIED/UNLIMITED <input type="checkbox"/> SAME AS RPT. <input type="checkbox"/> DTIC USERS   |  | 21. ABSTRACT SECURITY CLASSIFICATION<br>Unclassified  |                                  |
| 22a. NAME OF RESPONSIBLE INDIVIDUAL  |  | 22b. TELEPHONE (Include Area Code)<br>(817) 273-3496  | 22c. OFFICE SYMBOL<br>CAEDS - EE |



# TABLE OF CONTENT

|       |  |    |
|-------|--|----|
| 1.0   | INTRODUCTION and SUMMARY .....   | 1  |
| 2.0   | MAGNETOSTATIC ION-IMPLANTED REFLECTIVE ARRAY THEORY .....                      | 2  |
| 2.1   | Dispersion Relation and Transducer Modeling .....                              | 2  |
| 2.1.1 | Device Configuration Requirements .....  | 2  |
| 2.1.2 | Magnetostatic Waves .....  | 4  |
| 2.1.3 | The Polder Tensor .....  | 6  |
| 2.1.4 | Gilbert Damping .....  | 13 |
| 2.1.5 | Effects of Ion Implanting the Ferrite .....                                    | 19 |
| 2.1.6 | Solutions of the Magnetostatic Equation .....                                  | 21 |
| 2.1.7 | The Four Layer Boundary Value Problem .....                                    | 23 |
| 2.1.8 | Transducer Modeling .....  | 38 |
| 2.2   | Reflectivity Model .....   | 39 |
| 2.2.1 | Assumptions and Approximations .....   | 39 |
| 2.2.2 | Wave Impedance .....   | 42 |
| 2.3   | Array Modeling .....   | 48 |
| 2.3.1 | Normal Incidence Array Theory .....  | 48 |
| 2.3.2 | Oblique Incidence Array Theory .....   | 53 |
| 3.0   | SYNTHESIS TECHNIQUES .....   | 59 |
| 3.1   | Measure of Fit .....   | 59 |
| 3.1.1 | Taylor Criterion .....   | 60 |
| 3.1.2 | Direct Equation .....  | 60 |
| 3.1.3 | Chebyshev Criterion .....  | 61 |
| 3.1.4 | Mean Squared and Mean Absolute Error Criterion .....                           | 63 |
| 3.2   | Search Techniques .....  | 64 |
| 3.2.1 | Error Functions that Depend Linearly<br>on System Parameters .....             | 64 |
| 3.2.2 | Error Functions that are Nonlinear Functions<br>of the System Parameters ..... | 76 |
| 3.2.3 | Synthesis Using the Impulse Model .....  | 79 |
| 4.0   | ION IMPLANTED MSW REFLECTIVE ARRAYS<br>THEORY versus EXPERIMENT .....          | 91 |
| 4.1   | Device Fabrication and Measurement Details .....                               | 91 |
| 4.1.1 | Film Growth .....  | 91 |
| 4.1.2 | Array Implantation .....   | 92 |
| 4.1.3 | Microstrip Fabrication .....   | 93 |
| 4.1.4 | Measurement Details .....  | 93 |



Codes

Dist

A-1

|       |   |     |
|-------|---|-----|
| 4.2   | Normal Incidence Array Theory versus Experiment .....                                     | 93  |
| 4.2.1 | MSSW Biased Arrays .....  | 93  |
| 4.2.2 | MSFVW Biased Arrays .....   | 102 |
| 4.3   | Uniform Oblique Incidence MSFVW RAF .....   | 108 |
| 4.4   | Delay Graded Oblique Incidence .....  | 113 |
| 4.4.1 | Positive Delay Slope Array .....  | 113 |
| 4.4.2 | Negative Delay Slope Array .....  | 117 |
| 4.5   | Summary of Basic Array Types .....  | 121 |
| 5.0   | ELLIPTICAL GEOMETRY ION IMPLANTED MSFVW RAFs .....  | 124 |
| 5.1   | Elliptical Array Concept .....  | 124 |
| 5.1.1 | Operating Principle .....   | 124 |
| 5.1.2 | Advantages of Elliptical Arrays<br>over Conventional Arrays .....                         | 126 |
| 5.2   | Experiment versus Theory for the Elliptical Arrays .....                                  | 129 |
| 5.2.1 | Mirror Symmetric Confocal Elliptical Array .....  | 129 |
| 5.2.2 | Complimentary Confocal Elliptical Array .....   | 133 |
| 5.2.3 | Apodized Elliptical Array .....   | 136 |
| 5.2.4 | Grounded Center Spot Circular Transducers .....   | 145 |
| 5.3   | Unidirectional Transducer Designs .....   | 148 |
| 5.3.1 | Edge Reflector UDTs .....   | 148 |
| 5.3.2 | Phased Array UDT .....  | 151 |
| 6.0   | CONCLUSION .....  | 157 |
| 6.1   | Normal Incidence Experiments .....  | 157 |
| 6.2   | Oblique Incidence Experiments .....   | 158 |
| 6.3   | Elliptical Geometry Arrays .....  | 160 |
| 6.4   | Recommendations for Future Study .....  | 161 |
| 7.0   | MILLIMETER WAVE ISOLATORS BASED on FIELD DISPLACEMENT<br>in DIELECTRIC IMAGE GUIDES ..... | 163 |
| 7.1   | MM Wave Field Displacement Isolator Theory .....  | 163 |
| 7.2   | Experiments on MM Wave Field Displacement Isolators .....                                 | 170 |
| 8.0   | SUMMARY .....   | 183 |
| 9.0   | PUBLICATIONS RESULTING From ARO SUPPORT .....   | 184 |

|  |     |
|--|-----|
| APPENDIX A. WAVE IMPEDANCES .....                          | 185 |
| APPENDIX B. REFLECTION and TRANSMISSION COEFFICIENTS ..... | 191 |
| APPENDIX C. COMPUTER PROGRAMS .....                        | 195 |
| C.1 Normal Incidence MSSW Array Analysis .....             | 196 |
| C.2 Normal Incidence MSFVW Array Analysis .....            | 204 |
| C.3 Oblique Incidence MSFVW Array Synthesis .....          | 212 |
| REFERENCES .....   | 243 |

## 1.0 INTRODUCTION AND SUMMARY

The objective of this 3 year study is the further development of Microwave and Millimeter Wave signal Processing Devices based on Epitaxial Ferrites grown on insulating non magnetic substrates. Analog signal processing based on oblique reflection of magnetostatic waves from ion implanted periodic arrays in Epitaxial Yttrium Iron Garnet is of interest as well as the development of Millimeter Wave non-reciprocal components based on Epitaxial Ferrites. This final report summarizes the results of viable realizations of these goals.

Transversal filters at microwave frequencies based on oblique reflection of MSW from arrays of ion implanted zones has been theoretically modeled and experimentally tested. Existing models for transducer radiation characteristics and magnetic wave propagation properties have been applied in conjunction with a theory for the effects of implantation on wave propagation to predict experimental device performance. Synthesis procedures that allow realization of desired filter characteristics are presented and demonstrated in the design of experimental filters. Novel reflector geometries are discussed and experimentally compared to conventional schemes. Unidirectional transducer are theoretically discussed and experimentally varified as they apply to contoured reflective arrays.

Theoretical and experimental studies of Millimeter Wave non-reciprocal devices based on Epitaxial Ferrites grown on dielectric substrates which serve as Image Waveguides, has shown substantial progress. Low loss Image Waveguides have been demonstrated on substrates suitable for Epitaxial growth. Utilizing Epitaxial YIG, field displacement isolation has been demonstrated with forward/reverse isolation of  $> 20\text{db}$ , thus demonstrating the promise of this technology.

## CHAPTER 2

### MAGNETOSTATIC ION-IMPLANTED REFLECTIVE ARRAY THEORY

#### 2.1 Dispersion Relation and Transducer Modeling

##### 2.1.1 Device Configuration Requirements

There are three commonly used bias field orientations that result in "principal mode" operation of a magnetostatic wave device. All of these are characterized by wave propagation vectors that are exclusively normal to or parallel to the bias field direction, as shown in Figure 2.1.

Magnetostatic surface waves (MSSW) were chosen for use in the normal incidence array experiments for three reasons:

- 1) Of the three MSW modes, MSSW's exhibit the lowest overall insertion losses (2.1). These losses can be categorized into propagation attenuation, transducer conversion efficiency, and driving point mismatch. For like film thicknesses, path losses are lower for MSSW's than for volume waves corresponding to the smaller propagation delays. Forward transduction efficiencies are higher for MSSW's in response to the proximity of the launching structures to the ferrite film surface where MSSW energy concentrations are maximum. For a typical unmatched device, driving point mismatch is small and about the same for all three modes.

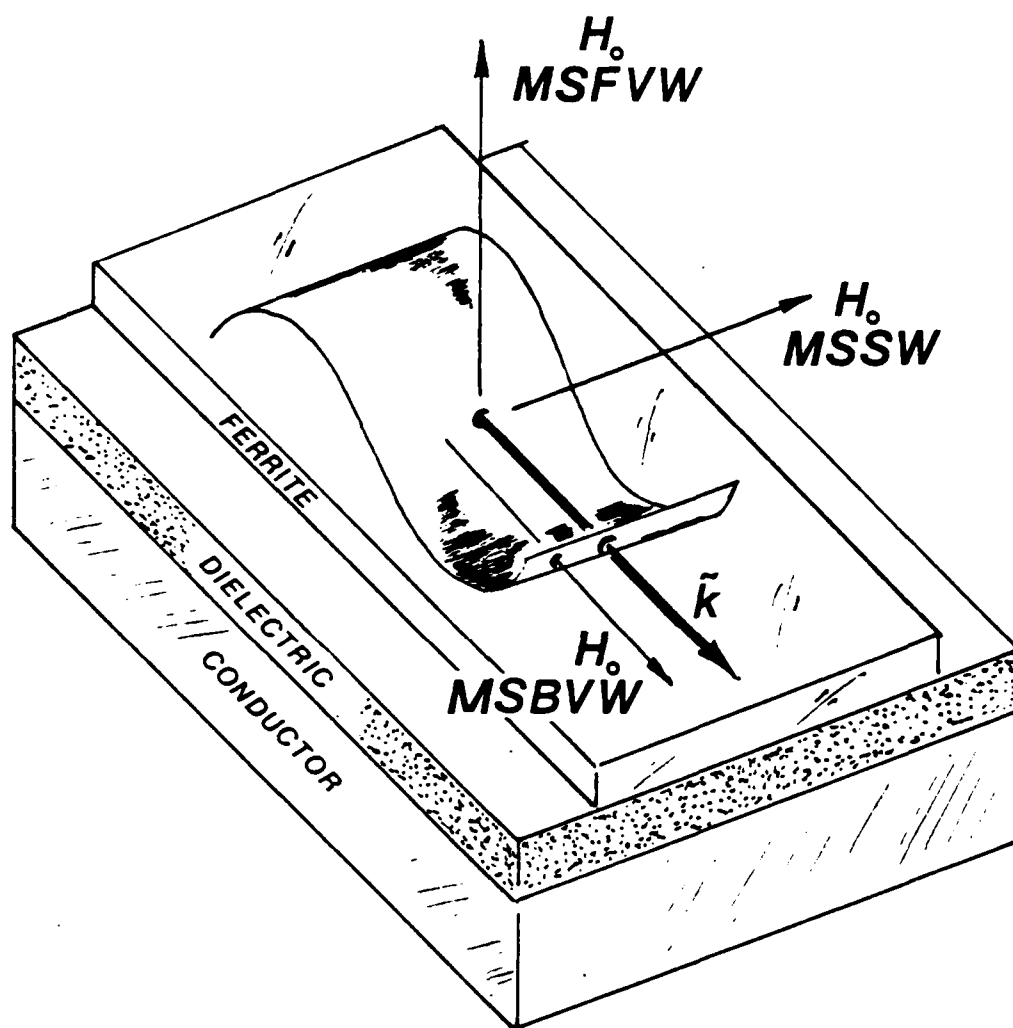


Figure 2.1. Bias field configurations and associated magnetic modes.

- 2) With MSSWs, larger implanted bar edge reflectivities are expected, since typical implants only penetrate to about 2% of the film thickness. This is sufficient to significantly interrupt the surface bound MSSW's, but would have comparatively less effect on volume energy concentrations such as MSFVW and MSBVW.
- 3) Earlier experiments indicate that conversion to vertical standing waves occurs when MSFVWs were used in conjunction with etched groove reflectors {2.2}. This problem has not appeared in experiments utilizing MSSW's with etched grooves {2.3,2.4,2.5,2.6, 2.7}.

MSFVW's were used in the oblique incidence implanted array experiments, since the isotropic character of MSFVW propagation allows transversal reflection without requiring a mode change. The possibility of oblique reflection of MSSW into MSBVW and visa versa was experimentally investigated, but no significant mode conversion was observed.

#### 2.1.2 Magnetostatic Waves

Magnetostatic waves propagate via the ordered electronic spin structure in a ferrite that is biased to the point of saturation by an external magnetic field. Under the influence of a saturating bias field, exchange forces are overcome, and a dynamic equilibrium is reached in which all magnetic moments of the outermost electrons in the ferric ions align to form a fixed angle with the bias field. To

maintain this dynamic equilibrium, the magnetic spin moments precess around the bias field producing a mechanical torque which just balances the magnetic torque. Alignment of the spins in this manner creates a significant mutual magnetic flux linkage among the spins of neighboring ferric ions. Since this flux linkage is the principal mechanism for energy transfer in a magnetostatic wave, the magnetic component of the wave is much larger than the electric counterpart. This justifies the magnetostatic approximation originally introduced by Mercereau and Feynman (2.8),

$$\begin{aligned}\text{curl}\{h\} &= J \\ \text{curl}\{e\} &= -\frac{\partial b}{\partial t} \\ \text{div}\{d\} &= 0 \\ \text{div}\{b\} &= 0\end{aligned}\tag{2.1}$$

in which displacement currents are considered negligible. Small letters signify the small signal, time-varying fields associated with the magnetostatic wave. Except in metalized regions such as transducer filaments, conduction currents are zero and Ampere's Law becomes,

$$\text{curl}\{h\} = 0,\tag{2.2}$$

allowing the use of a scalar magnetic potential to define the magnetic field according to Helmholtz's theorem,

$$h = \text{grad}(\tilde{V}_m).\tag{2.3}$$

Combining this with the constitutive relation and the



solenoidal law yields the magnetostatic equation,

$$\text{div}[\vec{\mu} \cdot \text{grad}(\tilde{V}_m)] = 0. \quad (2.4a)$$

Before this equation can be addressed in the ferrite regions, the permeability tensor must be evaluated for the desired bias field orientations.

### 2.1.3 The Polder Tensor

The following discussion deals with microscopic electronic spins for which the Gaussian system of units is used for convenience. The result is a dimensionless relative permeability tensor equally applicable in the SI system of units used in the wave solutions.

A derivation of the permeability tensor for a biased ferrite was first introduced by Polder [2.9] in 1949. Several simplifying assumptions are necessary for this model:

- The magnetostatic bias field is assumed to be uniform and sufficient to saturate the ferrite. This condition is particularly easy to satisfy in the planar epitaxial films used in this work.
- Effects of magnetocrystalline anisotropy are considered negligible in the presence of the saturating bias field. The validity of this assumption is supported by more general analyses done by others [2.10].
- The ferric ions possessing the involved magnetic moments occupy sites that are surrounded by oxygen ions which

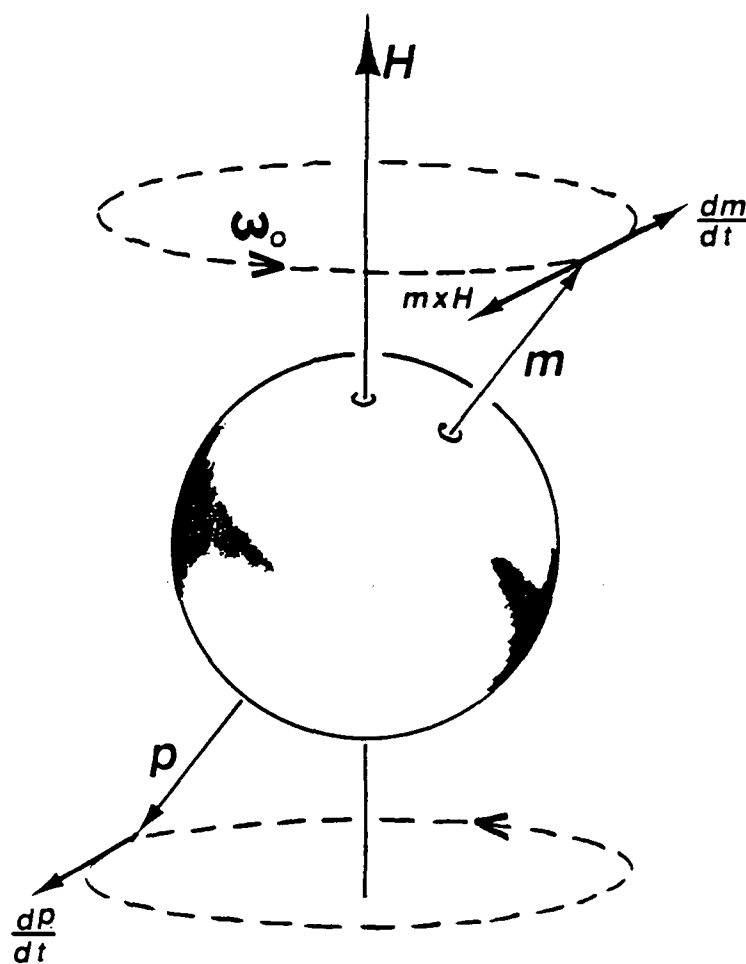


Figure 2.2. Torque balance on an electronic spin in a uniform magnetic field.

serve to isolate them and minimize the effects of exchange interaction. Thus, exchange contributions are assumed negligible. Calculations by others, c.f. Sodha and Srivastava (2.10), show that this approximation is accurate for magnetostatic wavelengths greater than about  $0.6 \mu\text{m}$ , which is well within the realm of this work.

- Fields associated with the magnetostatic wave are assumed to be small in comparison to the static bias related fields.

On a molecular level, the constituents are immersed in a vacuum so that the magnetic induction is the same as the magnetic field intensity. The torque on a magnetic dipole,  $\mathbf{m}$ , in a uniform magnetic field,  $\mathbf{B}$ , in vacuo is (Figure 2.2),

$$\mathbf{T} = \mathbf{m} \times \mathbf{B} = \mathbf{m} \times \mathbf{H}. \quad (2.5)$$

To maintain dynamic equilibrium, the dipole precesses around the bias field, causing its total angular momentum to vary with time, resulting in a mechanical torque,

$$\mathbf{T} = - \frac{d\mathbf{p}}{dt}. \quad (2.6)$$

Under equilibrium, these two torques must balance each other,

$$- \frac{d\mathbf{p}}{dt} + \mathbf{m} \times \mathbf{H} = 0. \quad (2.7a)$$

Total angular momentum and magnetic dipole moment are related

by the gyromagnetic ratio,

$$\mathbf{m} = -|\gamma|\mathbf{p} \quad (2.8a)$$

where,

$$\gamma = ge/2mc \quad (2.9)$$

g = Lande g-factor  
 e = electronic charge  
 m = electronic mass  
 c = speed of light in a vacuum

The Lande g-factor accounts for spin-orbit interaction set up by the nuclear field. It assumes a value of 1 for pure orbital momentum and 2 for pure spin. Ordinarily, both orbital momentum and spin would come into play, placing g somewhere between these extremes. However in a magnetic oxide, such as YIG, the proximity of the oxygen ions that surround its contributive ferric ions creates a strong crystalline field interaction that prevents the orbital motion from being significantly altered by the bias field, such that angular momentum doesn't appreciably participate in the magnetic moment. This "quenching" of the orbital angular momentum {2.11, 2.12} results in a gyromagnetic ratio (cgs),

$$|\gamma| = 17.6 \text{ Mrad/Oe.} \quad (2.8b)$$

With this, the torque balance (2.7a) can be expressed entirely as a function of magnetic quantities,

$$\frac{d\mathbf{m}}{dt} + |\gamma|\{\mathbf{m} \times \mathbf{H}\} = 0. \quad (2.7b)$$

Averaging over a volume with a maximum lineal dimension that is small compared to a magnetostatic wavelength (so H can be

considered uniform) converts this torque balance to a macroscopic form appropriate to the calculation of the material permeability tensor.

$$\frac{d}{dt} \left\{ \frac{\sum_{n=1}^N m_n}{\Delta V} \right\} + |\gamma| \left\{ \frac{\sum_{n=1}^N m_n}{\Delta V} \times H \right\} = 0 \quad (2.7c)$$

Using the definition of magnetization,

$$M \triangleq \frac{\sum_{n=1}^N m_n}{\Delta V}, \quad (2.10)$$

this simplifies to,

$$\frac{dM}{dt} + |\gamma| \{ M \times H \} = 0. \quad (2.7d)$$

In the absence of magnetostatic excitation, the magnetization must be a constant, equal in magnitude to the saturation magnetization,  $M_0$ , and directed along the internal bias field,  $H_0$ . Otherwise, the radiation that would result from the time varying B and H fields,

$$B - H = 4\pi M \quad (2.11)$$

would run the system down. As a magnetostatic wave traverses a point in the sample, the tip of the local magnetization moves about on a sphere centered at the point, as demonstrated by equation (2.12).

$$\frac{d|M|^2}{dt} = 2 \left\{ \frac{dM}{dt} \right\} \cdot M = -2|\gamma| (M \times H) \cdot M = 0 \quad (2.12)$$

The total fields consist of both constant bias related components and small signal magnetostatic time harmonics,

$$\begin{aligned}\tilde{H} &= H_0 + \sum h_n \exp\{j2\pi n f_1 t\} \\ \tilde{M} &= M_0 + \sum m_n \exp\{j2\pi n f_1 t\}\end{aligned}\quad (2.13)$$

Substituting these forms (2.13) into the macroscopic torque balance (2.7d) and requiring the linearly independent time variations to separately satisfy the equality imposes two conditions,

$$M_0 \times H_0 = 0 \quad (2.14a)$$

$$j2\pi n f_1 \tilde{m}_n = |\gamma| \{ M_0 \times \tilde{h}_n + \tilde{m}_n \times H_0 + \sum_{l=1}^{n-1} [\tilde{m}_l \times \tilde{h}_{n-l}] \} \quad (2.14b)$$

$$n = 1, 2, 3, \dots$$

The first of these equations (2.14a) reiterates the colinearity of the bias field and the saturation magnetization. Subject to the small signal model, subharmonic coupling to the  $n$ th harmonic, represented by the summation in (2.14b), can be regarded negligible. In addition to decoupling the equations, this approximation yields identical forms in each of the harmonics, so that the Polder tensor calculated from any of the equations is applicable to the general term, provided the appropriate frequency is used. Dropping subscripts and solving for the components of  $\tilde{m}$  in terms of the components of  $\tilde{h}$  leads to the complex susceptibility tensor,

$$\tilde{m} = \tilde{\chi} \cdot \tilde{h}, \quad (2.15)$$

from which the Polder tensor follows,

$$\bar{\mu} = \bar{I} + 4\pi\bar{\chi} = \begin{pmatrix} 1+4\pi\tilde{\chi}_{11} & 4\pi\tilde{\chi}_{12} & 4\pi\tilde{\chi}_{13} \\ 4\pi\tilde{\chi}_{12} & 1+4\pi\tilde{\chi}_{22} & 4\pi\tilde{\chi}_{23} \\ 4\pi\tilde{\chi}_{13} & 4\pi\tilde{\chi}_{23} & 1+4\pi\tilde{\chi}_{33} \end{pmatrix} \quad (2.16a)$$

Using dummy indexes a,b,c = cyclic permutation of x,y,z, the general tensor elements are,

$$\tilde{\chi}_{aa} = \frac{f(f_{mb}f_{ob} + f_{mc}f_{oc}) - jf_{oa}(f_{ob}f_{mc} - f_{mb}f_{oc})}{4\pi f(f_{oa}^2 + f_{ob}^2 + f_{oc}^2 - f^2)}$$

$$\tilde{\chi}_{ab} = \frac{ff_{ma}f_{ob} + j\{f^2f_{mc} + f_{oa}(f_{ma}f_{oc} - f_{oa}f_{mc})\}}{4\pi f(f_{oa}^2 + f_{ob}^2 + f_{oc}^2 - f^2)}$$

$$\tilde{\chi}_{ba} = \tilde{\chi}_{ab}^*$$

$$f_{oa,b, \text{ or } c} = \frac{|y|}{2\pi} H_{oa,b, \text{ or } c}$$

$$f_{ma,b, \text{ or } c} = \frac{|y|}{2\pi} 4\pi M_{oa,b, \text{ or } c}$$

The two special cases of this relative permeability tensor that apply to the work herein are as follows (Figure 2.1).

MSSW  $\{H_o = H_o \hat{z}, M_o = M_o \hat{z}\}$

$$\bar{\mu} = \begin{pmatrix} \mu_1 & -j\mu_2 & 0 \\ j\mu_2 & \mu_1 & 0 \\ 0 & 0 & 1 \end{pmatrix} \quad (2.16b)$$

MSFVW  $\{H_o = H_o \hat{x}, M_o = M_o \hat{x}\}$

$$\bar{\mu} = \begin{pmatrix} 1 & 0 & 0 \\ 0 & \mu_1 & -j\mu_2 \\ 0 & j\mu_2 & \mu_1 \end{pmatrix} \quad (2.16c)$$

where,

$$u_1 = 1 + \frac{f_o f_m}{f_o^2 - f^2}$$

$$u_2 = - \frac{f f_m}{f_o^2 - f^2}$$

$$f_o = \frac{|Y|}{2\pi} H_o$$

$$f_m = \frac{|Y|}{2\pi} 4\pi M_o$$

The Lamor frequency,  $f_o$ , is the rate with which the magnetization vector precesses around the bias field. Conversely,  $f_m$ , is just a convenient grouping of terms with the dimensions of frequency. Typical values for these quantities are given in TABLE 2.1 for operation at a 3 GHz center frequency.

TABLE 2.1  
TYPICAL PARAMETER VALUES FOR PURE YIG

| Qty.       | MSSW     | MSFVW    |
|------------|----------|----------|
| $4\pi M_o$ | 1750 Gs  | 1750 Gs  |
| $H_o$      | 375 Oe   | 880 Oe   |
| $f_o$      | 4900 MHz | 4900 MHz |
| $f_m$      | 1050 MHz | 2464 MHz |

#### 2.1.4 Gilbert Damping

In reflective arrays, which are intrinsically multipath devices, effects of ferrite loss must be incorporated into the propagation constant. This is done through a modification of the Polder tensor that results from an



additional term in the torque balance equation. At present, three phenomenological models have been suggested for obtaining this additional term (2.13). Of these, the Gilbert loss model (2.14), which is an adaptation of the Landau-Lifshitz model (2.15), was selected for this work. In this model, the magnitude of the magnetization vector is conserved as it spirals into the bias field in response to loss related precessional slowing (Figure 2.3). Such slowing reduces the gyrotopic torque, allowing the angle of precession to collapse into the bias direction until the resultant reduction in the magnetic torque is sufficient to reestablish the balance. Magnetization spiraling corresponds to an additional component in its vectorial derivative that is directed radially inward with respect to the precessional trajectory. The modified torque balance including the Gilbert loss term that contains this required radial component is,

$$\frac{d\mathbf{M}}{dt} = -|\gamma|\mathbf{M} \times \mathbf{H} + \zeta \frac{\mathbf{M}}{|\mathbf{M}|} \times \frac{d\mathbf{M}}{dt} \quad (2.7e)$$

With the harmonic form of equation (2.12) used for  $\mathbf{M}$  and with  $|\mathbf{M}|$  approximated by  $|\mathbf{M}_0|$ , inclusion of this term is equivalent to replacing the Larmor precession frequency in the lossless case by a complex value,

$$\begin{array}{ccc} f_{oa,b,c} & \longrightarrow & \tilde{f}_{oa,b,c} = f_{oa,b,c} + j\zeta f\left(\frac{M_{oa,b,c}}{|\mathbf{M}_0|}\right), \\ \text{lossless} & & \text{w/Gilbert Loss} \end{array} \quad (2.17)$$

making  $\mu_1$  and  $\mu_2$  complex quantities. For the two bias

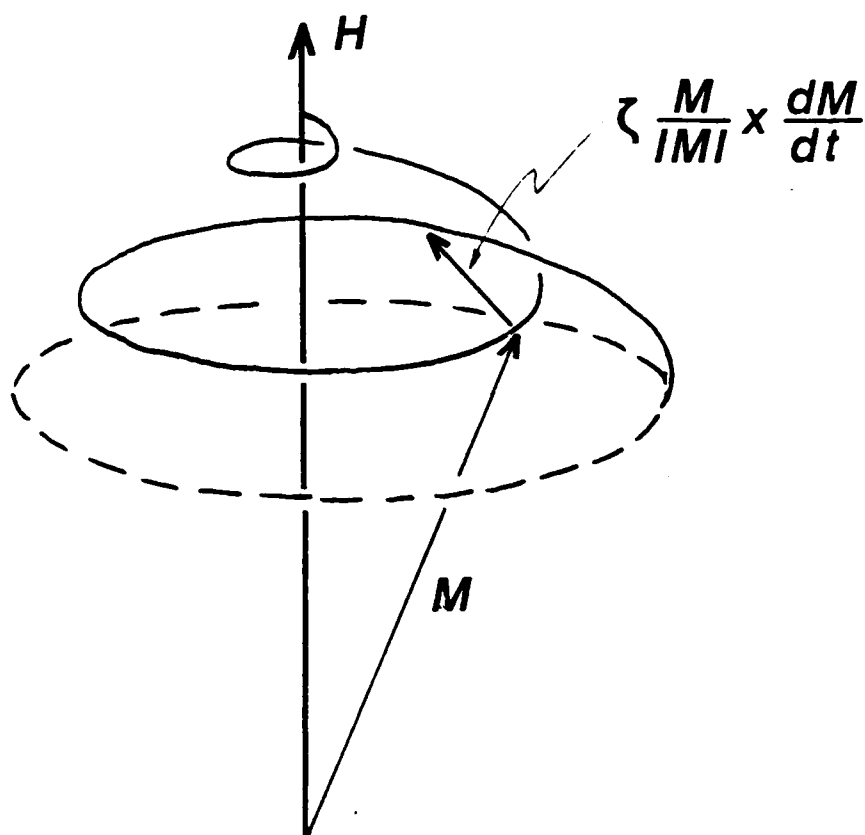


Figure 2.3. Precessional spiraling due to Gilbert damping term.

configurations of interest to this dissertation, the substitution of (2.17) into (2.16a) obtains,

$$\begin{aligned} \tilde{\chi}_{aa} = \tilde{\chi}_{bb} = & \frac{f_m f_o}{4\pi} \frac{\{f_o^2 - f^2(1 + \zeta^2)\} + 2\zeta^2}{\{f_o^2 - f^2(1 + \zeta^2)\}^2 + 4f^2 f_o^2} \\ & - \frac{j}{4\pi} \frac{\zeta f f_m \{f_o^2 + f^2(1 + \zeta^2)\}}{\{f_o^2 - f^2(1 + \zeta^2)\}^2 + 4f^2 f_o^2} \end{aligned} \quad (2.18)$$

$$\tilde{\chi}_{cc} = 1$$

$$\tilde{\chi}_{ab} = \tilde{\chi}_{ba}^* = \frac{f_m f_o}{4\pi} \frac{\{f_o^2 - f^2(1 + \zeta^2)\} + 2\zeta^2}{\{f_o^2 - f^2(1 + \zeta^2)\}^2 + 4f^2 f_o^2}$$

where, the indexes for the non-zero terms are given in TABLE 2.2.

TABLE 2.2

INDEXES FOR NON-ZERO MATRIX ELEMENTS

| MSSW | MSFVW |
|------|-------|
| a=1  | a=2   |
| b=2  | b=3   |
| c=3  | c=1   |

The magnitude of the Gilbert loss term,  $\zeta f$ , establishes the rate of spiraling and can be determined at a given frequency by a single experimental measurement of any quantity that involves it as the sole unknown. Measurement of the linewidth,  $\Delta H$ , is ordinarily used for this purpose, and is defined as the difference in bias field values at which the imaginary part of a diagonal component of the

susceptibility tensor attains half the resonant value (Figure 2.4). Using this definition, the linewidth obtained from equation (2.18) and shown in Figure 2.4 is,

$$\Delta H = \frac{4\pi\zeta f}{|\gamma|}, \quad (2.19)$$

which can be used to replace,  $\zeta f$ , in equation (2.17),

$$\tilde{f}_{oa,b,c} = f_{oa,b,c} + j\zeta f \left\{ \frac{M_{oa,b,c}}{|M_o|} \right\}. \quad (2.20)$$

This linewidth can be experimentally determined from the absorption notch of  $\tilde{S}_{11}$  observed in a waveguide measurement, because the two resonances exhibit the same aspect ratio.

A relative measurement such as this has the advantage of normalizing out the effects of coupling efficiency, ferrite sample size, and other proportionality factors between the resonance curves. Results from a typical linewidth measurement for a polished YIG sphere as a function of frequency at room temperature with  $H_o$  along the [111] axis are shown in Figure 2.5, from von Aulock [2.16]. A convenient approximation to this curve for use in numerical calculations is,

$$\Delta H \cong \frac{\Delta H_{\min}}{2} \left\{ \frac{f_{\min}}{f} + \frac{f}{f_{\min}} \right\} \quad (2.21)$$

where,

$\Delta H_{\min}$  = Minimum  $\Delta H$  [Oe]

$f_{\min}$  = Frequency at  $\Delta H = \Delta H_{\min}$  [GHz]

$f$  = Operating frequency [GHz]

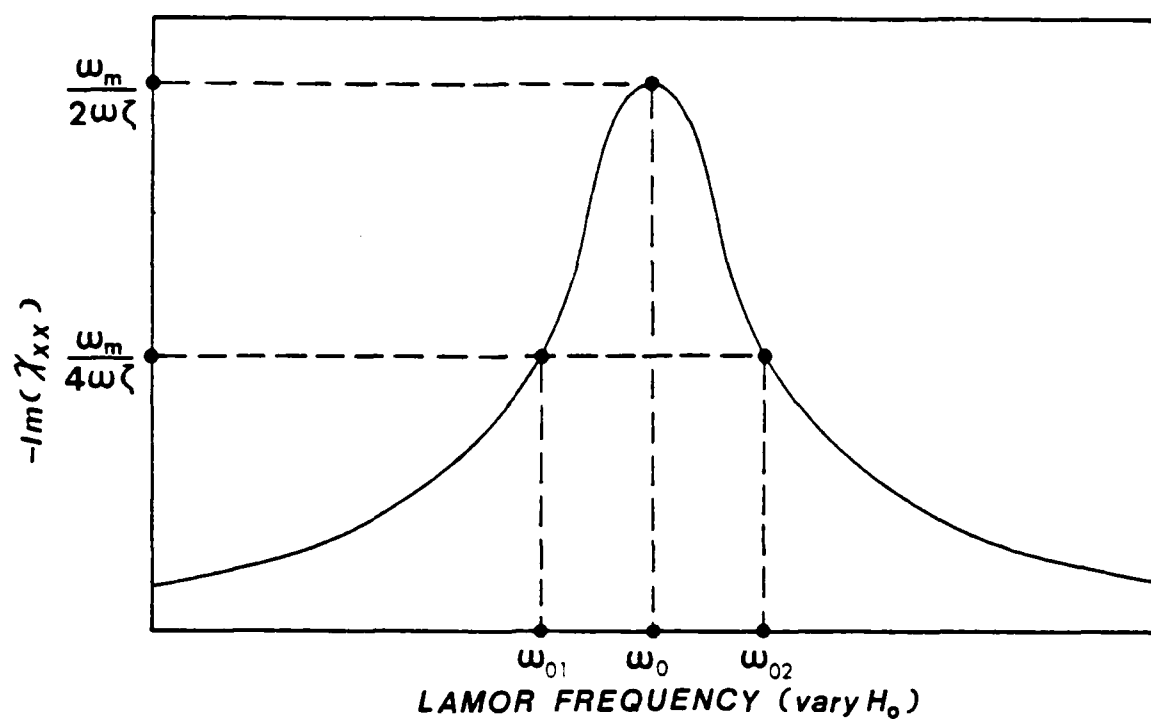


Figure 2.4. Resonance characteristic of the imaginary part of a diagonal term in the susceptibility tensor.

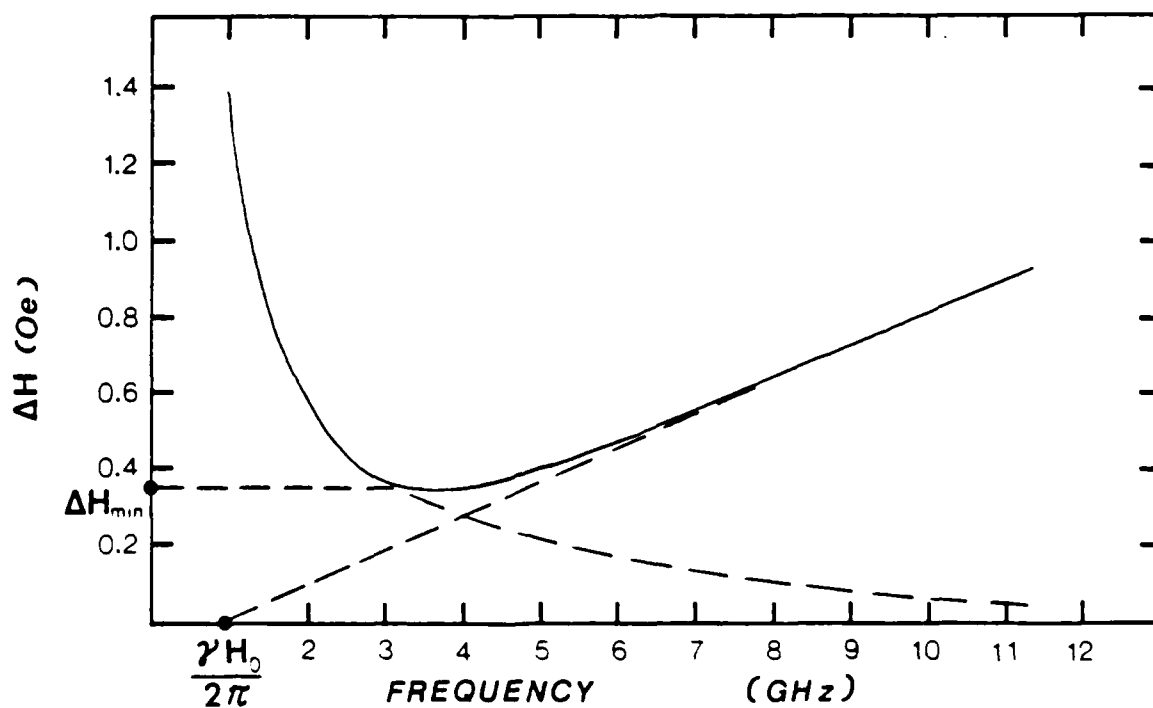


Figure 2.5. Linewidth of a polished YIG sphere at room temperature with  $H_0$  along [111] (von Aulock).

Incorporating ferrite losses in this manner appends an imaginary component to the propagation, corresponding to propagation loss in the field solutions and phase shifting upon reflection from an interface between implanted and unimplanted zones.

#### 2.1.5 Effects of Ion Implanting the Ferrite

Ion implantation has been in use for some time in the production of magnetic bubble devices {2.17}. The damage done to the lattice by ion bombardment causes the lattice to expand. If selective implantation of small regions is done, they are held in lateral compression by the adjacent regions, and the lattice expands only in a direction normal to the surface. Ferromagnetic resonance measurements on ion implanted garnet films {2.18, 2.19} have confirmed that the principal effects of ion implantation are a reduction in the uniaxial anisotropy and a reduction in the saturation magnetization. For small strains, the magnetostriction constant in the direction perpendicular to the surface can be used to estimate the degree of crystal damage and hence the fractional change in saturation magnetization.

MacNeal and Speriosu {2.20} reported on multiple implant techniques, varified by X-ray diffraction measurements, that can be used to determine the required doses and energies for a variety of strain profiles. For the proposes of modeling, it is desireable to have a constant

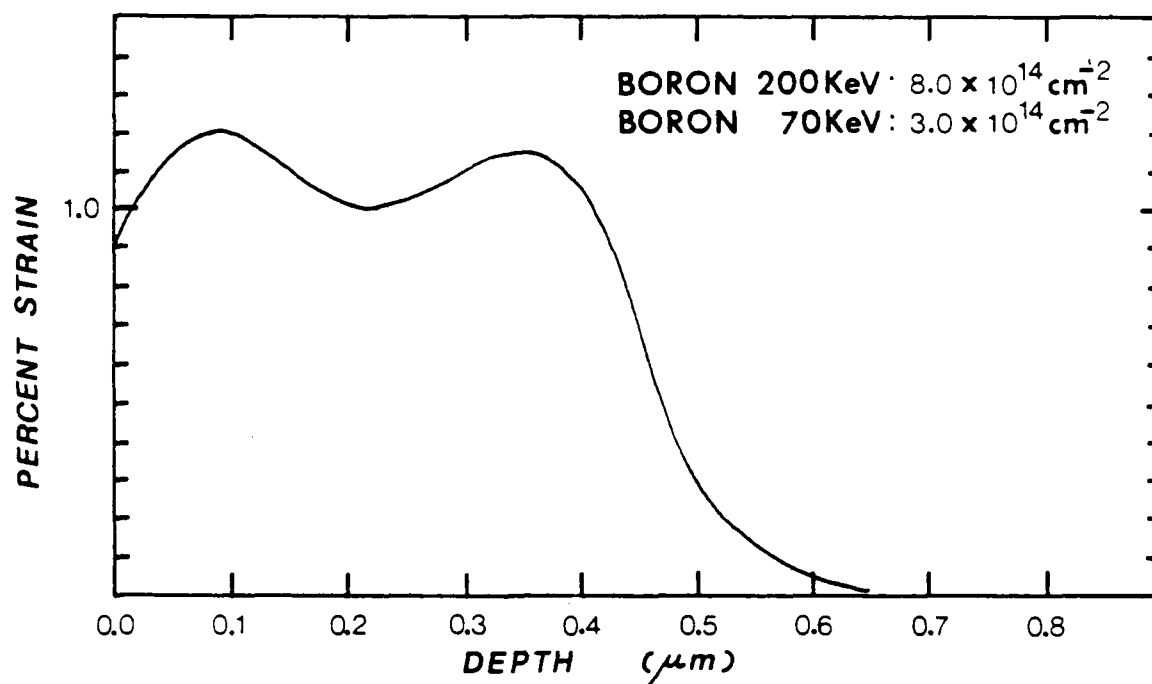


Figure 2.6. Strain profile for a double dose boron implant in YSmTmCaGeIG (from MacNeal and Speriosu).

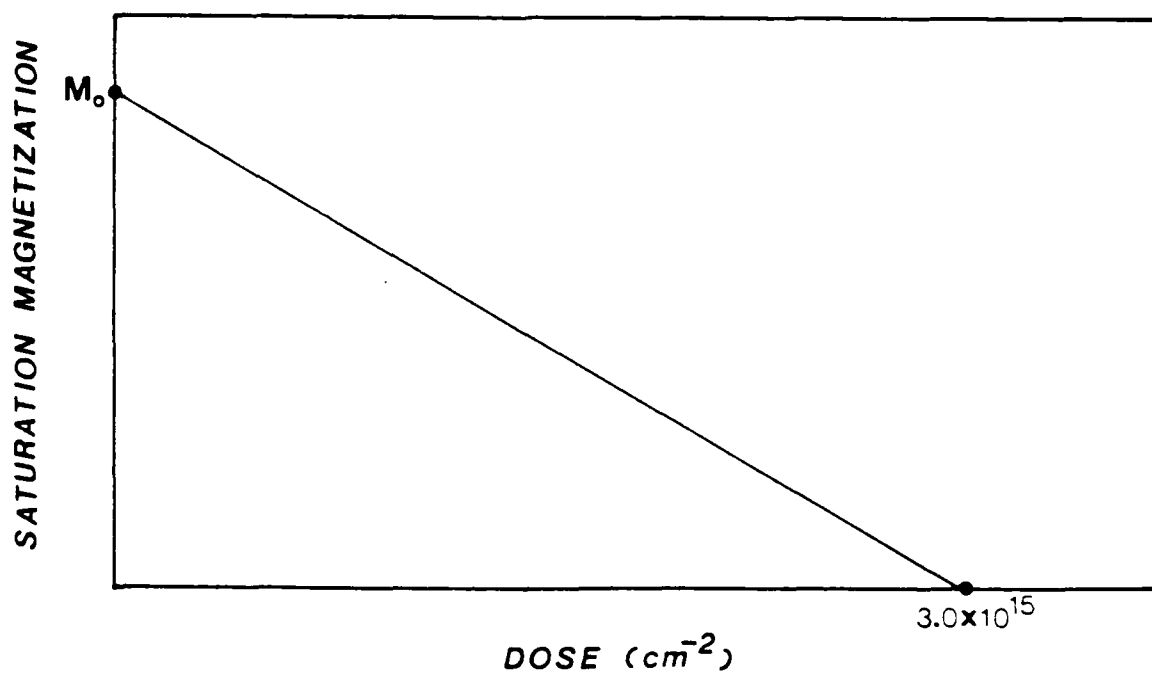


Figure 2.7. Projected magnetization change versus implant dose.

strain profile to the depth of the implant. MacNeal and Speriosu (Figure 2.6) demonstrated that a double staggered  $B^+$  implant with an initial fluence of  $8.0 \times 10^{14}$  ions/cm<sup>2</sup> at 200 KeV followed by a fluence of  $3.0 \times 10^{14}$  ions/cm<sup>2</sup> at 70 KeV in a 2  $\mu$ m thick YSmTmCaGeIG film produced a strain of  $1.07 \pm 0.09$  % to a depth of 0.36  $\mu$ m. Since these studies were based on bubble materials with about the same density as YIG and utilized the same crystallographic orientation as that used in the MSW work, the doses of that example were scaled to obtain the desired bar reflectivities. Exact data was not available for magnetization change versus dose, but the aforementioned studies [2.21] indicate that a dose of about  $3.0 \times 10^{15}$  ions/cm<sup>2</sup> renders the material paramagnetic. Using this known endpoint and that for zero strain, a linear interpolation was done to approximate the dosage necessary to achieve the required scaling of the saturation magnetization in the implanted layer that would yield the desired bar edge reflectivities (Figure 2.7).

#### 2.1.6 Solutions of the Magnetostatic Equation

Subject to the foregoing material model, the magnetostatic equation, (2.4a), simplifies to Laplace's equation in the dielectric and MSSW biased ferrite regions,

$$\frac{\partial^2 \tilde{V}_m}{\partial x^2} + \frac{\partial^2 \tilde{V}_m}{\partial y^2} = 0, \quad (2.4b)$$

which has the solution set given in TABLE 2.3a.



TABLE 2.3a

## MSSW BIASED FERRITE AND DIELECTRIC SOLUTION SET

| $\frac{1}{\tilde{A}(a)} \frac{\partial^2 \tilde{A}(f)}{\partial a^2} = \tilde{k}^2$ | $\frac{1}{\tilde{B}(b)} \frac{\partial^2 \tilde{B}(f)}{\partial b^2} = -\tilde{k}^2$ |
|---|--|
| $\cosh\{\tilde{k}a\}$   | $\exp\{j\tilde{k}b\}$  |
| $\sinh\{\tilde{k}a\}$   | $\exp\{-j\tilde{k}b\}$   |

Conversely, application of the MSFVW bias field conditions results in a "modified" Laplace's equation,

$$\frac{\partial^2 \tilde{V}_m}{\partial x^2} + \tilde{\mu}_1 \frac{\partial^2 \tilde{V}_m}{\partial y^2} = 0, \quad (2.4c)$$

with solutions given in TABLE 2.3b.

TABLE 2.3b

## MSFVW BIASED FERRITE SOLUTION SET

| $\frac{1}{\tilde{A}(a)} \frac{\partial^2 \tilde{A}(f)}{\partial a^2} = -(\tilde{\eta}k)^2$ | $\frac{1}{\tilde{B}(b)} \frac{\partial^2 \tilde{B}(f)}{\partial b^2} = -\tilde{k}^2$ |
|--|--|
| $\cos\{\tilde{\eta}ka\}$   | $\exp\{j\tilde{k}b\}$  |
| $\sin\{\tilde{\eta}ka\}$   | $\exp\{-j\tilde{k}b\}$   |
| $\tilde{\eta} = \sqrt{-\tilde{\mu}_1}$   |  |

An implicit harmonic time dependence,  $\exp(2\pi ft)$ , was adopted at the time the Polder tensor was developed. With small signal limitations, no loss of generality is accrued by this assumption, since with a linear system, any periodic

excitation satisfying the Dirichlet conditions in time or space can be represented by an exponential Fourier expansion.

It is arbitrary which directions these solutions are assigned to, as it is the dispersion relation that fixes directional behavior. However, associating the  $\tilde{B}(b)$  solution with the y-direction produces an immediately identifiable wave nature in that dimension.

#### 2.1.7 The Four Layer Boundary Value Problem

In cross section, the structure used to calculate the dispersion relation consisted of adjacent implanted and unimplanted ferrite layers sandwiched by dielectric layers, bound on the outside by ground planes as shown in Figure 2.8. The transducer filaments are located on the boundary common to the microstrip dielectric and ferrite (regions 1 and 2), entering into the model as z-directed sheet current densities. As a consequence of the solenoidal law, the normal components of the b-fields must be continuous across the interfaces separating the various regions. Application of Ampere's law requires continuity in the tangential components of the h-fields except where interrupted by the sheet current densities representing transducer filaments. Neglecting skin effect, these boundary conditions imply that the normal components of both  $\tilde{b}$  and  $\tilde{h}$  in the dielectric regions must vanish at the ground plane conductor surfaces. Considering forward and reverse propagation separately, the harmonic potentials derived from the set of eigenfunctions in

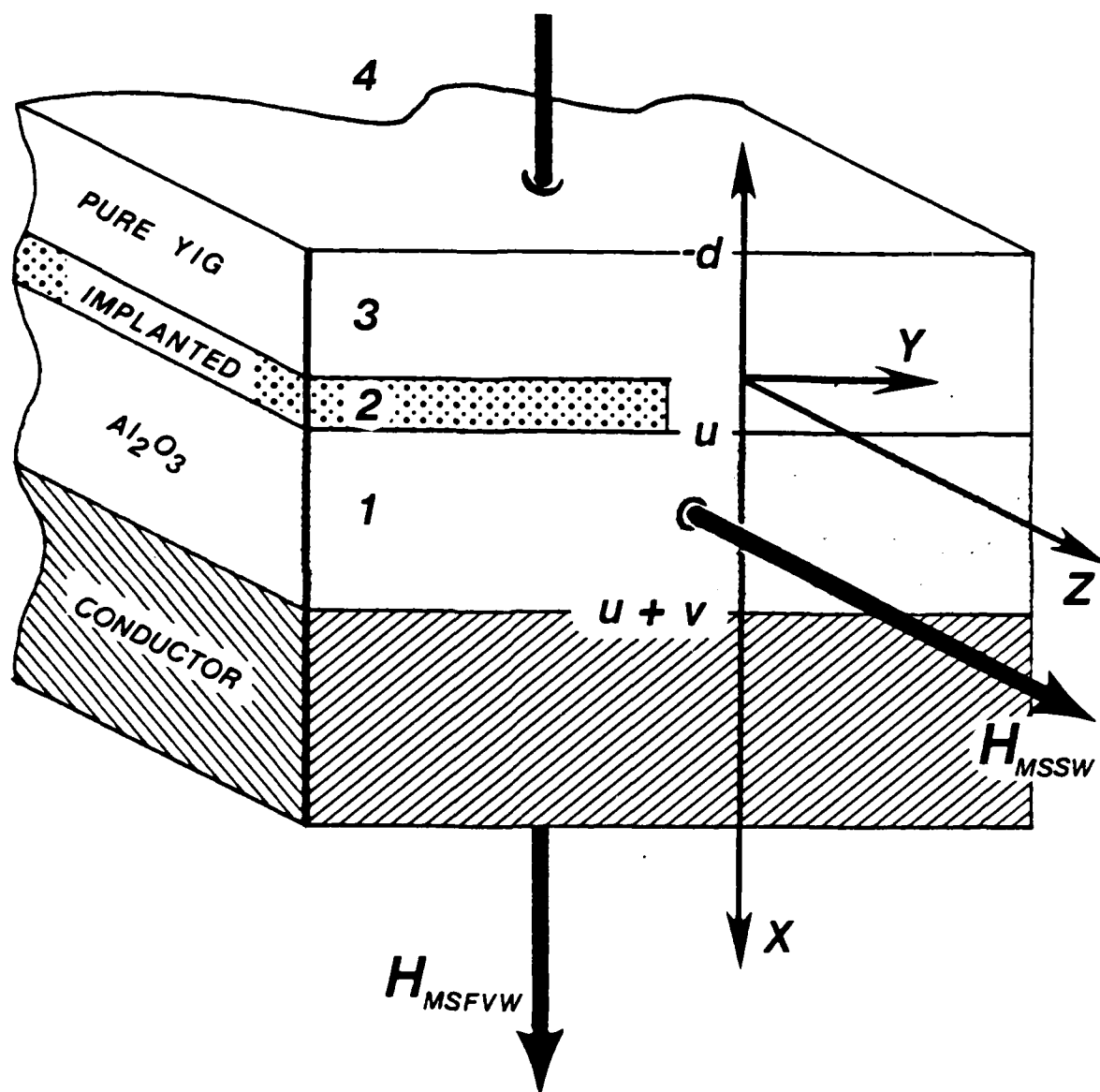


Figure 2.8. The layered structure used to calculate the dispersion relation.

TABLE 2.3 that satisfy this ground plane condition are given in equation (2.24) for MSSW and in equation (2.25) for MSFVW along with the corresponding harmonic solutions for the  $b$  and  $h$  fields that were calculated from the gradient relation in equation (2.3) and the constitutive relation respectively.

$$\tilde{V}_{m1}(\tilde{k}) = \tilde{A} \cosh[\tilde{k}(x-u-v)] \exp(-j\tilde{k}y) \quad (2.24a)$$

$$\tilde{V}_{m2}(\tilde{k}) = \{\tilde{B} \exp(\tilde{k}x) + \tilde{C} \exp(-\tilde{k}x)\} \exp(-j\tilde{k}y)$$

$$\tilde{V}_{m3}(\tilde{k}) = \{\tilde{D} \exp(\tilde{k}x) + \tilde{E} \exp(-\tilde{k}x)\} \exp(-j\tilde{k}y)$$

$$\tilde{V}_{m4}(\tilde{k}) = \tilde{F} \cosh[\tilde{k}(x+d+s)] \exp(-j\tilde{k}y)$$

$$\tilde{h}_1(\tilde{k}) = \tilde{A}\tilde{k} \sinh[\tilde{k}(x-u-v)] \exp(-j\tilde{k}y) \hat{x} \quad (2.24b)$$

$$-j\tilde{A}\tilde{k} \cosh[\tilde{k}(x-u-v)] \exp(-j\tilde{k}y) \hat{y}$$

$$\tilde{h}_2(\tilde{k}) = \tilde{k}\{\tilde{B} \exp(\tilde{k}x) - \tilde{C} \exp(-\tilde{k}x)\} \exp(-j\tilde{k}y) \hat{x}$$

$$-j\tilde{k}\{\tilde{B} \exp(\tilde{k}x) + \tilde{C} \exp(-\tilde{k}x)\} \exp(-j\tilde{k}y) \hat{y}$$

$$\tilde{h}_3(\tilde{k}) = \tilde{k}\{\tilde{D} \exp(\tilde{k}x) - \tilde{E} \exp(-\tilde{k}x)\} \exp(-j\tilde{k}y) \hat{x}$$

$$-j\tilde{k}\{\tilde{D} \exp(\tilde{k}x) + \tilde{E} \exp(-\tilde{k}x)\} \exp(-j\tilde{k}y) \hat{y}$$

$$\tilde{h}_4(\tilde{k}) = \tilde{F}\tilde{k} \sinh[\tilde{k}(x+d+s)] \exp(-j\tilde{k}y) \hat{x}$$

$$-j\tilde{F}\tilde{k} \cosh[\tilde{k}(x+d+s)] \exp(-j\tilde{k}y) \hat{y}$$

$$\tilde{b}_1(\tilde{k}) = \mu_0 \tilde{A}\tilde{k} \sinh[\tilde{k}(x-u-v)] \exp(-j\tilde{k}y) \hat{x} \quad (2.24c)$$

$$-j\mu_0 \tilde{A}\tilde{k} \cosh[\tilde{k}(x-u-v)] \exp(-j\tilde{k}y) \hat{y}$$

$$\tilde{b}_2(\tilde{k}) = \mu_0 \tilde{k}\{\tilde{B}\tilde{U}_1^1 \exp(\tilde{k}x) - \tilde{C}\tilde{U}_1^2 \exp(-\tilde{k}x)\} \exp(-j\tilde{k}y) \hat{x}$$

$$-j\mu_0 \tilde{k}\{\tilde{B}\tilde{U}_1^1 \exp(\tilde{k}x) + \tilde{C}\tilde{U}_1^2 \exp(-\tilde{k}x)\} \exp(-j\tilde{k}y) \hat{y}$$

$$\tilde{b}_3(\tilde{k}) = \mu_0 \tilde{k}\{\tilde{D}\tilde{U}_U^1 \exp(\tilde{k}x) - \tilde{E}\tilde{U}_U^2 \exp(-\tilde{k}x)\} \exp(-j\tilde{k}y) \hat{x}$$

$$-j\mu_0 \tilde{k}\{\tilde{D}\tilde{U}_U^1 \exp(\tilde{k}x) + \tilde{E}\tilde{U}_U^2 \exp(-\tilde{k}x)\} \exp(-j\tilde{k}y) \hat{y}$$

$$\begin{aligned}\tilde{b}_4(\tilde{k}) &= \mu_0 \tilde{F} \tilde{k} \sinh[\tilde{k}(x+d+s)] \exp(-j\tilde{k}y) \hat{x} \\ &\quad - j\mu_0 \tilde{F} \tilde{k} \cosh[\tilde{k}(x+d+s)] \exp(-j\tilde{k}y) \hat{y}\end{aligned}$$

$$\begin{aligned}\text{where, } \tilde{U}_\xi^1 &= \tilde{\mu}_{\xi 1} - \tilde{\mu}_{\xi 2} \\ \tilde{U}_\xi^2 &= \tilde{\mu}_{\xi 1} + \tilde{\mu}_{\xi 2} \\ \xi &= \begin{cases} i, & \text{implanted} \\ u, & \text{unimplanted} \end{cases}\end{aligned}$$

$$\begin{aligned}\tilde{V}_{m1}(\tilde{k}) &= \tilde{A} \cosh[\tilde{k}(x-u-v)] \exp(-j\tilde{k}y) & (2.25a) \\ \tilde{V}_{m2}(\tilde{k}) &= \{\tilde{B} \sin(\tilde{\eta}_i \tilde{k}x) + \tilde{C} \cos(\tilde{\eta}_i \tilde{k}x)\} \exp(-j\tilde{k}y) \\ \tilde{V}_{m3}(\tilde{k}) &= \{\tilde{D} \sin(\tilde{\eta}_u \tilde{k}x) + \tilde{E} \cos(\tilde{\eta}_u \tilde{k}x)\} \exp(-j\tilde{k}y) \\ \tilde{V}_{m4}(\tilde{k}) &= \tilde{F} \cosh[\tilde{k}(x+d+s)] \exp(-j\tilde{k}y)\end{aligned}$$

$$\begin{aligned}\tilde{h}_1(\tilde{k}) &= \tilde{A} \tilde{k} \sinh[\tilde{k}(x-u-v)] \exp(-j\tilde{k}y) \hat{x} & (2.25b) \\ &\quad - j\tilde{A} \tilde{k} \cosh[\tilde{k}(x-u-v)] \exp(-j\tilde{k}y) \hat{y} \\ \tilde{h}_2(\tilde{k}) &= \tilde{\eta}_i \tilde{k} \{\tilde{B} \cos(\tilde{\eta}_i \tilde{k}x) - \tilde{C} \sin(\tilde{\eta}_i \tilde{k}x)\} \exp(-j\tilde{k}y) \hat{x} \\ &\quad - j\tilde{k} \{\tilde{B} \sin(\tilde{\eta}_i \tilde{k}x) + \tilde{C} \cos(\tilde{\eta}_i \tilde{k}x)\} \exp(-j\tilde{k}y) \hat{y} \\ \tilde{h}_3(\tilde{k}) &= \tilde{\eta}_u \tilde{k} \{\tilde{D} \cos(\tilde{\eta}_u \tilde{k}x) - \tilde{E} \sin(\tilde{\eta}_u \tilde{k}x)\} \exp(-j\tilde{k}y) \hat{x} \\ &\quad - j\tilde{k} \{\tilde{D} \sin(\tilde{\eta}_u \tilde{k}x) + \tilde{E} \cos(\tilde{\eta}_u \tilde{k}x)\} \exp(-j\tilde{k}y) \hat{y} \\ \tilde{h}_4(\tilde{k}) &= \tilde{F} \tilde{k} \sinh[\tilde{k}(x+d+s)] \exp(-j\tilde{k}y) \hat{x} \\ &\quad - j\tilde{F} \tilde{k} \cosh[\tilde{k}(x+d+s)] \exp(-j\tilde{k}y) \hat{y}\end{aligned}$$

$$\begin{aligned}\tilde{b}_1(\tilde{k}) &= \mu_0 \tilde{A} \tilde{k} \sinh[\tilde{k}(x-u-v)] \exp(-j\tilde{k}y) \hat{x} & (2.25c) \\ &\quad - j\mu_0 \tilde{A} \tilde{k} \cosh[\tilde{k}(x-u-v)] \exp(-j\tilde{k}y) \hat{y} \\ \tilde{b}_2(\tilde{k}) &= \mu_0 \tilde{\eta}_i \tilde{k} \{\tilde{B} \cos(\tilde{\eta}_i \tilde{k}x) - \tilde{C} \sin(\tilde{\eta}_i \tilde{k}x)\} \exp(-j\tilde{k}y) \hat{x} \\ &\quad - j\mu_0 \tilde{U}_{i1} \tilde{k} \{\tilde{B} \sin(\tilde{\eta}_i \tilde{k}x) + \tilde{C} \cos(\tilde{\eta}_i \tilde{k}x)\} \exp(-j\tilde{k}y) \hat{y} \\ &\quad + \mu_0 \tilde{U}_{i2} \tilde{k} \{\tilde{B} \sin(\tilde{\eta}_i \tilde{k}x) + \tilde{C} \cos(\tilde{\eta}_i \tilde{k}x)\} \exp(-j\tilde{k}y) \hat{z}\end{aligned}$$

$$\begin{aligned}
\tilde{b}_3(\tilde{k}) &= \mu_0 \tilde{\eta}_U \tilde{k} \{ \tilde{D} \cos(\tilde{\eta}_U \tilde{k} x) - \tilde{E} \sin(\tilde{\eta}_U \tilde{k} x) \} \exp(-j\tilde{k}y) \hat{x} \\
&\quad - j\mu_0 \tilde{U}_{U1} \tilde{k} \{ \tilde{D} \sin(\tilde{\eta}_U \tilde{k} x) + \tilde{E} \cos(\tilde{\eta}_U \tilde{k} x) \} \exp(-j\tilde{k}y) \hat{y} \\
&\quad + \mu_0 \tilde{U}_{U2} \tilde{k} \{ \tilde{D} \sin(\tilde{\eta}_U \tilde{k} x) + \tilde{E} \cos(\tilde{\eta}_U \tilde{k} x) \} \exp(-j\tilde{k}y) \hat{z} \\
\tilde{b}_4(\tilde{k}) &= \mu_0 \tilde{F} \tilde{k} \sinh[\tilde{k}(x+d+s)] \exp(-j\tilde{k}y) \hat{x} \\
&\quad - j\mu_0 \tilde{F} \tilde{k} \cosh[\tilde{k}(x+d+s)] \exp(-j\tilde{k}y) \hat{y}
\end{aligned}$$

where,

$$\begin{aligned}
\tilde{\eta}_i &= \sqrt{-\tilde{\mu}_{i1}} \quad ; \text{ in the implanted region,} \\
\tilde{\eta}_U &= \sqrt{-\tilde{\mu}_{U1}} \quad ; \text{ in the unimplanted region}
\end{aligned}$$

These solutions are the spacial harmonics at a given frequency with  $\tilde{k}$  representing the "guide" propagation constant along the y-direction in the layered structure. Energy can propagate in a continuum of directions within the x-y plane (the structure is assumed infinite in the z-direction) corresponding to a continuous distribution of  $\tilde{k}$ -values along the y-direction. In order to accomodate the general guide boundary condition at a particular frequency, a linear combination of these spacial harmonics in the form of an inverse Laplace transform is required,

$$\tilde{H}_i(x, y, f) = \frac{1}{2\pi j} \int_{-\alpha-j\infty}^{-\alpha+j\infty} \tilde{h}_i(x, \tilde{k}, f) d(j\tilde{k}) \quad (2.26a)$$

Integration is carried out over the Bromwich contour in the left half  $\tilde{k}$ -plane, with "α" representing the absolute loss factor associated with the y-direction. Superposition of the resulting frequency spectral components multiplied by the adopted basis function,  $\exp(j2\pi ft)$ , in the form of a Fourier

inverse transform,

$$\tilde{v}_i(x,y,t) = \int_{-\infty}^{\infty} \tilde{H}_i(x,y,f) e^{j2\pi ft} df \quad (2.26b)$$

yields the time response that would be intercepted at the (x,y) point of observation.

The spacial harmonics are linearly independent for different values of  $\tilde{k}$ , which requires that they separately satisfy the boundary conditions. Application of the electromagnetic boundary conditions to the individual spacial harmonics accross the internal boundaries generates six equations in each bias configuration for the frequency dependent coefficients  $\tilde{A}$ ,  $\tilde{B}$ ,  $\tilde{C}$ ,  $\tilde{D}$ ,  $\tilde{E}$ , and  $\tilde{F}$ , as given in equations (2.27) and (2.28).

MSSW (2.27)

$$\begin{bmatrix} \sinh(\tilde{k}v) & 0 & 0 & 0 & \tilde{U}_1^1 \exp(\tilde{k}u) & -\tilde{U}_1^2 \exp(-\tilde{k}u) \\ 0 & \tilde{U}_1^1 & -\tilde{U}_1^2 & 0 & -\tilde{U}_1^1 & \tilde{U}_1^2 \\ 0 & \tilde{U}_1^1 \exp(-\tilde{k}d) & -\tilde{U}_1^2 \exp(\tilde{k}d) & -\sinh(\tilde{k}s) & 0 & 0 \\ \cosh(\tilde{k}v) & 0 & 0 & 0 & -\exp(\tilde{k}u) & -\exp(-\tilde{k}u) \\ 0 & 1 & 1 & 0 & -1 & -1 \\ 0 & \exp(-\tilde{k}d) & \exp(\tilde{k}d) & -\cosh(\tilde{k}s) & 0 & 0 \end{bmatrix} \begin{bmatrix} \tilde{A} \\ \tilde{B} \\ \tilde{C} \\ \tilde{D} \\ \tilde{E} \\ \tilde{F} \end{bmatrix} = \begin{bmatrix} 0 \\ 0 \\ 0 \\ \tilde{I}(\tilde{k}) \\ 0 \\ 0 \end{bmatrix}$$

MSFVW (2.28)

$$\begin{bmatrix} \sinh(\tilde{k}v) & 0 & 0 & 0 & \tilde{n}_1 \cos(\tilde{n}_1 \tilde{k}u) & -\tilde{n}_1 \sin(\tilde{n}_1 \tilde{k}u) \\ \cosh(\tilde{k}v) & 0 & 0 & 0 & -\sin(\tilde{n}_1 \tilde{k}u) & -\cos(\tilde{n}_1 \tilde{k}u) \\ 0 & \tilde{n}_1 & 0 & 0 & -\tilde{n}_1 & 0 \\ 0 & 0 & 0 & 0 & 0 & -1 \\ 0 & \tilde{n}_1 \cos(\tilde{n}_1 \tilde{k}d) & \tilde{n}_1 \sin(\tilde{n}_1 \tilde{k}d) & -\sinh(\tilde{k}s) & 0 & 0 \\ 0 & \sin(\tilde{n}_1 \tilde{k}d) & -\cos(\tilde{n}_1 \tilde{k}d) & \cosh(\tilde{k}s) & 0 & 0 \end{bmatrix} \begin{bmatrix} \tilde{A} \\ \tilde{B} \\ \tilde{C} \\ \tilde{D} \\ \tilde{E} \\ \tilde{F} \end{bmatrix} = \begin{bmatrix} 0 \\ \tilde{I}(\tilde{k}) \\ 0 \\ 0 \\ 0 \\ 0 \end{bmatrix}$$

Matching at each value of  $\tilde{k}$  across the interface containing the transducer filaments requires that the sheet currents be expressed in terms of the Laplace transform,

$$\tilde{I}(\tilde{k}) = \int_{-\infty}^{\infty} K_z(y) \exp\{j\tilde{k}y\} dy, \quad (2.29)$$

to be consistent with the representation of the spacial harmonics.

All of the  $\tilde{k}$ 's in the above expressions represent the y-projections of the total propagation vectors in the guiding structure. Bias field induced anisotropy causes the magnitude of the total propagation vector (a characteristic of the material and direction, independent of boundary conditions: frequency  $\leftrightarrow$  velocity  $\leftrightarrow$  wavelength) to vary with direction. In addition to this effect, a continuum of wavelengths and hence guide propagation constants can be projected onto the y-direction by simply varying the angle of the total propagation vector relative to that direction. At any given frequency, only certain of these total propagation vectors satisfy the boundary conditions established by the interfaces between the various regions in the guide. The relationship between frequency and the y-projections of the characteristic propagation vectors determines the spacial modes that are launched from the transducers as well as the propagation behavior of these modes in the regions between the transducers. Since this dispersion relation is a characteristic of the guiding structure, it is independent of



the excitation currents and can be obtained by setting the current contribution to zero in the above equations and looking for nontrivial solutions. The set of homogeneous equations that result have nontrivial solutions only if one of them is linearly dependent on the others, which is equivalent to requiring that the determinant of the coefficients be identically zero. Dispersion relations obtained in this manner for MSSW and MSFVW are given in equations (2.30) and (2.31), respectively.

#### MSSW

$$\exp(2\tilde{k}d) = \frac{(\tilde{U}_n^1 - \tanh(\tilde{k}s))([\tilde{U}_i^1 + \tilde{U}_U^2][\tilde{U}_i^2 - \tanh(\tilde{k}v)] + [\tilde{U}_U^2 - \tilde{U}_i^2][\tilde{U}_i^1 + \tanh(\tilde{k}v)]\exp(+2\tilde{k}u))}{(\tilde{U}_U^2 + \tanh(\tilde{k}s))([\tilde{U}_U^1 - \tilde{U}_i^1][\tilde{U}_i^2 - \tanh(\tilde{k}v)] + [\tilde{U}_i^2 + \tilde{U}_U^1][\tilde{U}_i^1 + \tanh(\tilde{k}v)]\exp(2\tilde{k}u))} \quad (2.30)$$

#### MSFVW

$$\tan\{\tilde{k}(\tilde{\eta}_i u + \tilde{\eta}_U d)\} = \frac{\tilde{\eta}_i \tanh(\tilde{k}s) + \tilde{\eta}_U \tanh(\tilde{k}v)}{\tilde{\eta}_i \tilde{\eta}_U - \tanh(\tilde{k}s) \tanh(\tilde{k}v)} \quad (2.31)$$

Distribution of fields in these two bias configurations is governed by the tendency to minimize the energy stored in the wave, which translates into concentrating the fields into regions in which the material characteristics result in minimum energy density for a given field intensity. The energy density in a magnetic field is proportional to the product of the magnetic field intensity and magnetic induction.

In MSSW the orientation of the electronic spins places the dominant magnetic field component parallel to the plane

of the ferrite film. Continuity in this tangential component of the magnetic field at the surfaces of the ferrite,

$$B_{t\{\text{dielectric}\}} = B_{t\{\text{ferrite}\}} - 4\pi M_t, \quad (2.32)$$

results in a weaker dominant induction field outside the ferrite film. Thus, the MSSW attaches itself to the film surface so as to concentrate its fields in the dielectric where the material properties allow the energy density to be lower. MSSW attachment to the film surfaces results in a composite wave made up of separate top and bottom surface counterparts. At high frequencies these two surface wave counterparts experience essentially the same ground plane spacing and propagate with the same dispersion relation. However, at lower frequencies (near the lower cut off) an operating region is entered in which the wavelengths become long enough for the waves to be significantly perturbed by the proximity of the ground plane. In this region the bottom surface wave, being closer to the ground plane, is affected more than the top surface wave, and the dispersion relations become distinct. As even longer wavelengths are considered, the film thickness constituting the distinction, becomes negligible compared to a wavelength, and the two dispersion relations merge once more.

The adopted phase dependence,  $\exp[j[2\pi ft - \tilde{k}y]]$ , shows that reverse propagation corresponds to replacing frequency by minus frequency. This substitution conjugates the Polder

tensor, which in MSSW results in a difference between the forward and reverse propagation characteristics, representing anisotropic behavior. Even though the total propagation vector for surface bound MSSWs does not penetrate the film, a continuum of y-projected wavelengths are possible by varying the angle formed by the total propagation vector with the y-direction in the plane of the film.

In the MSFVW configuration, alignment of the electronic spins result in a dominant magnetic field that is normal to the film surface. Continuity of the corresponding normal component of the magnetic induction field at the ferrite surfaces shows that the magnetic field is stronger in the dielectric,

$$H_{n(\text{dielectric})} = H_{n(\text{ferrite})} + 4\pi M_n, \quad (2.33)$$

favoring field concentration in the bulk of the ferrite in order to minimize energy density. Thus a single volume distribution of energy is indicated, and the rotational symmetry of the structure in the absence of significant crystalline anisotropy about a normal to the plane of the film requires that this single wave have the same propagation characteristics in all directions in the plane of the film. Correspondingly, the effects of conjugating the Polder tensor can be factored out of the MSFVW dispersion relation, indicating isotropic propagation characteristics.

Another consequence of surface attachment in the lossless case of MSSW is single forward and reverse guide propagation modes, since the wave has only one path available to it. Mathematically, this is manifested in the fact that the dispersion relation is made up of single-branch functions for a real argument. Including ferrite loss introduces multimode MSSW behavior, with the various branches of  $\tilde{k}$  confined to corridors parallel to the real axis in the complex plane. This indicates that the introduction of loss frees the MSSW from being surface bound, allowing it to interact with the top and bottom surfaces of the ferrite in the same way as do MSFVWs. The dominant mode lies in the branch nearest to the origin where actual path lengths and hence propagation losses are least.

Conversely, MSFVWs are intrinsically free to interact with both top and bottom surfaces of the ferrite and exhibit multimode behavior even in the lossless case. In the dispersion relation this is characterized by the multibranch nature of the inverse tangent function for a real argument ( $\mu_1 < 0$ ). These modes, often called thickness modes, are associated with the finite thickness of the ferrite film. From a ray-optics point of view, the waves bounce back and forth between effective mirror planes in the vicinity of the top and bottom surfaces of the ferrite as they travel along the structure. At any given frequency, only certain trajectories satisfy the boundary conditions at both top and

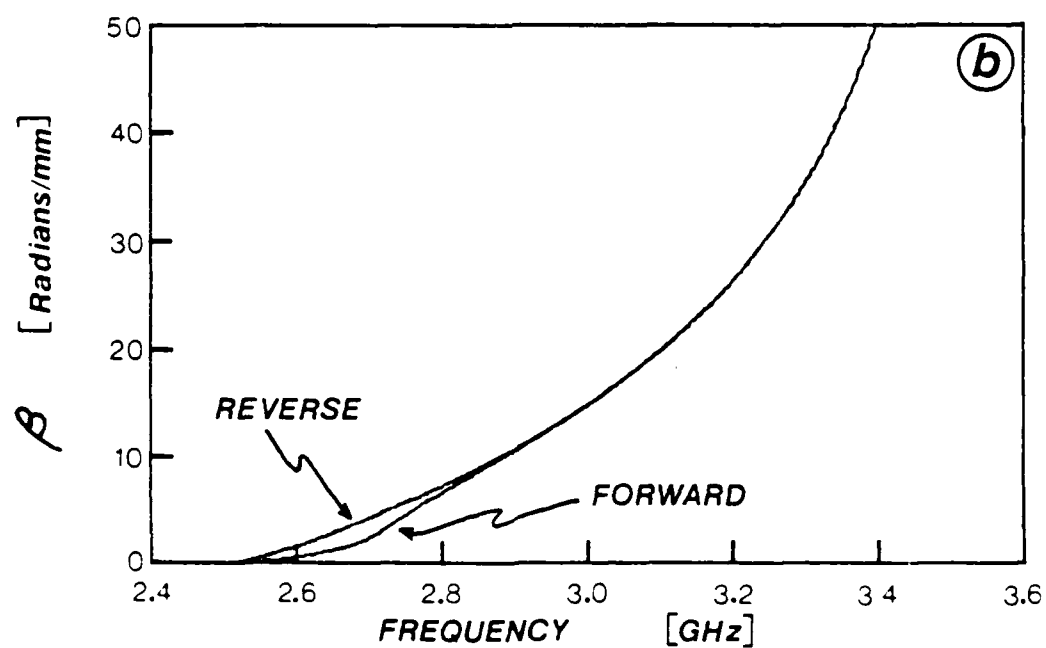
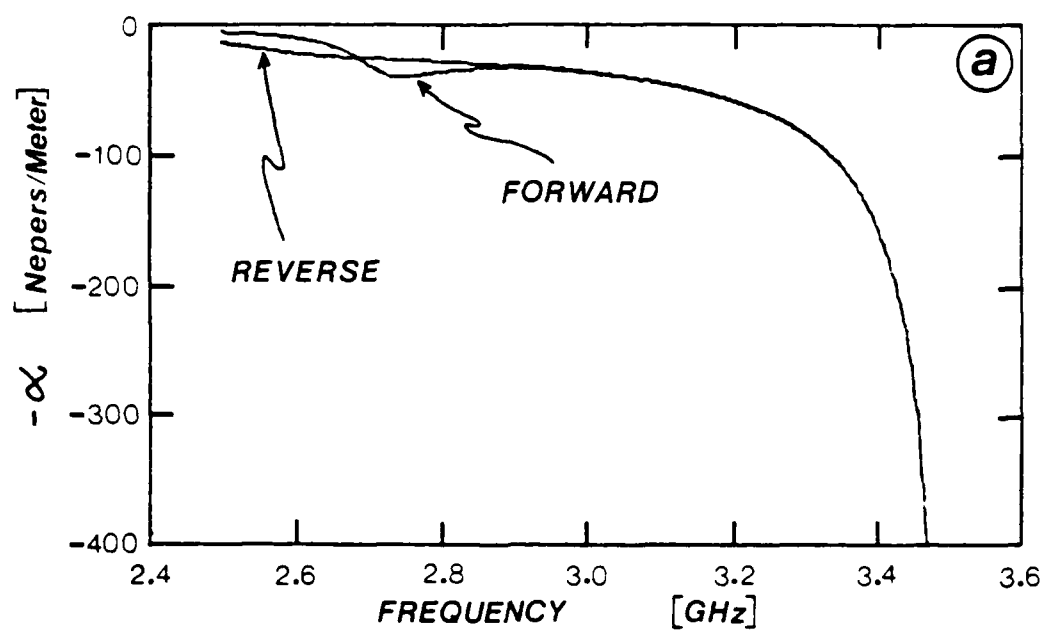


Figure 2.9. Unimplanted MSSW dispersion relation  $YIG = 20\mu$ ,  
 $H_0 = 375$  Oe,  $\Delta H_{\min} = 0.5$  Oe:  
 (a) forward and reverse loss factor,  
 (b) forward and reverse phase factor.

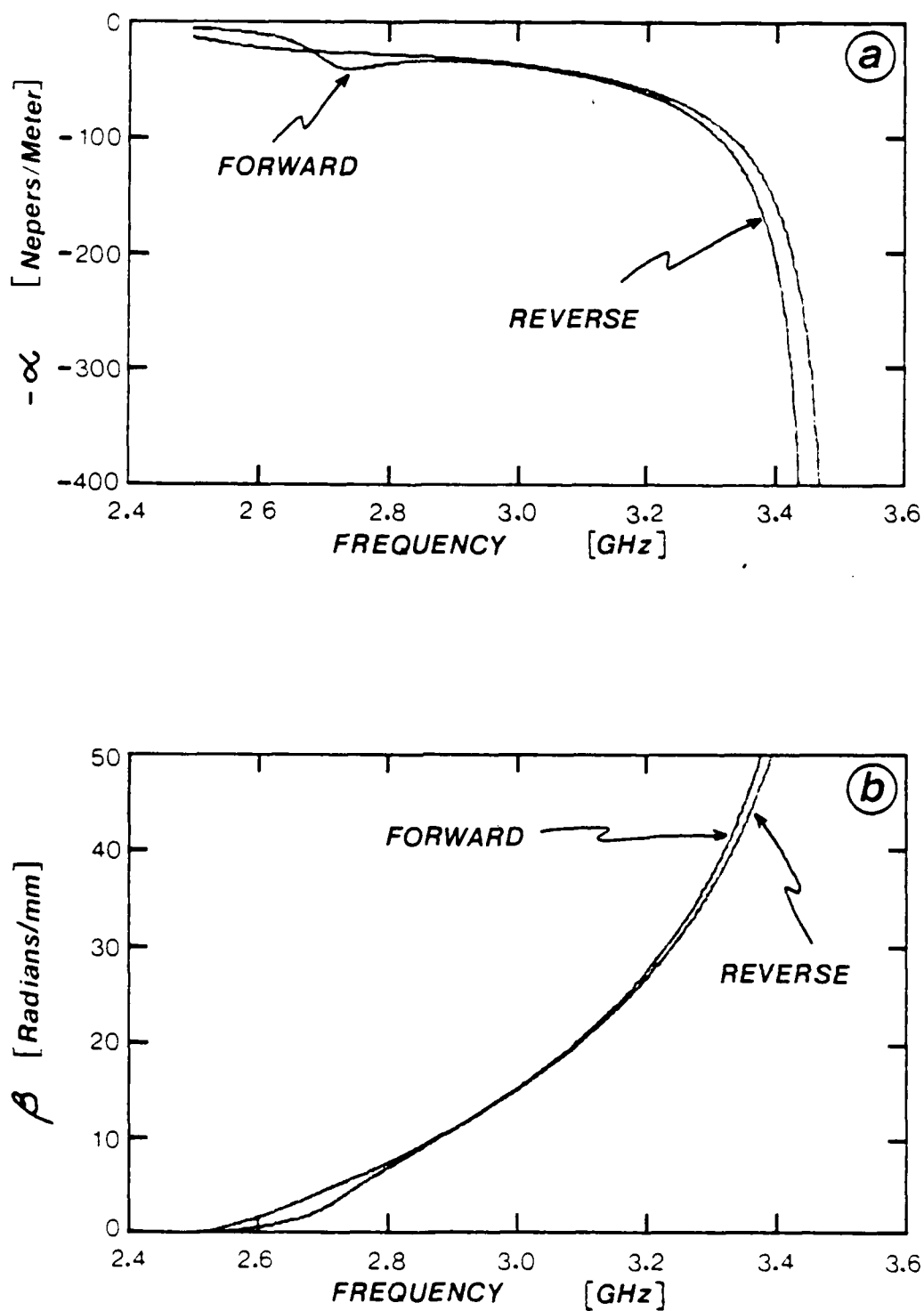


Figure 2.10. Implanted MSSW dispersion relation YIG =  $20\mu$ ,  $H_0 = 375$  Oe,  $\Delta H_{\min} = 0.5$  Oe,  $M_{\text{imp}}/M_{\text{pu}} = 0.5$ , Implant Depth =  $0.36 \mu\text{m}$ :  
 (a) forward and reverse loss factor,  
 (b) forward and reverse phase factor.

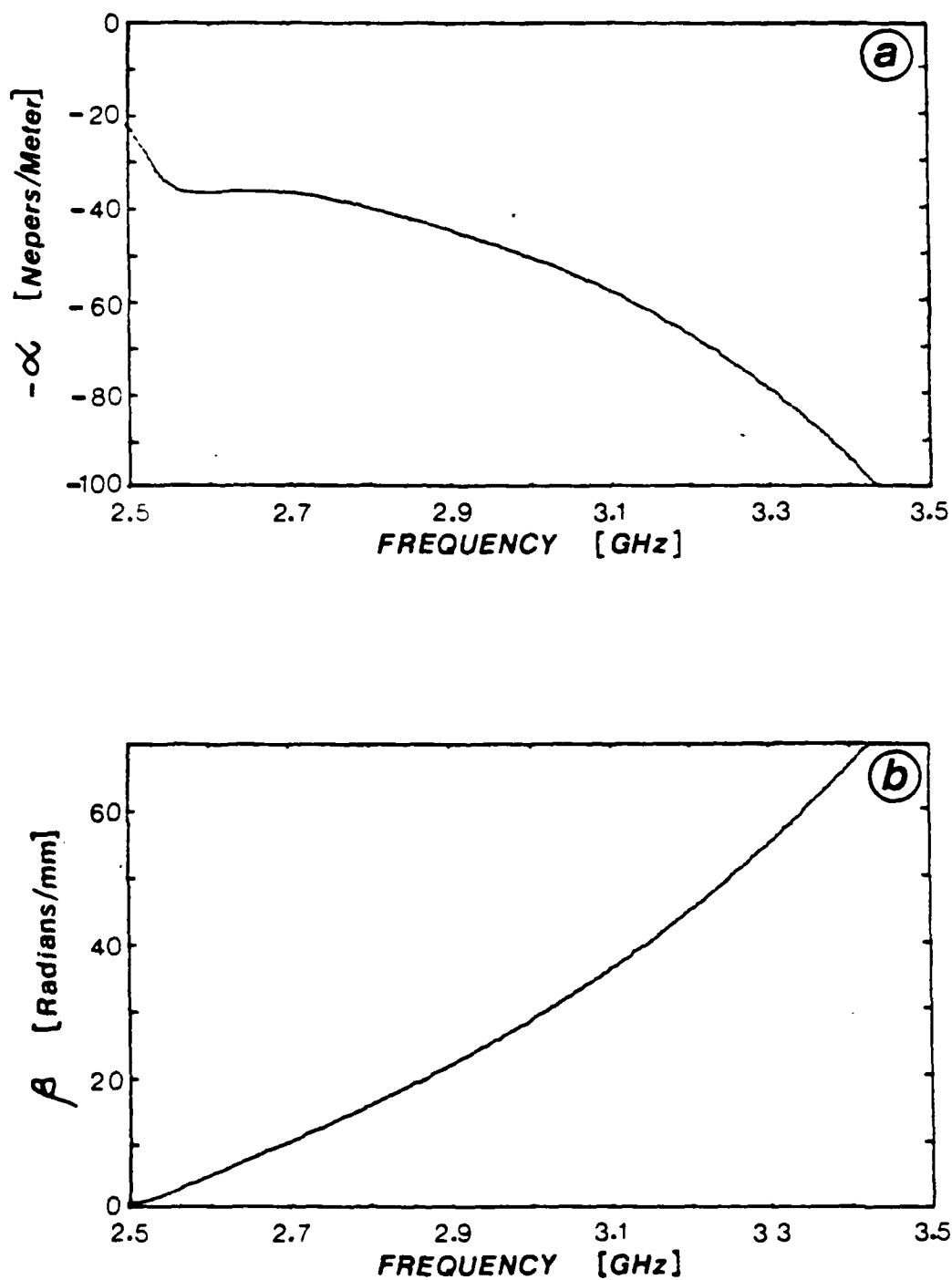


Figure 2.11. Unimplanted MSFVW dispersion relation  
 $YIG = 20 \mu m$ ,  $H_0 = 880 \text{ Oe}$ ,  $\Delta H_{\min} = 0.5 \text{ Oe}$ :  
 (a) loss factor  
 (b) phase factor.

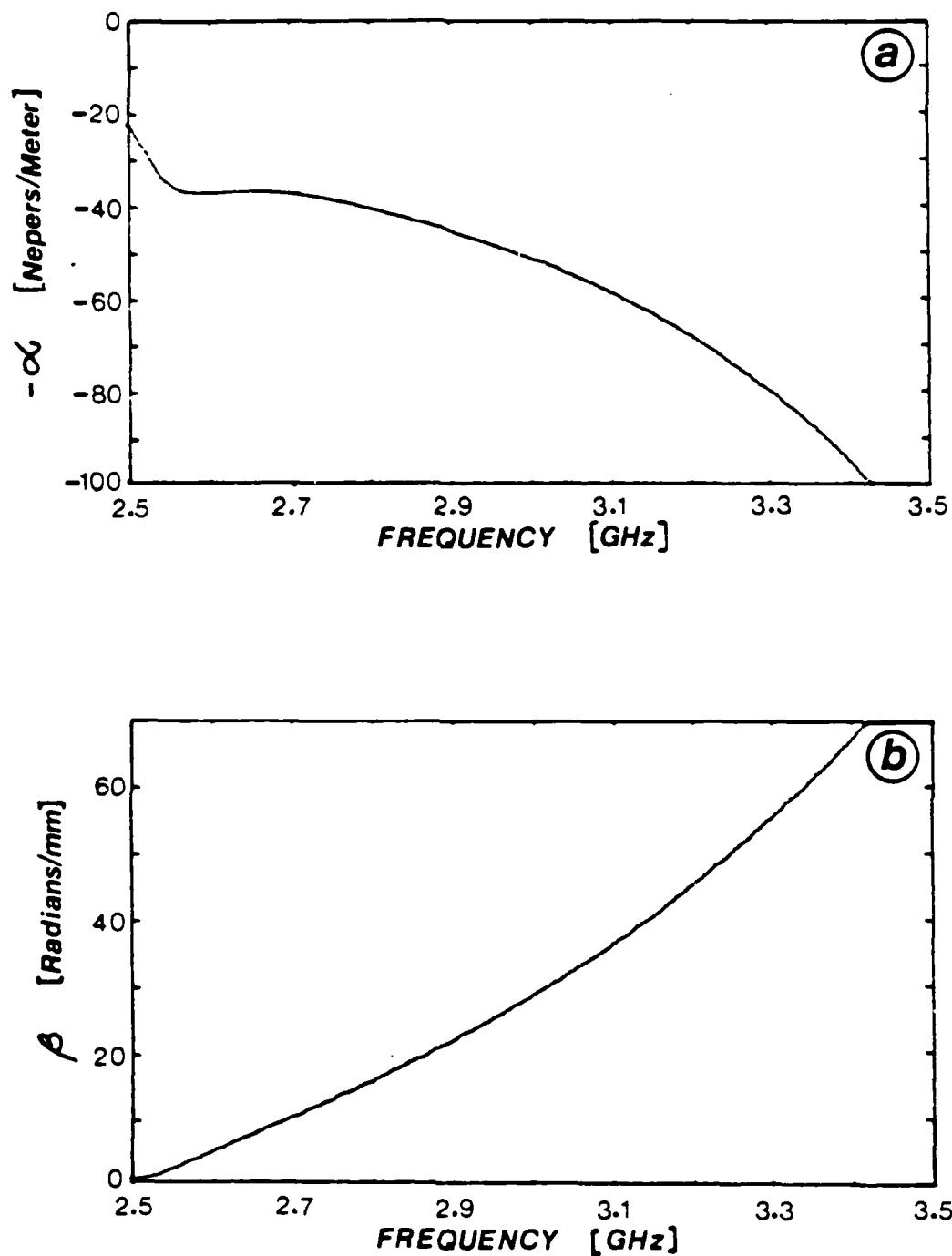


Figure 2.12. Implanted MSFVW dispersion relation  
 $YIG = 20 \mu m$ ,  $H_0 = 880 Oe$ ,  $\Delta H_{min} = 0.5 Oe$   
 $M_{imp}/M_{py} = 0.5$ , Implant Depth =  $0.36 \mu m$ :  
 (a) loss factor  
 (b) phase factor.



bottom surfaces of the film, resulting in distinct branches in the guide propagation constant. The lowest order mode takes the most direct path, accruing the least loss and is characterized by the longest wavelengths. Typical complex main mode dispersion relations for MSSW and MSFVW are shown in Figures 2.9 through 2.12.

#### 2.1.8 Transducer Modeling

Transducer contributions to the transfer characteristic were modeled after Wu [2.1], using a lossless form of the dispersion relationships. In Wu's development, the transducers are treated as sheet current distributions in order to obtain the magnetic field solutions in the ferrite, which amounts to determination of the constants A through F. Faraday's law is used to calculate the electric fields in terms of the magnetic fields, from which the Poynting vector is obtained. Integration of the y-component of the Poynting vector over surfaces bounding the sheet currents and cutting through the cross section of the layered structure normal to the propagation direction yields the radiated power, from which a radiation resistance is calculated. Since radiation impedance is an observable, it is analytic permitting the radiation reactance to be calculated from the Hilbert transform of the radiation resistance. The driving point characteristics of the transducers are calculated in terms of a lossy microstrip model in which finite conductivity and radiation into the ferrite are the principal contributors to

loss. Separation of the microstrip driving point impedance into terms associated with the microstrip and terms associated with radiation, yields a lumped parameter model of the transducer suitable for calculation of conversion loss as a function of frequency. Overall filter transfer functions are composed of transmitter and receiver contributions multiplied with the delay line or array transfer characteristic.

## 2.2 Reflectivity Model

### 2.2.1 Assumptions and Approximations

In the plane of the ferrite film, the three layer "land" sections and the four layer "bar" sections are characterized by slightly different propagation properties. MSW theory effectively models the behavior of the waves within these regions, but the primary effect of the array on the MSW is the beam splitting and phase shifting that occurs at the boundaries of the two regions. In this work the interface between regions is modeled as an abrupt discontinuity with uniform properties on either side.

There are two commonly used methods for modeling reflection and transmission at an interface,

- (1) Lumped Element Circuit Model,
- (2) Plane Wave Analogy  
(Wave Impedance).

Initial determination of suitable lumped element circuit

model topologies and element values is generally a formidable task, but once established the circuit model technique can predict subtle response details and offer insight into their origins. To date the circuit models developed for discontinuities in planar magnetostatic devices {2.22} have proven accurate only for very small arrays and involve complexity that makes them undesirable for synthesis oriented work.

Considerable simplicity can be realized using a plane wave analogy where possible, enabling tractable analytical calculations to be made on large complex reflective structures as well as facilitating closed form solutions in many situations. The plane wave analogy carries with it a large body of established techniques and computational tools such as the Smith chart and a variety of optimization and analytical software such as Compact, that contribute to the desirability of this approach. Of key importance to this work, the plane wave analogy opens up the potential for implementing desired filter functions using simple synthesis techniques.

In all of the foregoing calculations, the magnetostatic wave has been treated as a superposition of plane waves propagating in the y-direction. Although the wave fronts are not uniform, within the context of the magnetostatic approximation, all points on a given front with a particular wavelength travel down the guiding structure parallel to the

y-axis with the same velocity. Thus, each magnetostatic wave can be interpreted as a bundle of uniform plane-wavelets with identical propagation characteristics at any given cross section, traveling down separate channels parallel to the y-axis. The principal effect of disturbances in the continuity of the guiding structure, associated with thin surface anomalies on the ferrite such as etched grooves, metal bars, or implanted zones is a modification of the boundary conditions that determine the guide dispersion relation, exerting a uniform influence over the entire cross section. In the immediate vicinity of the surface perturbation the material characteristics may change drastically, but this causes only slight bending of longitudinal flux lines if the anomalous zone is thin compared to the film thickness. In addition, the power associated with this local flux bending is only a small percentage of the total power in the wave. Thus, the behavior at any point on a magnetostatic wave front as it traverses a guide discontinuity shall be treated as representative of the front as a whole.

Another assumption that is essential to the plane wave analogy is that transfer of energy down the guide is determined primarily by the transverse field components according to the Poynting vector. This assumption hinges on the fact that in all cases dealt with in this work the wave vector is along a principal axis, obviating the effects of

birefringence. Therefore, the transmission and reflection coefficients obtained by satisfying the boundary conditions for the transverse field components govern reflection and transmission of energy at discontinuities in the guide. Following the plane wave analogy (2.23), these transmission and reflection coefficients are conveniently expressed in terms of a wave impedance as suggested by Schelkunoff (2.24),

$$\tilde{Z}^{\pm}(y) = \frac{\tilde{e}_t^{\pm}(y)}{\tilde{h}_t^{\pm}(y)}, \quad (2.34)$$

where the subscript, "t", denotes transverse components, and the superscripts identify forward (+) and reverse (-) waves. With small signal excitations the film behaves linearly, so that forward and reverse waves propagate independently of each other, coupling only at longitudinal discontinuities in the structure. Thus, separate wave impedances must be defined for forward and reverse waves, in terms of exclusively forward or exclusively reverse field components.

### 2.2.2 Wave Impedance

The dual wave nature of the MSSW complicates determination of a suitable wave impedance, but a clue to the solution is suggested by the splitting of the forward and reverse dispersion relations in the region where the ground plane effects them unequally. The forward wave exhibits a more pronounced disturbance in its phase constant (beta) and

higher loss ( $\alpha$ ) in this region, as would be expected if it were predominantly composed of the surface wave counterpart closest to the ground plane (Figure 2.9). Associating forward propagation with one surface and reverse propagation with the other surface leads to the conclusion that reflection from a discontinuity effectively transfers the reflected energy to the opposite surface from that of the incident wave. The existence of a combination of forward and reverse waves on both surfaces of the ferrite (as is the case in the field solutions given in equation (2.24)), however, does not preclude the use of this model for reflection. Unilateral properties characteristic of delay line performance corroborate the interpretation that forward propagation is primarily associated with a particular surface and reverse propagation the other. Higher coupling to the surface nearest the transducers is expected, so the typical 10 dB difference between forward and reverse delay line insertion losses suggests that waves radiated in opposite directions from the transmitter are on opposite faces of the ferrite.

Subject to the above constraints, application of Faraday's law using the electric field component,  $e_z$ , responsible for principal axis energy transfer down the guide (APPENDIX A), yields the wave impedances given in TABLE 2.4. Thus, a MSSW has four identifiable impedances associated with it, corresponding to the various combinations of two possible

surfaces the wave can be bound to and two distinct directions of propagation relative to the bias field. The foregoing interpretation of the reflection process corresponds to

TABLE 2.4  
MSSW CHARACTERISTIC IMPEDANCES

|         | BOTTOM SURFACE WAVE                                     | TOP SURFACE WAVE  |
|---------|---|---|
| FORWARD | $\frac{2\pi f \mu_0}{\tilde{k}_+} \{ \mu_1 + \mu_2 \}$  | $\frac{2\pi f \mu_0}{\tilde{k}_+} \{ \mu_1 - \mu_2 \}$  |
| REVERSE | $-\frac{2\pi f \mu_0}{\tilde{k}_-} \{ \mu_1 - \mu_2 \}$ | $-\frac{2\pi f \mu_0}{\tilde{k}_-} \{ \mu_1 + \mu_2 \}$ |

requiring wave eigenfunctions with similar forms in their impedances to satisfy the boundary conditions independently (major-diagonal only or minor-diagonal only in TABLE 2.4). Since the Polder tensor is a material attribute that is independent of propagation direction and of the surface perturbation in the portion of the ferrite outside the thin perturbed layer (carrying the majority of the power), the only distinction between incident, transmitted, and reflected wave impedances is the dispersion constant. This permits all other terms to cancel in the transmission and reflection coefficients that result from matching the boundary conditions (APPENDIX B) for the transverse fields over the cross sections between three-layer unperturbed zones (lands) and four-layer perturbed zones (bars). In a biaxial anisotropic medium, as is the case with the MSSW bias

configuration, the transmission and reflection coefficients at a boundary for a forward going wave are different from those for a reverse wave. The four required coefficients for the boundary between adjacent regions denoted 1 and 2 are given in equation (2.35),

$$\tilde{\rho}_{\xi\zeta}^+ = \tilde{\kappa}_+ \cdot \frac{\tilde{Z}_\zeta^+ - \tilde{Z}_\xi^+}{\tilde{Z}_\zeta^+ + \tilde{Z}_\xi^+} = \tilde{\kappa}_+ \cdot \frac{1/\tilde{k}_\zeta^+ + 1/\tilde{k}_\xi^+}{1/\tilde{k}_\zeta^+ + 1/\tilde{k}_\xi^-} \quad (2.35a)$$

$$\tilde{\tau}_{\xi\zeta}^+ = \tilde{v}_+ \cdot \frac{\tilde{Z}_\zeta^+ + \tilde{Z}_\xi^-}{\tilde{Z}_\zeta^+ + \tilde{Z}_\xi^+} = \tilde{v}_+ \cdot \frac{1/\tilde{k}_\zeta^+ + 1/\tilde{k}_\xi^-}{1/\tilde{k}_\zeta^+ + 1/\tilde{k}_\xi^-}$$

$$\tilde{\rho}_{\xi\zeta}^- = \tilde{\kappa}_- \cdot \frac{\tilde{Z}_\xi^- - \tilde{Z}_\zeta^-}{\tilde{Z}_\xi^- + \tilde{Z}_\zeta^+} = \tilde{\kappa}_- \cdot \frac{1/\tilde{k}_\xi^- - 1/\tilde{k}_\zeta^-}{1/\tilde{k}_\xi^- + 1/\tilde{k}_\zeta^+} \quad (2.35b)$$

$$\tilde{\tau}_{\xi\zeta}^- = \tilde{v}_- \cdot \frac{\tilde{Z}_\xi^- + \tilde{Z}_\xi^+}{\tilde{Z}_\xi^- + \tilde{Z}_\zeta^+} = \tilde{v}_- \cdot \frac{1/\tilde{k}_\xi^- + 1/\tilde{k}_\xi^+}{1/\tilde{k}_\xi^- + 1/\tilde{k}_\zeta^+}$$

where + and - signify forward and reverse propagation respectively, and region  $\xi$  precedes region  $\zeta$  for a forward wave. Regions  $\xi$  and  $\zeta$  are distinguished by different dispersion relations, and the reflection and transmission coefficients for the electric and magnetic fields differ by the factors  $\tilde{\kappa}_\pm$  and  $\tilde{v}_\pm$ , which are unity for the magnetic field and  $\tilde{\kappa}_+ = \tilde{Z}_\xi^- / \tilde{Z}_\xi^+$ ,  $\tilde{\kappa}_- = \tilde{Z}_\zeta^+ / \tilde{Z}_\zeta^-$ ,  $\tilde{v}_+ = \tilde{Z}_\zeta^+ / \tilde{Z}_\xi^+$ ,  $\tilde{v}_- = \tilde{Z}_\xi^- / \tilde{Z}_\zeta^-$  for the electric field.

As pointed out earlier, the effect of loss is to make the dispersion relation complex, which in turn makes the



transmission and reflection coefficients at an interface complex. This represents phase shifting upon transmission and reflection that is associated with energy storage in the fringe fields at the discontinuity. Introduction of loss results in a time constant for reradiation of this energy back into the traveling wave, separating the transmission and reflection products from the incident wave by a phase shift.

In this work, an effective MSSW wave impedance applicable to the calculation of reflection and transmission coefficients is used,

$$\tilde{Z}^{\pm} = \pm \frac{2\pi f \mu_0}{\tilde{k}_{\pm}}, \quad (2.36)$$

in which the cancelable Polder terms are dropped, retaining the correct dimensions and a form comparable to the wave impedances familiar to uniform plane waves.

Application of Faraday's law to the MSFVW bias configuration (APPENDIX A) leads directly to an unambiguous wave impedance, identical to that obtained for uniform, isotropic guiding structures. The resulting impedance is expressible in the form of equation (2.36) with the simplification that isotropic waves such as MSFVW, have identical forward and reverse propagation constants,

$$\tilde{Z}^{\pm} = \pm \frac{2\pi f \mu_0}{\tilde{k}}. \quad (2.37)$$

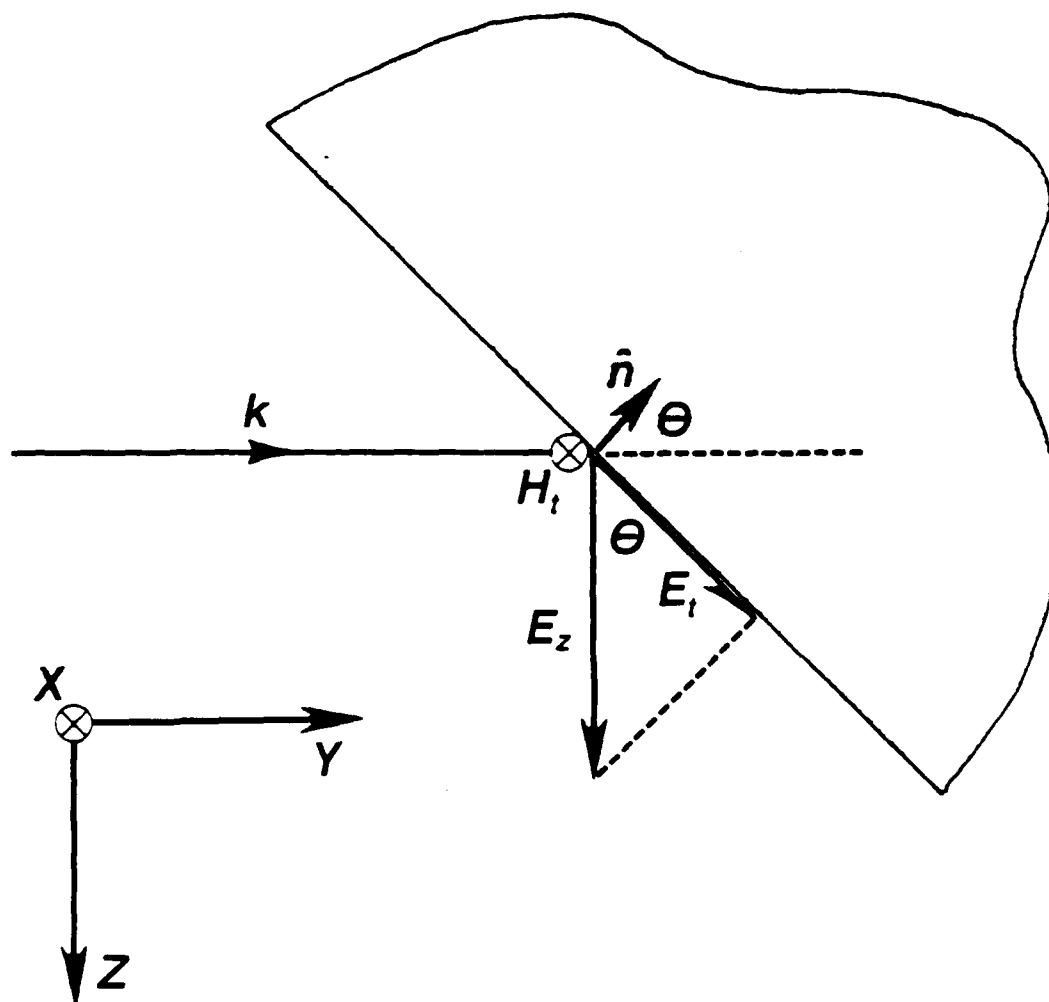


Figure 2.13 Oblique incidence on a boundary.

The primary array applications of MSFVW are those requiring oblique incidence, in which the boundary condition on the tilted interface involves components of the incident fields. The combined assumptions,

- negligible z-variation
- negligible crystalline anisotropy

and, • harmonic time variation

with the magnetostatic field solutions in Ampere's law indicate that the electric field is in the z-direction,

$$\text{curl}\{\tilde{h}\} = \hat{z} \left[ \frac{\partial \tilde{h}_y}{\partial x} - \frac{\partial \tilde{h}_x}{\partial y} \right] = j2\pi f \epsilon \tilde{e} \quad (2.38)$$

When the electric field is in the plane of incidence (the plane of the film), its projection onto a tilted land/bar interface whose normal forms an angle  $\theta$  with the incident propagation vector (Figure 2.13), includes a  $\cos \theta$  factor that does not occur in the projection of the x-component of the h-field. This, factor therefore appears in the wave impedance pertinent to the satisfaction of the tangential boundary conditions on the oblique land/bar interface,

$$\tilde{Z}^{\pm} = \pm \frac{2\pi f \mu_0}{k} \cos \theta \quad (2.39)$$

## 2.3 Array Modeling

### 2.3.1 Normal Incidence Array Theory

The unapodized normal incidence arrays investigated in this work are approximated by negligible beam refraction at

reflector interfaces and uniform element illumination by the wave and its scattering products. This allows the array to be modeled as a series of two port transmission elements, reducing array calculations to multiplication of transmission matrices.

Since the primary effect of axial discontinuities in the structure is to scatter the waves, some insight into the reflection process is preserved by first determining scattering matrices for the leading (unimplanted to implanted) and trailing (implanted to unimplanted) edges of a reflector zone, and then transforming to transmission matrices more suitable for mathematical manipulation (Figure 2.14). The scattering matrices, written in terms of the transmission and reflection coefficients given in equation (2.35), are shown in equation (2.40).

$$\text{Leading Edge} \quad \begin{bmatrix} \tilde{h}_U^- \\ \tilde{h}_i^+ \end{bmatrix}_L = \begin{bmatrix} \tilde{\rho}_{Ui}^+ & \tilde{\tau}_{Ui}^- \\ \tilde{\tau}_{Ui}^+ & \tilde{\rho}_{Ui}^- \end{bmatrix} \begin{bmatrix} \tilde{h}_U^+ \\ \tilde{h}_i^- \end{bmatrix}_L \quad (2.40a)$$

$$\text{Trailing Edge} \quad \begin{bmatrix} \tilde{h}_i^- \\ \tilde{h}_U^+ \end{bmatrix}_T = \begin{bmatrix} \tilde{\rho}_{iU}^+ & \tilde{\tau}_{iU}^- \\ \tilde{\tau}_{iU}^+ & \tilde{\rho}_{iU}^- \end{bmatrix} \begin{bmatrix} \tilde{h}_i^+ \\ \tilde{h}_U^- \end{bmatrix}_T \quad (2.40b)$$

These can be transformed to transmission matrices using equation (2.41).

$$\begin{aligned} \tilde{T}_{11} &= \tilde{S}_{21} - \tilde{S}_{11}\tilde{S}_{22}/\tilde{S}_{12} \\ \tilde{T}_{12} &= \tilde{S}_{22}/\tilde{S}_{12} \\ \tilde{T}_{21} &= -\tilde{S}_{11}/\tilde{S}_{12} \\ \tilde{T}_{22} &= 1/\tilde{S}_{12} \end{aligned} \quad (2.41)$$

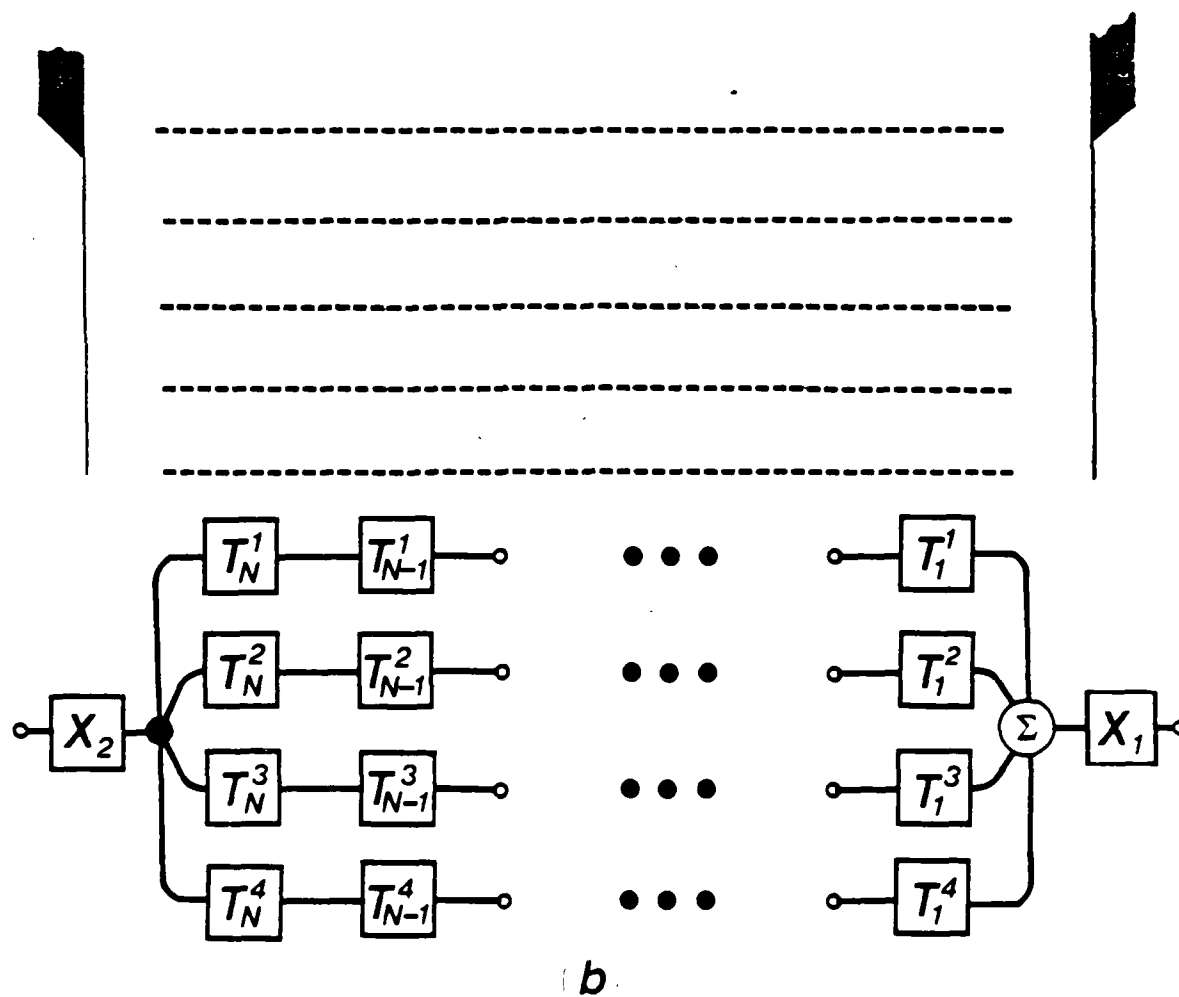
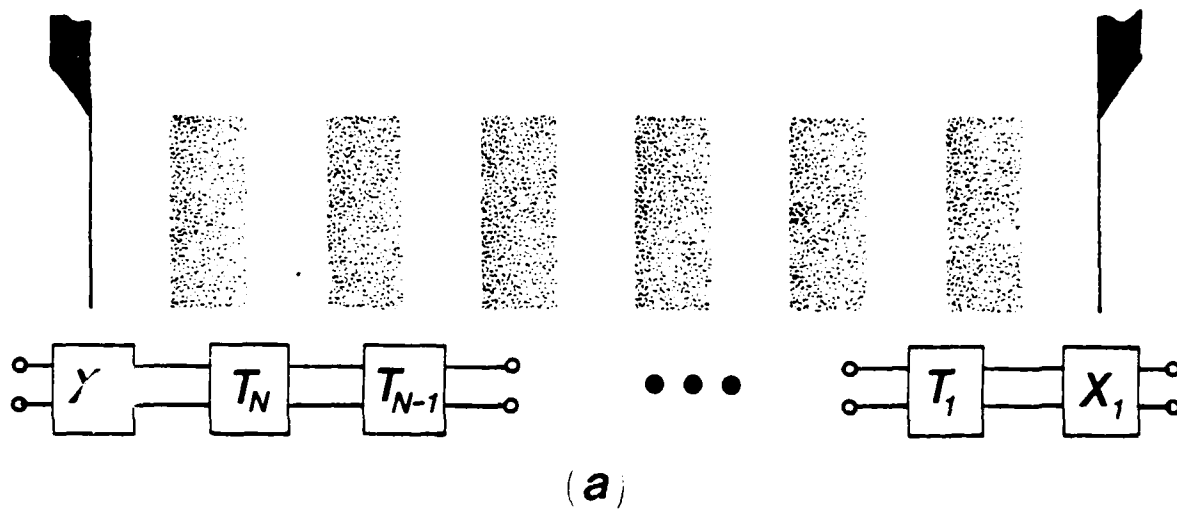


Figure 2.14. Normal incidence array structure.  
 (a) Unapodized  
 (b) Apodized

The paths between zone interfaces contribute loss and a phase shift, most naturally viewed in terms of transmission matrices. A matrix is needed to connect the waves on the inside of the leading and trailing edges of the reflector zone,

$$\text{Inside Bar} \quad \begin{bmatrix} \tilde{h}_i^+ \\ \tilde{h}_i^- \end{bmatrix}_T = \begin{bmatrix} \exp\{-j\tilde{k}(f)w_n\} & 0 \\ 0 & \exp\{+j\tilde{k}(f)w_n\} \end{bmatrix} \begin{bmatrix} \tilde{h}_i^+ \\ \tilde{h}_i^- \end{bmatrix}_L \quad (2.40c)$$

and one is needed to connect waves on the interfaces bounding unimplanted land zones,

$$\text{Between Bars} \quad \begin{bmatrix} \tilde{h}_u^+ \\ \tilde{h}_u^- \end{bmatrix}_T = \begin{bmatrix} \exp\{-j\tilde{k}(f)w_n\} & 0 \\ 0 & \exp\{+j\tilde{k}(f)w_n\} \end{bmatrix} \begin{bmatrix} \tilde{h}_u^+ \\ \tilde{h}_u^- \end{bmatrix}_L, \quad (2.40d)$$

where,  $w_i$  is the width of the reflector along the propagation direction.

A transmission matrix for the unapodized array shown in Figure 2.14a, can be constructed by selecting the appropriate element matrices from those given in equation (2.40), and arranging them in a reverse ordered product as is done in equation (2.42).

$$[\tilde{T}_{1,N}] = [\tilde{T}_{N-1,N}][\tilde{T}_{N-2,N-1}] \cdots [\tilde{T}_{1,2}]$$

where,

$$\begin{bmatrix} \tilde{h}_N^+ \\ \tilde{h}_N^- \end{bmatrix} = [\tilde{T}_{1,N}] \begin{bmatrix} \tilde{h}_1^+ \\ \tilde{h}_1^- \end{bmatrix}. \quad (2.42)$$

For the purposes of this work, the transmission matrices for the dominant magnetic waves were required ( $\tilde{\kappa}_\pm$  and  $\tilde{v}_\pm$  in

(2.35) are unity). If the transmission matrices for the electric field are to be calculated, care should be taken to use the correct multipliers in equation (2.35).

Further simplification is possible if all lands are identical and all bars are identical, for which a hybrid element matrix representing a land/bar combination is formulated and raised to a power corresponding to the number of bars in the array. A procedure for obtaining the transfer matrix for a recursive, normal incidence array aided by Sylvester's theorem is described by Brinlee (2.25).

The array contributions to the filter transmission and return transfer functions are expressable in terms of the elements of the overall transmission matrix, as follows,

$$\begin{aligned}\tilde{T}_A(f) &= \tilde{T}_{11} - \frac{\tilde{T}_{12}\tilde{T}_{21}}{\tilde{T}_{22}} && \text{(Transmission)} \\ \tilde{R}_A(f) &= - \frac{\tilde{T}_{21}}{\tilde{T}_{22}} && \text{(Return)}\end{aligned}\tag{2.43}$$

The transfer function for the overall filter,  $F(f)$ , is obtained as the product of the array transmission coefficient with the input and output transducer transfer functions,  $\tilde{X}_1(f)$ , and  $\tilde{X}_2(f)$ ,

$$\tilde{F}(f) = \tilde{X}_1(f) \cdot \tilde{T}_A(f) \cdot \tilde{X}_2(f) . \tag{2.44a}$$

An apodized array, as shown in Figure 2.14b, can be sectorized into parallel channels of unapodized subarrays, in the manner

of Tancrell and Holland (2.26), in which case the overall filter response is,

$$\tilde{F}(f) = \frac{1}{N} \cdot \tilde{X}_1(f) \cdot \tilde{X}_2(f) \cdot \sum_{n=1}^N \tilde{T}_A^n(f), \quad (2.44b)$$

where  $\tilde{T}_A^n(f)$  is the transmission coefficient for the  $n$ th unapodized subarray.

The principal application of this theory is with MSSWs, since they exhibit lower insertion losses than MSFVW, their unilateral radiation properties are essential in Fabry-Perot resonator applications, and their relationship to the bias field tends to keep them channelized (2.27), simplifying power sampling calculations in the apodized case. The theory is equally applicable to MSFVW, however, if the appropriate dispersion relation is used.

A computer program based on this theory that generates transmission and return loss for a recursive array of implanted normal incidence reflectors, taken from Brinlee (2.25) is given in APPENDIX C.

### 2.3.2 Oblique Incidence Array Theory

In the case of oblique incidence, the effects of,

- beam refraction upon transmission through a bar/land interface,
- wave front sampling, and
- beam divergence due to finite aperture transducer and reflector elements,

must be assessed. Severe beam refraction at land/bar



interfaces would cause the wave in reflector regions to follow an off-axis path that is significantly longer than anticipated by modeling it as traveling straight down the array axis. A phase increment accompanied by a lateral displacement in the wave front would result each time the front traverses a reflector zone, complicating determination of the power sampling strength of successive reflectors. In addition, signal degradation due to progressive sampling of the wave as it traverses the array distorts the signal available for subsequent sampling. Both of these effects limit the use of a simple impulse model if the reflectivities of the array elements made large. Fortunately, reflectivities encountered with normal surface disturbances such as etched grooves and ion implanted zones are small enough to fall within the scope of the impulse model. Conversely, the impulse model (superposition model) is applicable only to very small arrays of metal stripes, since the currents induced in them generate fields that penetrate deep into the film, resulting in large reflectivities. Also, with the isotropic propagation characteristics used in oblique incidence, there is no tendency for the waves to be channelized. Inaccuracies are introduced if the signal sampling contribution of a very short reflector is modeled as its projection onto the transducer aperture. When it is necessary to incorporate short reflectors (compared to the signal aperture), a finite aperture model is required. A

related source of computational inaccuracy is simple beam divergence when the axial length of the array is made large compared to the signal aperture at the launching transducer. This effect is usually neglected in MSW devices, because the relatively large propagation losses (compared to SAW) impose an upper bound on the useable length of an array. Reflectors placed beyond about 2 cm from the launching transducer both experimentally and theoretically have negligible contribution to the filter response. Attempts to compensate for the natural exponential attenuation of signals from bars beyond the 2 cm limit yield impractical near in reflector lengths and high filter insertion losses. Amplitude and phase equilization of the parts of the wave front that bypass the shorter reflectors can be accomplished by appending extensions onto the ends of the reflectors that reach out to the edge of the signal aperture and are oriented normal to the array axis.

The phase velocity is only slightly perturbed in the reflector zones, so that the obliquity factor,  $\cos \theta$ , in the wave impedance is essentially the same for both land and bar regions, allowing it to drop out of the reflectivity calculation. Typical zone edge reflectivities for 0.4  $\mu\text{m}$  implants are real, falling in the range 0.001 to 0.01, and are independent of frequency. This permits the use of a noninteractive model in which the array response is calculated as a superposition of independent weighted

reflector contributions. Launching transducers are kept short compared to an electrical wavelength corresponding to a uniform current distribution along the length of the filament, providing an approximately uniform MSW wave front. If reflector length variations are moderate, small reflectivities and the approximately uniform wave front yield a signal contribution from each reflector that is equal to its projection onto the signal aperture of the launching transducer. This follows from the fact that flux linkage at the output transducer is directly proportional to the reflected beam width, inducing a correspondingly proportional current in the fixed load. In addition to the weighting factor, the reflection contribution from each bar consists of leading and trailing edge components (Figure 2.15) which interact to give a wavelength selectivity that initially peaks when the bar width (measured along the array axis) is half the MSW wavelength and at wavelength intervals thereafter,

$$w_i = \lambda(n + 1/2) , \quad n = 0, 1, 2, \dots \quad (2.45)$$

In terms of this model, the array transfer function is,

$$\tilde{T}_A(f) = j2 \tilde{\rho}(f) e^{-j\tilde{k}z_0} \sum_{i=1}^N \{l_i/l_t\} e^{-jk y_i} \sin\left(\frac{\tilde{k} w_i}{2}\right) \quad (2.46)$$

where,  $z_0$  is the distance from the array axis to the output transducer,  $y_i$  is the distance from the input transducer to

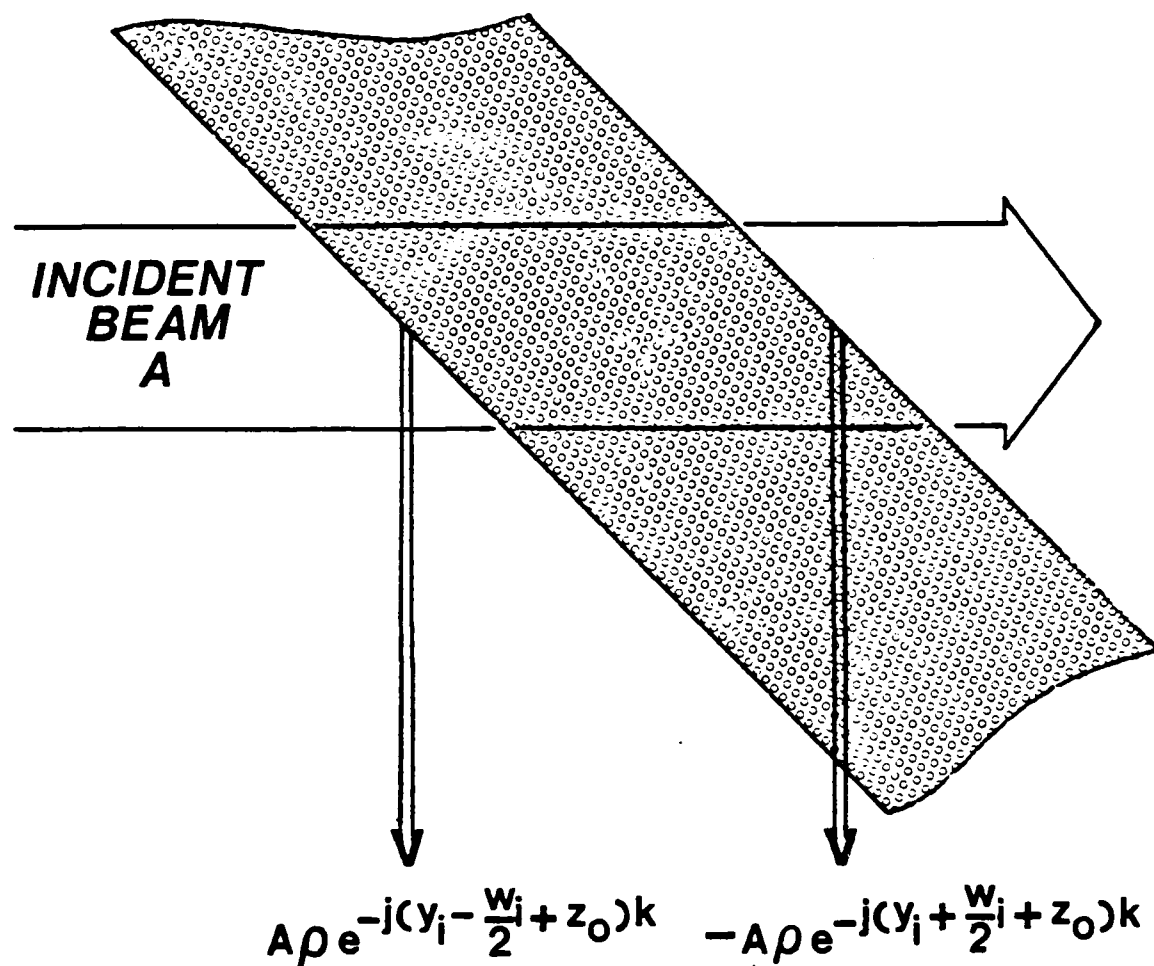


Figure 2.15. Reflection components from an implanted zone.

the center of the  $i$ th bar,  $l_i/l_t$  is the projection of the  $i$ th bar onto the input transducer,  $w_i$  is the width of the  $i$ th bar measured along the array axis, and  $\tilde{\rho}(f)$  is the reflection coefficient for an unimplanted to implanted zone interface. The overall filter response is given by the product of the array transfer function with the input and output transducer responses,

$$\tilde{F}(f) = \tilde{X}_1(f) \cdot \tilde{T}_A(f) \cdot \tilde{X}_2(f) . \quad (2.47)$$

## CHAPTER 3

### SYNTHESIS TECHNIQUES

#### 3.1 Measure Of Fit

Before attempting to fit a physical system to a set of desired characteristics, it is essential to select one that is "reasonably" conformable. This procedure is usually aided by viewing the system in a highly simplified model, such as the impulse model, in which the natural trends in the system behavior are revealed. For example, reflective arrays particularly lend themselves to the realization of filter functions in which the amplitude and delay (phase slope) are specified independently, since the geometry of the reflectors makes them somewhat wavelength selective. Placement of a reflector relative to the input and output roughly determines the delay associated with the wavelength (frequency) it represents, and adjustment of the reflector length roughly controls the power reflected at that wavelength (frequency). The effects of the distributed wavelength response of a reflector, fringing at the ends, beam spreading, etc. can be dealt with mathematically once potential conformability has been established.

The next step in choosing the adjustable system parameters that "best fit" the desired response, is to define a measure of what is meant by a "good fit". An accurate representation of the system response, as a function of the

adjustable system parameters,  $p_n$ , is required for this purpose, either in tabular or preferably analytic form. This system response is also a function of the independent variables that define the space in which the fit must occur,  $x_m$ , (time or frequency in the case of a signal filter) and often (but not necessarily) takes the form of a complex transfer function, as is represented by equation (3.1).

$$\begin{array}{ll} \tilde{F}(\bar{x}, \bar{p}) & \text{(system response)} \\ \tilde{T}(\bar{x}) & \text{("target" response)} \end{array} \quad (3.1)$$

There are a variety of ways to define an "optimal" fit.

### 3.1.1 Taylor Criterion

In the Taylor criterion (3.1), for example, both the system representation (transfer function) and the desired characteristic are expressed as Taylor series expansions. Corresponding coefficients in the two series are then equated, beginning with the most significant terms and proceeding until the adjustable parameters have all been specified. This approach has the disadvantage that it deals with the functions and their derivatives at a single point in the space formed by the independent variables.

### 3.1.2 Direct Equation

Alternately,  $\tilde{T}$  and  $\tilde{F}$  can be directly equated at as many points in  $x$ -space as there are adjustable parameters,

$$\tilde{F}(\bar{x}_m, \bar{p}) = \tilde{T}(\bar{x}_m) \quad m = 1, 2, \dots, N \quad (3.2)$$

forming a complete set of linearly independent equations that can be solved for  $p_n$ . If the resulting equations are nonlinear in  $p_n$ , then the usual procedure is to expand each of them in a first-order Taylor series in parameter space about an initial guess point,  $\{p_{10}, p_{20}, \dots, p_{N0}\}$ . The solution to this linear set of equations is then used as the initial guess in the next iteration, etc. This technique achieves an exact fit to the desired response at the chosen points in  $x$ -space, but provides no guarantee of what will happen in between, nor does it control the behavior of the derivatives of the response at these points.

### 3.1.3 Chebyshev Criterion

The Chebyshev or equiripple criterion (3.1) approaches the problem of "best fit" by seeking to minimize the largest value of the absolute difference between the system response and the target response in the region of interest in  $x$ -space. The result is uniform ripple in the absolute error function within this region. If the desired uniform ripple has a magnitude of,  $\xi$ , then a function,  $z_\xi(\bar{x}, \bar{p})$ , can be formed which has zeros where the absolute error function is equal to  $\xi$  as shown in equation (3.3).

$$z_\xi(\bar{x}, \bar{p}) = \xi^2 - E^2(\bar{x}, \bar{p}) \quad \text{where,} \quad (3.3)$$

$$E^2(\bar{x}, \bar{p}) = \{\tilde{T}(\bar{x}) - \tilde{F}(\bar{x}, \bar{p})\} \cdot \{\tilde{T}(\bar{x}) - \tilde{F}(\bar{x}, \bar{p})\}^*.$$

The extrema in the error function,  $E(\bar{x}, \bar{p})$ , occur both on the



boundary of the region in  $x$ -space and at the points where the derivatives in  $x$ -space vanish. In the special case of filter synthesis,  $x$ -space consists of the single variable, frequency. The region of interest becomes an interval bounded by the frequencies  $f_1$  and  $f_2$ , where  $f_1 < f < f_2$ . A function,  $z_e(\bar{x}, \bar{p})$  that has zeros at the extrema of the error function is given in equation (3.4).

$$z_e(\bar{x}, \bar{p}) = (f_2 - f)(f - f_1) \frac{dE}{df} \quad (3.4)$$

The equiripple criterion is satisfied by forcing the points where the error function equals  $\xi$  to correspond with the points where the extrema are located. This can be accomplished by setting  $z_\xi$  proportional to  $z_e$  (scale factor  $N^2$ ), if the two are polynomials, since a polynomial is uniquely defined by its zeros to within an amplitude factor,

$$\xi^2 - E^2(\bar{x}, \bar{p}) = \frac{1}{N^2} (f_2 - f)(f - f_1) \frac{dE}{df}. \quad (3.5)$$

The solutions to this differential equation are the Chebyshev polynomials of order,  $N$ ,

$$C_N(f) = \xi \cos\{N \cos^{-1}[2\xi(\frac{2f}{f_2 + f_1} - 1)]\}. \quad (3.6)$$

At this point, the problem is to select the adjustable parameters in the physical system that "best fit" the error function, defined in equation (3.3), to the appropriate order Chebyshev polynomial as determined by the number of adjustable parameters. If the target function is expressible

as a finite order polynomial, then there are known system topologies that can achieve an exact fit. However, if the system topology is fixed, a SAW RAF for example, and/or the target function is not a finite order polynomial, say a Hamming linear delay response, then the designer is again faced with the problem of obtaining a "best fit", but now to the Chebyshev criterion.

### 3.1.4 Mean Squared and Mean Absolute Error Criterion

Although equiripple is extremely useful in channel filters, it is not necessarily the optimal design for wave shaping filters. These filters rely on average correlation, a property that makes them effective in discriminating against extraneous signals such as noise and renders them insensitive to flaws in the received signal introduced by the environment. In the context of wave shaping filters, a far more appropriate definition of a "good fit" would address the minimization of average absolute or squared errors over the passband of the filter.

$$E_{msq}(\bar{p}) = \frac{1}{f_2 - f_1} \int_{f_1}^{f_2} w(f) \{ \tilde{T}(f) - \tilde{F}(f, \bar{p}) \} \{ \tilde{T}^*(f) - \tilde{F}^*(f, \bar{p}) \} df$$

MEAN SQUARED ERROR

$$E_{mab}(\bar{p}) = \frac{1}{f_2 - f_1} \int_{f_1}^{f_2} w(f) \sqrt{ \{ \tilde{T}(f) - \tilde{F}(f, \bar{p}) \} \{ \tilde{T}^*(f) - \tilde{F}^*(f, \bar{p}) \} } df.$$

MEAN ABSOLUTE ERROR

(3.7)

A weighting function,  $w(f)$  is included to allow the fit to be emphasized at critical parts of the passband.

The Mean Absolute Error and the Mean Squared Error have different values for the same set of system parameters, but lead to the same "optimal" set when they are minimized. Generally, the Mean Squared Error criterion is preferred for its relative computational simplicity, although choice of the criterion can be based its convergence properties in conjunction with the search algorithm used to locate the extrema.

### 3.2 Search Techniques

Location of the minima in the error surface, although mathematically straight forward, constitutes a major part of the synthesis task, depending on how the system parameters enter into the error function. Convergence properties depend heavily upon the shape of the error surface in the vicinity of the minima and the search algorithm used to explore it.

#### 3.2.1 Error Functions That Depend Linearly on System Parameters

When the error function is a linear combination of the adjustable system parameters,  $p_n$ , a closed form solution for the "optimal" parameters is possible. Setting the partial derivatives of the error function with respect to each of the  $N$  adjustable parameters to zero yields a matrix of  $N$  linear, linearly independent equations that can be algebraically inverted to obtain the required parameter values. For example, this situation occurs in phased arrays of noninteracting reflectors or transmitters for which the

spectral amplitude response is the only critical specification, allowing the nonlinearly contributing element positions to be preselected (usually it is advantageous to place them on wavelength intervals from the receiver). The remaining parameters to be chosen are the relative contributions from each element, represented by the weighting factors in the linear superposition that constitutes the overall array response, equation (3.8),

$$\tilde{F}(f) = \sum_{n=1}^N p_n \tilde{G}_n(f) \exp\{-jk(f)d_n\}, \quad (3.8)$$

where,  $\tilde{G}_n(f)$  is the individual transfer characteristic for the  $n$ th array element with zero transmission path,  $\tilde{k}(f)$  is the lossy dispersion relation in the propagation medium of the phased array, and  $d_n$  is the propagation path between the  $n$ th element and the receiver antenna. Depending on whether sampling is accomplished by discarding energy or by simply not radiating it, the element weighting factors take on slightly different meanings. In a reflective array, the square of an element weighting factor represents the fraction of incident power that is available for reflection to the output by the element. If the reflector uniformly samples the entire transmitted beam (corresponding to a reflector that spans the full width of the input transducer aperture in a  $45^\circ$  incidence RAF) then the square of the weighting factor is unity. Thus, in a  $45^\circ$  incidence RAF the squares of the weighting factors should be normalized to represent the

transducer. Conversely, if element weighting is achieved in a noninteracting transducer array using a matched power splitter (if elements interact the techniques described below for nonlinear dependence on system parameters must be used), then the weighting factors should be normalized to the square root of the sum of the squares of the weighting factors, to satisfy conservation of power.

Direct Equation results in the following set of equations for the unnormalized weighting coefficients,  $p_n$ , of the individual elements,

$$\tilde{T}(f_m) = \sum_{n=1}^N p_n \tilde{G}_n(f_m) \exp[-jk(f_m)d_n] \quad m = 1, 2, \dots, N \quad (3.9)$$

In general, the  $p_n$ 's obtained from this set will be complex, indicating that an external phase shift is required in addition to that of the phased array itself. Since the phased array is intended to provide all of the filtering functions, phase shifting included, another design approach is preferable.

The Mean Squared Error Criterion provides an alternative that allows the designer to force the  $p_n$ 's to be real. The only reason that the weighting coefficients are complex (corresponding to an external phase shifter) is that in this special case the element locations have not been included in the synthesis, for the purpose of preserving linear dependence of the transfer function on the system parameters.

Inclusion of the element positions in the synthesis is preferably treated using a modified approach, but incorporates the required phase shifting within the phased array itself. The MSQ error function that applies to the phased array (whether or not the element positions are included in the synthesis) is,

$$E_{msq}(\bar{p}) = \int_{f_1}^{f_2} w(f) \left\{ \tilde{T}(f) - \sum_{n=1}^N p_n \tilde{G}_n(f) \exp[-jk(f)d_n] \right\} \cdot \left\{ \tilde{T}(f) - \sum_{n=1}^N p_n \tilde{G}_n(f) \exp[-jk(f)d_n] \right\}^* df, \quad (3.10)$$

in which the constant multiplier has been omitted. Differentiating with respect to the arbitrary weighting coefficient,  $p_m$ , and setting the result to zero yields  $N$  linear equations,

$$\begin{aligned} \frac{\partial E_{msq}}{\partial p_m} = & - \int_{f_1}^{f_2} w(f) \tilde{G}_m^*(f) e^{-jk^*(f)d_m} \left\{ \tilde{T}(f) - \sum_{n=1}^N p_n \tilde{G}_n(f) e^{-jk(f)d_n} \right\}^* df \\ & - \int_{f_1}^{f_2} w(f) \tilde{G}_m^*(f) e^{jk^*(f)d_m} \left\{ \tilde{T}(f) - \sum_{n=1}^N p_n \tilde{G}_n(f) e^{-jk(f)d_n} \right\} df \\ & = 0 \end{aligned} \quad (3.11)$$

$$m = 1, 2, \dots, N.$$

The integrals are conjugates of each other, so the sum can be expressed as twice the real part. Some manipulation yields,

$$\begin{aligned}
 & \left[ \begin{array}{c} f_2 \\ \text{Re} \int_{f_1}^{f_2} w(f) \tilde{G}_m(f) \tilde{G}_n^*(f) \exp[j\tilde{k}^*(f)d_m - \tilde{k}(f)d_n] df \\ f_1 \end{array} \right] [p_m] \\
 & = \left[ \begin{array}{c} f_2 \\ \text{Re} \int_{f_1}^{f_2} w(f) \tilde{G}_m^*(f) \tilde{T}(f) \exp[j\tilde{k}^*(f)d_m] df \\ f_1 \end{array} \right] \quad (3.12)
 \end{aligned}$$

which can be algebraically inverted to obtain the unnormalized element weighting coefficients, once the numerical integration has been carried out on the matrix elements ( $m$  and  $n$  are the ROW and COLUMN indices respectively). An interval for the numerical integration should be selected that is much smaller than the minimum frequency interval required for the exponential phasor to execute one rotation within the region of integration. The weighting coefficients were constrained to be real by their removal from under the  $\text{Re}\{\}$  when equation (3.11) was simplified to equation (3.12). As written, this result implies that all parts of an individual array contribution have the same path length to the output, representing effectively an infinite aperture or far-field case. In cases for which this is not true, the distributed effects of an array element can be accounted for by replacing  $\tilde{G}_n(f)$  with an integration over the length of the element. However, in most filter designs the array elements are configured so that such an integration is unnecessary, and in antenna designs, the receiver is usually located in the far field.

A significant special case occurs when a unity weighting function is used with identical broadband elements,

$$\begin{aligned} \bullet w(f) &= 1 \\ \bullet \tilde{G}(f) &\cong G_0, \end{aligned} \quad (3.13a)$$

in a lossless, nondispersive medium,

$$\tilde{k}(f) = \frac{2\pi f}{c}, \quad (3.13b)$$

where  $G_0$  is a real constant, and  $c$  is the speed of light in the medium. The off diagonal matrix elements on the left side of equation (3.12) have the form,

$$I = \int_{\theta_1}^{\theta_2} e^{j\theta} d\theta, \quad (3.14)$$

which is zero if  $\theta_2 - \theta_1 = 2M\pi$ , corresponding to,

$$\frac{2\pi f_2}{c} (d_m + d_n) + \frac{2\pi f_1}{c} (d_m + d_n) = 2M\pi$$

or,

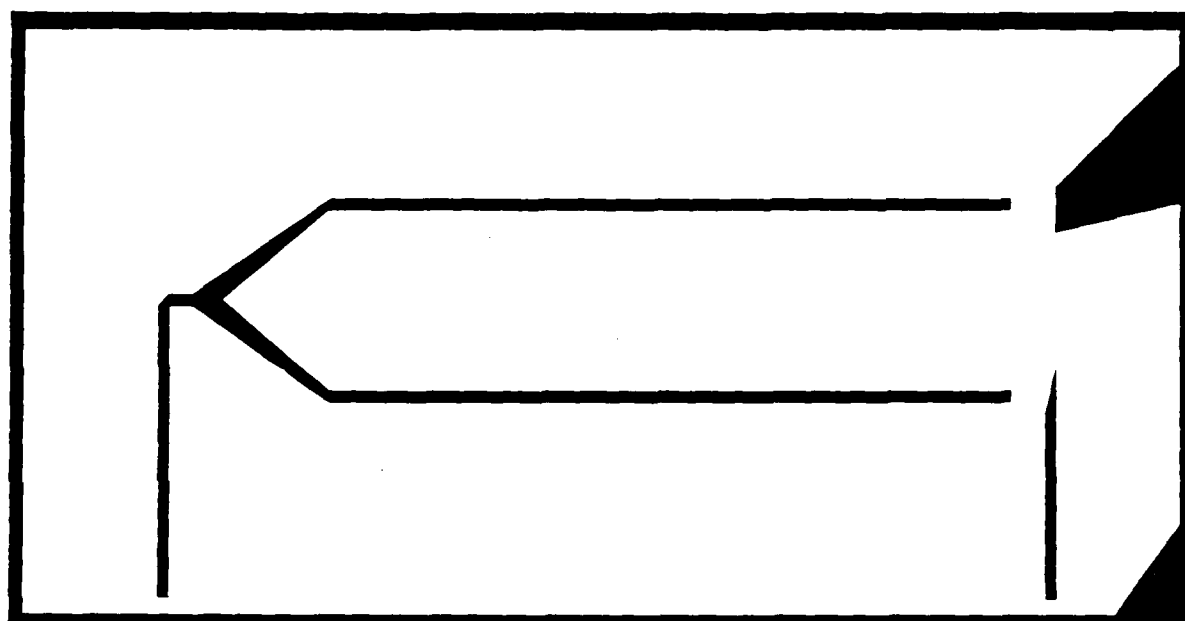
$$d_m = M(\lambda_2 - \lambda_1).$$

For an octave bandwidth filter, this condition corresponds to placing the array elements at intervals equal to the wavelength at the upper band edge. The "optimal" choice of the weighting coefficients for this case reduces to the Fourier transform,

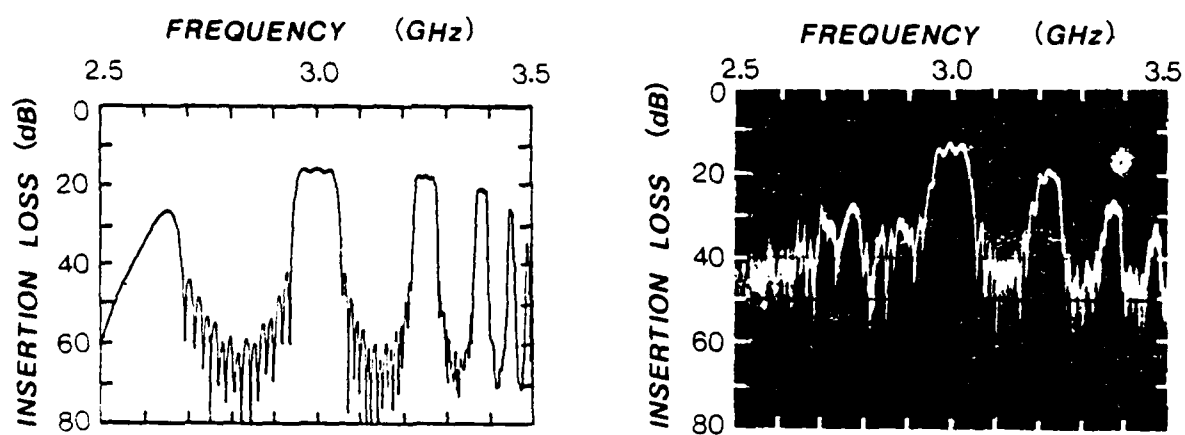
$$P_n = \frac{\int_{f_1}^{f_2} \tilde{T}(f) e^{-j2\pi f d_n} df}{G_0 (f_2 - f_1)}. \quad (3.16)$$



A practical example of the lossy, dispersive case is provided by the MSSW channel filter synthesis done by Ataiyan (3.2). In this work, a comb transducer array was used, as in Figure 3.1a, with electrically short microstrip filaments extending into the aperture from both sides, separated from their counterpart by a small gap. Mutual coupling among the transducer filaments was neglected, including the capacitive effects at the filament gaps. Reflections off the transducer splines and modifications in the propagation constant under them were neglected. Longitudinal current distributions in the electrically short splines were assumed to be zero at the gaps, increasing linearly in magnitude with distance away from the gaps, and exhibiting no relative phase shift along the length. Currents on opposite sides of the microstrip feeder fork are spatially  $180^\circ$  out of phase, so that when the gap is placed in the center of the aperture, waves launched from the opposing splines cancel at the receiver transducer, which extends across and uniformly samples the aperture. Viewing the longitudinal current distribution in the transducer splines in terms of even and odd components, the symmetry of the odd component prevents it from contributing any net radiation. However, the even component radiates an amount proportional to the mean of the linear current distribution. So, the weighting factor for a spline pair varies linearly with the displacement of the associated gap off the center line of the



(a)



(b)

Figure 3.1 (a) Transducer structure used by Ataiiyan.  
(b) Comparison of target and obtained frequency responses.

array, passing through zero at the center and assuming opposing signs on opposite sides of the center. Thus, the weighting scheme is plotted in the displacement of the gaps about the center line of the array and turns out to be nearly a sinc function (corresponding to the "box car" frequency response) even in the presence of dispersion and loss. Use of MSSW helps to channelize the waves, improving the effectiveness of the uniform wave front approximation. Phase shifts in the feeder structure were ignored, which led to limitations on the tunability of the device. The frequency response of the experimentally realized device weighted according to equation (3.12) is compared to the target and theoretically predicted frequency responses in Figure 3.1b. Placement of an identical receiver array at the location of the image of the transmitter array as projected in the existing receiver filament would double the skirt steepness and out of band rejection without requiring additional design effort.

Another practical synthesis example in which the system response depends linearly on the weighting factors is illustrated by the delay line work done by Chang {3.3}. The object of this work was to generate a filter with a linear group delay by cascading MSSW delay lines with different dispersion relations as governed by their ground plane spacing from the ferrite surface, Figure 3.2. Since the dispersion relation and associated group delay vary

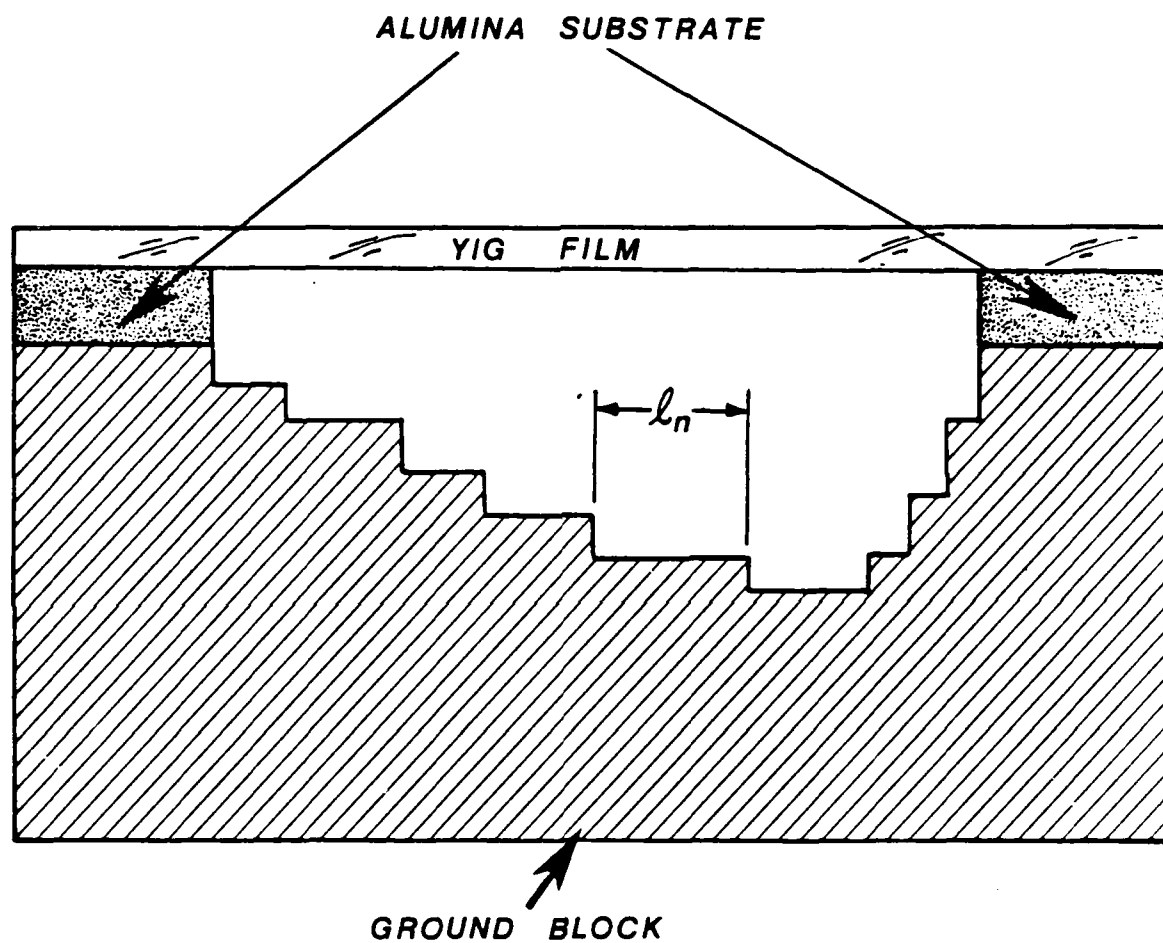


Figure 3.2. Cascaded MSSW delayline prototype {Chang}

nonlinearly with distance from the ferrite to the ground plane, the number of serial sections and their ground plane spacings should be chosen in advance. The system response in this case is the group delay for the composite delay line, consisting of the sum of the delays in the separate sections,

$$F(f) = \frac{1}{2\pi} \sum_{n=1}^N \left| \frac{d\beta_n}{df} \right| l_n \quad (3.17)$$

where,  $\beta_n$  is the lossless wavenumber ( $\tilde{k} = \alpha + j\beta$ ) in the  $n$ th serial delay section,  $l_n$  is the length of the  $n$ th serial delay section, and there are  $N$  sections. The target delay can be expressed,

$$T(f) = \kappa[f - f_0] + \tau_0 \quad (3.18)$$

where  $\kappa$  is the desired delay slope with dimensions [nsec/MHz] and  $\tau_0$  is the desired delay at  $f_0$  with dimensions [nsec]. Either direct equation or the MSQ error criterion can be applied easily to this problem yielding closed form solutions.

Direct equation takes the form,

$$\frac{1}{2\pi} \sum_{n=1}^N \left| \frac{d\beta_n}{df} \right|_{f_m} l_n = \kappa[f_m - f_0] + \tau_0 \quad (3.19)$$

$m = 1, 2, \dots, N$

Solution of this set of linear equations for the delay line segment lengths,  $l_n$ , requires inversion of an  $N \times N$  matrix, where  $N$  is the number of crossover points. The crossover

points needn't be spaced at equal intervals, in fact the solution can be optimized by grouping them more densely around critical points.

Using the MSQ error method, equation (3.12) specializes to the specific form represented by the  $m$ -matrix element given in equation (3.20).

$$\begin{bmatrix} f_2 \\ \int_{f_1}^{f_2} w(f) \left| \frac{d\beta_m}{df} \right| \left| \frac{d\beta_n}{df} \right| df \\ f_1 \end{bmatrix} [l_m] = 2\pi \begin{bmatrix} f_2 \\ \int_{f_1}^{f_2} w(f) \left| \frac{d\beta_m}{df} \right| T(f) df \\ f_1 \end{bmatrix} \quad (3.20)$$

Solving for the  $l_m$  in this set of linear equations requires that the matrix elements on both sides of the equation be determined by numerical integration over the spectral region of interest,  $f_1$  to  $f_2$ , followed by an  $N \times N$  matrix inversion. Selection of the sampling interval used for numerical integration can be based on the Nyquist sampling theorem and the maximum message or signal duration used in the time domain.

In this simple case, no real advantage is accrued by choosing the direct equation method since the solutions in both cases are obtained without iteration. The MSQ error criterion is actually simpler because it doesn't leave the designer with the problem of placing the crossover points to obtain a "best fit" as does the direct equation technique. Also the MSQ error approach minimizes the RMS error.

representing a measure of quality in a matched filter application, as these filters intrinsically average input signals.

### 3.2.2 Error Functions That Are Nonlinear Functions of the System Parameters

In general the system response function and consequently the error function vary nonlinearly with the system parameters. Partial differentiation of the error function, equation (3.7), with respect to each of the system parameters and setting the result to zero gives,

$$\frac{\partial E_{\text{msq}}(\bar{\mathbf{p}})}{\partial p_m} = -2 \int_{f_1}^{f_2} \text{Re} \left\{ \frac{\partial \tilde{F}^*(f, \bar{\mathbf{p}})}{\partial p_m} [\tilde{T}(f) - \tilde{F}(f, \bar{\mathbf{p}})] \right\} df = 0, \quad (3.21)$$

$m = 1, 2, \dots, N$

a complete set of nonlinear algebraic equations in the system parameters, locating the extrema. These equations can each be expanded in a Taylor series of  $N$  variables about an initial guess,  $\bar{\mathbf{p}}_0^{-1}$ , in parameter space and truncated to retain only the linear terms. System parameters are observables and are therefore real variables, allowing removal from the  $\text{Re}\{\}$ ,

$$[\Delta \bar{\mathbf{p}}^{-i+1}] =$$

$$\left[ \int_{f_1}^{f_2} w(f) \text{Re} \left\{ \frac{\partial \tilde{F}^*(f, \bar{\mathbf{p}}_0^{-i})}{\partial p_m} \frac{\partial \tilde{F}(f, \bar{\mathbf{p}}_0^{-i})}{\partial p_n} - \frac{\partial^2 \tilde{F}^*(f, \bar{\mathbf{p}}_0^{-i})}{\partial p_m \partial p_n} [\tilde{T}(f) - \tilde{F}(f, \bar{\mathbf{p}}_0^{-i})] \right\} df \right]^{-1}$$

$$\cdot \left[ \int_{f_1}^{f_2} w(f) \text{Re} \left\{ \frac{\partial \tilde{F}^*(f, \bar{\mathbf{p}}_0^{-i})}{\partial p_m} [\tilde{T}(f) - \tilde{F}(f, \bar{\mathbf{p}}_0^{-i})] \right\} df \right] \quad (3.22a)$$

where the superscripts,  $i$ , indicate the iteration,  $\bar{p}_0^i$  is the  $i$ th parameter-set guess, and subsequent parameter-set guesses are obtained from,

$$\bar{p}_0^{i+1} = \bar{p}_0^i + \Delta \bar{p}^{i+1} . \quad (3.22b)$$

If the nonlinear MSQ error function is expanded in a Taylor series prior to differentiating with respect to the system parameters and then truncated to linear, the result is identical to equation (3.22a) with the exception that the mixed partial derivative is absent. This approach tends to be extremely cumbersome, because each iteration requires that  $N(N+1)$  matrix elements be numerically integrated, followed by an  $N \times N$  matrix inversion. Calculation of the integrand at each numerical integration point is complicated by the need to determine several derivatives using the fundamental theorem of calculus. Convergence of this algorithm is typically oscillatory and slow, as the errors introduced by the approximations into the functional dependence on frequency of the integrand are accumulated throughout the integration. Also, this method seeks extrema in the error surface by locating points in parameter space where the slope goes to zero. Subsequently, the points at which the algorithm converges must be tested to determine if they are minima, maxima, or saddle points.

A gradient search provides a computationally simpler and operationally more systematic approach to the location



of minima in the error surface. This technique converges exclusively at relative minima, so that further testing is not required. If more than one minimum is found inside the allowed domain in parameter space, the best one is easily identified by outputting the MSQ error, already calculated as an intermediate step within the algorithm. At each point in parameter space beginning with an initial guess, the negative gradient of the error function is used to point the way for the next step. Calculation of the gradient of the MSQ error,

$$\text{grad}_{\vec{p}}\{E_{\text{msq}}\} = -2 \sum_{n=1}^N \hat{u}_n \int_{f_1}^{f_2} w(f) \text{Re}\left\{\frac{\partial \tilde{F}^*(f, \vec{p})}{\partial p_n} [\tilde{T}(f) - \tilde{F}(f, \vec{p})]\right\} df \quad (3.23)$$

involves only  $N$  numerical integrations (compared to  $N \times N$  above), each of which contains only a single derivative, and determination of the  $\Delta p_n$ 's for the next step,

$$\begin{aligned} \Delta p_m &= \left\{ \frac{-\text{grad}_{\vec{p}}(E_{\text{msq}}) \cdot \hat{u}_m}{|\text{grad}_{\vec{p}}(E_{\text{msq}})|} \right\} \delta_{\text{step}} \\ &= \frac{\delta_{\text{step}} \int_{f_1}^{f_2} w(f) \text{Re}\left\{\frac{\partial \tilde{F}^*(f, \vec{p})}{\partial p_m} [\tilde{T}(f) - \tilde{F}(f, \vec{p})]\right\} df}{\sqrt{\sum_{n=1}^N \left[ \int_{f_1}^{f_2} w(f) \text{Re}\left\{\frac{\partial \tilde{F}^*(f, \vec{p})}{\partial p_n} [\tilde{T}(f) - \tilde{F}(f, \vec{p})]\right\} df \right]^2}} \end{aligned} \quad (3.24)$$

does not require an  $N \times N$  matrix inversion. In the above

expressions,  $\hat{u}_n$  is a unit vector along the direction of the  $p_n$  axis in parameter space, and  $\delta_{\text{step}}$  is the vectoral magnitude of a step.

In a two dimensional sense, the trajectory followed by this algorithm is effectively that of a viscously damped ball rolling on the contoured error surface, subject to a uniform gravitational field. Normalization of the step vector in equation (3.24) serves to dampen overshooting in the trajectory, analogous to viscous damping of the inertial overshoot in the ball model. Just as with the ball, both excessive overshooting (step size too large) and excessive damping (step size too small) slows progress toward the minimum. A subprogram can be included in the algorithm to vary the step size while monitoring the rate of descent, so as to optimize this quantity.

### 3.2.3 Synthesis Using The Impulse Model

In the case of MSW reflective arrays, the impulse model {3.4, 3.5} provides a very good approximation to actual device performance. The reflectivities of the zone interfaces exhibit a broad, flat spectral response, allowing them to be modeled as having an ideal impulse response. A reflector zone contributes a pair of reflected waves to the filter response from the leading and trailing edges, and interaction between these paired reflections yields a very narrow reflector bandwidth (compared to the filter bandwidth). A spacially distributed array of narrow-band reflectors can be modeled as

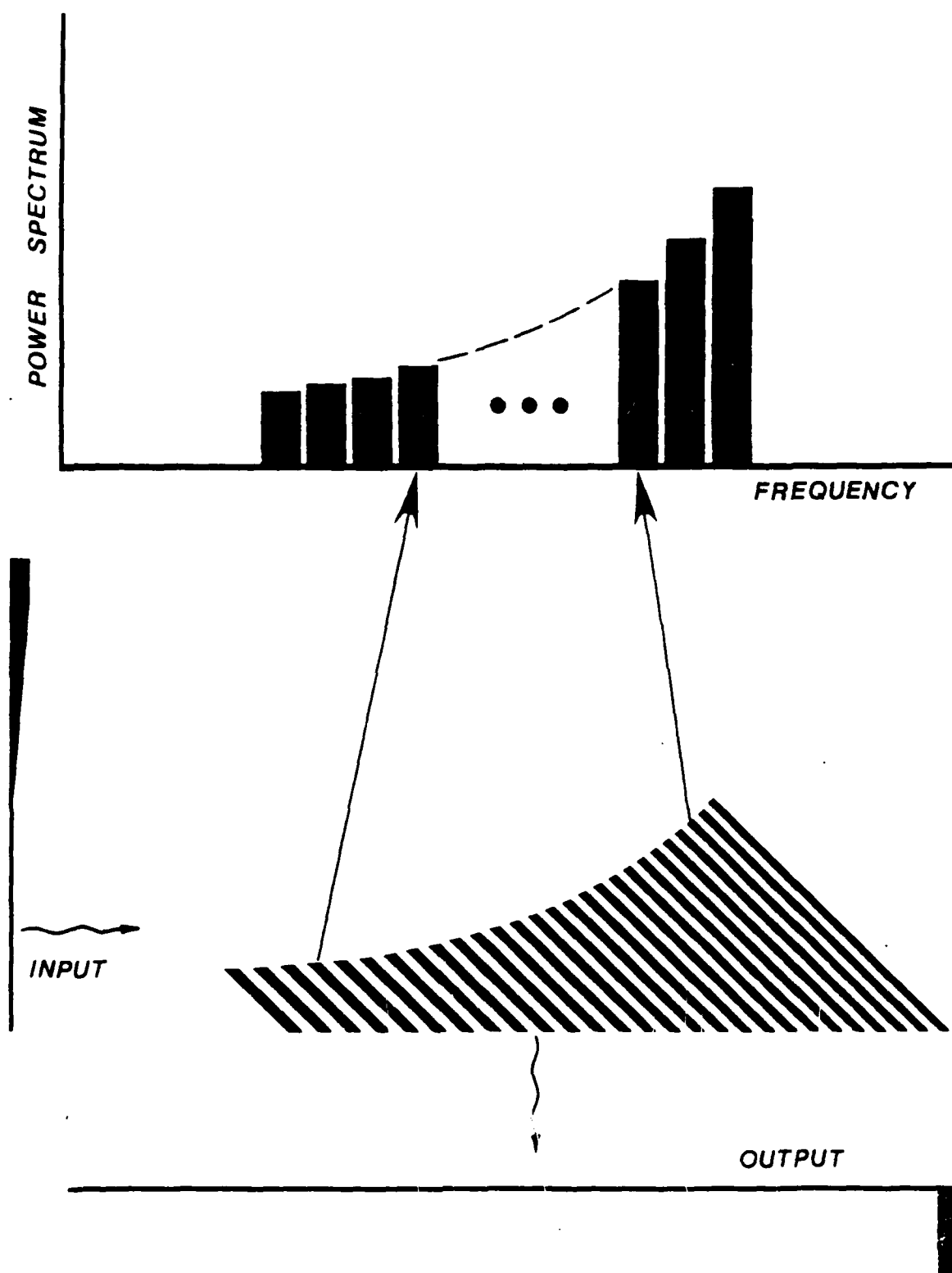


Figure 3.3 Impulse Model for RAF

a contiguous filter bank with adjacent but nonoverlapping passbands (Figure 3.3). Subject to this approximation, the Mean Squared Error (3.7) is minimized by equating the frequency response for the  $i$ th reflector to the target transfer function, normalized by the product of the transducer frequency responses, at  $f_i$ . By associating each reflector with a particular part of the overall spectrum, the group delay and spectral amplitude of the filter can be specified independently.

The spectral response of a reflector, governed solely by its geometry, achieves a maximum when the path lengths associated with leading and trailing edge reflections differ by an odd multiple of the wavelength. The frequency at which this occurs for the  $i$ th reflector is determined by the dispersion relation,

$$w_i = \frac{\pi}{\text{Im}\{\tilde{jk}(f_i)\}} \quad (3.25)$$

where,  $w_i$  is the path length difference from input to output between leading and trailing edge reflections for the  $i$ th reflector (this is the reflector width along the array axis in the  $45^\circ$  incidence case). Reflector placement relative to the input and output determines the transmission path length and thus assigns a group delay to the frequency that the reflector responds to,

$$\tau_g(f_i, y_i) = \frac{1}{2\pi} \left| \frac{d\text{Im}\{\tilde{jk}(f_i)\}}{df} \right| y_i. \quad (3.26)$$

where,  $y_i$  is the mean transmission path length between leading and trailing edge reflections from the  $i$ th reflector. According to the approximate impulse model, these group delays must be equated to the desired group delay,  $\tau(f_i)$ , with the group delay associated with the transducers and driving point mismatch subtracted off,

$$\tau(f_i) - \tau_t(f_i) = \frac{1}{2\pi} \left| \frac{d\text{Im}\{\tilde{jk}(f_i)\}}{df} \right| y_i . \quad (3.27)$$

Eliminating frequency from equations (3.25) and (3.27) gives an implicit relation between  $y_i$  and  $w_i$  that can be iterated until the change in  $y_i$  from its value at the leading edge of the zone that is being positioned (land or bar) equals  $w_i/2$ , corresponding to the zone center. Application of this procedure to determine the center of a land region is equivalent to locating the leading edge of the subsequent reflector region and results in equal land and bar spacings.

The signal contribution of each reflector is determined by the fraction of the incident beam that it samples, corresponding to its projection onto the input transducer. When significant propagation loss is present, as is the case with MSW RAFs, reflector lengths must be modified to compensate. In general, the reflector length should be chosen according to the square root of the normalized reflected power ratio given in equation (3.28).

$$\frac{l_i}{l_0} = \left\{ \frac{\tilde{T}(f_i) \cdot \tilde{T}^*(f_i)}{\tilde{X}_1(f_i) \cdot \tilde{X}_1^*(f_i) \cdot \tilde{X}_2(f_i) \cdot \tilde{X}_2^*(f_i)} \right\}^{1/2} \exp[\operatorname{Re}\{j\tilde{k}(f_i)\}y_i] \quad (3.28)$$

where,  $l_i/l_0$  is the normalized projection of the  $i$ th reflector onto the input transducer,  $f_i$  is the center frequency reflected by the  $i$ th reflector,  $\tilde{T}(f)$  is the target filter transfer function,  $\tilde{k}(f)$  is the dispersion relation for the layered structure (approximately the same for both implanted and unimplanted sections), and  $\tilde{X}_1(f)$  and  $\tilde{X}_2(f)$  are the input and output transducer frequency responses.

An illustration of the application of this approximate synthesis technique is provided by Figures 3.4 through 3.8. These designs also demonstrate the limitations of the MSW RAF technology subject to realistic constraints. Electrical wavelengths in the transducers are about 40 mm, making it desirable to keep the filament lengths and associated MSW wave aperture less than 4 mm. Typical MSW wavelengths are on the order of 300  $\mu$ m so that the ratio of the longest reflector to the shortest reflector (bar length ratio) is in practice limited to about a factor of 10, which imposes one of the principal limitations on ultimate device performance. When only moderate passband modifications are required, as illustrated by the constant amplitude linear delay filters in Figures 3.4 and 3.5, a bar length ratio of 10 is adequate. These designs entailed only a slight flattening of an already approximately flat passband, and the linear delay slopes were

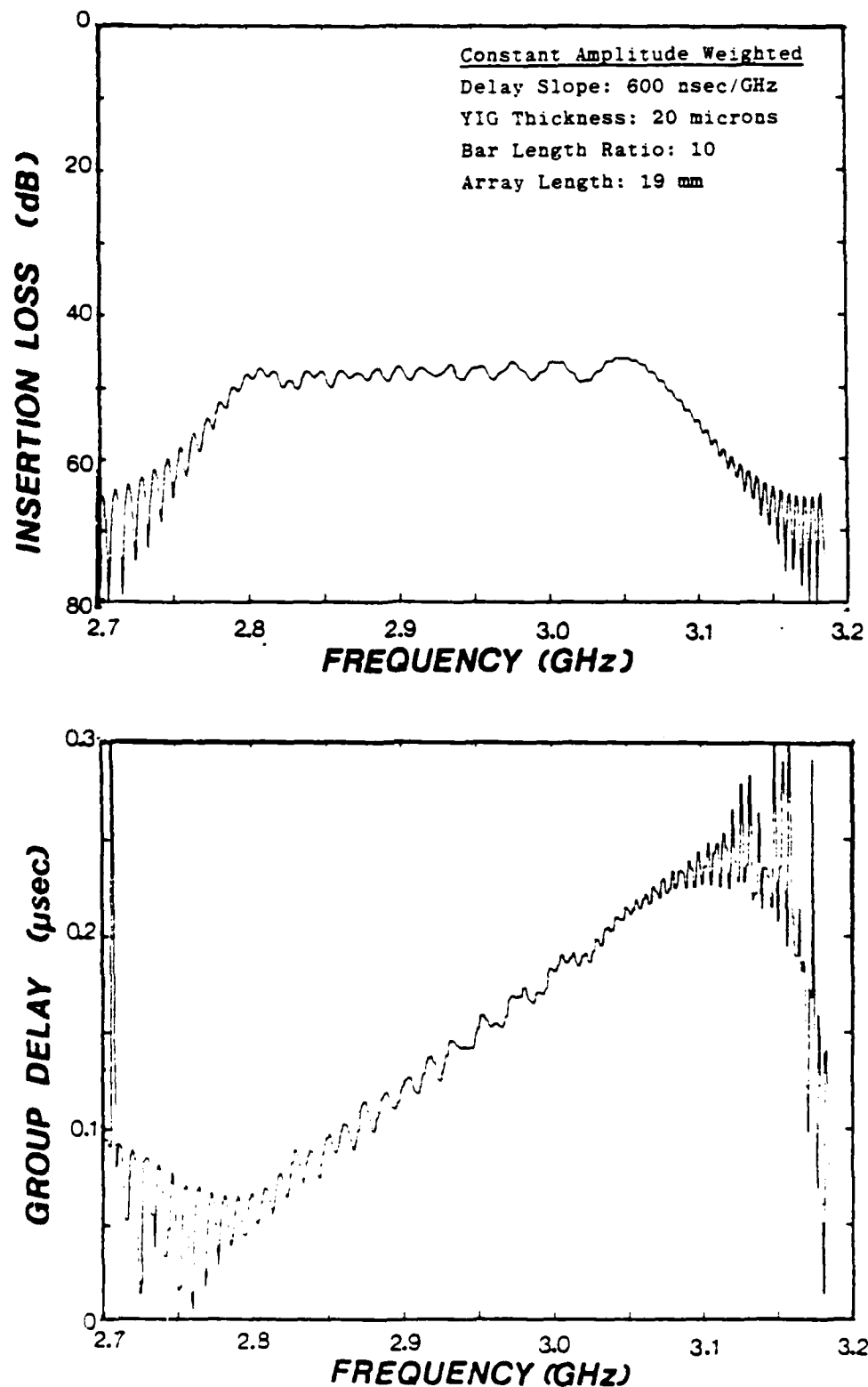


Figure 3.4. Positive slope constant amplitude MSFVW filter synthesized using the approximate impulse model technique.

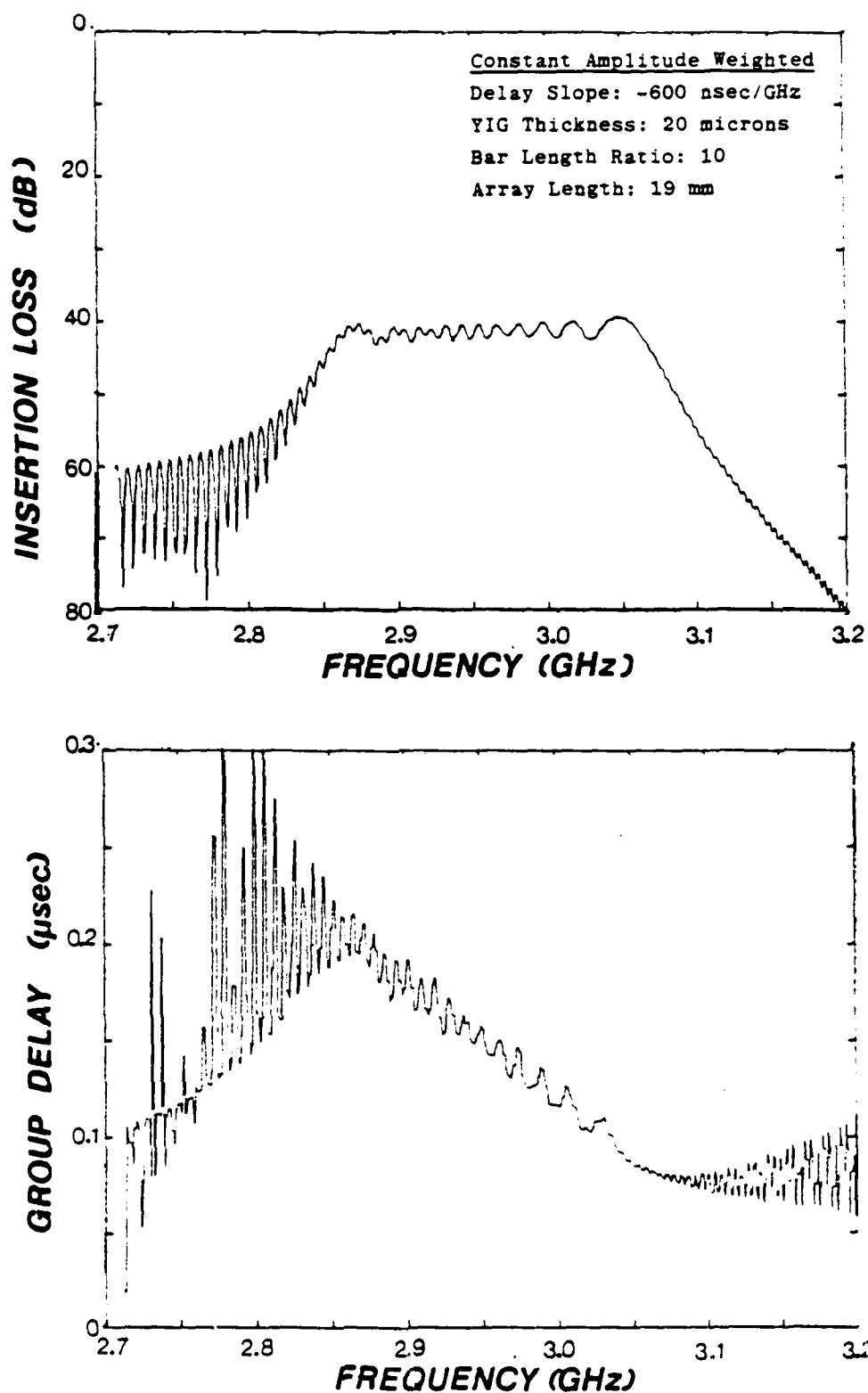
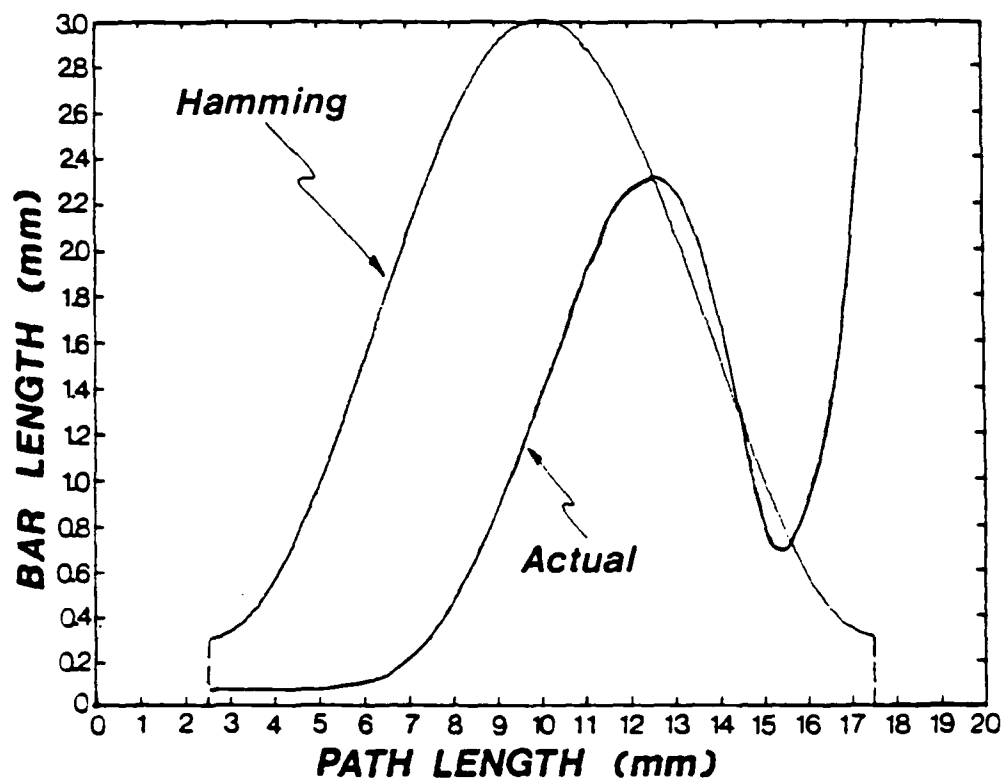


Figure 3.5. Negative slope constant amplitude MSFVW filter synthesized using the approximate impulse model technique.



chosen to fit the mean slope of the intrinsic delay curve, requiring only mild smoothing on the gradual parabolic curvature. The characteristically large insertion losses shown by these results are primarily due to propagation loss and represent severe limitations on the dynamic range of MSW reflective arrays. When losses are in excess of 40 to 50 dB, reflections from the crystal edges constitute a major portion of the transmitted signal. Edge reflections on a well terminated crystal using the current techniques are at about -50 dB, well above the -75 dB thermal noise floor. Thus, the practical dynamic range of a reflective array is determined by the quality of the terminations on the crystal edges. Propagation losses result in a linear roll-off of the frequency response in the passband of a uniform array. The edge of the passband with the highest insertion loss defines the best loss that is achievable if the array is apodized to obtain a flat passband. Long axial array dimensions are required to generate broadband responses, and thus propagation loss imposes a trade-off between filter bandwidth and dynamic range.

A theoretical investigation of a linear delay Hamming weighted filter is presented in Figures 3.6 through 3.8. The bar length variation that is required to obtain a Hamming weighted passband is shown in Figure 3.6, compared to the pattern that would be used in the absence of propagation loss. Although Hamming passband variations span only about a



- Amplitude Weighting: Hamming
- Bandwidth (Hamming): 250 MHz
- Array Length: 19 mm
- Stop Band: 0.01 x

Figure 3.6. Bar length profile for Hamming weighted filter.

factor of 10, compensation for MSW propagation losses distorts the apodization pattern into a curve that spans a bar length ratio of nearly 1000. The amplitude and delay responses obtained from application of the impulse model to the synthesized design are shown in Figure 3.7. The bandwidth of the desired Hamming weighting was 300 MHz, but approximations in the synthesis technique made it necessary to shoot for a bandwidth of 250 MHz to obtain this result. This design demonstrates that an excellent linear delay Hamming weighted filter can theoretically be synthesized if limits placed on the bar length ratio are relaxed. A 600 nsec/GHz delay slope was specified in the synthesis algorithm, and the slope from the impulse model matches this value quite effectively.

Conversely, the effects limiting the bar length ratio to 20, while holding all other parameters constant are shown in Figure 3.8. Severe degradation in both the amplitude fit to the Hamming weighting and the linearity of the delay characteristic occurs.

Realization of sophisticated filter functions is beyond the scope of the MSW reflective array technology. The approximate synthesis technique has proven to be a useful tool in the establishment of this limit and for the design of simpler devices. Provided loss is not a critical factor, MSW RAFs still hold promise for resonators, narrow band channel filters, and moderate bandwidth compressive filters.

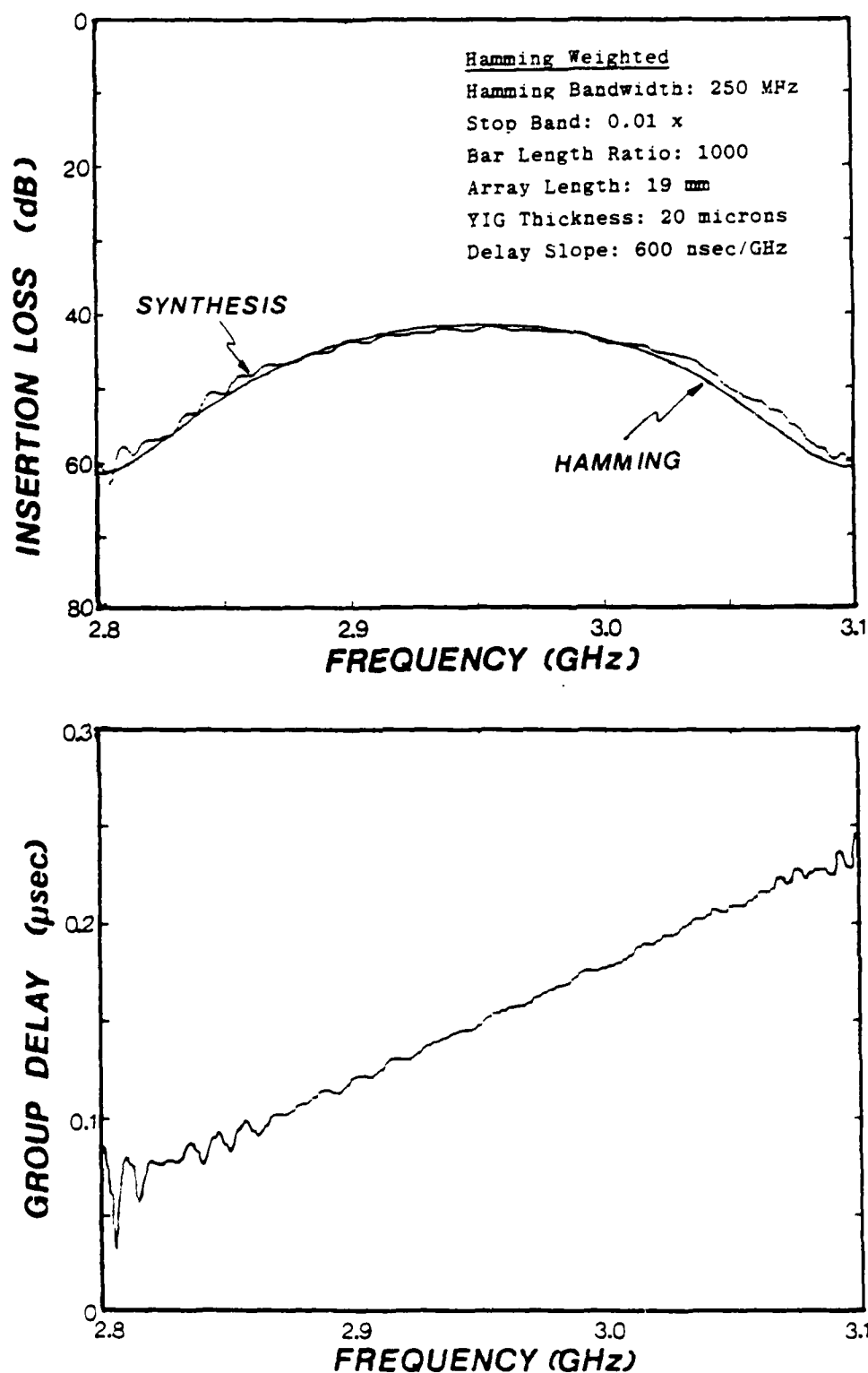


Figure 3.7. Impulse model response for Hamming weighted linear delay filter, synthesized using the approximate procedure.

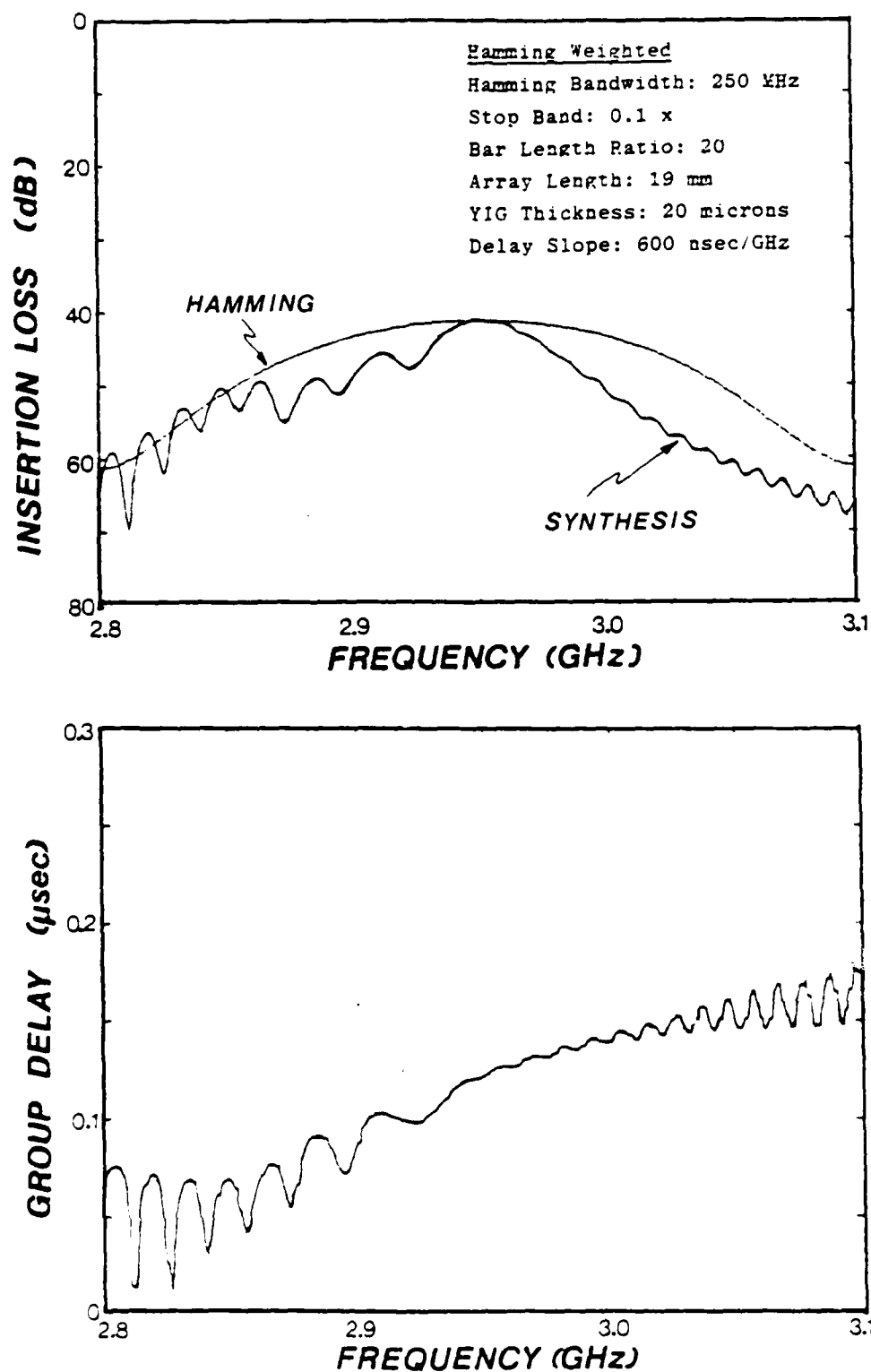


Figure 3.8. Result of Hamming synthesis with the bar length ratio limited to 20.

## CHAPTER 4

ION IMPLANTED MSW REFLECTIVE ARRAYS  
THEORY versus EXPERIMENT4.1 Device Fabrication and Measurement Details

## 4.1.1 Film Growth

The Yttrium Iron Garnet ( $Y_3Fe_5O_{12}$ ) films used in the experiments were grown on one inch polished [111] oriented Gadolinium Gallium Garnet (GGG) wafers, by liquid phase epitaxy. A Tolksdorf melt ( $Y_2O_3$ :1.40 gm,  $Fe_2O_3$ :11.82 gm,  $B_2O_3$ :4.04 gm,  $PbO$ :182.71 gm) with a saturation temperature of  $920^\circ C$ . A supersaturated melt was obtained by dissolving the constituents and holding them at  $1100^\circ C$  for 4 hours and then slowly lowering the temperature to approximately  $10^\circ C$  below the saturation temperature where the crystal growth sequence was begun. The seed crystals (GGG) were lowered to the surface of the melt using a rotating (240 rpm) three fingered chuck that held the polished face tangent to the surface of the melt. The polished face was allowed to just contact the surface of the melt so that the back side of the crystal was not immersed during the growth. Crystal growth rates ranged from  $0.5 \mu m/min$  to  $1.0 \mu m/min$ , depending on the state of the melt. The melt temperature was allowed to drop approximately  $5^\circ C$  between each growth to compensate for the depletion from the previous growth.

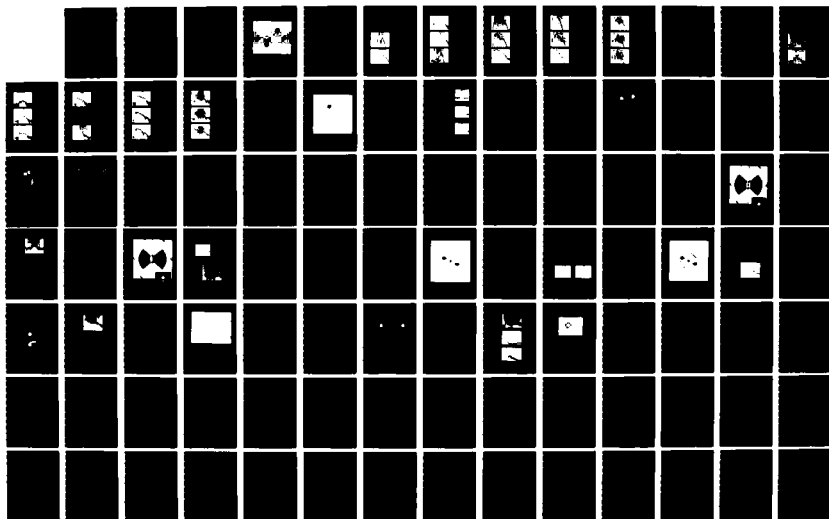
AD-A175 472

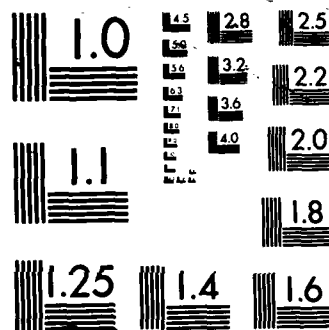
TUNABLE MICROWAVE TRANSVERSAL FILTERS AND DISPERSIVE  
DELAY LINES BASED ON (U) TEXAS UNIV AT ARLINGTON DEPT  
OF ELECTRICAL ENGINEERING J M OWENS ET AL 30 SEP 86  
ARO-17685 1-EL DAAG29-82-K-0073 F/G 9/3

2/3

UNCLASSIFIED

NL





XEROCOPY RESOLUTION TEST CHART



Following the growth, the excess flux was stripped from the wafers using a 24 hr. glacial acetic acid bath. The crystals were weighed before and after the growth to determine the film thickness according to,

$$\text{Thickness } [\mu\text{m}] = \Delta\text{Weight } [\text{gm}] \cdot 383.3. \quad (4.1)$$

Typical values for the Gilbert loss parameter in Figure 2.5,  $\Delta H_{\text{min}}$ , range from 0.1 Oe to 1.0 Oe. A value of 0.5 Oe was assumed, unless stated otherwise.

#### 4.1.2 Array Implantation

The array implantation masks were made of 4  $\mu\text{m}$  thick aluminum, with openings where the surface implant zones were to be located. These masks were fabricated by evaporating the YIG/GGG wafers with aluminum, patterning with photoresist using standard photolithographic techniques, and then etching in phosphoric acid at 70°C. The mask thickness was chosen according to tabulated range data {4.1}, indicating that at 200 KeV acceleration potential, the fluence of boron ions is down by a factor of  $10^{-8}$  from the incident value after passing through 4  $\mu\text{m}$  of aluminum, considered adequate for this application.

The masked wafers were boron implanted using the dose ratios prescribed by MacNeal and Speriosu {2.20} for a nearly uniform strain profile to a depth of 0.36  $\mu\text{m}$ , and the approximate data for magnetization change versus dose given in Figure 2.7. This data is summarized by equation (4.2).

$$\text{DOSE}_{200\text{KeV}} [\text{cm}^{-2}] = -2.875 \times 10^{15} \cdot \frac{M_I}{M_O} + 2.9000 \times 10^{15} \quad (4.2)$$

$$\text{DOSE}_{70\text{KeV}} [\text{cm}^{-2}] = -1.0875 \times 10^{15} \cdot \frac{M_I}{M_O} + 1.1000 \times 10^{15}$$

#### 4.1.3 Microstrip Fabrication

Contact masks for the transducer structures were patterned using standard photolithographic techniques. The microstrips were up plated in gold to a thickness of 3  $\mu\text{m}$  through a photoresist mask on a 250  $\mu\text{m}$  thick alumina substrate, which served as the ground plane spacer for the microstrips. During the up plating process the back of the alumina was uniformly plated to assure a smooth ground plane. Silver epoxy was used to bond the microstrip substrate to a brass ground block, and solder connections were made to flat-tab OSM coaxial launchers at the input and output ports.

#### 4.1.4 Measurement Details

Manual measurements were taken on an HP-8409 network analyzer, and the automatic analyzer results were obtained using an HP-9845B computer/controller.

### 4.2 Normal Incidence Array Theory versus Experiment

#### 4.2.1 MSSW Biased Arrays

Single-bar transducers were used in the MSSW normal incidence experiments, spanning a 3 mm MSW signal aperture, with 30  $\mu\text{m}$  wide filaments, yielding a 100  $\Omega$  characteristic impedance. The feeder lines connecting the coaxial connectors

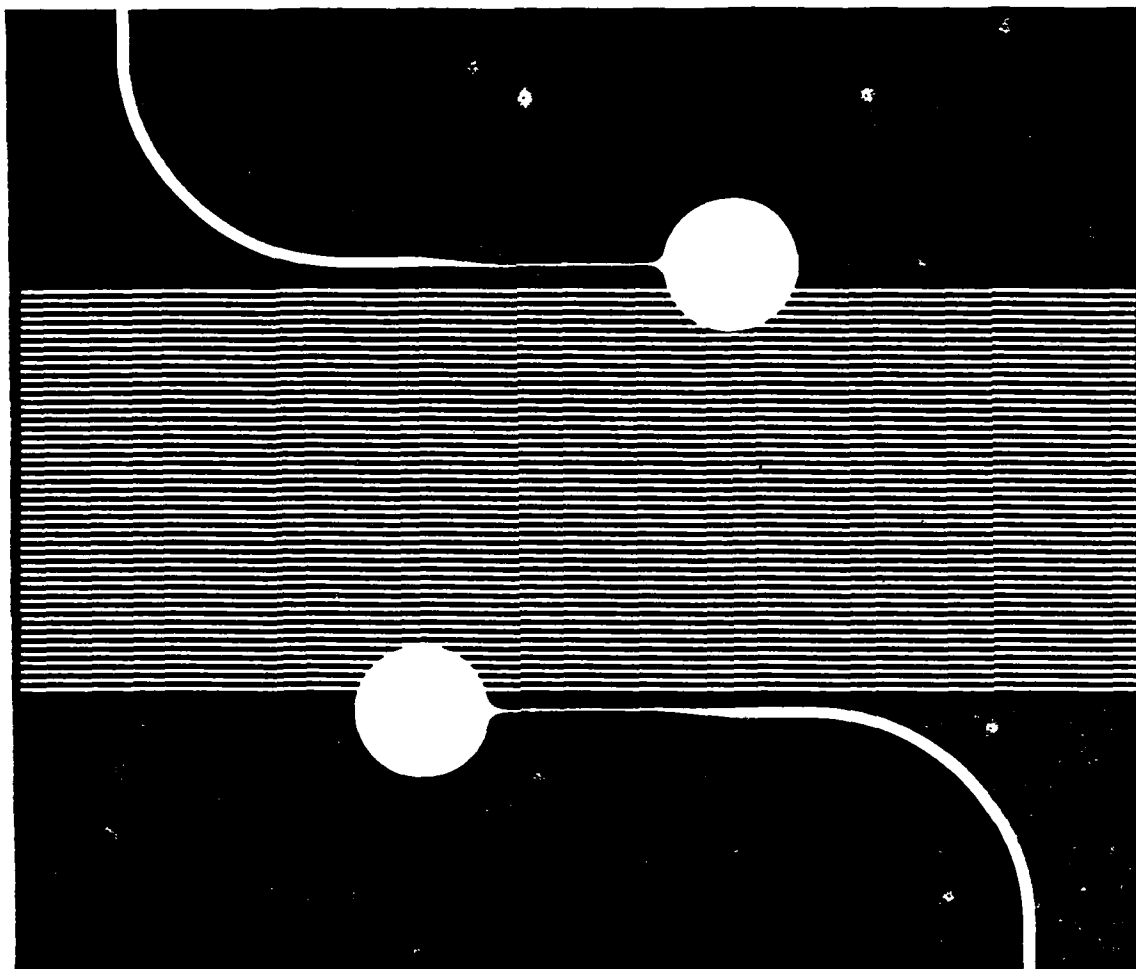


Figure 4.1. Experimental device for both the MSSW and MSFVW normal incidence array measurements.

to the transducer filaments were 250  $\mu\text{m}$  wide, corresponding to a 50  $\Omega$  characteristic impedance. The ferrite array was placed face down on the transducer structure (Figure 4.1). All of the experiments done, consisted of uniform arrays of 46 stripes. The effect of varying YIG thickness and implant dose was investigated, and the devices tested are summarized in TABLE 4.1 (based on equation (4.2)).

TABLE 4.1  
BORON IMPLANT SCHEDULE FOR THE NORMAL INCIDENCE  
MSSW AND MSFVW EXPERIMENTAL DEVICES

| YIG Thickness<br>[ $\mu\text{m}$ ] | Acceleration Potential @ 200 KeV |                      | Acceleration Potential @ 70 KeV |                      | $M0_{\text{imp}}$ |
|------------------------------------|----------------------------------|----------------------|---------------------------------|----------------------|-------------------|
|                                    | Dose<br>[ $\text{cm}^{-2}$ ]     | Charge<br>[Coulombs] | Dose<br>[ $\text{cm}^{-2}$ ]    | Charge<br>[Coulombs] | $M0_{\text{pu}}$  |
| 12.7                               | ---                              | ---                  | ---                             | ---                  | ---               |
|                                    | $4.0 \times 10^{14}$             | $4.6 \times 10^{-3}$ | $1.5 \times 10^{14}$            | $1.7 \times 10^{-3}$ | 0.5               |
|                                    | $8.0 \times 10^{13}$             | $9.1 \times 10^{-4}$ | $3.0 \times 10^{13}$            | $3.4 \times 10^{-4}$ | 0.9               |
| 13.2                               | $8.0 \times 10^{14}$             | $9.1 \times 10^{-3}$ | $3.0 \times 10^{14}$            | $3.4 \times 10^{-3}$ | 0.1               |
|                                    | $4.0 \times 10^{14}$             | $4.6 \times 10^{-3}$ | $1.5 \times 10^{14}$            | $1.7 \times 10^{-3}$ | 0.5               |
|                                    | $8.0 \times 10^{13}$             | $9.1 \times 10^{-4}$ | $3.0 \times 10^{13}$            | $3.4 \times 10^{-4}$ | 0.9               |
| 15.7                               | $8.0 \times 10^{14}$             | $9.1 \times 10^{-3}$ | $3.0 \times 10^{14}$            | $3.4 \times 10^{-3}$ | 0.1               |
|                                    | $4.0 \times 10^{14}$             | $4.6 \times 10^{-3}$ | $1.5 \times 10^{14}$            | $1.7 \times 10^{-3}$ | 0.5               |
|                                    | $8.0 \times 10^{13}$             | $9.1 \times 10^{-4}$ | $3.0 \times 10^{13}$            | $3.4 \times 10^{-4}$ | 0.9               |
| 18.7                               | $8.0 \times 10^{14}$             | $9.1 \times 10^{-3}$ | $3.0 \times 10^{14}$            | $3.4 \times 10^{-3}$ | 0.1               |
|                                    | $4.0 \times 10^{14}$             | $4.6 \times 10^{-3}$ | $1.5 \times 10^{14}$            | $1.7 \times 10^{-3}$ | 0.5               |
|                                    | $8.0 \times 10^{13}$             | $9.1 \times 10^{-4}$ | $3.0 \times 10^{13}$            | $3.4 \times 10^{-4}$ | 0.9               |
| 22.5                               | $8.0 \times 10^{14}$             | $9.1 \times 10^{-3}$ | $3.0 \times 10^{14}$            | $3.4 \times 10^{-3}$ | 0.1               |
|                                    | $4.0 \times 10^{14}$             | $4.6 \times 10^{-3}$ | $1.5 \times 10^{14}$            | $1.7 \times 10^{-3}$ | 0.5               |
|                                    | $8.0 \times 10^{13}$             | $9.1 \times 10^{-4}$ | $3.0 \times 10^{13}$            | $3.4 \times 10^{-4}$ | 0.9               |

Corresponding theoretical and experimental array transmission responses are shown in Figures 4.2 through 4.6. Since the

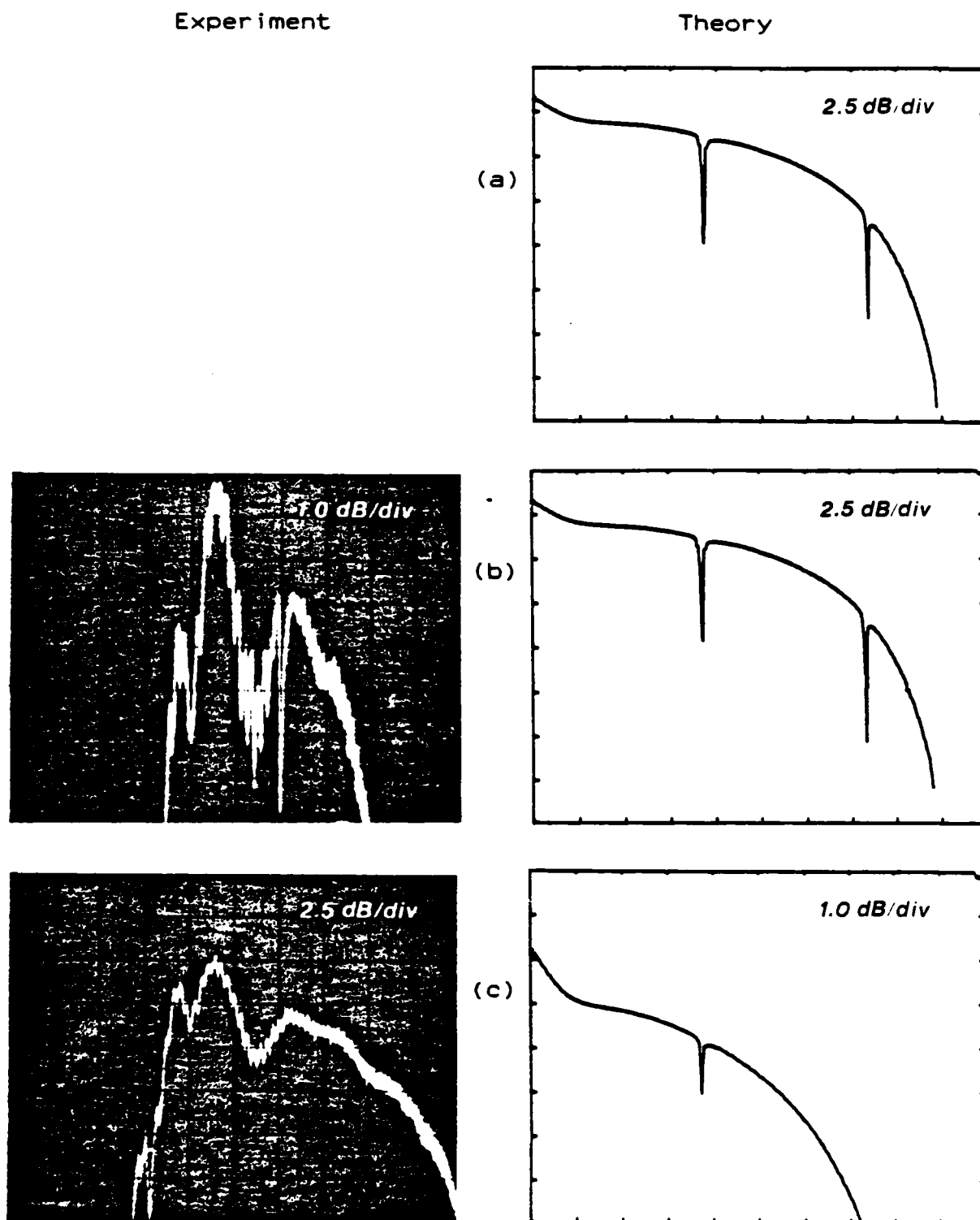


Figure 4.2. Theory versus Experiment for normal incidence MSSW arrays on  $12.7 \mu\text{m}$  YIG (2.5-3.5 GHz).

- (a)  $M0_{\text{imp}}/M0_{\text{pu}} = 0.1$   
 (b)  $M0_{\text{imp}}/M0_{\text{pu}} = 0.5$   
 (c)  $M0_{\text{imp}}/M0_{\text{pu}} = 0.9$

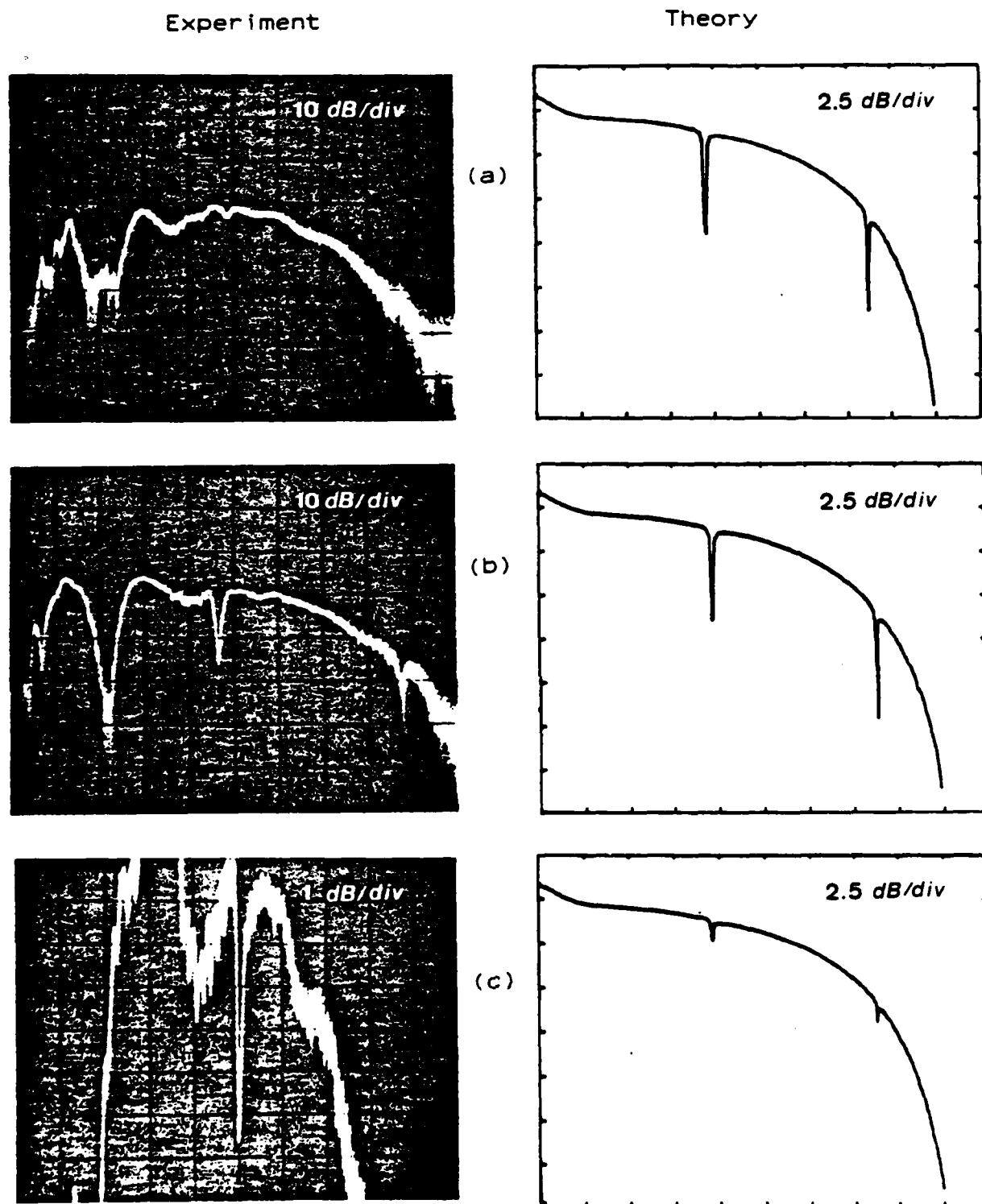
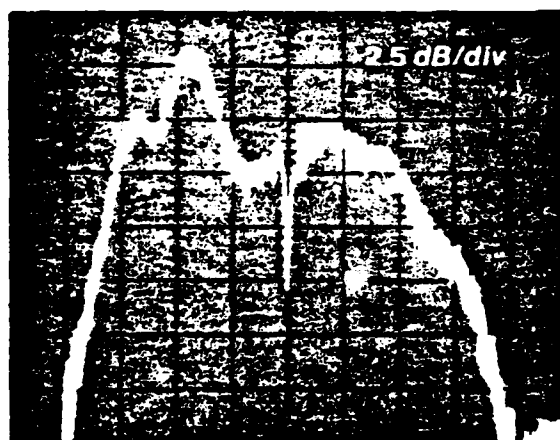


Figure 4.3. Theory versus Experiment for normal incidence MSSW arrays on  $13.2 \mu\text{m}$  YIG (2.5-3.5 GHz).

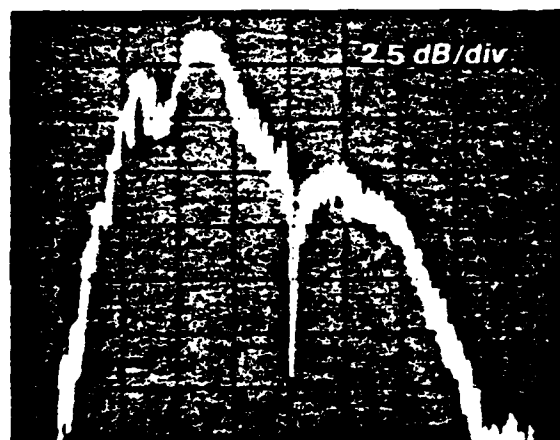
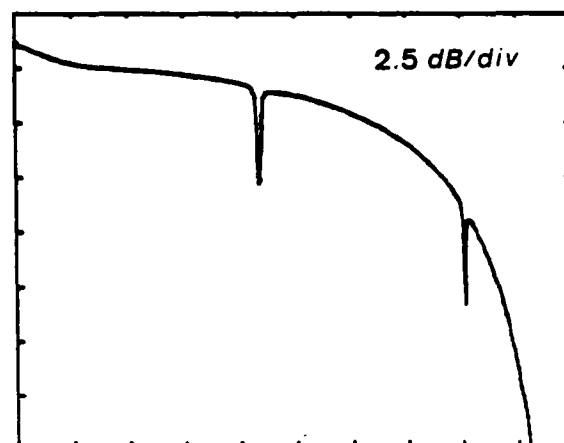
- (a)  $M0_{\text{imp}}/M0_{\text{pu}} = 0.1$   
 (b)  $M0_{\text{imp}}/M0_{\text{pu}} = 0.5$   
 (c)  $M0_{\text{imp}}/M0_{\text{pu}} = 0.9$

Experiment

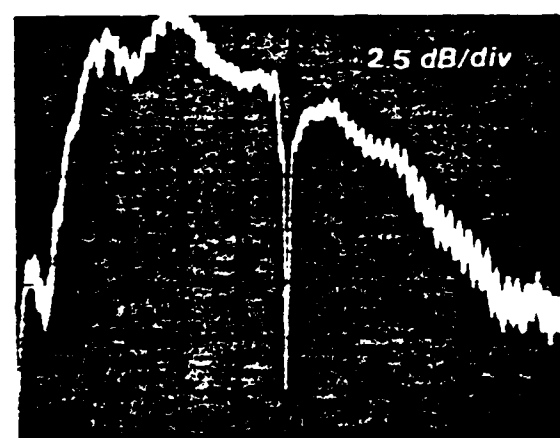
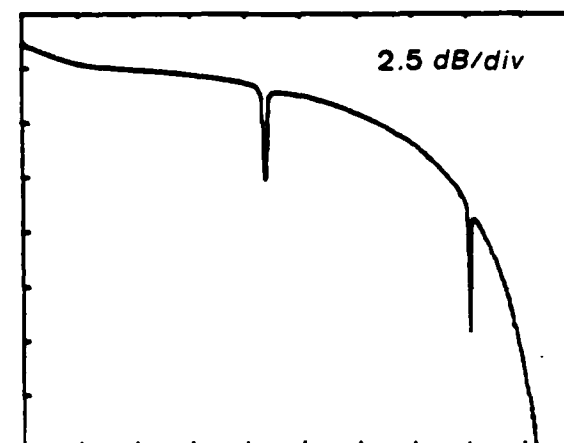
Theory



(a)



(b)



(c)

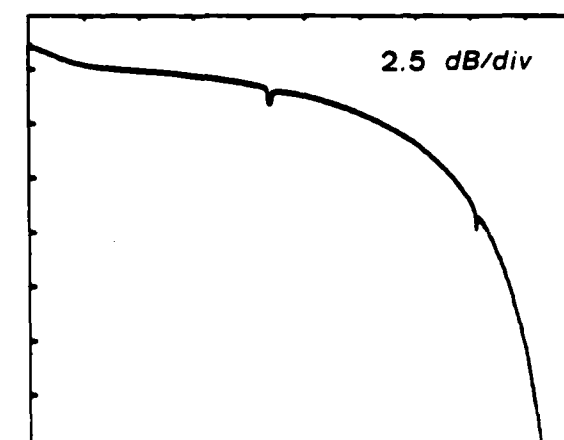


Figure 4.4. Theory versus Experiment for normal incidence MSSW arrays on 15.7  $\mu\text{m}$  YIG (2.5–3.5 GHz).

(a)  $M_{0\text{imp}}/M_{0\text{pu}} = 0.1$

(b)  $M_{0\text{imp}}/M_{0\text{pu}} = 0.5$

(c)  $M_{0\text{imp}}/M_{0\text{pu}} = 0.9$

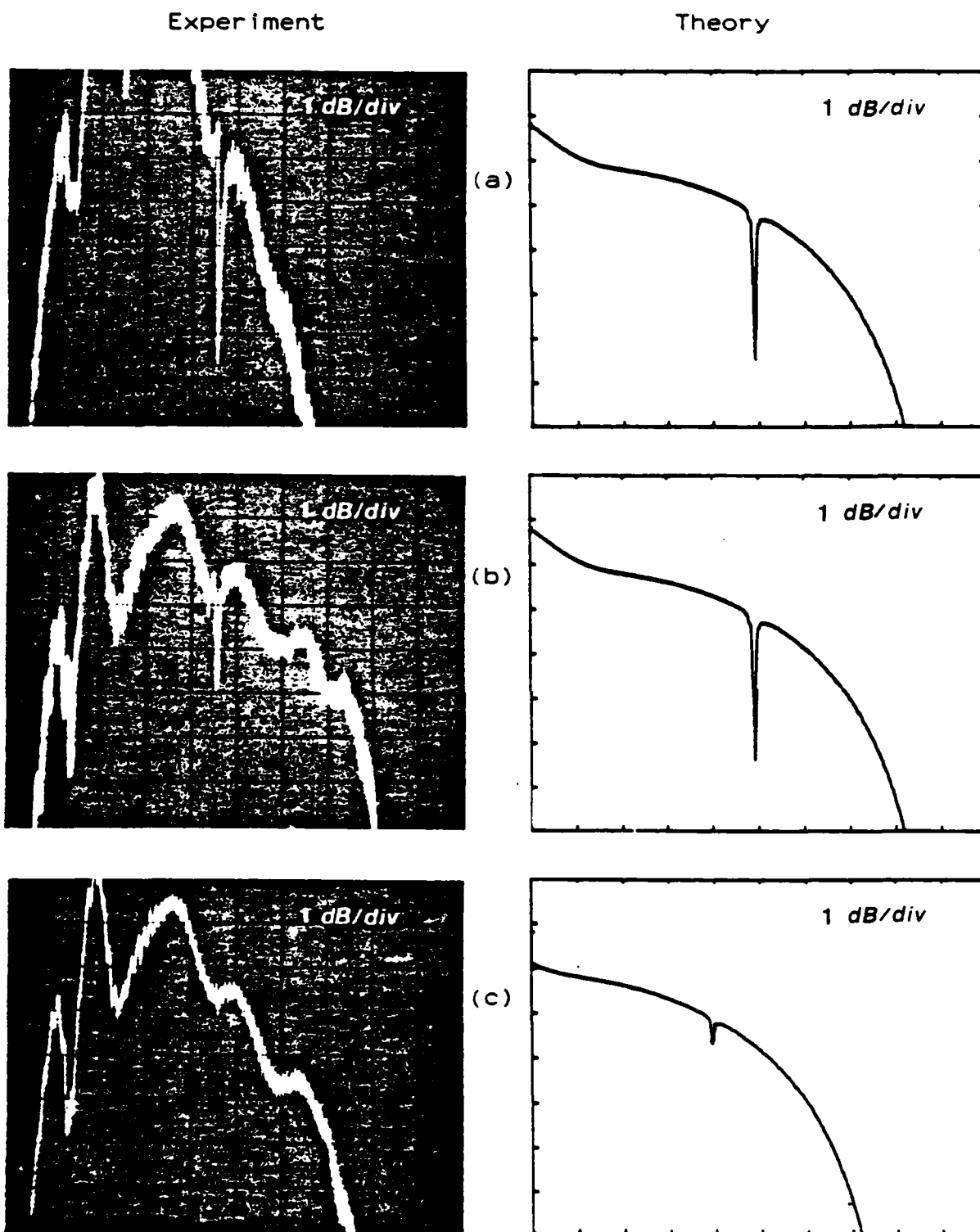


Figure 4.5. Theory versus Experiment for normal incidence MSSW arrays on  $18.7 \mu\text{m}$  YIG (2.5-3.5 GHz).

- (a)  $M0_{\text{imp}}/M0_{\text{pu}} = 0.1$   
 (b)  $M0_{\text{imp}}/M0_{\text{pu}} = 0.5$   
 (c)  $M0_{\text{imp}}/M0_{\text{pu}} = 0.9$



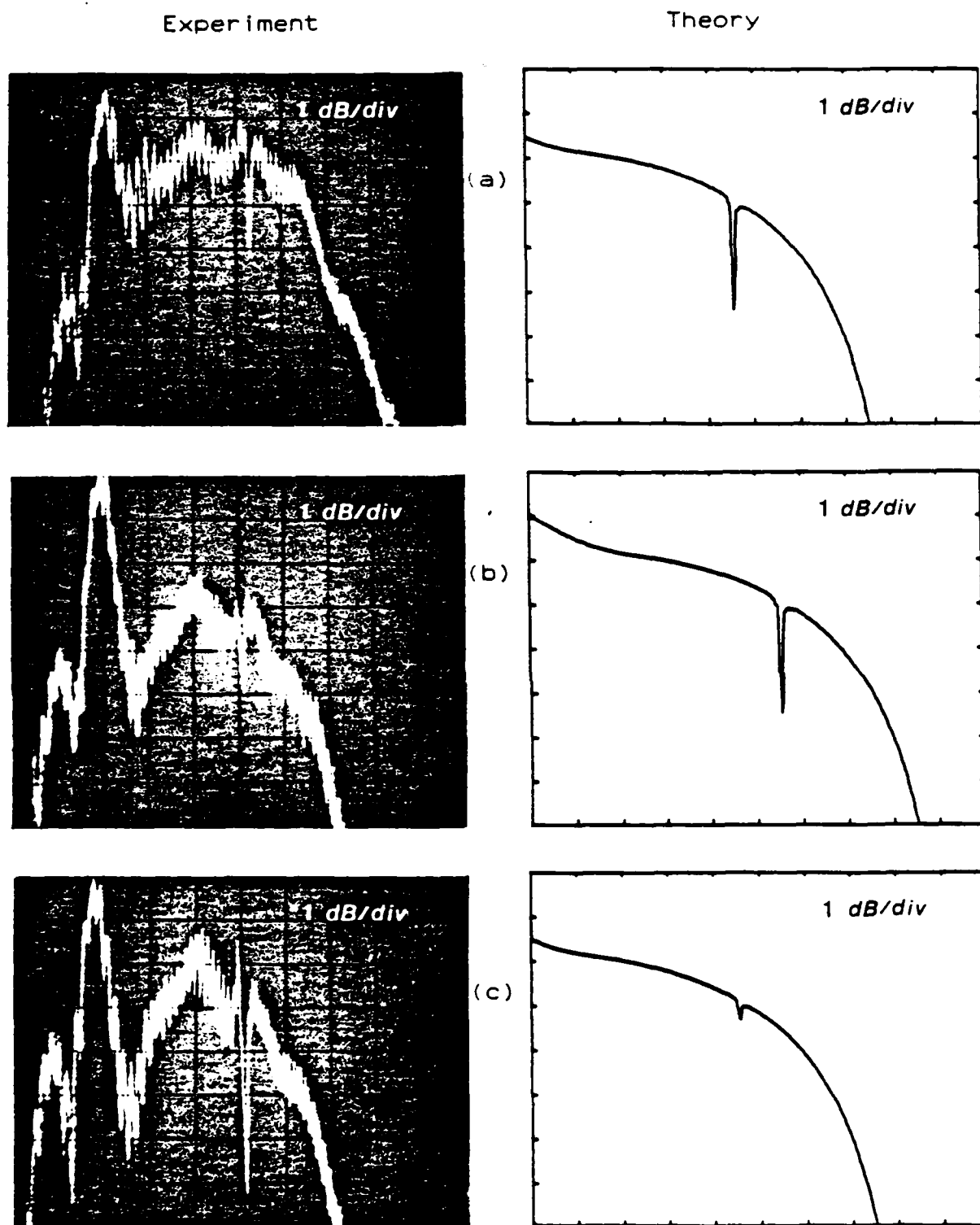


Figure 4.6. Theory versus Experiment for normal incidence MSSW arrays on 22.5  $\mu\text{m}$  YIG (2.5-3.5 GHz).

- (a)  $M0_{\text{imp}}/M0_{\text{pu}} = 0.1$   
 (b)  $M0_{\text{imp}}/M0_{\text{pu}} = 0.5$   
 (c)  $M0_{\text{imp}}/M0_{\text{pu}} = 0.9$

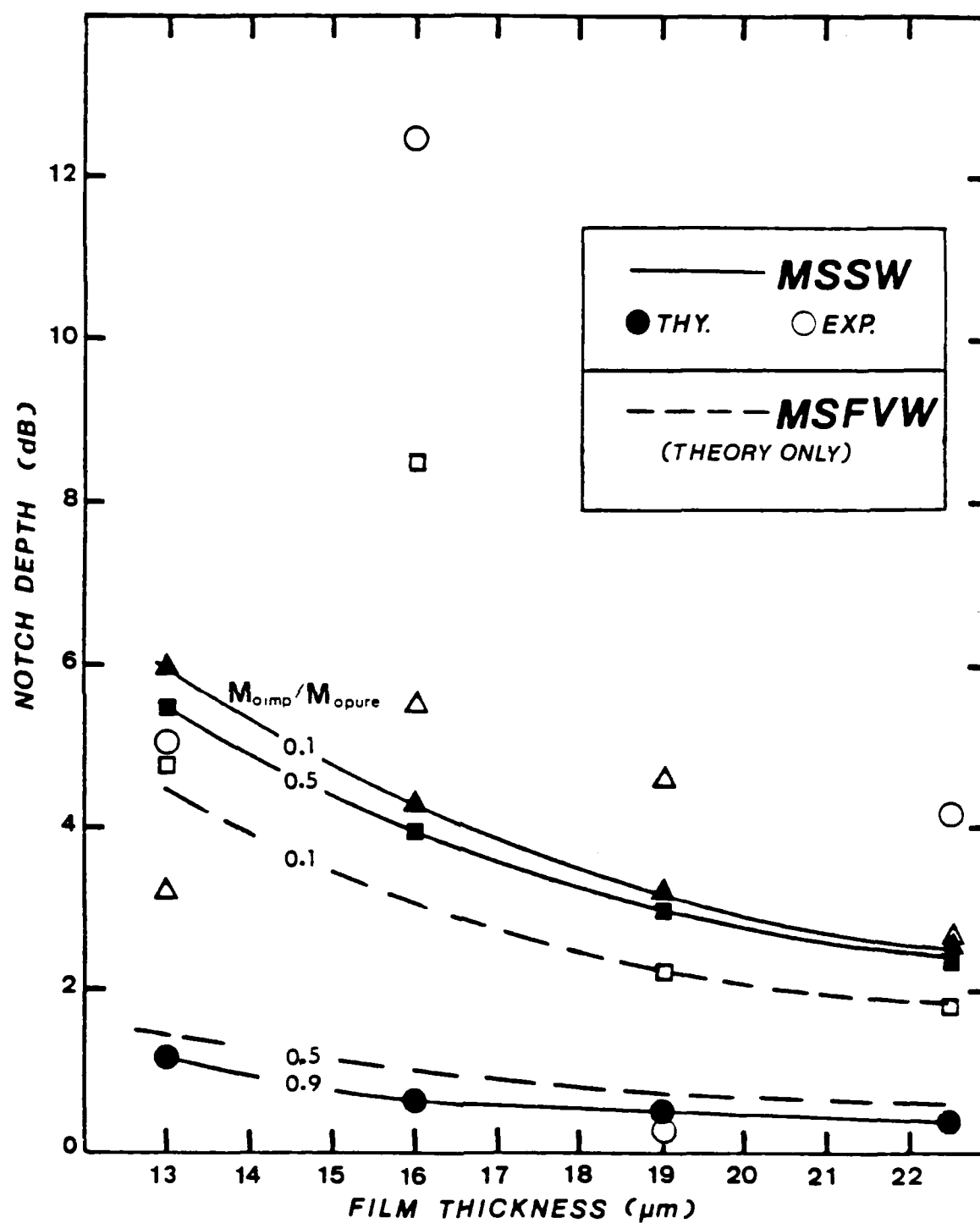


Figure 4.7. Comparison of experimental and theoretical notch depths as a function of implant dose for the MSSW and MSFVW normal incidence arrays.

object of these experiments was to characterize the reflectivities, determined by the notch depth, as a function of implant dose, the theoretical results do not include the transducer responses.

A comparison of theoretical and experimental notch depths for corresponding devices as a function of implant dose is given in Figure 4.7. The experimental notch depths were small and extremely sensitive to device fabrication variations, alignment in the magnet, and interaction with width mode resonances. Width mode resonances have been shown (4.2) to tune at a different rate than the array resonances, and large periodic variations observed in the notch depths as the magnetic bias field was slowly and monotonically tuned, indicates that width mode interaction is a dominant contributor to the uncertainty in the notch depths.

Inspite of the measurement difficulties, the experimental notch depths were in the range predicted by theory, and a rough correlation between the two is evident in Figure 4.7.

#### 4.2.2 MSFVW Biased Arrays

The same devices used in the MSSW experiments were biased for MSFVW operation, and the measured array transmission responses are compared to the theoretical MSFVW array transmission responses in Figures 4.8 through 4.12. The theoretical MSFVW notch depths as a function of dose and film thickness are summarized in Figure 4.7.

Experiment

Theory

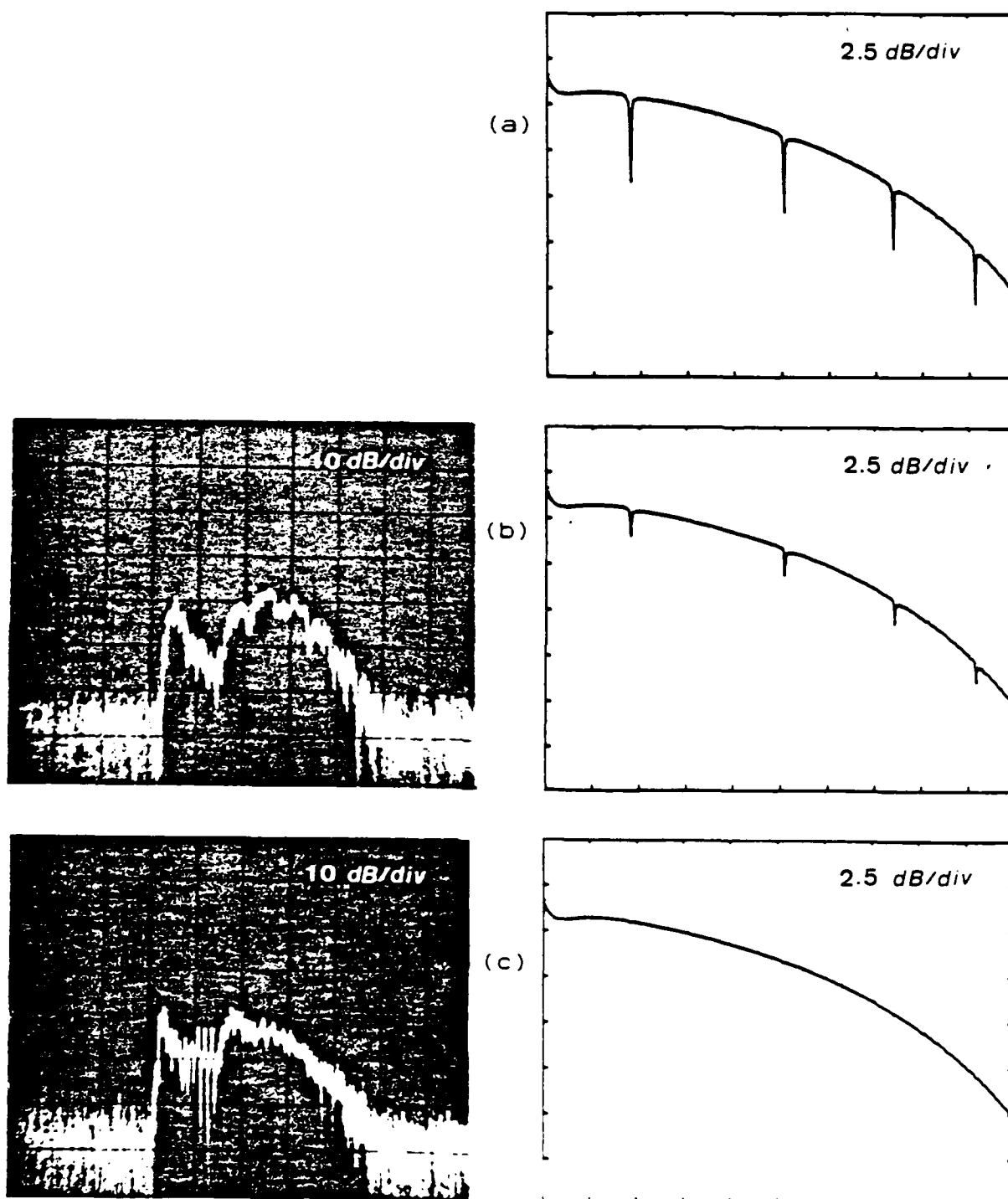


Figure 4.8. Theory versus Experiment for normal incidence MSFVW arrays on 12.7  $\mu\text{m}$  YIG (2.5-3.5 GHz).

- (a)  $M0_{imp}/M0_{pu} = 0.1$   
 (b)  $M0_{imp}/M0_{pu} = 0.5$   
 (c)  $M0_{imp}/M0_{pu} = 0.9$

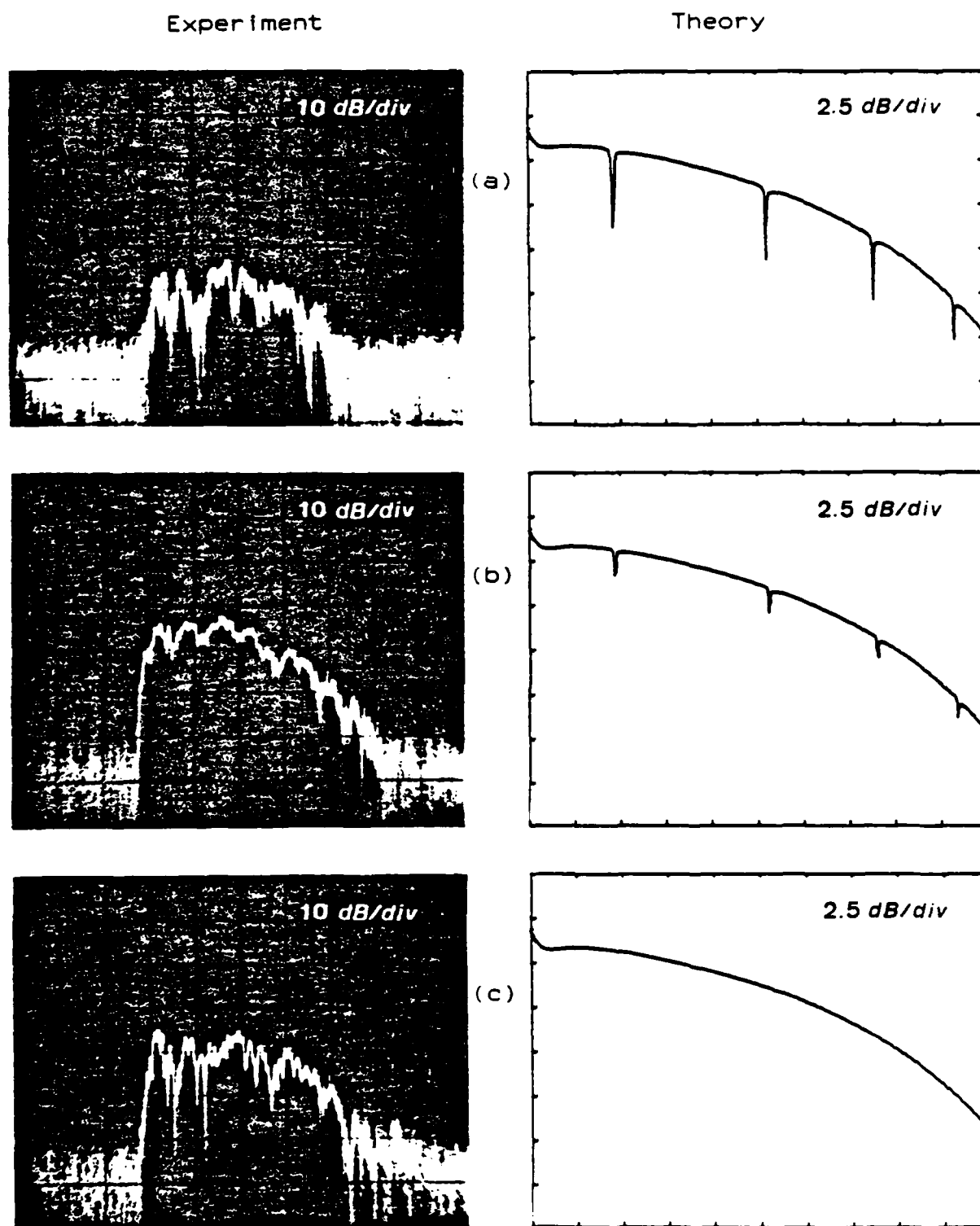


Figure 4.9. Theory versus Experiment for normal incidence MSFVW arrays on 13.2  $\mu$ m YIG (2.5-3.5 GHz).

- (a)  $M0_{imp}/M0_{pu} = 0.1$   
 (b)  $M0_{imp}/M0_{pu} = 0.5$   
 (c)  $M0_{imp}/M0_{pu} = 0.9$

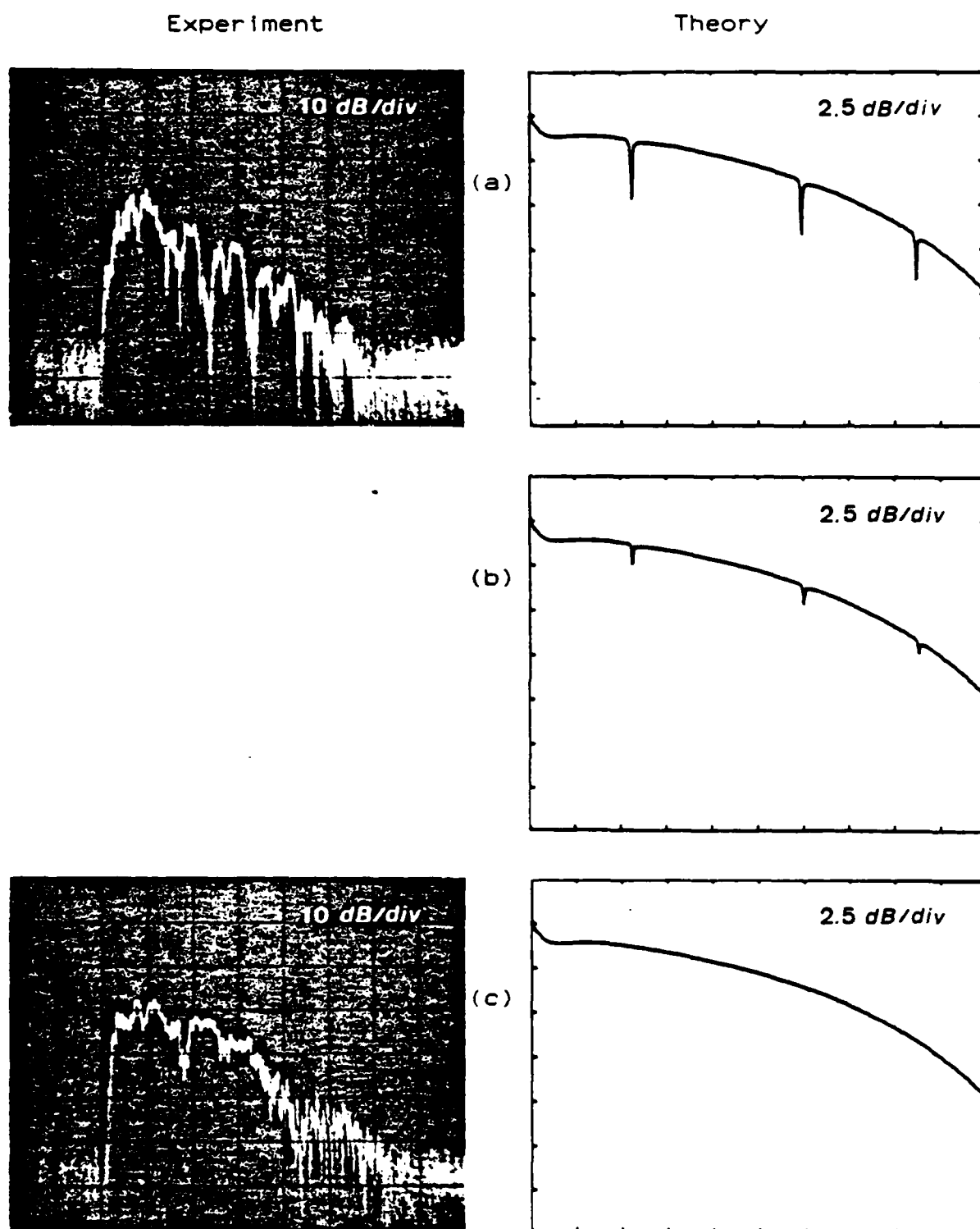


Figure 4.10. Theory versus Experiment for normal incidence MSFVW arrays on 15.7  $\mu\text{m}$  YIG (2.5-3.5 GHz).

- (a)  $M0_{\text{imp}}/M0_{\text{pu}} = 0.1$   
 (b)  $M0_{\text{imp}}/M0_{\text{pu}} = 0.5$   
 (c)  $M0_{\text{imp}}/M0_{\text{pu}} = 0.9$

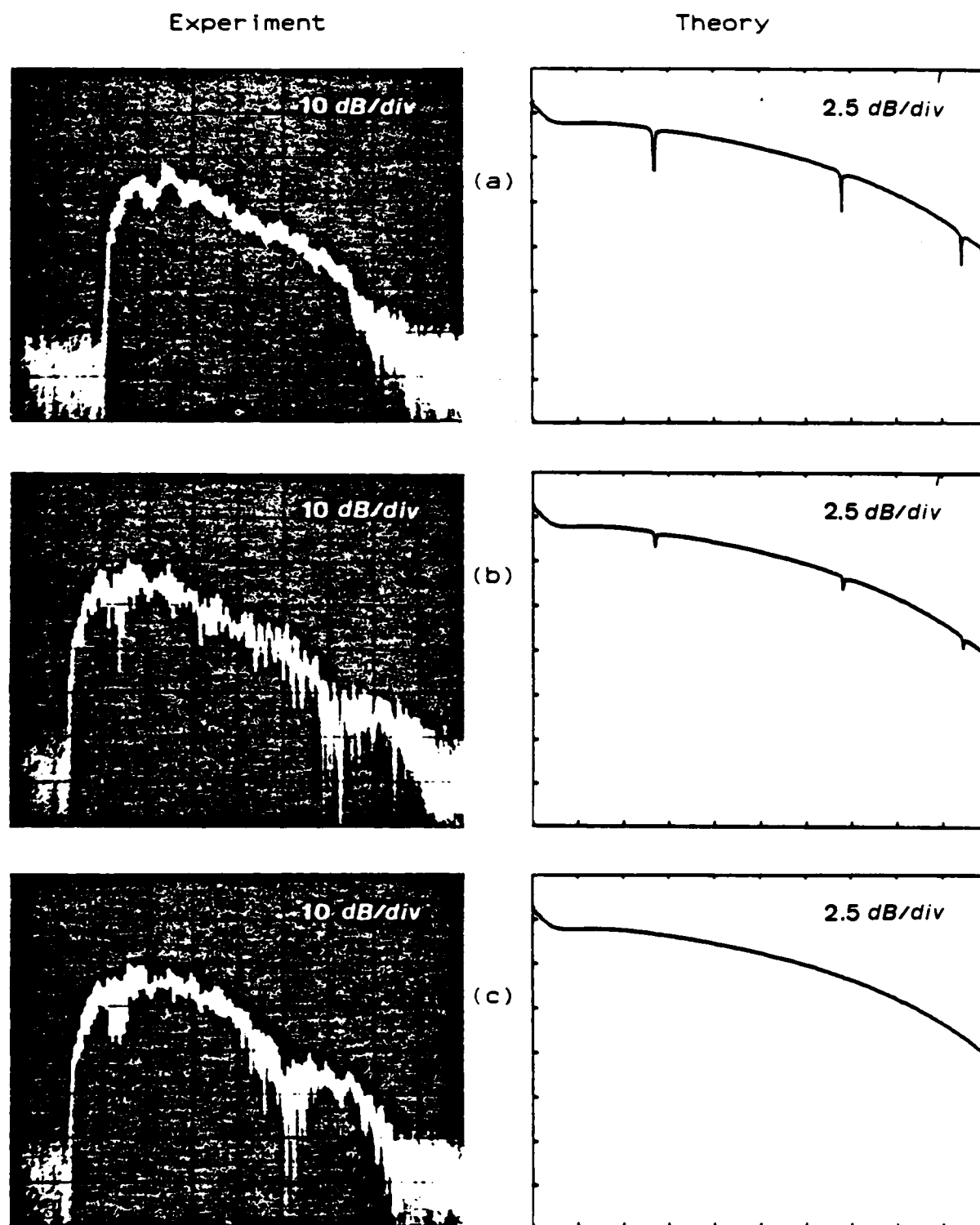


Figure 4.11. Theory versus Experiment for normal incidence MSFVW arrays on 18.7  $\mu\text{m}$  YIG (2.5-3.5 GHz).

- (a)  $M_{0\text{imp}}/M_{0\text{pu}} = 0.1$   
 (b)  $M_{0\text{imp}}/M_{0\text{pu}} = 0.5$   
 (c)  $M_{0\text{imp}}/M_{0\text{pu}} = 0.9$

Experiment

Theory

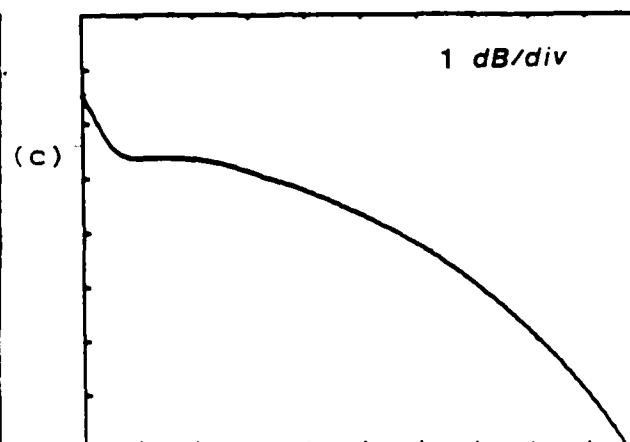
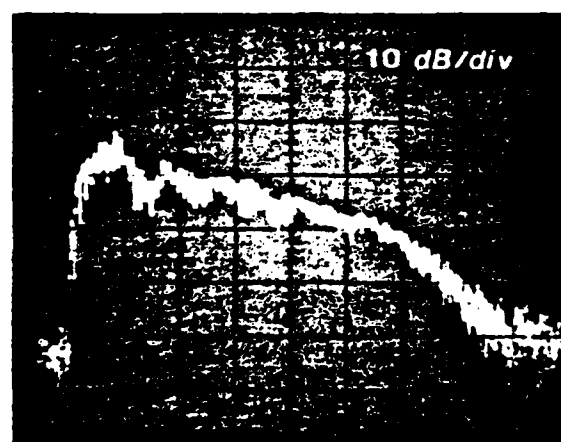
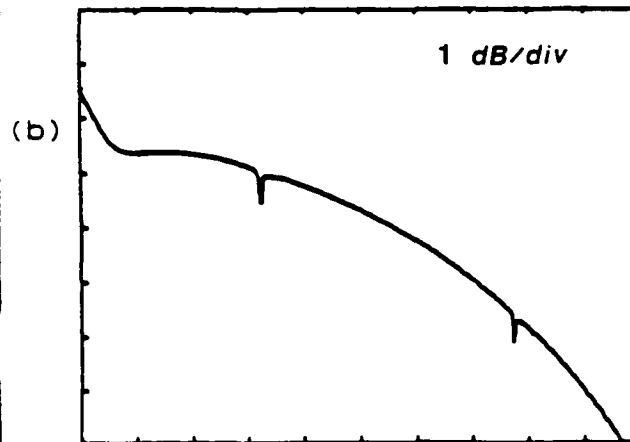
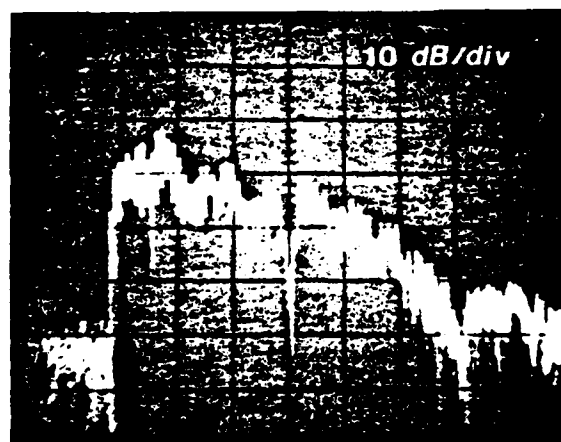
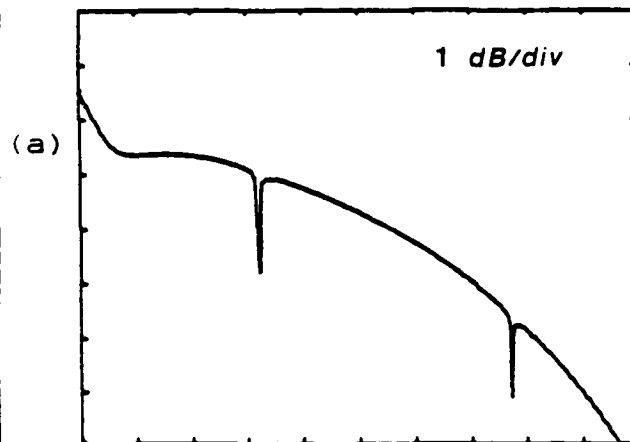
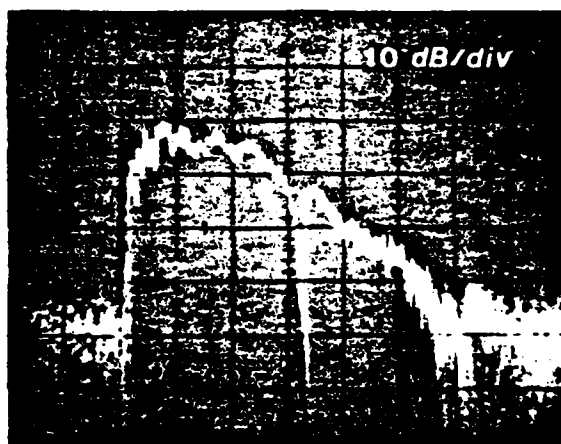


Figure 4.12. Theory versus Experiment for normal incidence MSFVW arrays on 22.5  $\mu\text{m}$  YIG (2.5-3.5 GHz).

- (a)  $M_{0\text{imp}}/M_{0\text{pu}} = 0.1$   
 (b)  $M_{0\text{imp}}/M_{0\text{pu}} = 0.5$   
 (c)  $M_{0\text{imp}}/M_{0\text{pu}} = 0.9$



In MSFVW, the energy is concentrated in the center of the film resulting in weaker reflections from the surface perturbations induced by the implanted zones. Smaller MSFVW reflectivities coupled with higher overall insertion losses compounded the problems encountered in the MSSW measurements, and the correlation between theory and experiment is very poor.

In an effort to obtain a more reliable method for characterizing the relationship between zone boundary reflectivities and implant dose, it was concluded that many of the problems could be eliminated by observing the presence of a signal at the resonance of an oblique incidence array rather than the absence of a signal at the antiresonance of a transmission device.

#### 4.3 Uniform Oblique Incidence MSFVW RAF

Three MSFVW uniform, 20 bar,  $45^\circ$  incidence transversal filters were fabricated to test the accuracy of the theory for different implant doses (Figure 4.13). The implanted reflectors were  $100\text{ }\mu\text{m}$  wide with  $200\text{ }\mu\text{m}$  centers in the propagation direction and a 3 mm transverse aperture. A loop input transducer was used to suppress the low frequency uniform spin mode, with a  $50\text{ }\mu\text{m}$  wide,  $100\text{ }\mu\text{m}$  center spaced, 3 mm aperture filament. The output transducer was a single 7 mm long,  $50\text{ }\mu\text{m}$  wide, shorted microstrip, and being electrically short ( $\lambda @ 3\text{ GHz} \approx 40\text{ mm}$ ) acted as a summer for the reflected waves.

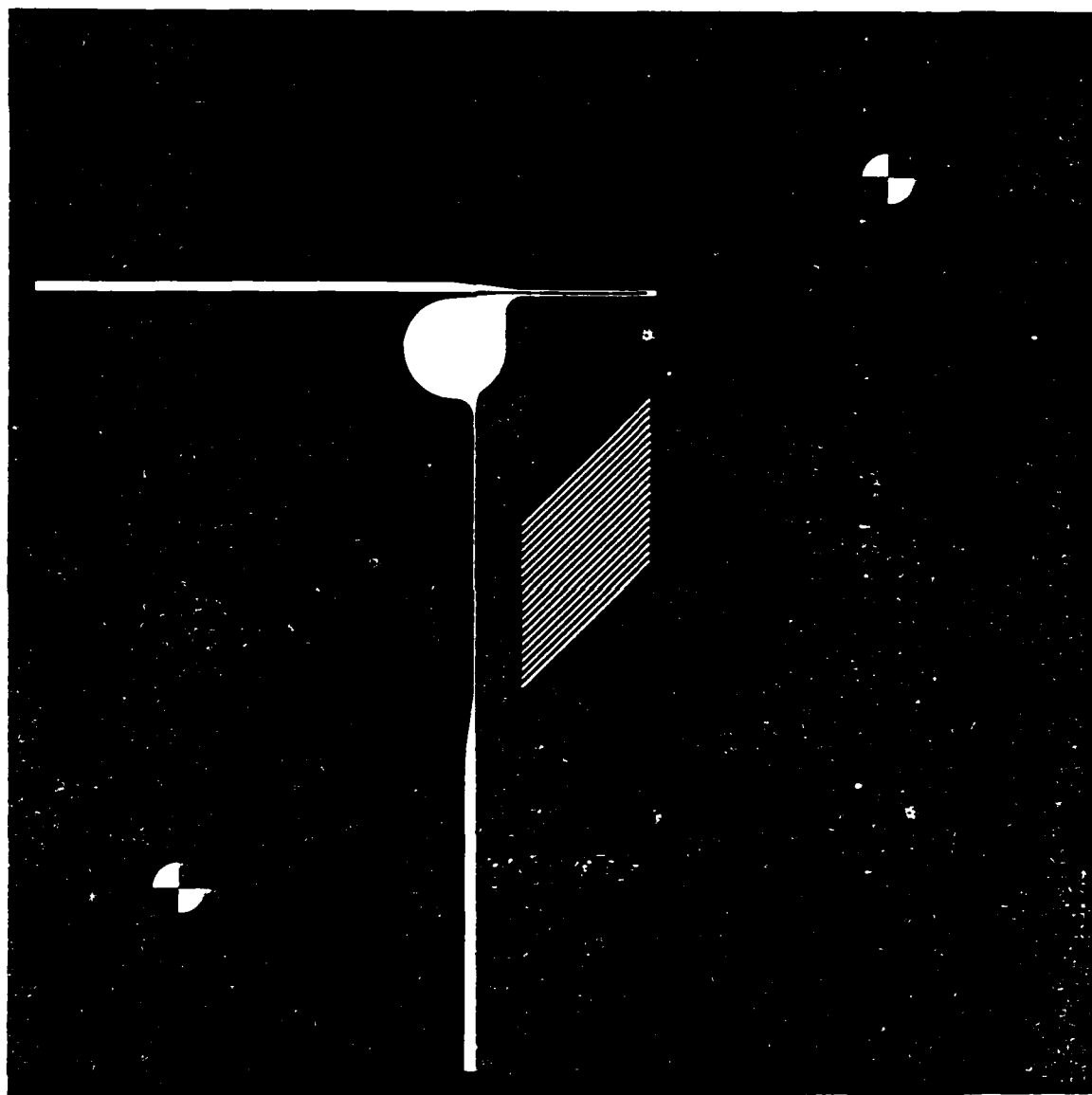


Figure 4.13. Experimental layout for the uniform 20 bar oblique incidence MSF/W array devices.

Dose levels based on equation (4.3), acceleration potentials, and YIG thicknesses used in these experiments are given in TABLE 4.2. Films of nearly equal thicknesses were used in order to investigate the effects of varying implant doses alone on the observed reflectivities.

TABLE 4.2

BORON IMPLANTATION SCHEDULE FOR THE  
UNIFORM 20-BAR OBLIQUE INCIDENCE MSFVW RAF EXPERIMENTS

| YIG<br>Thickness<br>[ $\mu\text{m}$ ] | Dose #1<br>@200-keV<br>[ $\text{cm}^{-2}$ ] | Dose #2<br>@70-keV<br>[ $\text{cm}^{-2}$ ] | Projected<br>$M0_{\text{imp}}/M0_{\text{pure}}$ |
|---------------------------------------|---|--|---|
| 22.3                                  | $6.0 \times 10^{14}$                        | $2.3 \times 10^{14}$                       | 0.8   |
| 23.0                                  | $1.2 \times 10^{15}$                        | $4.5 \times 10^{14}$                       | 0.6   |
| 23.0                                  | $2.9 \times 10^{15}$                        | $1.1 \times 10^{14}$                       | 0.0   |

Theoretical and experimental results are compared on identical scales for the three implant doses in Figure 4.14. The highest implantation dose resulted in extensive crystal damage, and it was assumed that the impulse model was no longer valid for this device. This crystal damage has been observed by others when high implant dose levels were used. According to SEM investigations, the excessive strain that results from high implant doses causes cracks to develop in the ferrite film that span the land regions. Such cracks exhibit broadband reflectivities that would tend to mask the response.

The ripple superimposed on the experimental frequency

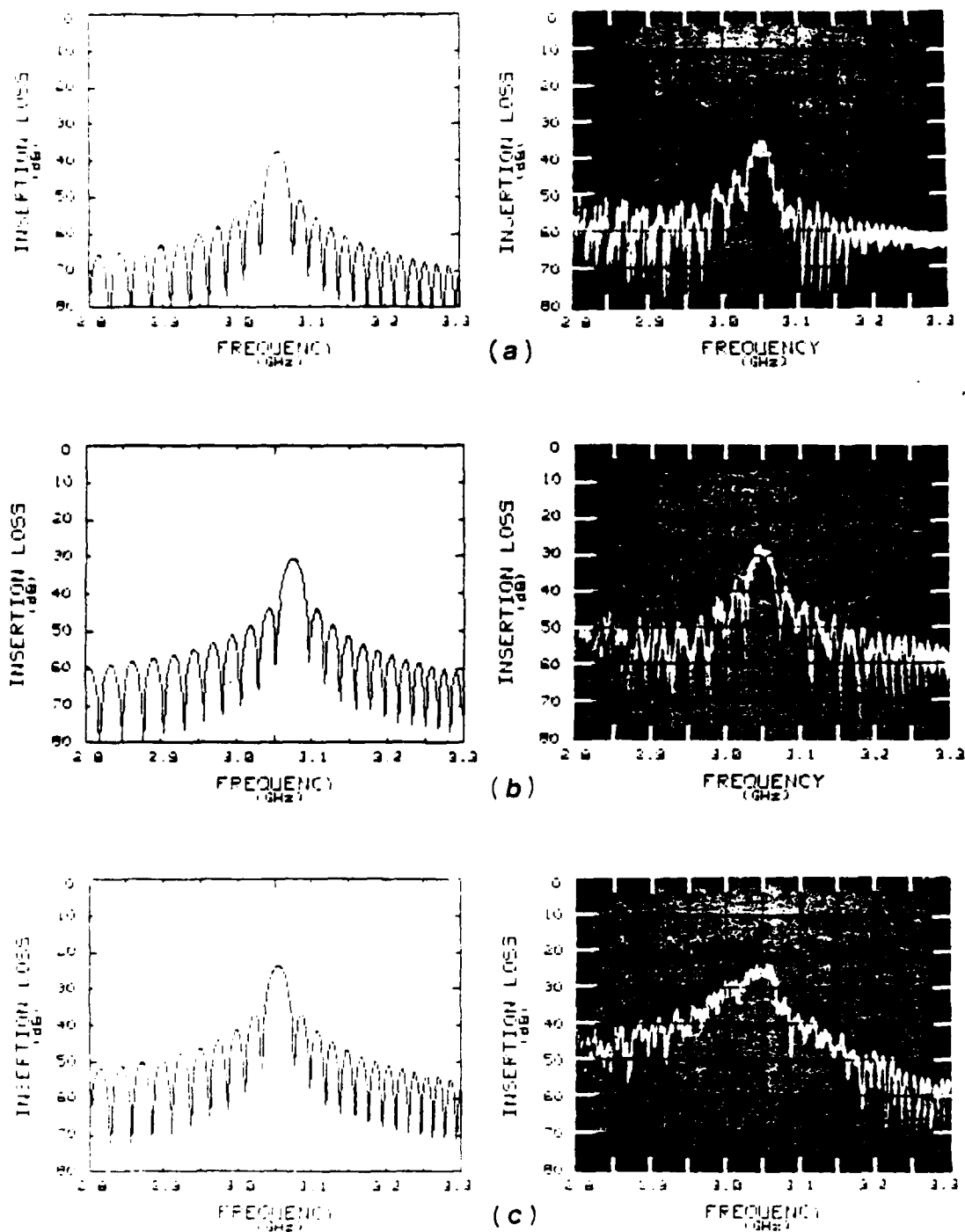


Figure 4.14. Experiment versus Theory for the uniform, 20-bar, oblique incidence MSFVW RAF's.

- (a)  $M0_{imp}/M0_{pure} = 0.8$
- (b)  $M0_{imp}/M0_{pure} = 0.6$
- (c)  $M0_{imp}/M0_{pure} = 0.0$

responses is due to crystal edge reflections. Angle lapping the crystal edges ( $2^\circ$  is typical) helps this problem, but it is difficult to avoid when insertion losses are greater than 20 dB. Since the signal level of the edge reflections is independent of the level of the array reflected signal, the problem is more pronounced in higher loss devices. The two lower dose experiments showed good agreement with theory in peak insertion loss, main lobe width, sidelobe suppression, and sidelobe width. A comparison of the critical parameters is summarized in TABLE 4.3.

TABLE 4.3

THEORY/EXPERIMENT FOR THE  
UNIFORM 20-BAR OBLIQUE INCIDENCE MSFVW RAF's

| $M0_{imp}$<br>$M0_{pure}$ | Peak I.L.<br>[dB] | Sidelobe<br>Suppression<br>[dB] | Main Lobe<br>Width<br>[MHz] | Sidelobe<br>Width<br>[MHz] |
|---------------------------|-------------------|---------------------------------|-----------------------------|----------------------------|
| 0.8                       | 36.5/37           | 13.3/12                         | 42.0/40                     | 21.0/20                    |
| 0.6                       | 30.5/29           | 13.3/13                         | 42.0/45                     | 21.0/22                    |
| 0.0                       | 22.6/25           | 13.3/NA                         | 42.0/50                     | 21.0/NA                    |

This preliminary investigation indicates good agreement between experimental ion implanted MSFVW reflective arrays and a theory based on the magnetostatic approximation and an impulse model. The assumption that a bar-gap interface can be modeled as a simple wave impedance discontinuity in a plane wave structure is verified. It was shown that ion implanted reflectors work well for MSFVW transversal filters, avoiding

sharp discontinuities encountered with etched grooves that cause fringe field coupling to vertical spin waves. A more complete characterization of the effect of implantation dose on saturation magnetization would be desirable.

#### 4.4 Delay Graded Oblique Incidence MSFVW RAF

##### 4.4.1 Positive Delay Slope Array

A  $45^\circ$  incidence, boron implanted MSFVW RAF was designed for a linear group delay of 600 nsec/GHz on the basis of the impulse model and constructed (Figure 4.15). The array consisted of 61 implanted reflector zones with a uniform 3 mm transverse aperture. A double dose boron implant with an initial fluence of  $5.56 \times 10^{14} \text{ cm}^{-2}$  at 70 KeV followed by  $1.46 \times 10^{-2}$  at 200 KeV was used, corresponding to a projected uniform step reduction in the saturation magnetization of 50% to a depth of 0.36  $\mu\text{m}$ . The implanted reflectors varied from 0.082 mm to 0.192 mm in width along the propagation direction, obtaining the maximum bandwidth possible for unsectioned bars without harmonic overlap. A loop input transducer was used to suppress the uniform spin mode, with a 50  $\mu\text{m}$  wide, 100  $\mu\text{m}$  center spaced, 3 mm aperture filament. The output transducer was a single 19 mm long, 50  $\mu\text{m}$  wide shorted microstrip.

Theoretical and experimental  $S_{21}$  amplitude and group delay results are compared in Figure 4.16 on identical scales and are quantitatively summarized with the design goal in TABLE 4.4.

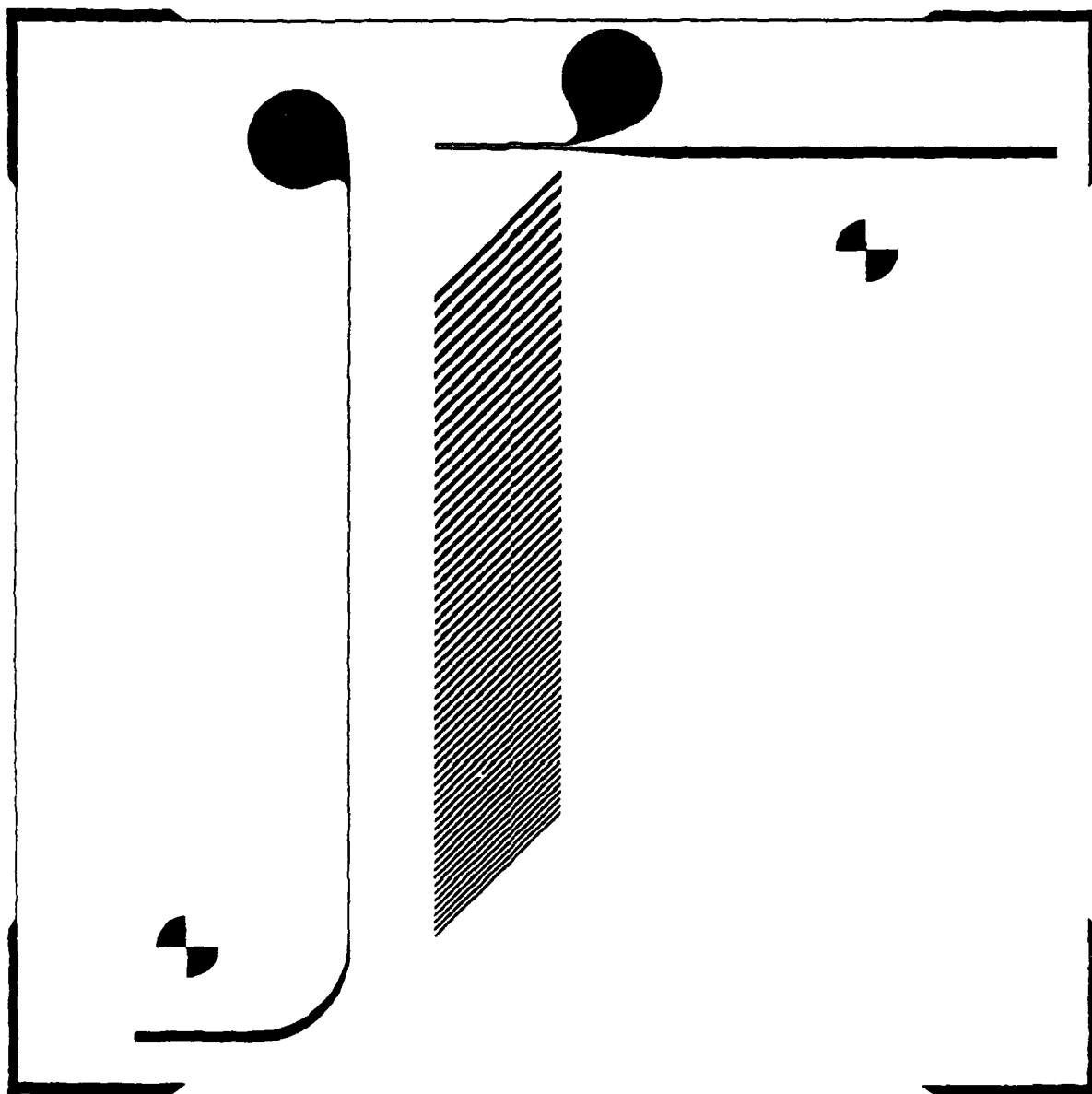


Figure 4.15. Experimental layout for the positive delay slope oblique incidence MSFVW RAF.

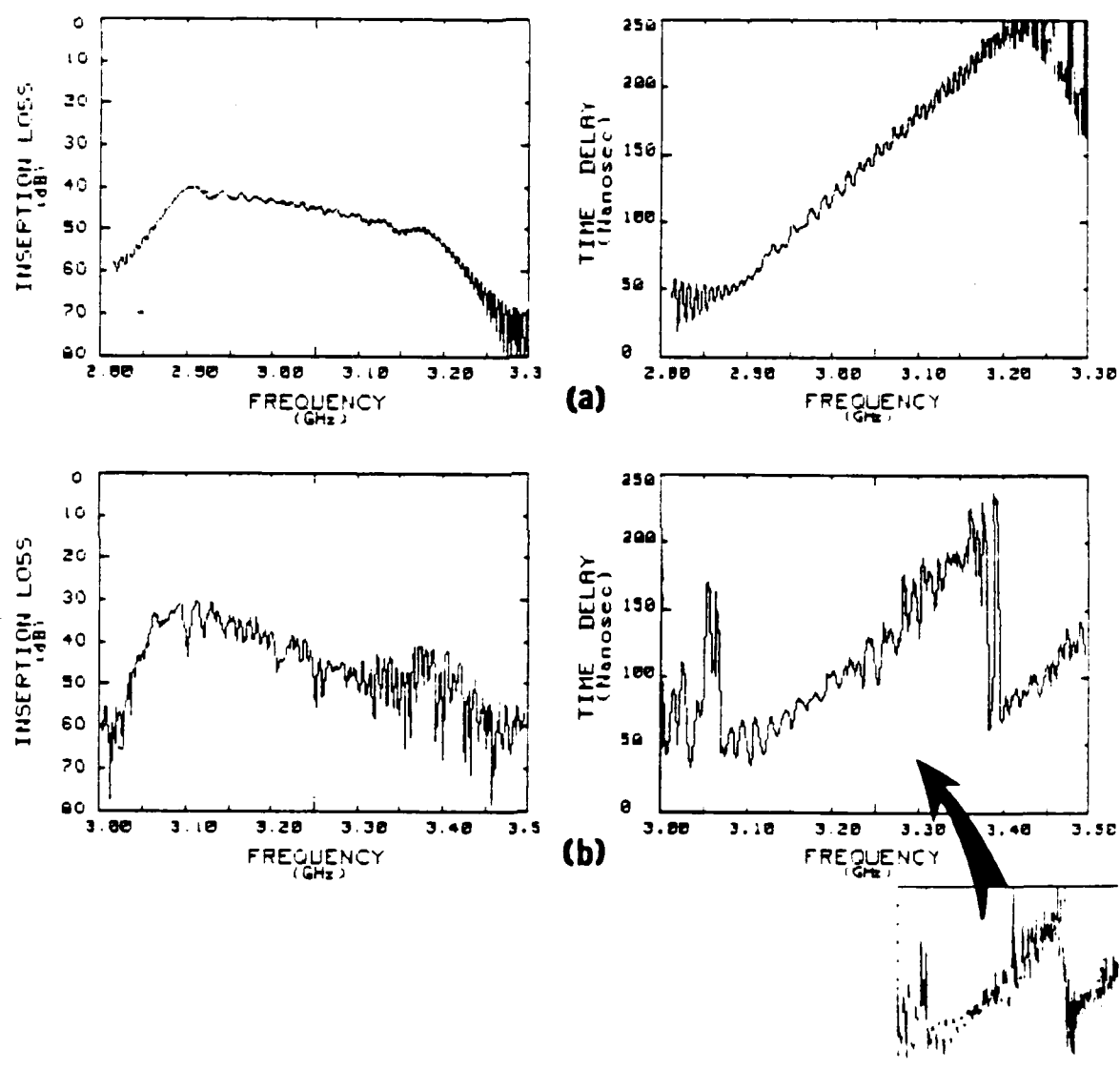


Figure 4.16. Performance of the positive delay slope MSFVW RAF.

- (a) Theoretical transmission insertion loss and group delay.
- (b) Experimental transmission insertion loss and group delay.



TABLE 4.4

QUANTITATIVE COMPARISON OF RESULTS FOR THE  
POSITIVE DELAY SLOPE OBLIQUE INCIDENCE MSFVW RAF

|      | DELAY                   |                        |                         | INSERTION LOSS       |                      | TBW<br>PRODUCT |
|------|-------------------------|------------------------|-------------------------|----------------------|----------------------|----------------|
|      | Slope<br>[nsec<br>/GHz] | @ 3.2<br>GHz<br>[nsec] | rms<br>ripple<br>[nsec] | @ 3.1<br>GHz<br>[dB] | @ 3.2<br>GHz<br>[dB] |                |
| DES. | 600.0                   | 120                    | ---                     | free                 | free                 | free           |
| THY. | 590.0                   | 120                    | 5.69                    | 40                   | 47                   | 77.4           |
| EXP. | 605.7                   | 100                    | 8.22                    | 33                   | 47                   | 77             |

The experimental insertion loss shows a peaking at the lower frequencies that is not predicted by the theory. This effect is attributed to the frequency response of the electrically long output transducer ( $l = 19$  mm and  $\lambda_{3\text{GHz}} = 3$  cm), which was modeled as electrically short in the theory. Use of a lower permittivity substrate material such as quartz should eliminate this problem. A greater rms deviation from linear is expected in the experimental results with the effects of crystal edge reflections added to the Fresnel ripple anticipated by theory. Sandblasting was used on the crystal edges to reduce reflections, but angle lapping and poleface end beveling have subsequently been shown to be more effective for this purpose. A 6 MHz wide moving window average was used to smooth out the effects of noise and edge reflections in the group delay data, which are the cause of the sharp spike like ripple. The original data is shown in the insert of Figure 4.16b. Delay slopes and intercepts for

the theory and experiment are in satisfactory agreement, allowing for uncertainties in array alignment and film thickness, both of which could add curvature or absolute delay to the overall response. The sudden retrace in the experimental group delay at about 3.4 GHz is a computer artifice and not a characteristic of the experimental device. The location of this sudden retrace and the number of such retraces is determined by the value of the aperture variable in the HP-11863D software.

#### 4.4.2 Negative Delay Slope Array

An MSFVW RAF with a negative-slope group delay is considerably more difficult to realize, because it opposes the intrinsic dispersion characteristic of the ferrite film. According to the impulse theory a negative-slope device is possible, but the resulting bandwidths and insertion losses are not as good as those obtainable for a physically comparable positive-slope array.

A  $45^\circ$  incidence, unapodised MSFVW RAF with a group delay of  $-600$  nsec/GHz was synthesized according to the impulse theory and fabricated (Figure 4.17). A single 3 mm long,  $50\text{ }\mu\text{m}$  wide shorted microstrip input transducer was used to maximize bandwidth and minimize insertion loss. The output transducer was a  $50\text{ }\mu\text{m}$  wide, 19 mm long shorted microstrip. The array consisted of 110 boron implanted reflectors of equal length. A double dose implant identical

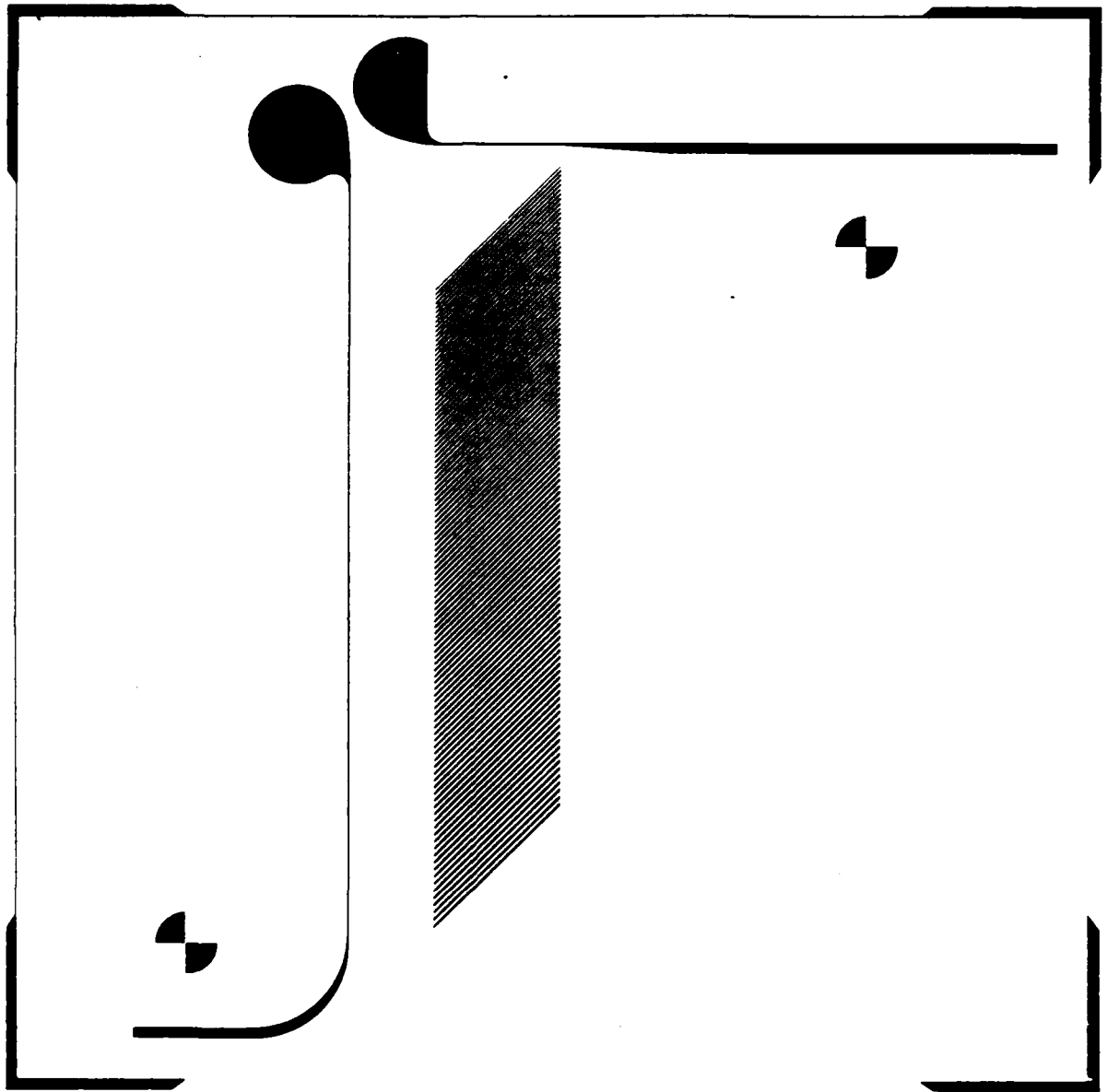


Figure 4.17. Experimental layout for the negative slope, linear group delay MSFVW RAF.

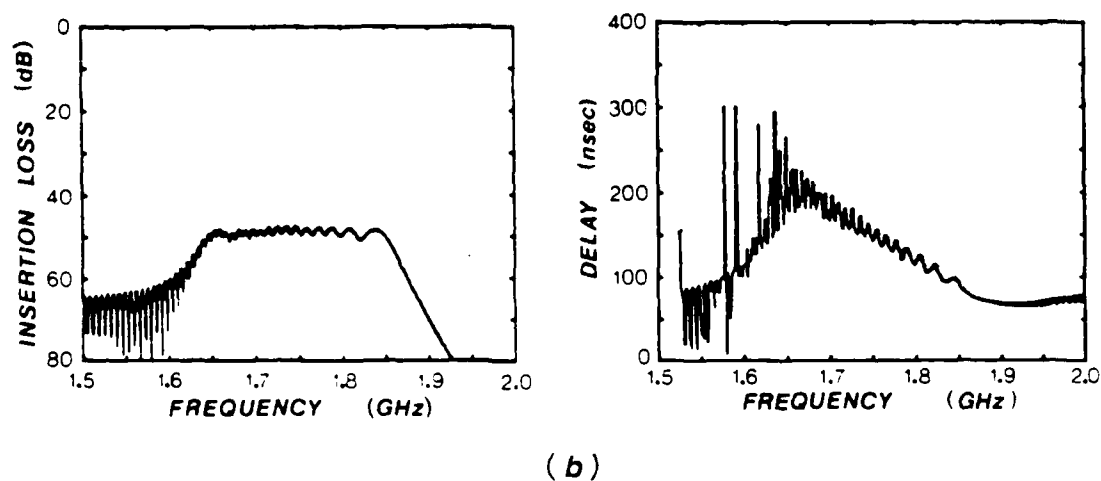
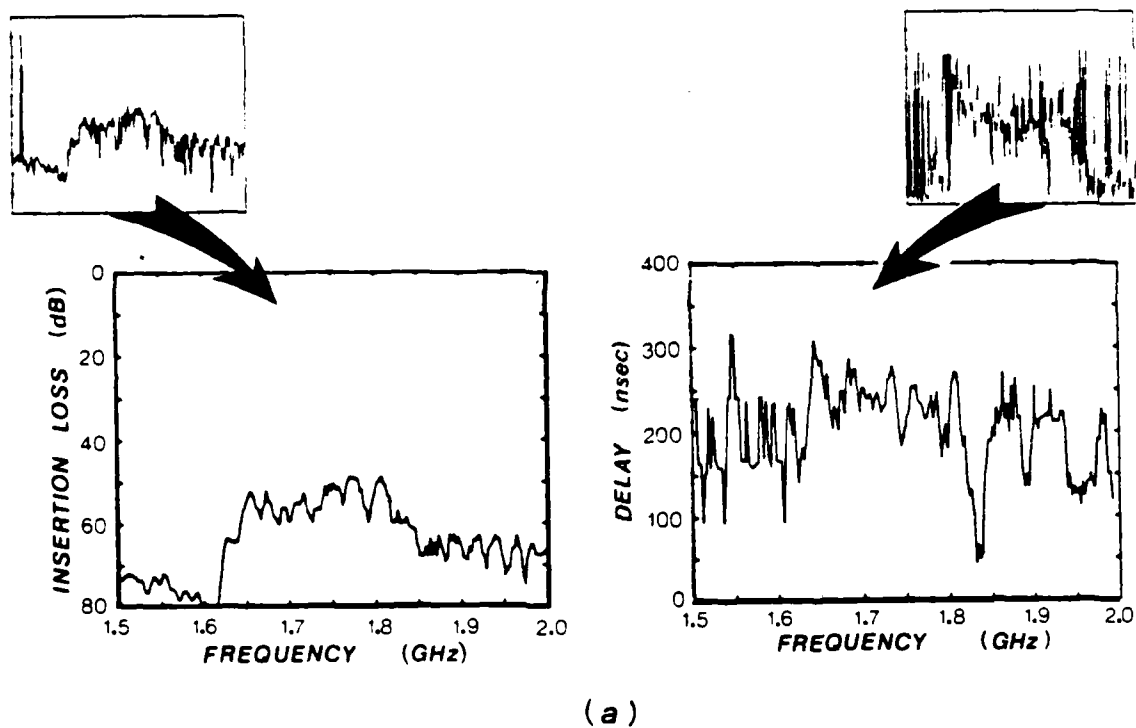


Figure 4.18. Comparison of experiment and theory for the negative delay slope MSFVW RAF.  
 (a) Experiment.  
 (b) Theory.

to that used for the positive-slope experiment was used, yielding a 50% reduction in saturation magnetization in the surface layer.

The experimental transmission frequency response and group delay were measured with extended averaging and are compared to the theoretical design in Figure 4.18. These results are quantitatively summarized in TABLE 4.5.

TABLE 4.5

QUANTITATIVE COMPARISON OF RESULTS FOR THE  
NEGATIVE DELAY SLOPE OBLIQUE INCIDENCE MSFVW RAF

|      | DELAY                   |                         |                         | INSERTION LOSS        |                       | TBW<br>PRODUCT |
|------|-------------------------|-------------------------|-------------------------|-----------------------|-----------------------|----------------|
|      | Slope<br>[nsec<br>/GHz] | @ 1.75<br>GHz<br>[nsec] | rms<br>ripple<br>[nsec] | @ 1.65<br>GHz<br>[dB] | @ 1.80<br>GHz<br>[dB] |                |
| DES. | -600.0                  | 125                     | ---                     | free                  | free                  | free           |
| THY. | -600.0                  | 125                     | ---                     | 49                    | 49                    | 30.8           |
| EXP. | -500.0                  | 225                     | ---                     | 55                    | 50                    | 17.0           |

In this particular experiment, it was necessary to use  $\Delta H_{\min} = 1.0$  Oe in the Gilbert loss model to make the theoretical insertion loss correspond to the experimental value. This variation is within the range expected for these films. The experimental amplitude spectrum has a 200 MHz bandwidth, comparing favorably to the theoretical bandwidth of 225 MHz. The passband slopes down slightly toward the lower frequencies, and is probably due to variations in the film thickness and quality along the length of the array. Other

experiments have shown that mild surface quality variations, such as flux spots, can greatly affect the reflectivity of a surface implant. A 6 MHz wide moving window average was used to smooth the group delay data so that the linearity and slope could be sorted out of the ripple caused by edge reflections and noise. The original group delay data is shown in the insert of that figure. Reasonable linearity was obtained in the experimental group delay, subject to severe interference by edge reflections. The experimental delay slope of 400 nsec/GHz is within an acceptable range of the design value of 600 nsec/GHz.

#### 4.5 Summary of Basic Array Types

Large insertion losses at the bottom of the transmission resonances that characterize the frequency response of normal incidence MSSW transmission arrays render these devices extremely susceptible to interference by edge reflections. The resonance notches tend to be only a few decibels deep, and the overall insertion loss is sufficiently high to allow the edge reflections on a terminated crystal to be a significant portion of this notch depth. The resulting ambiguity in the measurements, makes a reliable determination of the relation between reflectivity and implant dose impossible.

Conversely, significant correspondence was obtained between theory and experiment with the oblique incidence MSFVW RAF's. The principle causes of differences were process

control, crystal alignment in the bias field, and extraneous signals such as noise and edge reflections.

With typical observed insertion losses in excess of 30 dB in the MSFVW oblique incidence arrays, crystal edge reflections place a severe limitation on ultimate device performance. Even on a well terminated crystal by the standards of transmission devices with less than 20 dB of insertion loss, minute edge reflections are still a significant part of the signal received at the output transducer in a reflection device with large array losses. This problem can be addressed either by establishing more effective ways of terminating crystals than those currently in use such as angle lapping and bias field gradation, or by developing reflectors with higher reflectivities. The reflectivities obtainable with ion implantation are limited by the catastrophic crystal damage that accompanies doses much in excess of  $10^{15} \text{ cm}^{-2}$ . Other approaches that yield large reflectivities, such as metal bars or etched grooves, suffer their own limitations. Metal bars exhibit such large reflectivities that the incident beam cannot penetrate very deeply into the array, cutting down on the usable size of the structure and hence the obtainable time-bandwidth product. In the course of generating large reflectivities, etched grooves create fringe fields that couple heavily to transverse spin wave resonances, thus punctuating the passband with deep periodically spaced notches. The results

from these approaches indicate that better ways of eliminating edge reflections should be investigated rather than seeking to increase reflectivities.

With the  $45^\circ$  incidence MSFVW RAFs, the problem of edge reflections is intensified by the large receiver transducer that essentially bisects the crystal. Reduction of the size of the output transducer requires recompression of the beam. This is usually done by employing a double bounce array, but this also doubles the reflection loss of the array, which is unacceptable with losses already in excess of 30 dB. The next chapter describes a method of reducing the output transducer aperture by compressing the signal beam with a single reflection.

Other sources of loss in these devices such as propagation and mismatch loss should ultimately be addressed, but are of secondary importance in the sense that reducing them will not effect the relative interference by edge reflections. Propagation losses place an upper bound on the usable array length, and therefore limit the time-bandwidth product obtainable. Lower loss ferrites are the answer to this problem, and currently better results have been reported by others [4.4] using different melt compositions. Coupling losses can be effectively eliminated by matching at the microstrip ports, but 50% of the launched power is still discarded at both the input and output transducers due to bidirectional losses.



## CHAPTER 5

## ELLIPTICAL GEOMETRY ION IMPLANTED MSFVW RAFs

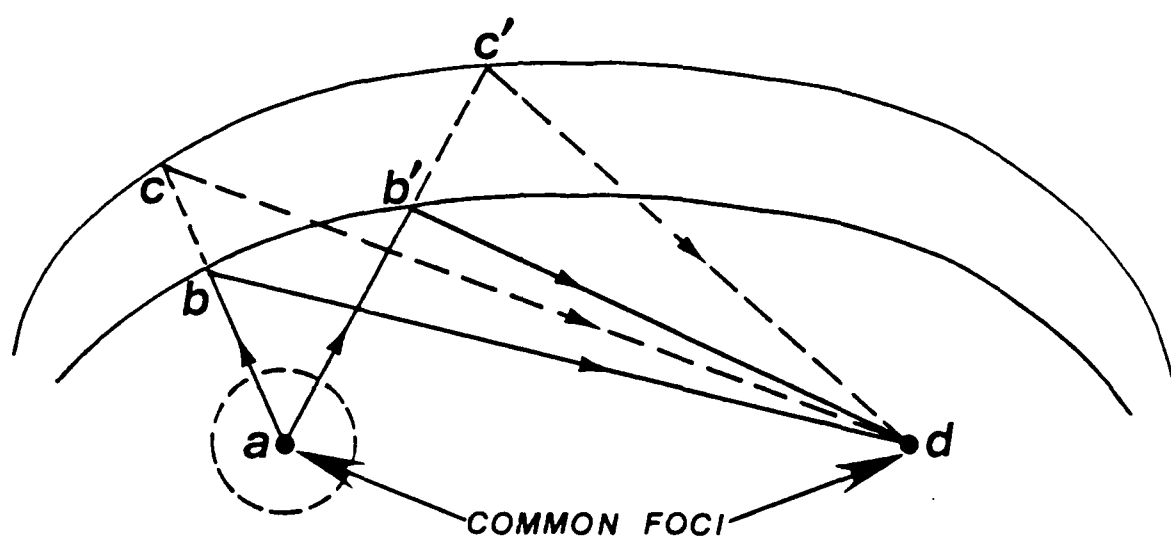
5.1 Elliptical Array Concept

## 5.1.1 Operating Principle

One way to recompress the reflected beam in an oblique incidence RAF is to curve the reflectors into a lens, with the focal point at the output transducer. There are a multiplicity of reflector shapes that would serve this purpose, but for simplicity these lens structures should,

- correspond to the same input-to-output path length at every point along their length, and
- couple to the same wavelength at every point along their length.

Both of these requirements are satisfied by confocal elliptical reflectors, with circular input and output transducers, centered at the respective foci (Figure 5.1). By definition, all wavelets originating at a focus of an ellipse that arrive at the other focus after executing equal angle reflections off the ellipse (MSFVW is isotropic) trace identical path lengths, regardless of what part of the ellipse they reflect from. Secondly, the differential path length between reflections from confocal ellipses is constant



$$ab + bd = ab' + b'd$$

$$[ab + bd] - [ac + cd] = [ab' + b'd] - [ac' + c'd]$$

Figure 5.1. Elliptical array concept.

regardless of the points on either ellipse at which the reflections occur. Thus, the effective reflector width of an implanted zone whose boundaries form consecutive nested ellipses is the same at all points along the reflector.

Circular transducer filaments centered on the foci do not introduce phase distortion, as they subtract a fixed radius from all trajectories. The size of the transducers can be arbitrarily chosen to satisfy alignment and electrical requirements. Reflector apodization is achievable by varying the angular projections onto the circular transducers.

#### 5.1.2 Advantages of Elliptical Arrays Over Conventional Arrays

Conventional  $45^\circ$  incidence arrays are characterized by a minimum obtainable insertion loss of 6 dB, due to the bidirectionality of the input and output transducers. Half of this lost power could be salvaged by placing an identical array and corresponding receiver behind the input transducer, but this would require a ferrite film that is twice as large and would necessitate coupling the separate receiver transducers in phase. With confocal elliptical arrays, the transducers are naturally surrounded by the array structure, eliminating all of the 6 dB bidirectional loss. Also, since the prereflected and postreflected legs of the trajectory are approximately equal, a confocal elliptical array of radius,  $R$ , is equivalent to a linear array of length,  $2R$ . This yields space advantages if only one hemisphere is used.

The confocal elliptical geometry reduces the effects of edge reflections in several ways. The contoured structure provides spacial filtering that discriminates against reflections from the crystal edges and local imperfections. Divergence in the radiated circular wavefronts reduces signal intensity at all points on the crystal, except at the receiver focus where the array reflected signal is selectively intensified. Output transducers can be made as small as 1 mm in diameter while keeping crystal alignment feasible. These small output transducers make better summers, and present a much lower cross section to unwanted signals. Use of point image radiators conforms to the intrinsic characteristic of the medium so that fringe fields correspond to the desired radiation.

A barrier must be placed between the input and output transducers, sufficiently large to completely shadow the output from direct radiation. Conventional array structures require a similar barrier to prevent off-axis wavefronts from directly illuminating the output transducer, but cannot be placed to completely eliminate the problem. In the elliptical geometry, a small centrally located barrier (sandblasted spot) is sufficient to completely eliminate direct breakthrough, without interfering with the array operation. If the right and left hemispheres of the array are complements of each other (photographic negatives), and the output transducer is held symmetric while the input

transducer is designed to radiate  $180^\circ$  out of phase into these hemispheres (or vice versa), then a barrier is not needed. Complementing an array is equivalent to interchanging  $Z_1$  and  $Z_2$  in the reflection coefficients for the interfaces, and introduces a sign change in the reflected energy. If the transmitter antenna launches inverted signals into the complementary reflector halves, the reflected signals from the two sides arrive in phase at the receiver and add. Signals in the opposing hemispheres that arrive at the output via a direct path are still out of phase and cancel in the receiver transducer. Unfortunately this mechanism cannot be used to further discriminate against edge reflections since, typical wavelengths are only about  $300\text{ }\mu\text{m}$  long and only a half wavelength of transverse misalignment in the crystal results in a complete rotation of the relative phase between signals reflected from opposite crystal edges. Even if exact alignment were possible, the crystal edges are not identical, and variations in their reflective properties would generate a difference signal at the output.

When a center barrier is used, arrays that occupy different, possibly contiguous, frequency bands can be located in the opposite hemispheres of the structure. If the filament gaps on the two sides of the input transducer are tuned to the corresponding frequency bands, the overall filter bandwidth can be broadened. This effect can be realized either geometrically or by a transverse step

discontinuity in the magnetic bias field.

## 5.2 Experiment versus Theory for the Elliptical Arrays

### 5.2.1 Mirror Symmetric Confocal Elliptical Array

A uniform, symmetric confocal elliptical array was designed and implanted on a 20  $\mu\text{m}$  YIG film, using the double dose schedule for 50% reduction in saturation magnetization. A mirror symmetric array of 48 reflectors on each side of the elliptical cavity (Figure 5.2a) was boron implanted on a 20  $\mu\text{m}$  YIG film and placed face down on the 250  $\mu\text{m}$  thick alumina microstrip substrate. All reflectors in the uniform array had effective widths of 150  $\mu\text{m}$  and included equal projections onto the radiated beam. The elliptical contours were approximated using off center circles, fitted so that the two exact points divided the ideal elliptical sector into equal parts. The transducers were identical circular 30  $\mu\text{m}$  wide gold loop filaments with 0.65 mm radii centered on grounded metal spots (Figure 5.2b) located at the foci of the confocal ellipses. The foci were separated by a center spacing of 4 mm, allowing a practical minimum path length for reflection from the innermost reflector of 5 mm. Neglecting metal losses, the boundary conditions on the grounded center spot are such that the magnetic field vector reflects without inverting. Thus, the transducer filaments were spaced radially out from the center spots by 150  $\mu\text{m}$ , corresponding to a half of the center wavelength for a reflected round trip phase length of  $360^\circ$ . Further shadowing of the output

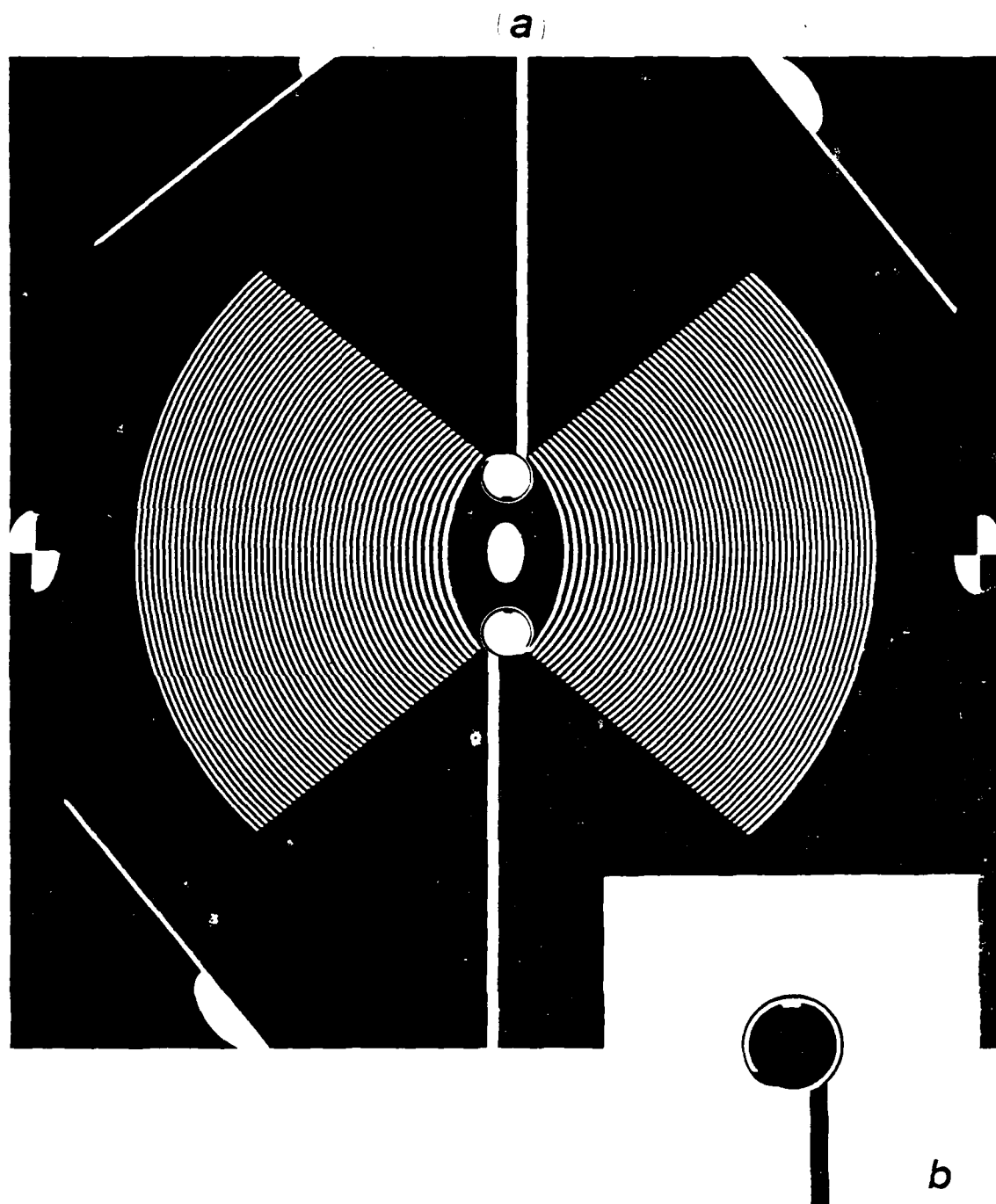
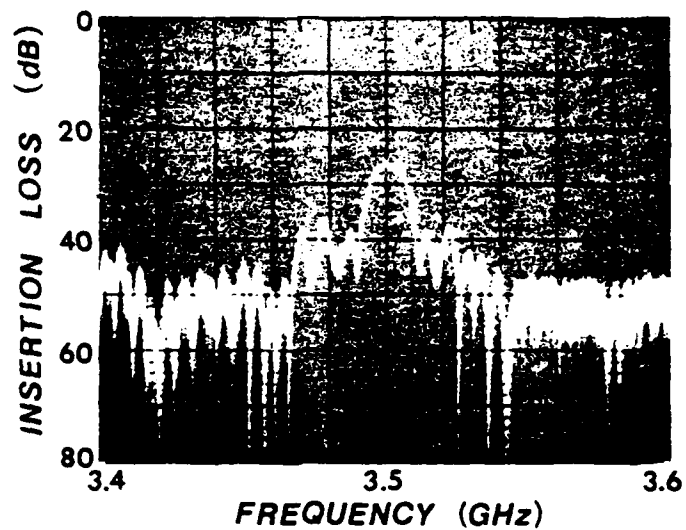


Figure 5.2. (a) Mirror symmetric, uniform elliptical array experiment.  
(b) Monopolar circular loop transducer.

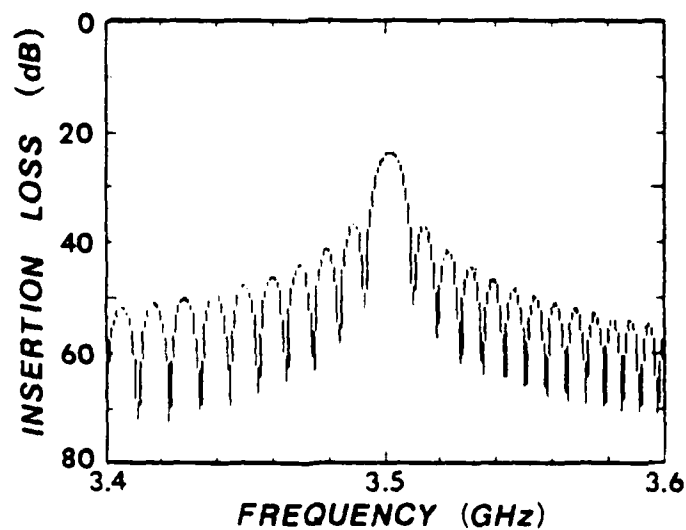
transducer was affected by indenting the center spots by an additional  $75\text{ }\mu\text{m}$  ( $\lambda_0/4$ ) in the arc subtending the opposing loop, so as to make this region antiresonant in the operating band of the filter and avoid wasted radiation that would degrade the insertion loss. The  $250\text{ }\mu\text{m}$  wide,  $50\text{ }\Omega$  feeder microstrips were brought into the cavity through openings radiating from the foci at the respective perigees. No waves originate at the back of the circular transducers where the feeder connection is made, so reflectors are not required there.

The experimental transmission response for a symmetric elliptical array is compared to the theoretical curve on identical scales in Figure 5.3. A main lobe width of 50 MHz was experimentally realized, with a minimum insertion loss 26 dB. Measured near in sidelobe levels were 13 dB down from the peak, as expected for a boxcar spacial distribution. Sidelobe widths of 25 MHz on the low side and 20 MHz on the high side were obtained. While these are roughly half the main lobe width predicted by theory, the antisymmetry is in excess of what is expected due to curvature in the dispersion curve. A clearer understanding of the cause of sidelobe antisymmetry is obtained in section 5.2.4. The measured transmission characteristics are subject to a variety of experimental factors such as array alignment, implant zone definition, ferrite film thickness, etc., and in light of such imperfections, they compare favorably with the





(a)



(b)

Figure 5.3. Uniform symmetric elliptical array.  
(a) Experiment  
(b) Theory

corresponding theoretical figures.

Comparison to the similar  $45^\circ$  incidence array results obtained earlier, verifies that improved rejection of crystal edge reflections was realized by this design. Notch depths between the lobes are less distinct due to the reflector width modulation accompanying the circular approximation to the elliptical contours.

#### 5.2.2 Complementary Confocal Elliptical Array

A complementary 48-bar elliptical array pattern was generated by photographically reversing one hemisphere on the array mask for the mirror symmetric design (Figure 5.4). The complementary pattern was boron implanted on a  $20\text{ }\mu\text{m}$  YIG film using the double dose implant for 50% reduction in the saturation magnetization, facilitating comparison to the performance of the symmetric device. A monopolar circular transducer with the same design as those used in the symmetric device was placed at one of the elliptical foci, and a dipolar circular transducer, as shown in Figure 5.4b, was used at the other focus. With the transducer center spot grounded, the conditions for resonance of the dipolar configuration are the same as for the monopolar type, so the radii of the center spot and filament loop were made the same.

The complementary symmetry makes a center barrier unnecessary, and designing the connection of the filament to

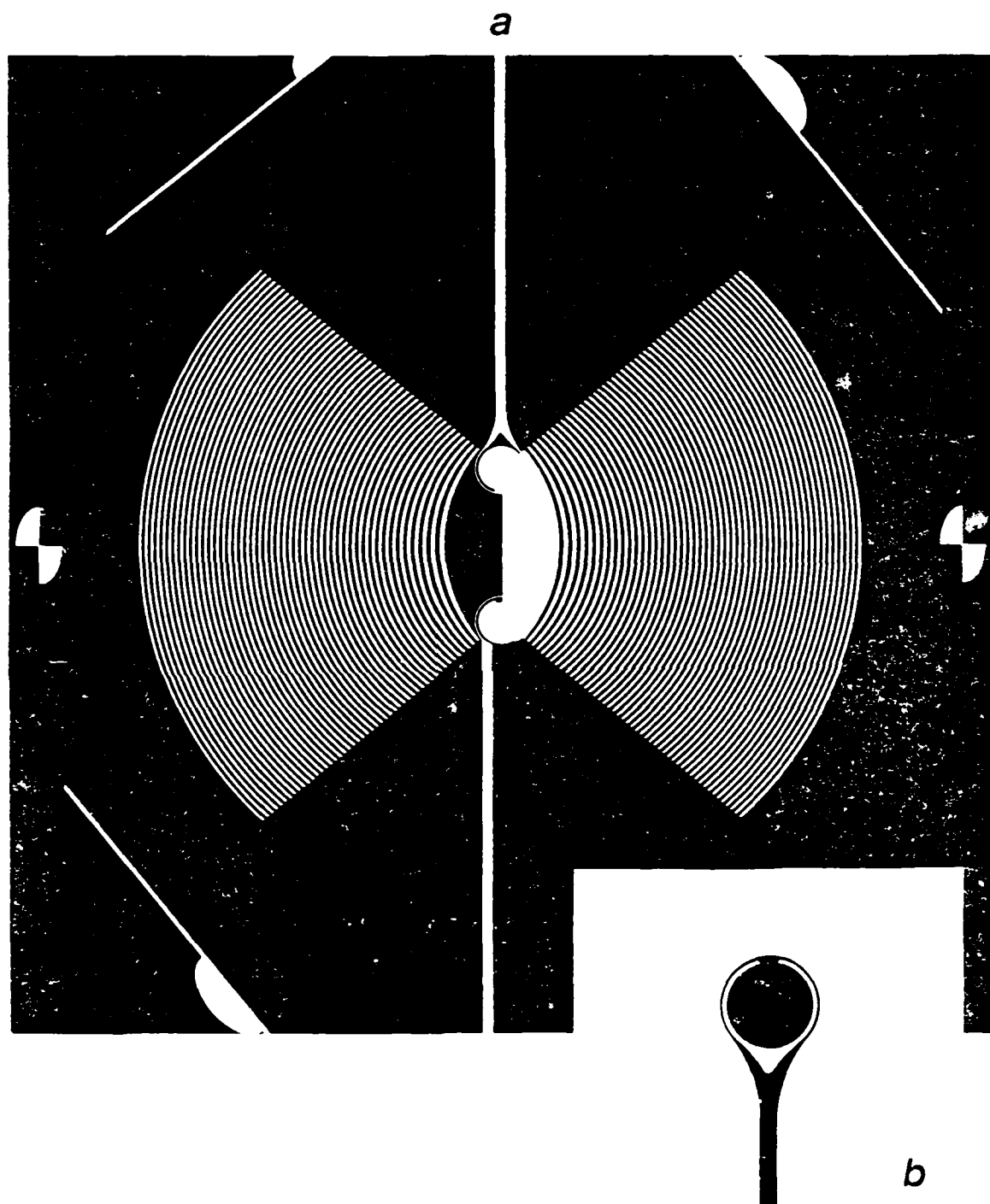
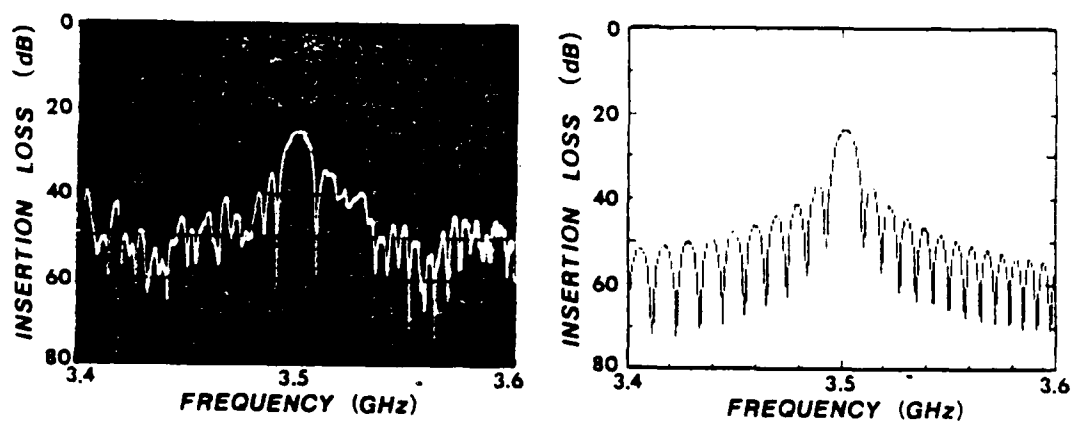
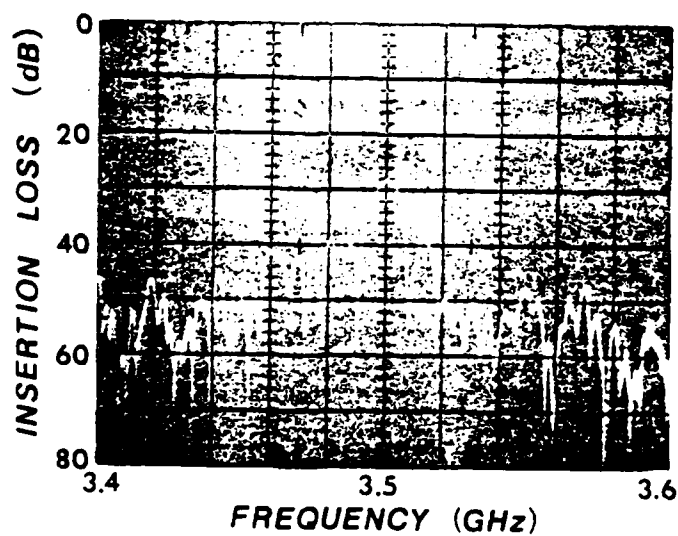


Figure 5.4. (a) Experimental complementary 48-scan array; (b) Silicon transducer.



(a)



(b)

Figure 5.5. Uniform complementary elliptical array experiment.  
 (a) Experiment versus theory.  
 (b) Equivalent symmetric array.

the center spot so that it fills the arc subtended by the opposing transducer provides additional suppression of direct breakthrough.

The measured transmission response for the complementary filter is compared to the theoretical response in Figure 5.5a. The main lobe width, minimum insertion loss, and sidelobe rejection are consistent with the values predicted by theory, within the expected range of experimental variation. As with the mirror symmetric array, an antisymmetry occurs in the sidelobe widths that is not sufficiently explained by the curvature of the dispersion relation alone, and is reviewed in section 5.2.4.

Figure 5.5b indicates that the array performance is not observably altered by the use of complementary symmetry. Suppression of ripple due to edge reflections is significantly improved over the conventional array designs, as was obtained with the symmetric elliptical array.

### 5.2.3 Apodized Elliptical Array

In order to test the ultimate potential of the MSW RAF technology for signal processing applications, a 100 MHz wide boxcar spectral response was synthesized, as shown in Figure 5.6. The impulse model of equation (2.46) was used to represent the array transfer characteristic in equation (3.12). Phase was specified to correspond with the average delay path in the array. The problem was simplified to a

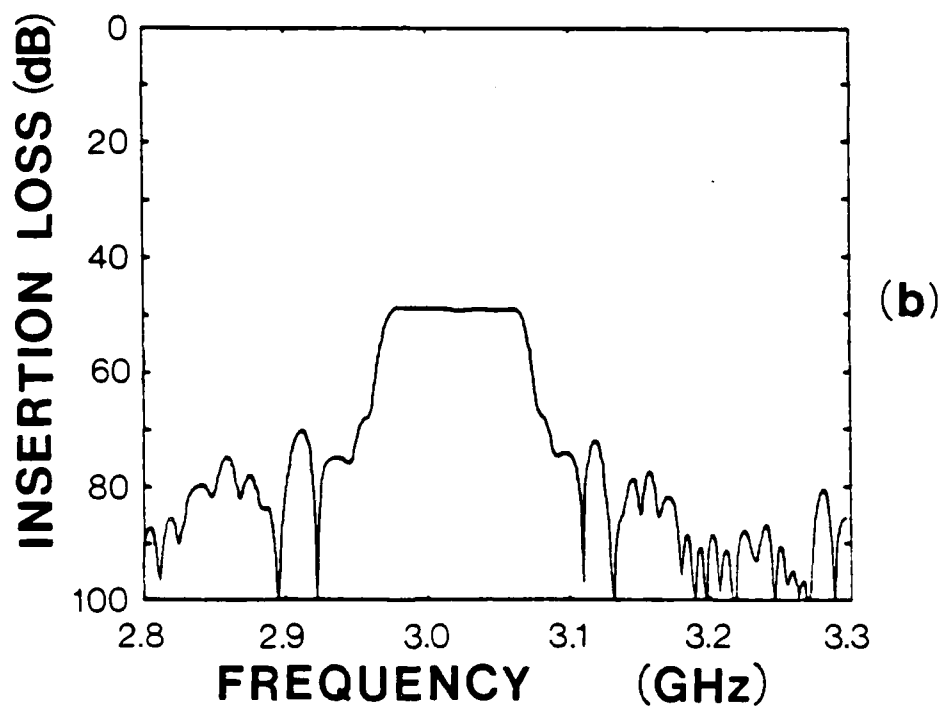
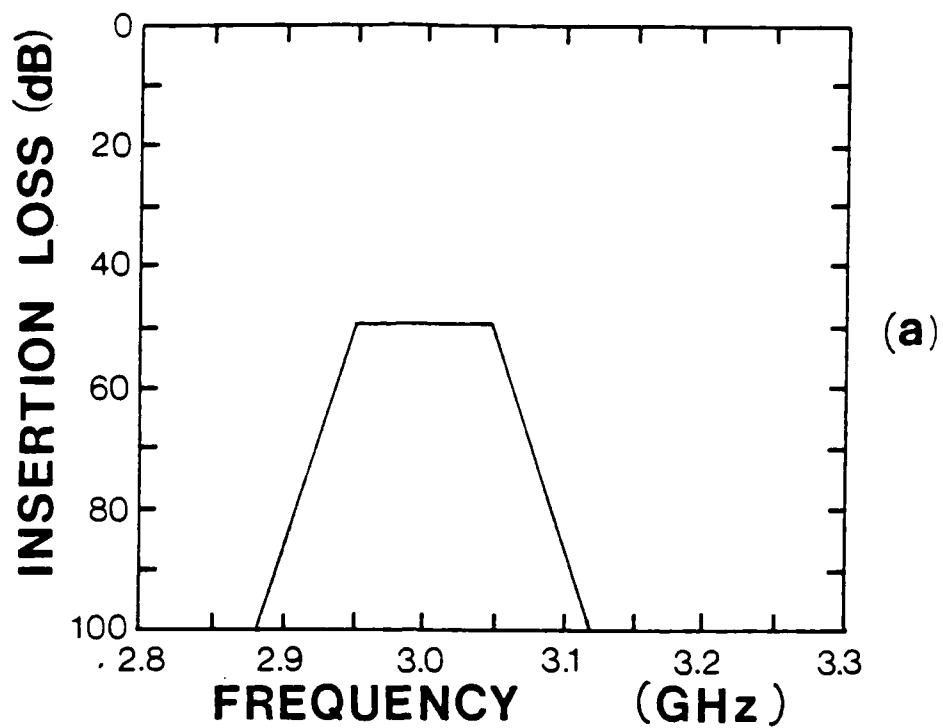


Figure 5.6. Boxcar channel filter.  
(a) Target spectral response.  
(b) Synthesized spectral response.

linear set of equations by selecting a recursive structure of equal effective width land and bar sections, corresponding to round trip path differentials of  $150\text{ }\mu\text{m}$  for reflections from consecutive elliptical interfaces. For simplicity, all parts of the spectrum received equal emphasis by selecting a constant weighting function,  $w(f)$ . The semicircular loop transducers at the input and output had  $150\text{ }\mu\text{m}$  filament center-to-center spacings and circular radii of  $0.5\text{ mm}$ . Use of loop transducers helped to suppress the uniform spin mode, sidelobe levels and first array harmonic. The zero path transfer characteristic for the single loop transducer pair,  $\tilde{G}_m(f)\tilde{G}_n^*(f)$ , was taken directly from Wu (5.1) and accrued the same value for all reflectors,  $\tilde{G}_m(f)\tilde{G}_n^*(f) = |\tilde{G}(f)|^2$ . The values obtained for the weighting coefficients,  $[p_m]$ , represent the angular projections of the respective reflectors onto the semicircular input transducer loop. The resulting array is shown in Figure 5.7 with the transducer structures superimposed. A double dose implant yielding a 40% reduction in saturation magnetization ( $MO_{imp}/MO_{pure}=0.6$  in TABLE 4.2) was used to pattern the array. Negative reflector contributions were obtained by offsetting the corresponding reflectors by an effective path length of half a wavelength,  $150\text{ }\mu\text{m}$ . The ratio of the largest to the smallest tapping factor was limited to 20, as this value was easily realized while keeping the minimum reflector lengths longer than the midband wavelength. This relatively large tap ratio is one of

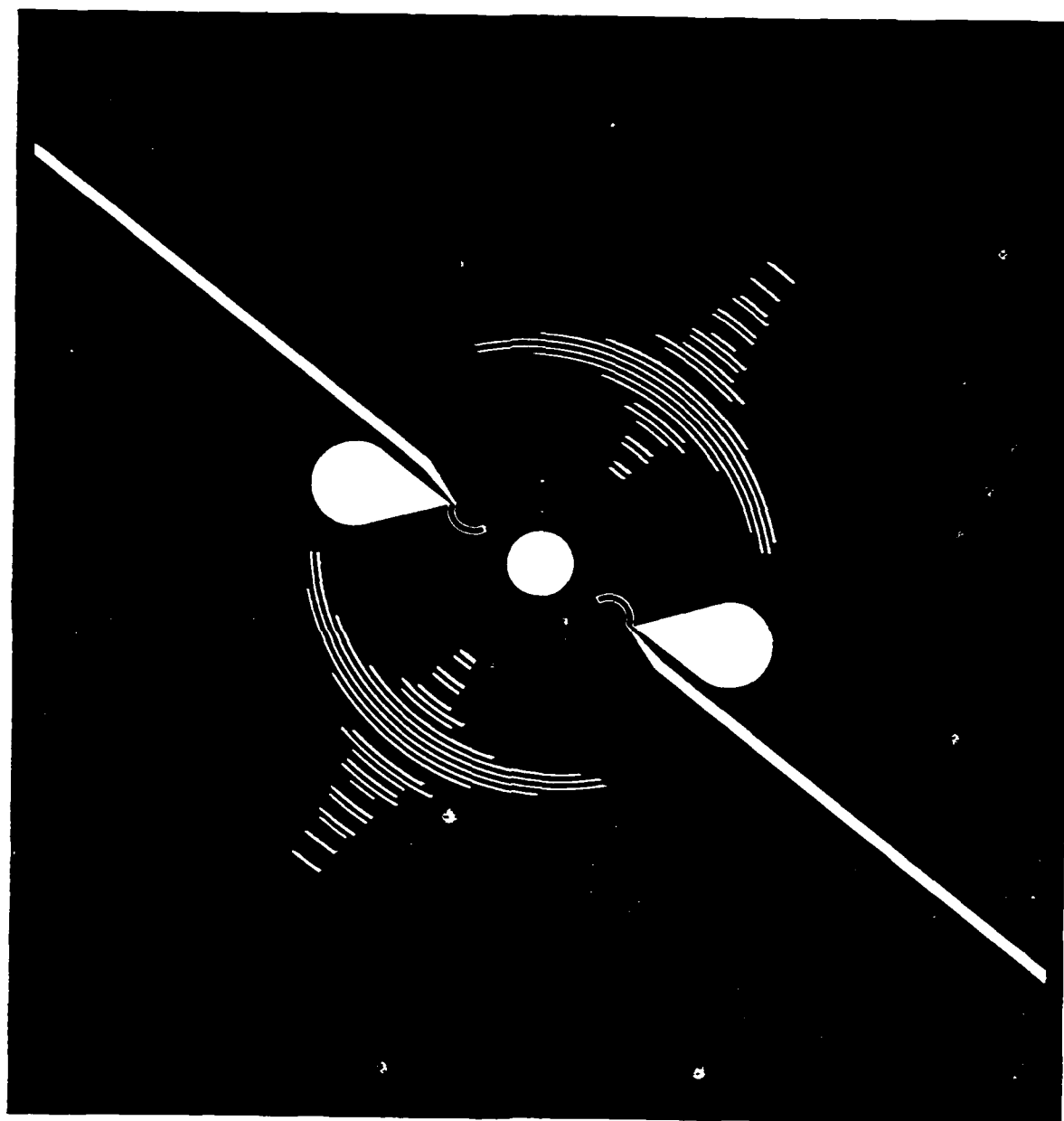


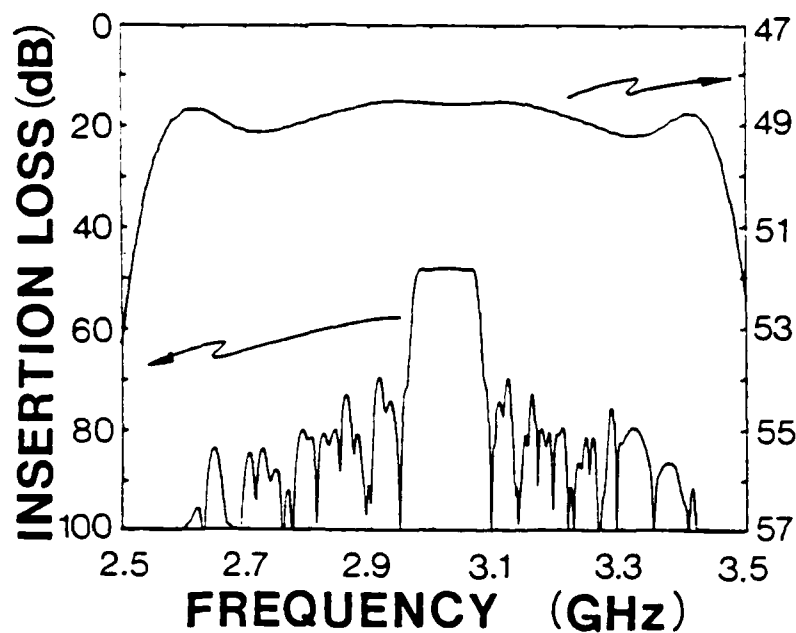
Figure 5.7. Array for the boxcar channel filter synthesized using an elliptical array of boron ion implanted reflectors.



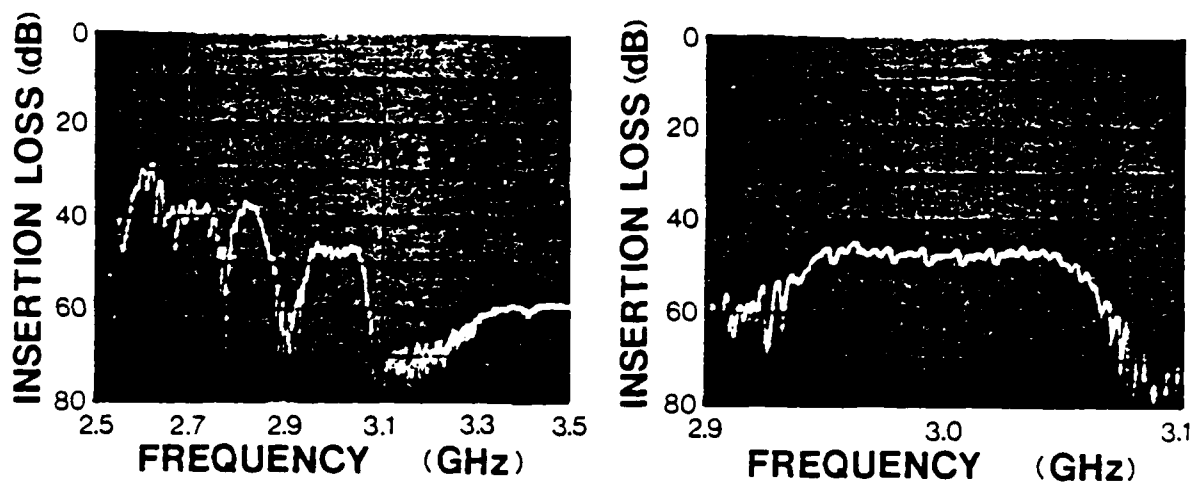
the features made possible through the use of an elliptical geometry.

A comparison between the measured response and the theoretical design is given in Figure 5.8. The synthesized array response is visible in the center of the experimental photographs. Except for edge reflections and direct breakthrough, excellent agreement was achieved between the theoretical array response and the measured response. Midband insertion loss for both is about 47 dB, spanning approximately equal bandwidths of 100 MHz. Out of band rejection, measured from the top of the skirt at the the band edge to the bottom of the skirt, is about 20 dB in the experiment as predicted by theory. The undesired breakthrough contributions in the experimental photographs can be identified as edge reflections (those that tune) and dielectric coupling between the input and output (those that do not tune, and typically smoother). The lobes on the left of the array response in the experimental result are due primarily to edge reflections. The smoother trace on the right of the array response is due to dielectric mode breakthrough.

This experiment indicates that improved crystal edge terminations are required, such as terbium doping, to reduce the contributions of edge reflections to the out of band response. Also, a complimentary array and transducer symmetry would greatly reduce the dielectric mode contributions.



(a)



(b)

Figure 5.8. Boxcar channel filter.

(a) Theoretical frequency response.

(b) Experimental frequency response.

An unapodized array was concurrently fabricated with the same reflector placements in order to indicate the effect of the apodization, as shown in Figure 5.9. The measured frequency response of the unapodized array is compared to the theoretically predicted frequency response in Figure 5.10. The experimental response exhibits the correct lobe structure and shape as indicated by theory. The insertion loss of the highest lobe on the left side of the response is experimentally about 32 dB, compared to 30 dB predicted by theory. Both theory and experiment show a roll-off of about 2 dB in the highest right hand lobe relative to the left hand one. This roll-off is due to the natural increase in the MSW loss factor at higher frequencies, in conjunction with reduced transducer coupling efficiency as frequency is increased. The lobe and notch levels in the experimental result differ slightly from the predicted values due to coherent interaction with the edge reflections. As the magnetic bias field is tuned, the observed lobe levels ripple up and down as the resonances corresponding to the edge returns are swept past them.

This experiment further verifies the effectiveness of the theoretical model and demonstrates that the boxcar response in the apodized experiment is in fact the product of apodization. Even with improved edge terminations, the characteristically large insertion losses limit the practicality of magnetostatic devices for filter realization.

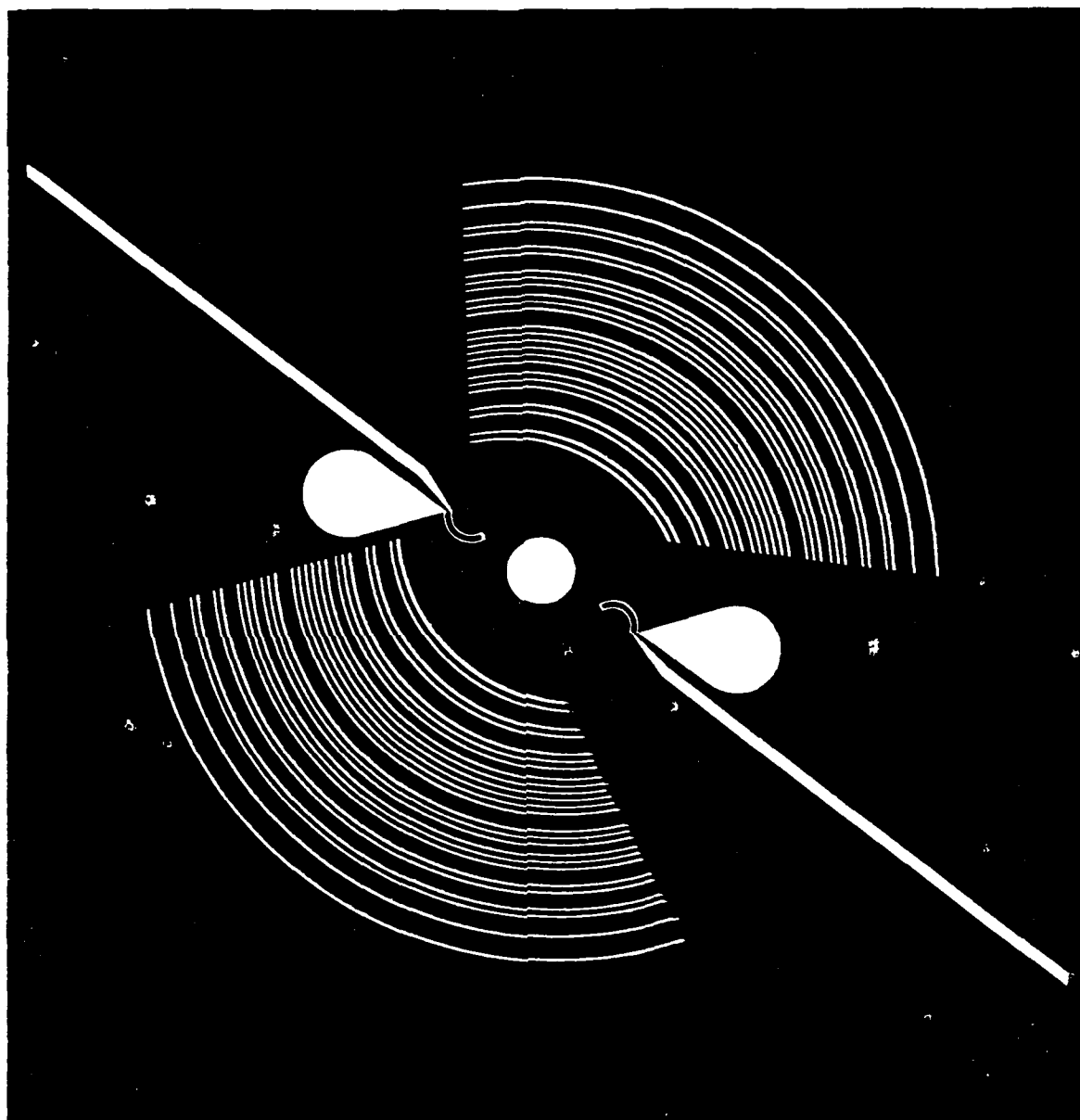
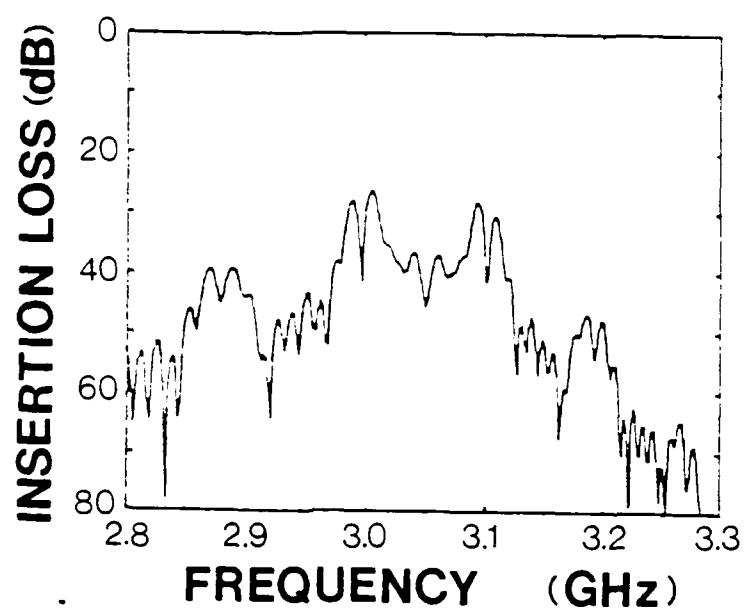
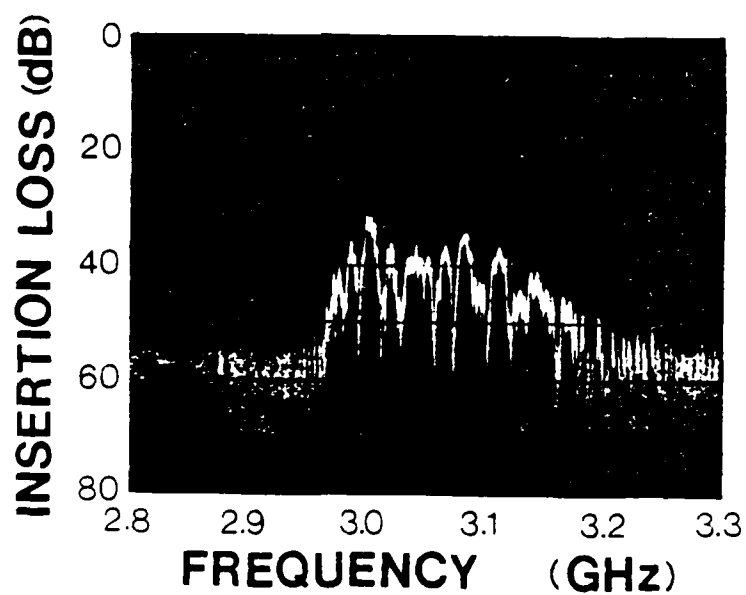


Figure 5.9. Unapodized array mask.



(a)



(b)

Figure 5.10. Unapodized array response.  
(a) Theory  
(b) Experiment

#### 5.2.4 Grounded Center Spot Circular Transducers

An investigation of the efficiency of the center reflector in the circular loop transducers was conducted, by unfolding the design into a hairpin with a grounded center pad (Figure 5.11). This scheme eliminated the signal degradation associated with circular beam divergence, and allowed the use of a wide selection of ferrite strips from past delay line experiments.

A single 30  $\mu\text{m}$  wide, 3 mm long grounded microstrip transducer was used as an analyzer, separated from the device under test (DUT) by a 1 cm delay path. The DUT consisted of a 1 mm center-spaced, 3 mm aperture, standard loop transducer configuration, with a 0.97 mm wide grounded metallic finger centered in the filament gap. The resulting 150  $\mu\text{m}$  gap between the filament and the center pad on both sides of the loop corresponds to the half wavelength spacing used in the circular designs.

The measured transmission response for this test structure is shown in Figure 5.12a, along with the theoretically predicted response of a 1 mm centerspaced loop transducer with no center barrier, in Figure 5.12b. The similarity between these results indicates that the grounded center barrier is nearly transparent to the reverse radiated energy, allowing signals from both transducers to interact and notch the transmission passband. Although surface metalizations provide relatively strong reflections when they

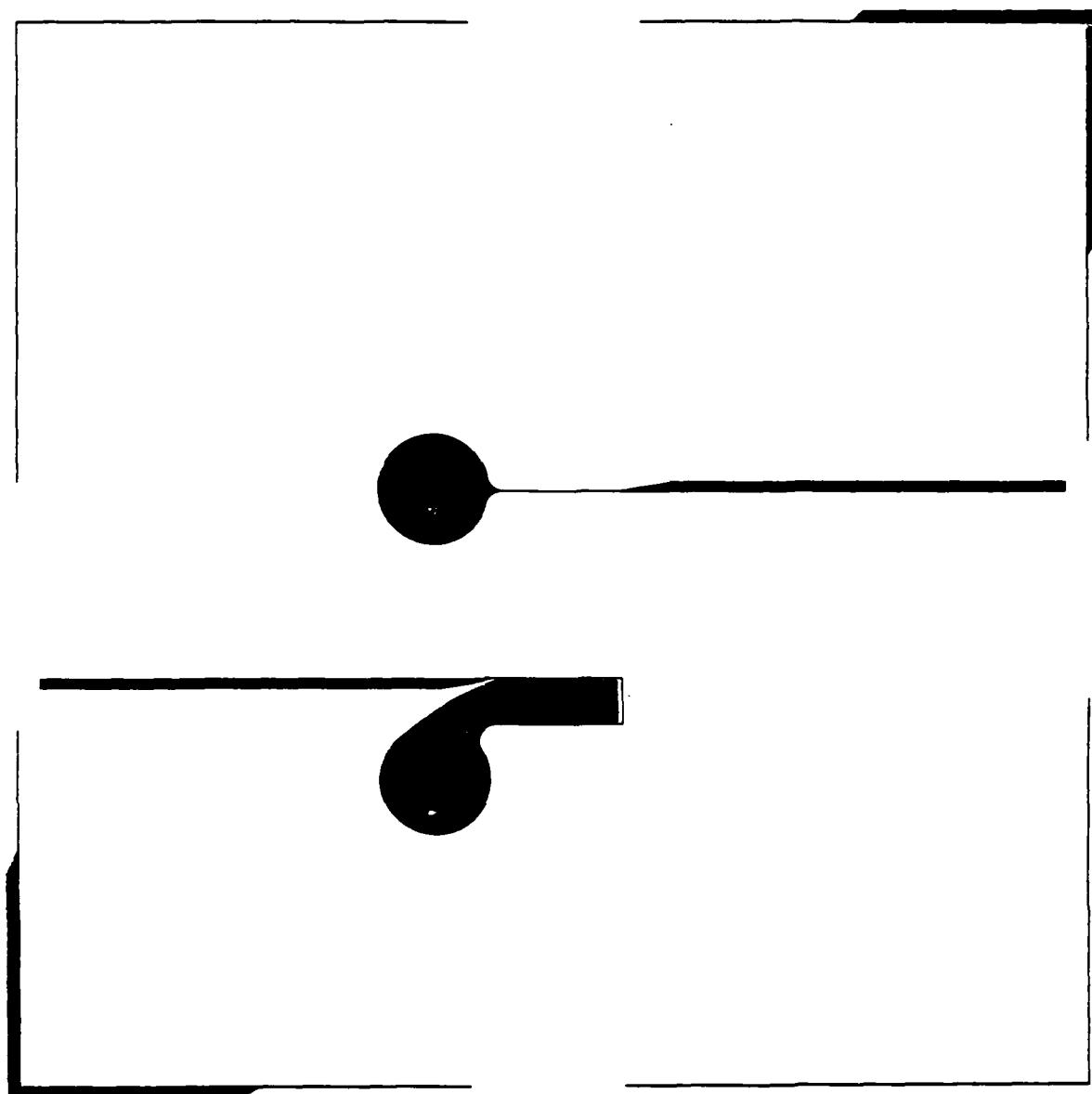
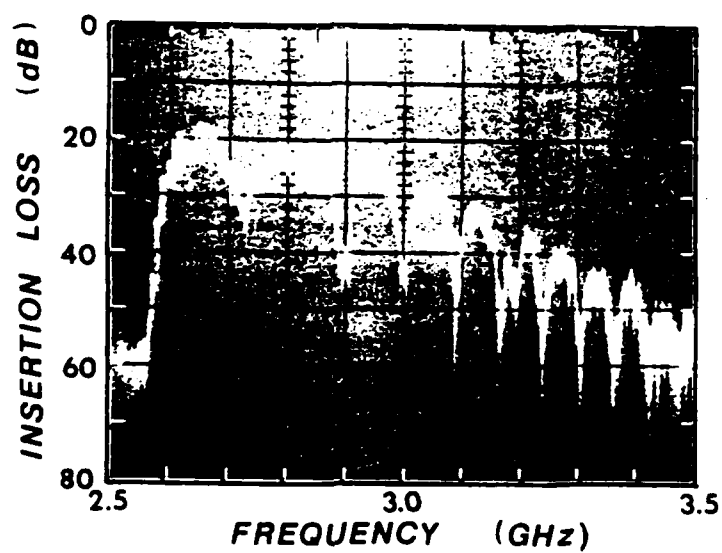
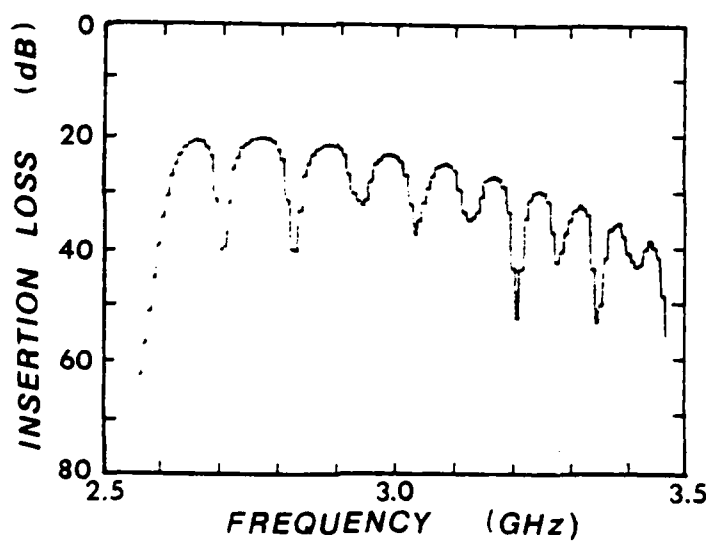


Figure 5.11. Test structure for the circular transducers used in the elliptical arrays.



(a)



(b)

Figure 5.12. Grounded center barrier loop transducer.  
(a) Measured transmission response.  
(b) Theoretical transmission response.



are used in a RAF context, the weak coupling to surface disturbances of volume concentrated energy distributions such as MSFVW yields reflectivities that are insufficient for use in mirror applications.

Placement of the array response off center in one of the lobes of the bifurcated transmission response of the grounded center barrier transducers would truncate one sidelobe more than the other, explaining the antisymmetry seen in the elliptical array experiments. A unidirectional circular transducer design would improve the correspondence of the uniform array performance with theory, and is essential for broadband elliptical geometry filter applications.

### 5.3 Unidirectional Transducer Designs

#### 5.3.1 Edge Reflector UDTs

Crystal edges approximate an open circuit to MSWs, as the electronic spin currents that support magnetostatic propagation abruptly vanish there. Experimentally they are known to produce good broadband reflections to the extent that they are a significant problem in most devices. In order to represent a good mirror plane, as is required in an edge reflector UDT, the reflectivity must be nearly unity.

A simple 3 mm wide, 1 cm long delay line was used to evaluate the unidirectional performance of a single-filament 30  $\mu\text{m}$  wide grounded microstrip, placed parallel to a cleanly

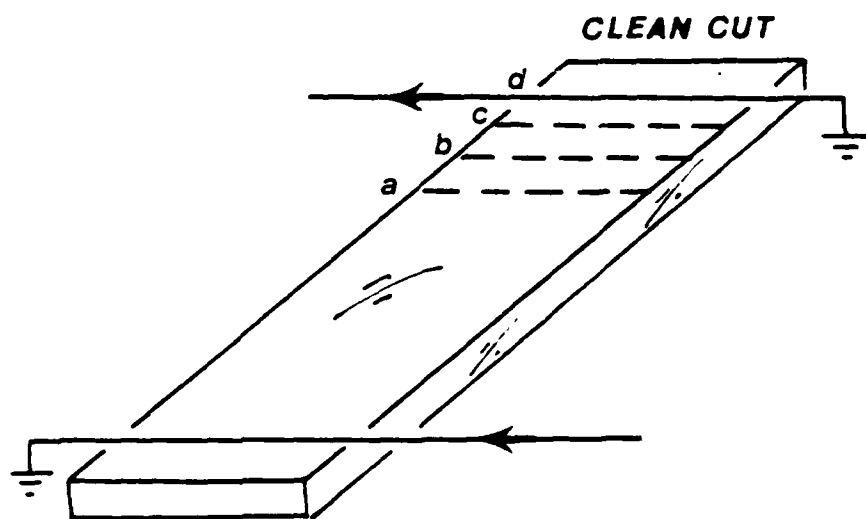
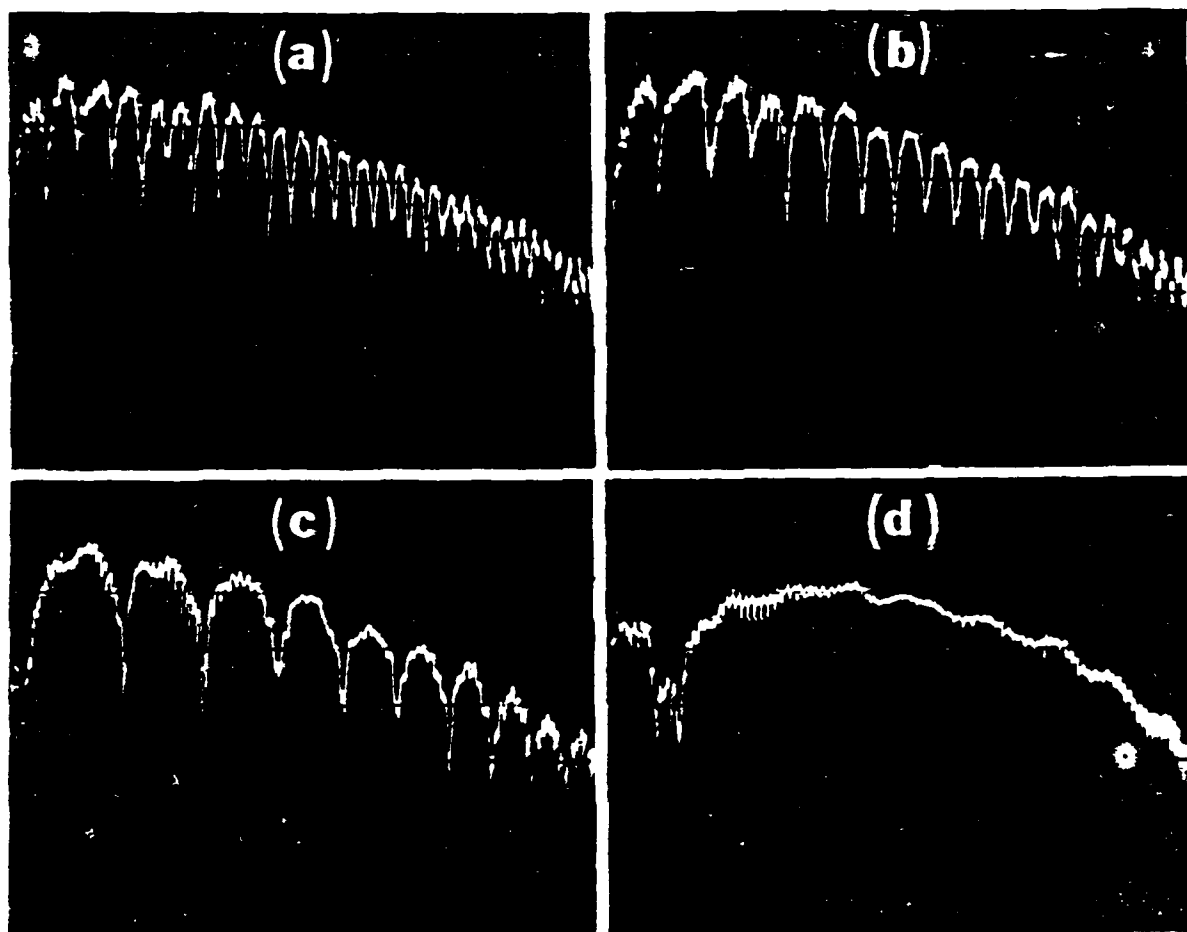


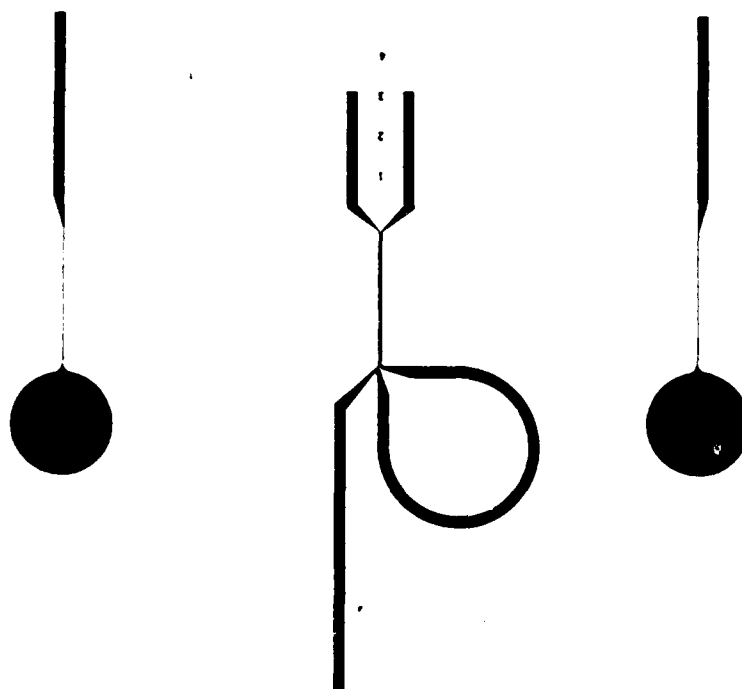
Figure 5.13. Edge reflector UDT.  
2.5 - 3.5 GHz. 10 dB/div

cut crystal edge. The analyzer was an identical single filament transducer, situated well away from the ends of the YIG strip so as not to interact with them. The 20  $\mu\text{m}$  YIG film was placed face down on the 250  $\mu\text{m}$  thick alumina microstrip substrate, and magnetically biased for MSFVW propagation.

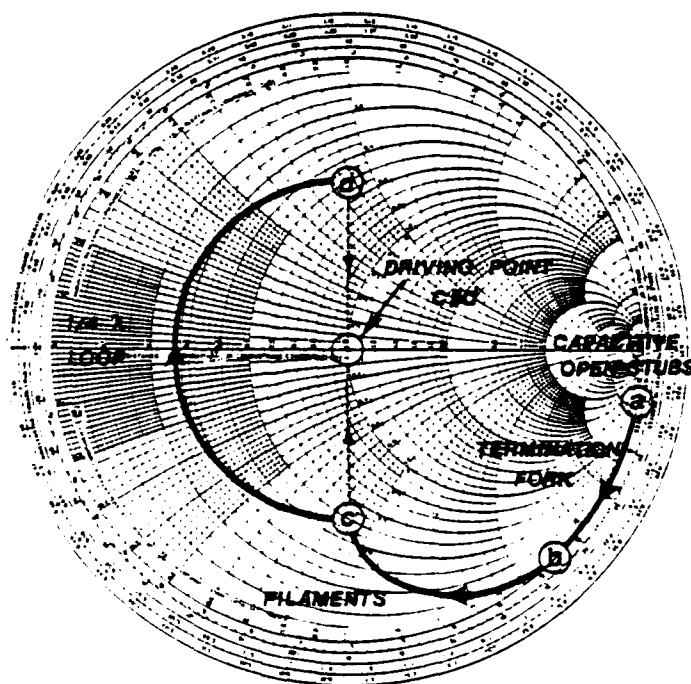
Several experimental transmission responses are shown in Figure 5.13, representing different filament spacings from the crystal edge. The last of these results corresponds to a spacing equal to a quarter of the center band wavelength, and indicates that a sharp crystal edge exhibits sufficient reflectivity to simulate a unidirectional loop transducer response. Implementation as a circular transducer would involve drilling or etching center spots in the YIG at the foci of the elliptical array. Alignment of these center reflectors inside the filament loops would be critical, requiring concentricity to within a fraction of a wavelength. Although it provides unidirectionality, this technique is characterized by a notch at the lower edge of the passband and exhibits higher insertion losses than obtained with a true loop. The notch is believed to be due to a fourth order transit involving an edge-transducer-edge reflection sequence. Higher insertion losses are the result of electromagnetic radiation by transducer fringe fields that reach beyond the immediate crystal edge. This additional loss mechanism subtracts from the gains accrued through the elimination of bidirectional loss.

### 5.3.2 Phased Array UDT

Magnetostatic phased array UDTs have been demonstrated in the past [5.2]. An alternate realization consisting of two elements driven in quadrature and spaced by a quarter of the MSFVW centerband wavelength on a 20  $\mu\text{m}$  thick YIG film was designed and fabricated (Figure 5.14a). Single bar 30  $\mu\text{m}$  wide shorted microstrip transducers were located 0.5 cm in front and in back of the DUT to analyze the forward and reverse radiation. The phased array consisted of two 30  $\mu\text{m}$  wide, 3 mm long microstrip filaments terminated by 50  $\Omega$  open circuited stubs. These served to rotate the reflection coefficient at the load end of the filaments a sufficient amount to place the driving point reflection coefficients on the imaginary axis (Figure 5.14b). At this point, a series quarter wave stub in one leg was used to obtain an equal current split between the elements with a quadrature phase relationship. On the Smith chart, this condition is represented by a purely real driving point impedance at the feeder split. Matching can be incorporated into the design by selecting the termination stubs and transducer lengths at the center wavelength so that the filament spirals on the Smith chart terminate at the intersection of the 0.5 conductance circle with the imaginary reflection coefficient axis. Conjugation by the series quarter wave stub places the driving point of the forward filament at the opposite intersection of the 0.5 conductance circle with the imaginary reflection axis. This



(a)



(b)

Figure 5.14. Phased array UDT.

(a) Transducer pattern.

(b) Smith Chart representation.

yields a parallel combination at the feeder split of  $50 \Omega$ .

Experimental measurements showing forward radiation superimposed on reverse radiation for three different devices with respective termination stub lengths of 2 mm, 3 mm, and 4 mm are given in Figure 5.15. These stub lengths were chosen in the vicinity of the value predicted for ideal open stubs, providing an empirical determination of the best length. Tuning the magnetic field changes the relationship between the electrical microstrip lengths and the MSW length of the filament gap, and each device was thus tuned for maximum unidirectionality. For this particular film thickness, 3 mm stubs provided the required transformation to the imaginary reflection axis, yielding greater than 15 dB of directivity over a 500 MHz bandwidth centered on 3.7 GHz. Improvements in forward insertion loss are realized as a dividend due to a reduction in driving point mismatch and reduced MSFVW backscattering, but are only on the order of about 3 dB, making the difference difficult to see on a device with an initial insertion loss of 20 dB.

Figure 5.16 shows the driving point impedance for the optimal device on a reflection display, spanning a 500 MHz sweep centered on the maximum directivity. The reference plane was placed at the point where the feeder microstrip splits into the two transducer filaments. This measurement illustrates the transformation of the input reflection coefficient to the real axis. The device achieves a moderate

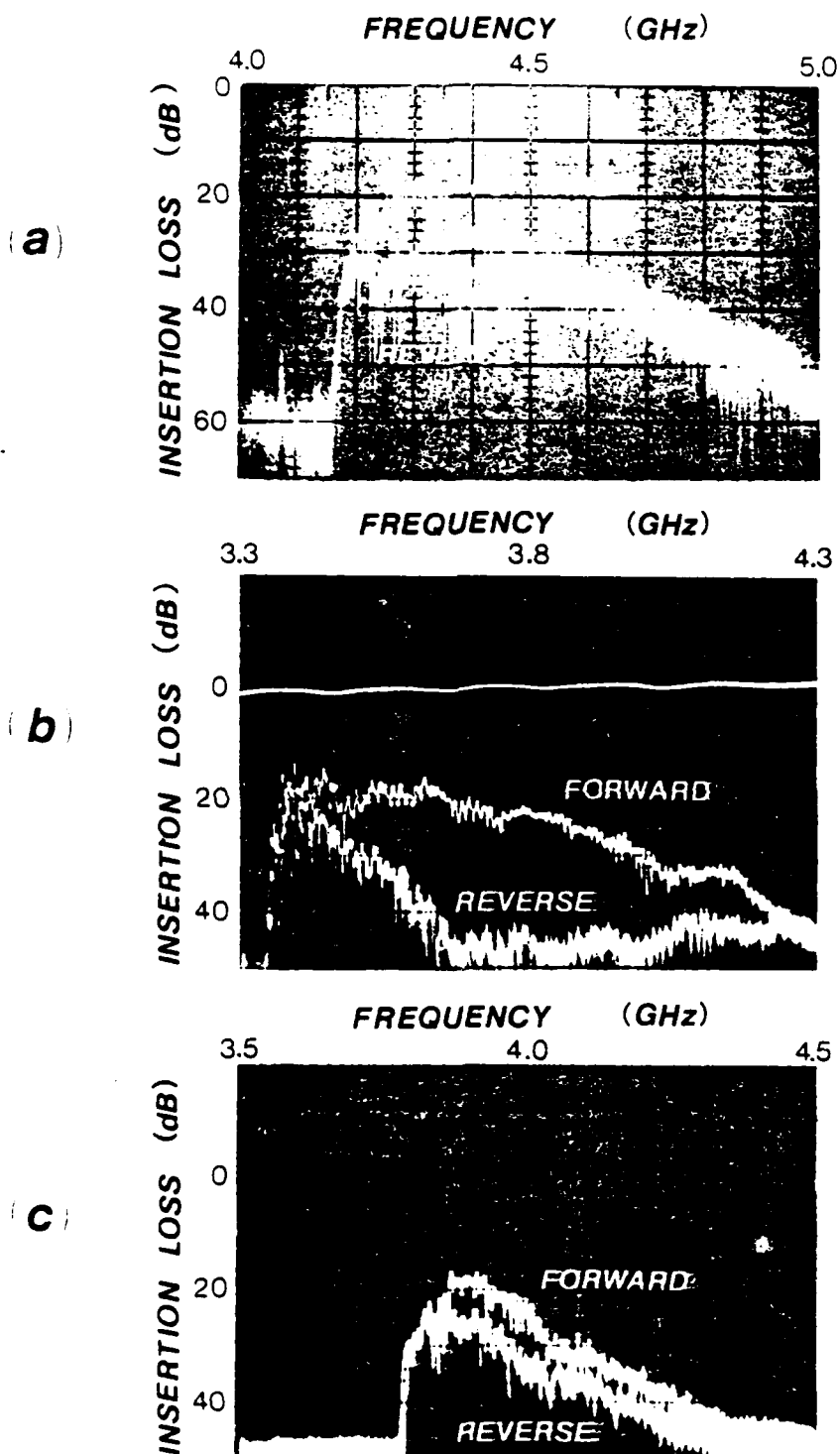


Figure 5.15. Experimental performance of the two phase MSFVW UDT ( $20\text{ }\mu\text{m YIG}$ ).

- (a) 2 mm termination stubs.
- (b) 3 mm termination stubs.
- (c) 4 mm termination stubs.



- 20  $\mu\text{m}$  YIG THICKNESS

- 3 mm FORK STUBS

- $\Delta f = 500 \text{ MHz}$

- $f_c = 3.7 \text{ GHz}$

Figure 5.16. MSFVW UDT driving point characteristics.



match over this region and passes through an exact match at the center wavelength.

## CHAPTER 6

## CONCLUSION

6.1 Normal Incidence Experiments

Theoretically projected notch depths for the ion implanted normal incidence transmission arrays ranged from 0.5 dB to 12 dB for the MSSW biased devices. Projected notch depths for comparable MSFVW arrays were only about 2 dB less, indicating a significant interaction of the centrally concentrated energy distribution with the boundary conditions at the film surface. Comparison of the field distributions in Chapter 2 to those generated by Damon and Eshbach [1.1] for a free ferrite slab, demonstrates that introduction of a ground plane extends the energy distribution more uniformly over the film cross section, resulting in greater coupling to surface aberrations. Experimental comparisons of unimplanted and uniformly implanted transmission responses show that doses sufficient to reduce the saturation magnetization by 50 % in the surface layer increases propagation losses by about 5 dB across the frequency band for MSSW and about twice that amount for MSFVW. The physical effects of implantation on the ferrite must be better understood in order to explain this unexpected result.

Correspondence between theoretical and experimental notch depths was marginal for MSSW due to interaction with

edge reflections. Higher intrinsic insertion losses and edge reflections are characteristic of MSFVW. This, coupled with increased degradation in the propagation loss from implantation, rendered the notches in these experiments unobservable.

Effective characterization of implanted zone reflectivities by normal incidence transmission measurements would require either improved techniques for crystal edge termination or a multiple measurement algorithm to discriminate against edge reflections. An increase in element reflectivities would also improve notch visibility in the presence of edge reflections. Reflectivities, however, are bounded by available acceleration potentials and an upper limit on the dose levels achievable.

Resonators are the primary application of normal incidence arrays for which the anisotropic propagation characteristics of MSSW are essential. Implanted reflectors do not offer any substantial advantages in this context, as etched grooves have been shown to perform well with MSSWs and are essentially free of limitations on the reflectivities obtainable.

## 6.2 Oblique Incidence Experiments

Except in resonator applications, oblique incidence is more applicable for realizing general filter functions and is better suited to performance characterization in that it involves measurement of the presence of a signal rather than

its absence. The oblique incidence ion implanted array experiments showed generally good agreement with theoretical predictions, although some variation in absolute insertion losses was observed among comparable devices. These differences are expected as the result of unavoidable film growth variations, array fabrication tolerances, and bias field alignment errors. Of key importance was the accurate prediction obtained for the amplitude shape factor across the frequency band in terms of relative lobe levels, widths, and locations. The impulse model was shown to be sufficiently accurate for use in the synthesis of simple delay graded filters. With insertion losses typically in excess of 40 dB for these broadband devices, the 60 dB noise floor of the analyzer made it essentially impossible to obtain clean responses. Processing the group delay data with a five point moving window average took advantage of the zero mean characteristic of the noise and allowed a reasonable comparison of the experimental results with theory. For the positive delay slope device, the midband insertion loss was 45 dB for both theory and experiment, and the theoretical delay slope was 590 nsec/GHz compared to an experimental value of 605.7 nsec/GHz. The experimental midband insertion loss for the negative delay slope device was 52 dB compared to a predicted value of 50 dB, and the experimental delay slope was -500 nsec/GHz compared to a theoretically predicted value of -600 nsec/GHz.

Increased reflectivities were attempted using the smaller  $H^+$  implant species, but no observable surface manifestation or experimental reflectivity was obtained. It was concluded and later verified by others that this particular ion does not efficiently disrupt the crystal lattice. However, results published by Volluet (6.1) and Volluet and Hartemann (6.2) using  $^4He^+$ , indicate that a considerable improvement in implant zone reflectivity can be realized by utilizing the higher doses ( $>10^{16}$  ions/cm<sup>2</sup>) possible with the smaller species without accumulating excessive strain in the regions between the implanted zones. Strain buildup in these intervening regions seems to result in a broadband reflection contribution that masks the desired array response.

### 6.3 Elliptical Geometry Arrays

Elliptical geometry reflectors are just one of many potentially useful configurations for reflective array filters. For example, parabolic reflectors could be used to realize an impedance transformer filter, by using an arbitrary length (but electrically short) straight bar transducer at the input and a circular "spot" transducer on the output, located at the focus of a graded confocal parabolic reflector array. Until recently, exotic structures such as this have been relatively uncommon due to limitations on mask cutting techniques. Currently the computer technology has made sophisticated pattern generating and mask cutting

utilities available, and the planar devices being made are reflecting this, for example, in the growing use of curved microstrips.

Contoured reflectors access the designer to complex spacial filtering functions that can be utilized to discriminate against spurious signals on the substrate. In particular, use of elliptical contours was shown to reduce the peak-to-peak ripple due to edge reflections appearing in the transmission response of uniform magnetostatic filters. The ripple was reduced in a 30 dB insertion loss device from 2 dB to 0.5 dB due to the use of elliptical reflectors. These arrays provide considerable design flexibility, including the use of electrically short input and output transducers without requiring a double bounce array, immersion of the radiators in the array structure for the elimination of bidirectional losses, and the ability to mask direct transmission through the use of complementary array hemispheres.

A by-product of the investigation of contoured arrays was the development of broadband unidirectional phased array transducers for MSFVW. The 15 dB to 20 dB bidirectionality over nearly 500 MHz obtained for these devices offers a multitude of applications in conventional structures, and was found to be essential for broadband elliptical arrays.

#### 6.4 Recommendations For Future Study

The principal application in which MSW ion implanted

arrays offer some limited practical potential is oblique incidence compressive filters. Ground plane contouring is a preferred technique, characterized by 20 dB insertion losses over 500 MHz bandwidths compared to insertion losses of 50 dB over maximum bandwidths of 250 MHz for reflective arrays. Reflective arrays cannot compete with transducer arrays in the fabrication of low loss spectral weighted filters, and etched grooves are capable of higher reflectivities allowing superior performance in resonator applications. In the context of oblique incidence compressive filters, implanted reflectors perform comparably to metal stripes without the conductive losses. Implanted reflective arrays, however, are characterized by relatively narrow bandwidths, small time-bandwidth products, and high insertion losses. Reflectivities are difficult to predict due to a considerable sensitivity to film surface quality. Although MSW RAFs promise little hope of ever equaling the performance of SAW devices (6.3, 6.4, 6.5), they have the advantage of operating in the 1-20 GHz frequency range and of magnetic tunability.

Future investigations should focus on improved crystal edge terminations, larger crystals and higher doses of smaller ions, such as  $4\text{He}^+$ , to enhance the ratio of array to edge reflected signals. Contoured reflectors should be incorporated, as they have been demonstrated to yield a reduction in interference by edge reflections, in addition to providing other significant advantages.

## 7.0 MILLIMETER WAVE ISOLATORS BASED ON FIELD DISPLACEMENT IN DIELECTRIC IMAGE GUIDES

At microwave or millimeter wave frequency range, ferrite materials play important roles in the design of nonreciprocal devices. Devices applying ferrite materials can be divided into two classes: devices for which the ferrite is tuned to ferromagnetic or ferromagnetic resonance (FMR) and devices which are magnetically tuned away from FMR.

Experimental work on a dielectric imageline guide loaded with ferrite was first conducted in 1976 [7.1]. The results showed that imageline guide when loaded with a ferrite can behave as a field displacement type isolator. A simplified version of imageline isolator called ferrite loaded stripline isolator was analyzed. This type of isolator much easier to analyze theoretically and can give us an understanding of the working of the more complicated imageline isolator.

Experiments have been carried out on image line isolators utilizing epitaxial YIG on gadolinium Gallium Garnet at 90-100GHz. These experiments have shown that the concept is feasible but that ferrite materials with high magnetization are desirable for practice devices.

### 7.1 MM WAVE FIELD DISPLACEMENT ISOLATOR THEORY

A pure dielectric waveguide is reciprocal, i.e. its field distribution in the transverse directions are symmetrical for both forward and reverse propagating waves. A piece of ferrite added to the edge of the dielectric waveguide will distort the field distribution and make them asymmetrical for the two directions of wave propagation. Therefore, a loaded waveguide



possesses a degree of nonreciprocity, and this is the property which is employed in a field displacement isolator.

For millimeter-wave application, a dielectric image line guide [7.2] [7.3] [7.4] is preferred for low conductor loss. In 1976, an image line loaded with ferrite was utilized to demonstrate field displacement isolation at 61.25GHz. Isolation of 11db and insertion loss of 3db was observed. The design was partly theoretical and partly empirical. Analytical solutions to the image line problem are very difficult.

The crosssection and transverse fields of an image line isolator is shown in Fig. 1. The solution of this problem is a very complex one.

We did not try to find the numerical solutions of this problem at this point in time. Instead, we concentrated on a simplified version of the isolator (Fig. 2) called ferrite loaded stripline isolator.

For the stripline isolator (Fig. 3), we concentrate on  $TE_{no}$  modes, the field components of which are uniform in y direction, the direction of the DC magnetic field. Because of coordinate change and including demagnetization factor, the polder tensor of the form:

$$\vec{\mu} = \mu_0 \begin{bmatrix} \mu_{11} & 0 & j\mu_2 \\ 0 & 1 & 0 \\ -j\mu_2 & 0 & \mu_{22} \end{bmatrix}$$

$$\mu_{11} = \frac{rM_0 \{ rM_0 N_z + [r(H_0 - N_y M_0)] \}}{(rH_0 + r(N_x - N_y) M_0) (rH_0 + r(N_z - N_y) M_0) - w^2} + 1$$

$$\mu_{22} = \frac{rM_0 (rH_0 + N_x rM_0)}{(rH_0 + r(N_x - N_y) M_0) (rH_0 + r(N_z - N_y) M_0) - w^2} + 1$$

$$\mu_{22} = \frac{\omega r M_0}{\{r H_0 + r(N_x - N_y) M_0\} \{r H_0 + r(N_z - N_y) M_0\} - \omega^2}$$

Field components  $E_y$ ,  $H_z$  need to be matched on the interfaces between different regions and are expressed as

$$E_y^{(1)}(x) = A_1 e^{jk_1 x} + B_1 e^{-jk_1 x}$$

$$E_y^{(2)}(x) = A_2 e^{jk_2 x} + B_2 e^{-jk_2 x}$$

$$E_y^{(3)}(x) = A_3 e^{-\eta(x-a)} + B_3 e^{\eta(x-a)}$$

$$E_y^{(4)}(x) = A_4 e^{\eta(x+a)}$$

$$E_y^{(6)}(x) = A_6 e^{-\eta(x-a-d)}$$

$$H_z = \frac{1}{j\omega\mu_0 (\mu_{11}\mu_{22} - \mu_2^2)} \left( B \mu_2 E_y - \mu_{11} \frac{\partial E_y}{\partial x} \right)$$

$$H_z^{(1)}(x) = \frac{1}{j\omega\mu_0} (jk_1) [-A_1 e^{jk_1 x} + B_1 e^{-jk_1 x}]$$

$$H_z^{(2)}(x) = \frac{1}{j\omega\mu_0 (\mu_{11}\mu_{22} - \mu_2^2)} \{ (B\mu_2 - j\mu_{11}k_2) A_2 e^{jk_2 x} + (B\mu_2 + j\mu_{11}k_2) B_2 e^{-jk_2 x} \}$$

$$H_z^{(3)} = \frac{1}{j\omega\mu_0} \eta [A_3 e^{-\eta(x-a)} - B_3 e^{\eta(x-a)}]$$

$$H_z^{(4)} = \frac{1}{j\omega\mu_0} \eta e^{\eta(x+a)} A_4$$

$$H_z^{(6)} = \frac{1}{j\omega\mu_0} A_6 \eta e^{\eta(x-a-d)}$$

Boundary conditions require that

$$E_{y(4)}(-a) = E_{y(1)}(-a)$$

$$H_{z(4)}(-a) = H_{z(1)}(-a)$$

$$E_{y(1)}(a-s) = E_{y(2)}(a-s)$$

$$\begin{aligned}
H_{z(1)}(a-s) &= H_{z(2)}(a-s) \\
E_{y(2)}(a) &= E_{y(3)}(a) \\
H_{z(2)}(a) &= H_{z(3)}(a) \\
E_{y(3)}(a+d) &= E_{y(6)}(a+d) \\
H_{z(3)}(a+d) - H_{z(6)}(a+d) &= \frac{E_{y(3)}(a+d)}{Z}
\end{aligned}$$

where  $Z$  is the sheet resistance for the resistive film.

Eliminating the amplitude unknowns, we obtain the dispersion relation equation  $F(\beta)=0$ . Since loss mechanism are included in the calculation, all the wavenumbers must be replaced by complex variables which are written as

$$\tilde{k}_1 = k_{1r} + jk_{1i} \quad k_{1r}, k_{1i} \geq 0,$$

$$\tilde{k}_2 = k_{2r} + jk_{2i} \quad k_{2r}, k_{2i} \geq 0,$$

$$\tilde{n} = n_r + jn_i \quad n_r \geq 0, n_i \leq 0,$$

$$\tilde{\beta} = \beta - j\alpha \quad \alpha \geq 0.$$

The parameters  $\tilde{k}_1, \tilde{k}_2, \tilde{n}, \tilde{\beta}$  are related to  $\tilde{\beta}$  as

$$\tilde{k}_{12} + \tilde{\beta}_2 = \epsilon_d k_o^2$$

$$\tilde{k}_2 + \tilde{\beta}_2 = \mu_{eff} \epsilon_f k_o^2$$

$$\tilde{\beta}_2 + \tilde{n}_2 = k_o^2$$

By Newton-Rapson Method, numerical solutions are obtained.

For 94 GHz application, low linewidth ferrite material should be used. Hence YIG is attractive. Figure 4 shows the results of numerical calculation for YIG. We can see that for DC magnetic field close to the resonance point we can observe significant difference in transmission loss

for two directions. The large DC magnetic field required is due to the fact that magnetization of YIG is low, 1760oe. The use of ferrites with higher magnetization is essential for practice devices.

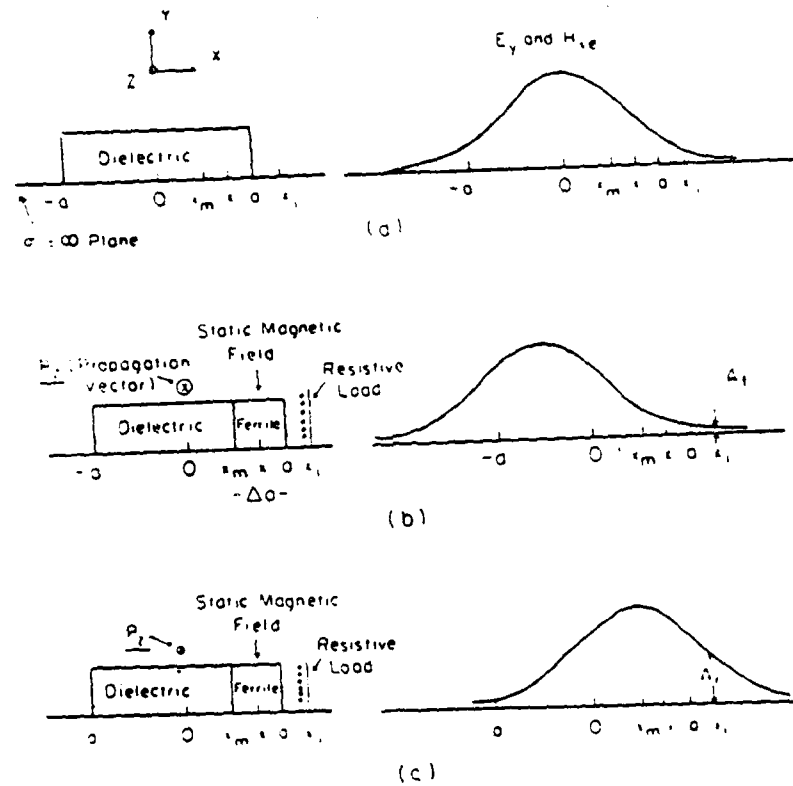


Figure 1. Transverse field representation in an image line isolator  
 (a) Transverse field for a typical dielectric guide;  
 (b) Transverse field for the forward-transmission case of ferrite loaded guide;  
 (c) Reverse-transmission case.

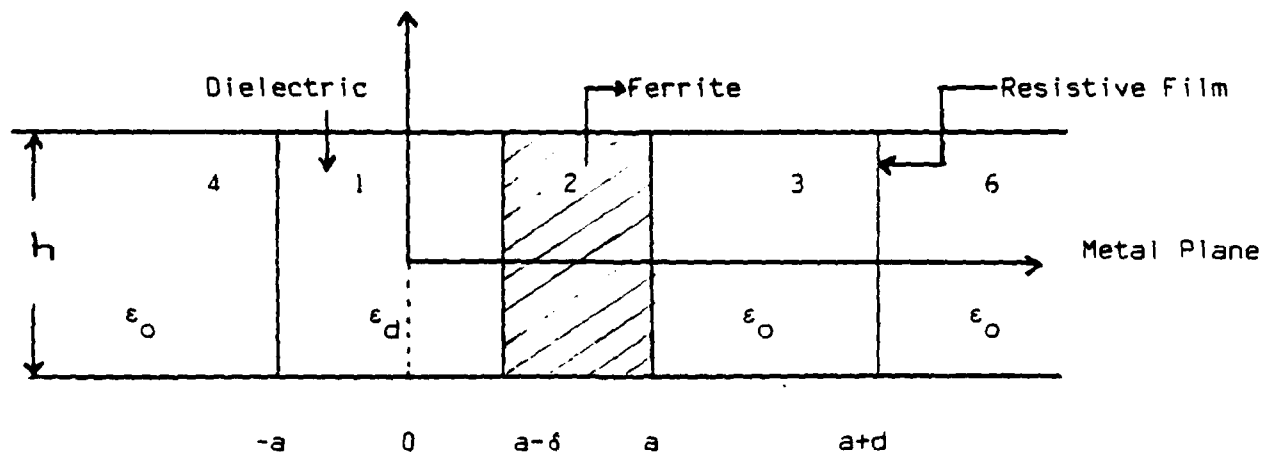


Figure 2. Strip Line Isolator

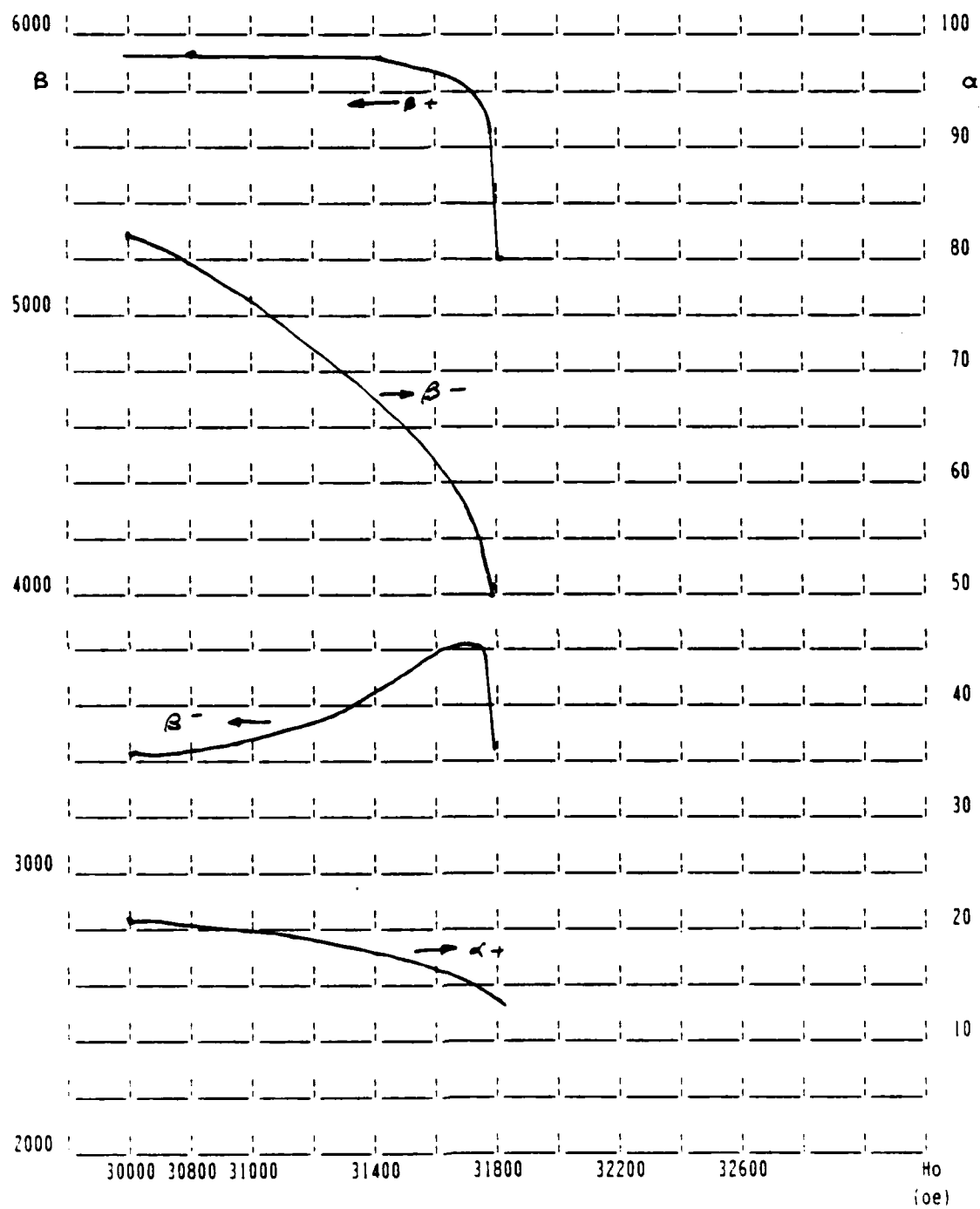
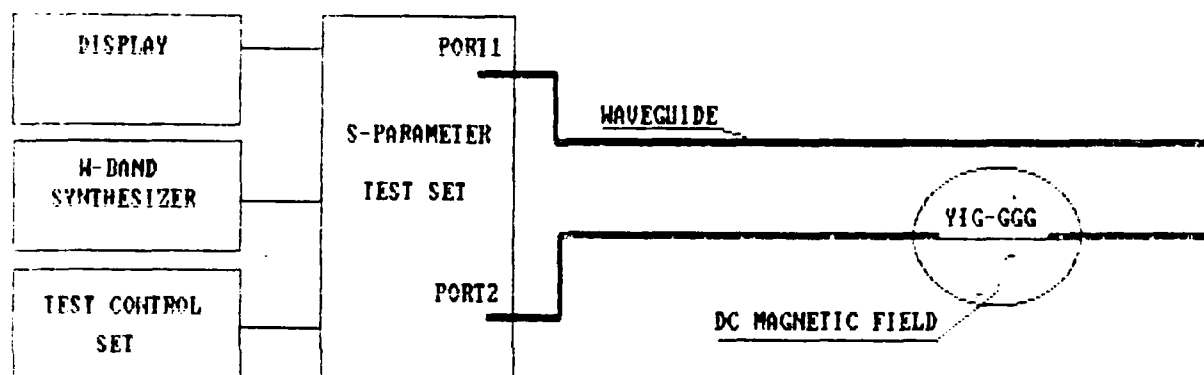


Figure 4. Forward and Reverse Propagation Characteristics for Strip Line Isolator in YIG

## 7.2 EXPERIMENTS ON MM WAVE FIELD DISPLACEMENT ISOLATORS.

Experimental work on W-band propagation characteristics of YIG-GGG dielectric image line under a DC magnetic field has been carried out in order to evaluate non-reciprocal propagation characteristics which can be used to develop W-Band field displacement isolators.

A Hughes S-parameter test system (Fig. 1) was used to measure the scattering coefficients of the test structures.



|                            |                  |
|----------------------------|------------------|
| Display -----              | HP8410, HP8412   |
| W-Band Synthesizer -----   | Hughes 4785      |
| Test Control Unit -----    | Hughes 786H.5000 |
| S-Parameter Test Set ----- | Hughes 4786HX    |

FIG. 1 A S-PARAMETER TEST SYSTEM

Initial studies were conducted utilizing a section of W band waveguide with the top and side walls milled out 0.750 inches in the longitudinal direction (Fig. 2). The bottom wall served as a ground plate of the dielectric image line. With no sample in place, the insertion loss of the structure was 25db. Test samples were inserted in the open ends of the

waveguide. This modified waveguide was connected to the W band S parameter test set and a DC magnetic field applied to the opening area utilizing a Harvey-Wells 12" electro-magnet with pole pieces tapered to a 0.75" diameter, 0.75" gap. Fields of up to 35KG could be obtained.

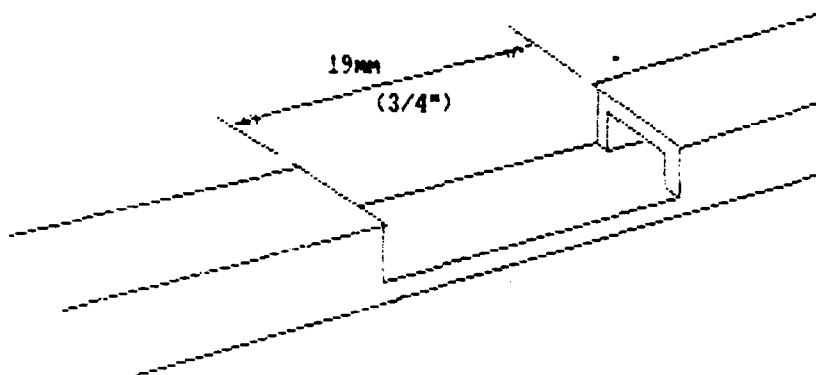


FIG. 2 WAVEGUIDE TEST STRUCTURE

The samples used were typically fabricated from 25 micron thick, liquid phase epitaxy YIG (Yttrium Iron Garnet) films grown on 0.5mm thick substrate of GGG (Gadolinium Gallium Garnet). Samples were angle lapped to optimize coupling into and out of the waveguide as shown in Figure 3. Optimum angles for minimum insertion loss were determined experimentally. The insertion loss of these samples was as low as 2.5db (0.1db/mm or 0.75db/wavelength).

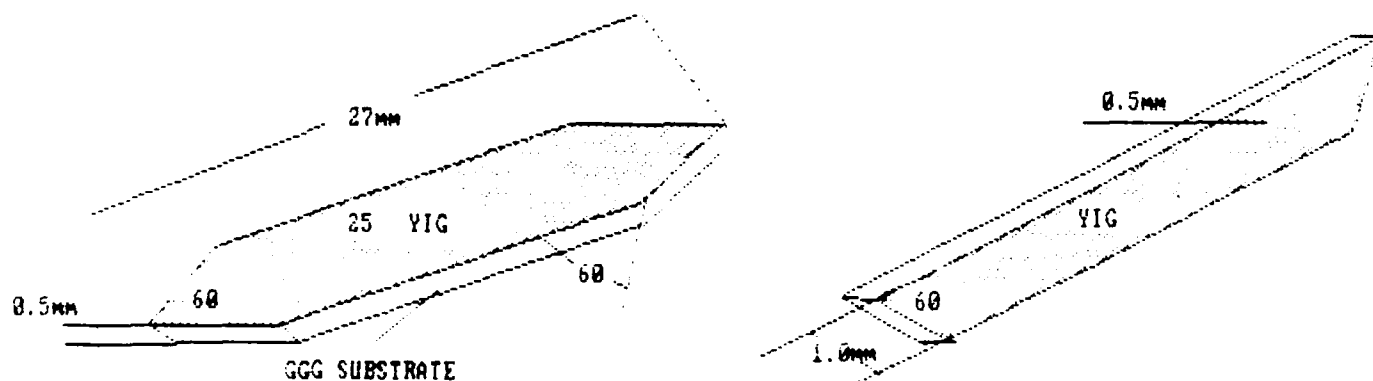


FIG. 3 TEST SAMPLES. LEFT: SAMPLE IN THE H-PLANE (OR XZ PLANE)

RIGHT: SAMPLE IN THE E-PLANE (OR YZ PLANE)



Typically, the YIG-GGG sample was placed at the center of the open ground plane and adjusted slightly to minimize the insertion loss.

The following coordinate system was used to define the experimental configurations (Fig. 3).

X ----- The wide side of the metal waveguide.

Y ----- The narrow side of the metal waveguide.

Z ----- The wave propagation direction.

XZ corresponds to the H-plane of  $TE_{10}$  wave.

YZ corresponds to the E-Plane of  $TE_{10}$  wave.

Figure 4 shows  $S_{21}$  and  $S_{12}$  of a H-plane YIG sample for different values of  $H_x$  (The DC magnetic field is in X-direction).

As  $H_x$  increases  $S_{21}$  becomes smaller over the entire 90-100GHz band. As the magnetic field exceeds 30KGs a "NOTCH" begins appear in the band and there was 5-7db difference between  $S_{12}$  and  $S_{21}$  demonstrating the nonreciprocal effect.

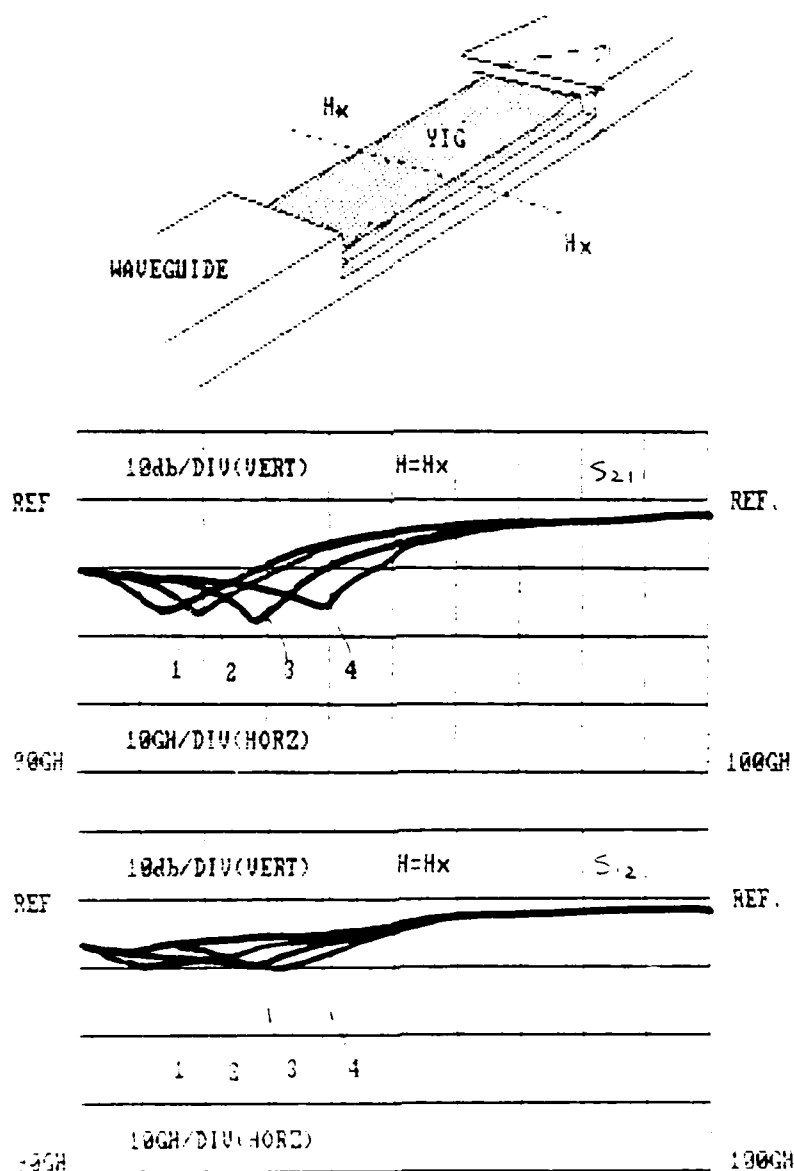


FIG. 4.  $S_{12}$  AND  $S_{21}$  OF H-PLANE YIG SAMPLE WITH THE DIFFERENT  $H_x$

1. 30KGS; 2. 32.5KGS; 3. 33.0KGS; 4. 33.5KGS

If a gold film ( $500\text{\AA}$ ) absorber is placed directly the top of the YIG sample  $S_{12}$  and  $S_{21}$  are shown in Fig. 5. The "NOTCH" turns flat and the difference between  $S_{12}$  and  $S_{21}$  becomes small.

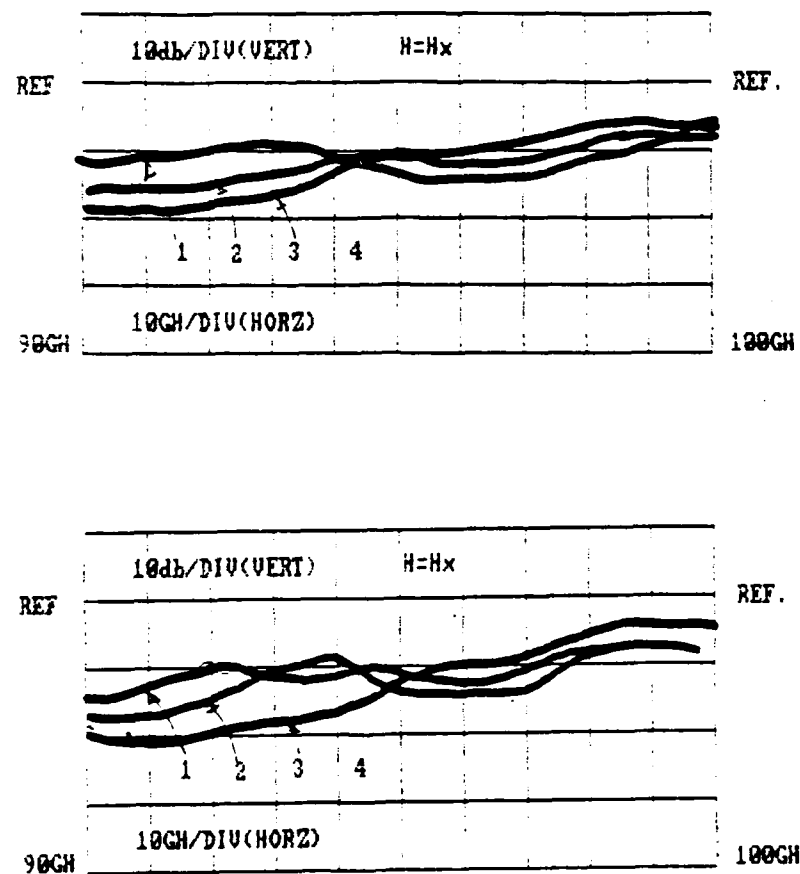


FIG. 5  $S_{12}$  AND  $S_{21}$  FOR H-PLANE YIG WITH THE GOLD ABSORBER  
WITH THE VARYING  $H_X$

1. 32KGs; 2. 32.5KGs; 3. 33KGs; 4. 33.5KGs

Fig. 6 shows the  $S_{21}$  of E-plane YIG under with an  $H_y$ . Like the proceeding when  $H_y$  is near resonance (for 90GHz  $H_0 \approx 32$ KGs) there is a "NOTCH", a very strong absorption, in the band.

Significant absorption occurred in both propagation directions. Since the DC field was perpendicular to the H-plane the absorption was much stronger than in the first case.  $S_{12}$  was almost identical and an absorber produced additional attention in both directions.

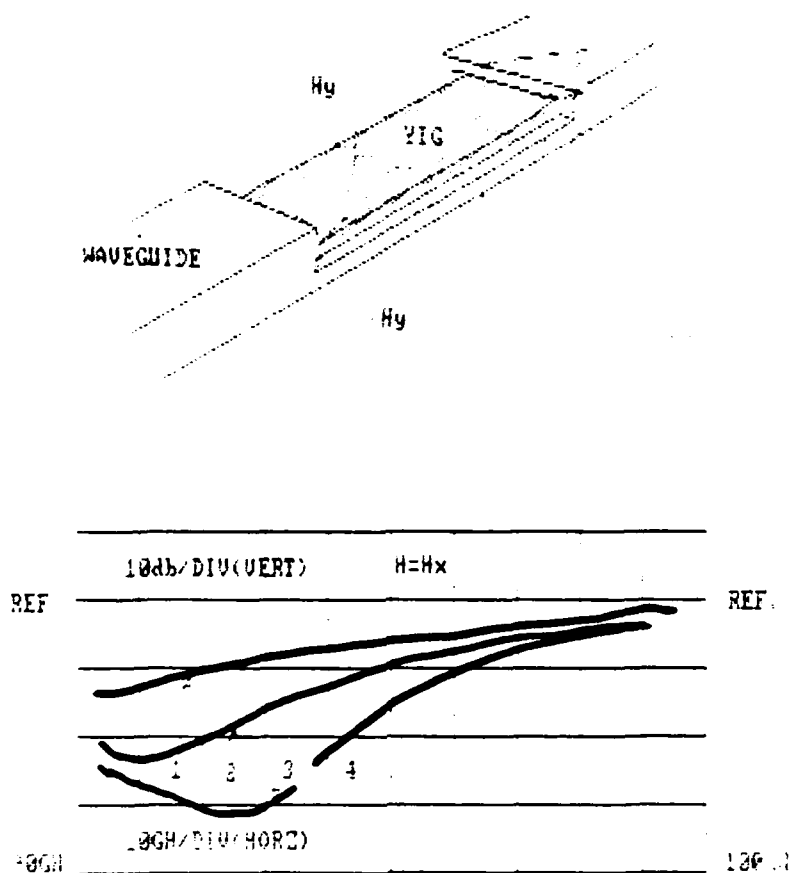


FIG. 6  $S_{21}$  FOR H-PLANE YIG, FOR VARYING  $H_y$   
 1. 28KGs; 2. 30KGs; 3. 32KGs

Fig. 7 shows the  $S_{21}$  and  $S_{12}$  of an E-plane sample under the different values of DC Field. Again, there is strong absorption and  $S_{21}$  and  $S_{12}$  are quite similar.

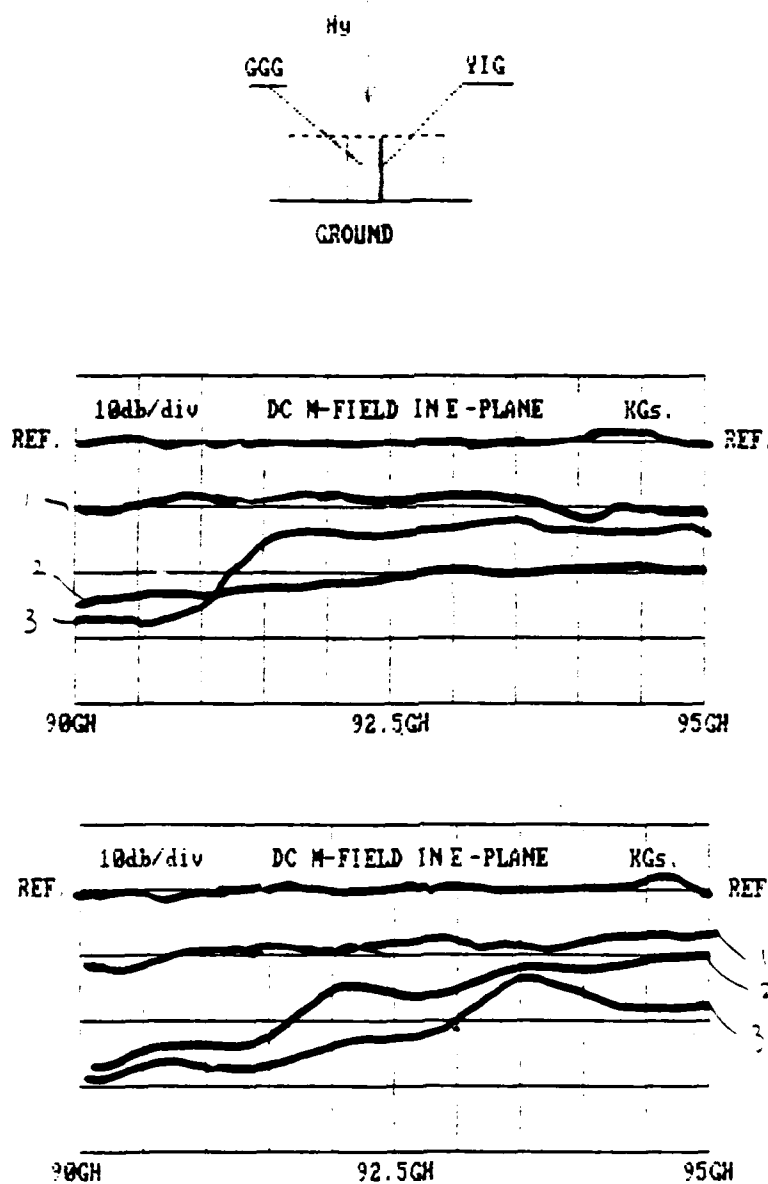


FIG. 7 THE E-PLANE YIG-GGG SAMPLE UNDER A DC  $H_y$ .

Figure 8 gives the results for E-plane YIG-GGG sample which shows  $S_{12}$  and  $S_{21}$ . A 500Å chrome film absorber under varying  $H_y$ .

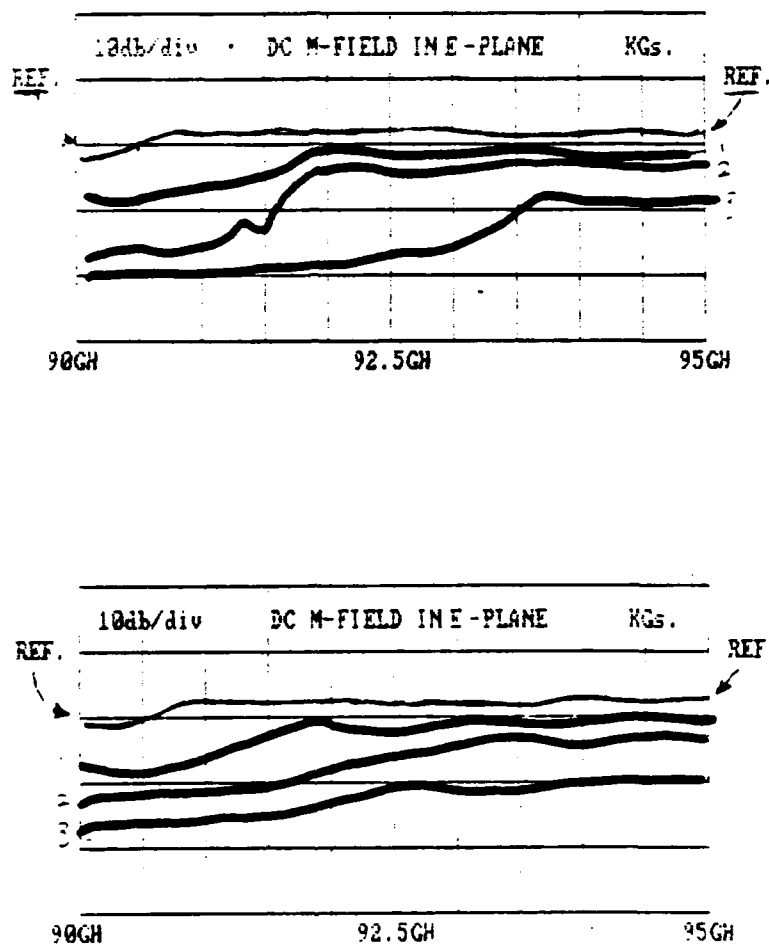


FIG. 8  $S_{21}$  AND  $S_{12}$  E-PLANE YIG-GGG WITH A CHROME FILM ABSORBER ON THE YIG SURFACE.

The non reciprocal effect is small. (<5db).

Figure 9 shows the same configuration but with a  $330\Omega\text{-cm}$ ,  $0.016''$  thick silicon wafer spaced  $0.010''$  from the YIG surface.

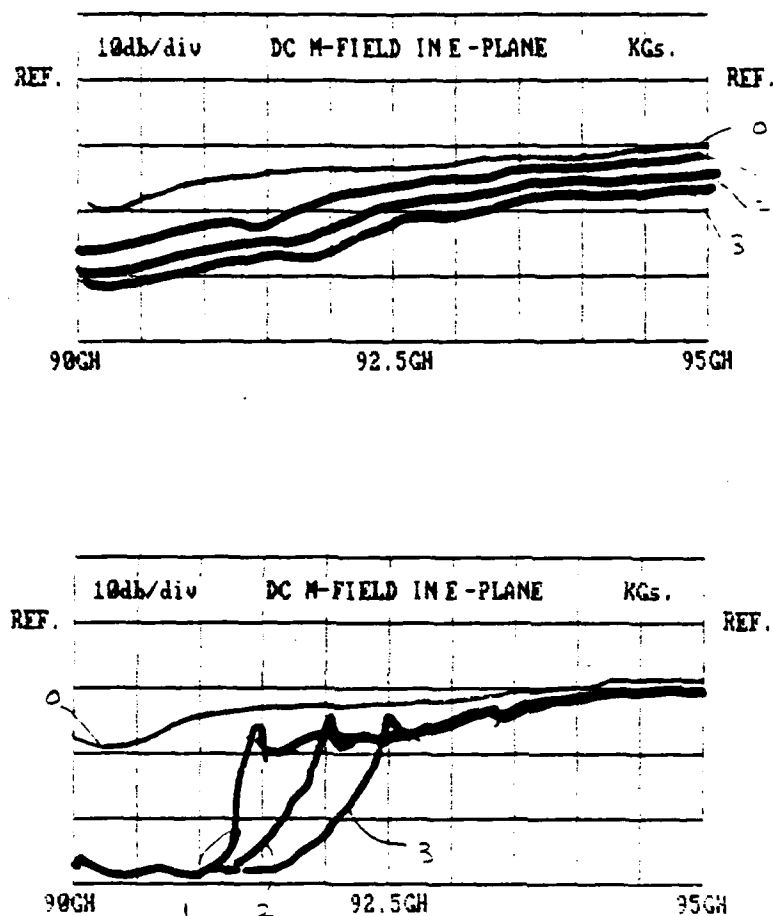


FIG. 9  $S_{21}$  AND  $S_{12}$  OF AN E-PLANE SAMPLE  
AND A SILICON ( $\rho=330\Omega\text{cm}$ )

- 0. 0 KGs
- 1. 32.0 KGs
- 2. 32.5 KGs
- 3. 33.0 KGs

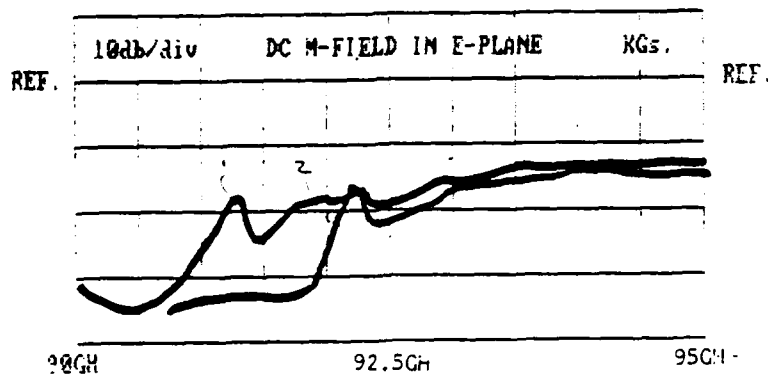
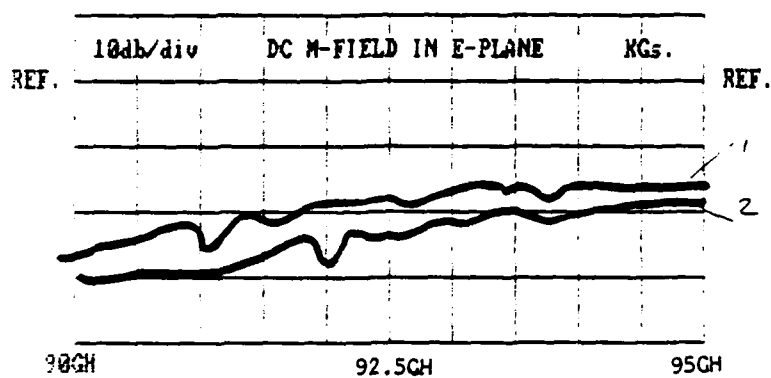
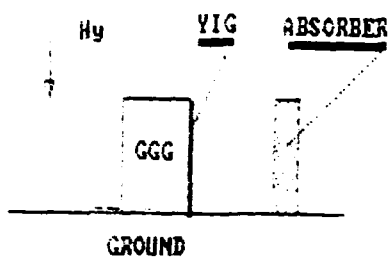
FIG. 9B  $\rho_{s1} = 330 \Omega\text{-cm}$ 

Figure 10  $S_{21}$  and  $S_{12}$  of an E-plane sample  
as in Figure 9,  $\rho = 80 \Omega\text{-cm}$ .

As can be seen  $S_{21}$  and  $S_{12}$  change sharply with frequency, and  $S_{21}$  and  $S_{12}$  are significantly different.



Figure 11 shows the  $S_{12}$  and  $S_{21}$  with the same conditions as in Figure 9, except that the silicon wafer is on the other side of the YIG-GGG sample. (i.e. The silicon wafer is not facing the surface of the YIG.)

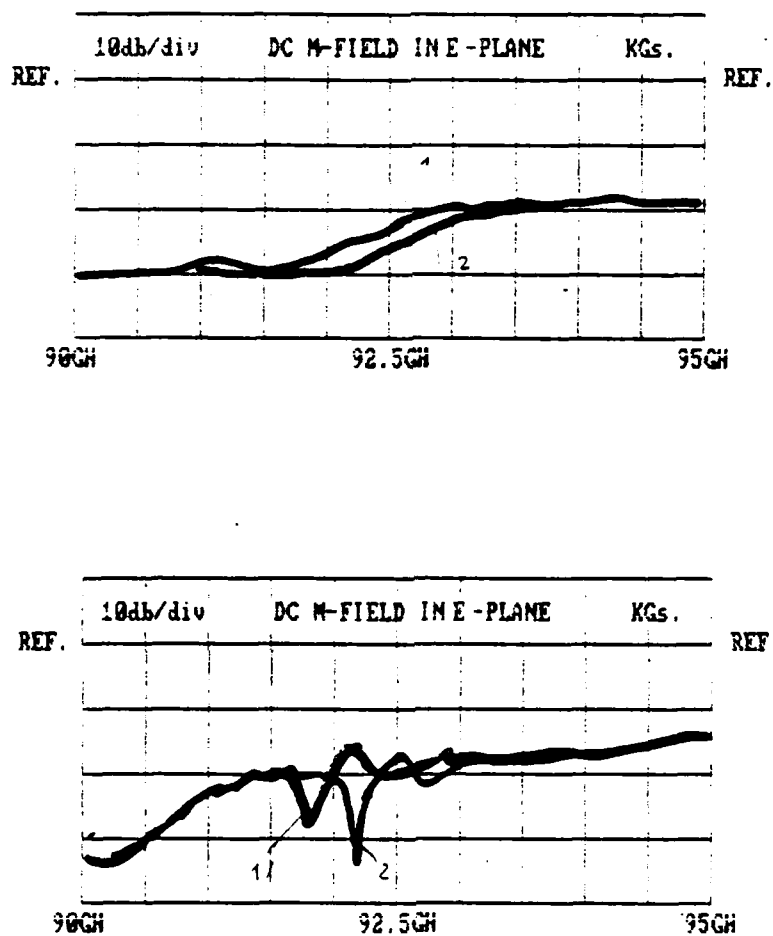


FIG. 11       $S_{21}$  AND  $S_{12}$  OF AN E-PLANE SAMPLE WITH A SILICON ABSORBER  
OPPOSITE TO THE YIG FACE.

- 1. 32 KGs
- 2. 33 KGs

Figure 12 demonstrates the effect of distance between the sample and the absorber on  $S_{21}$  and  $S_{12}$ .

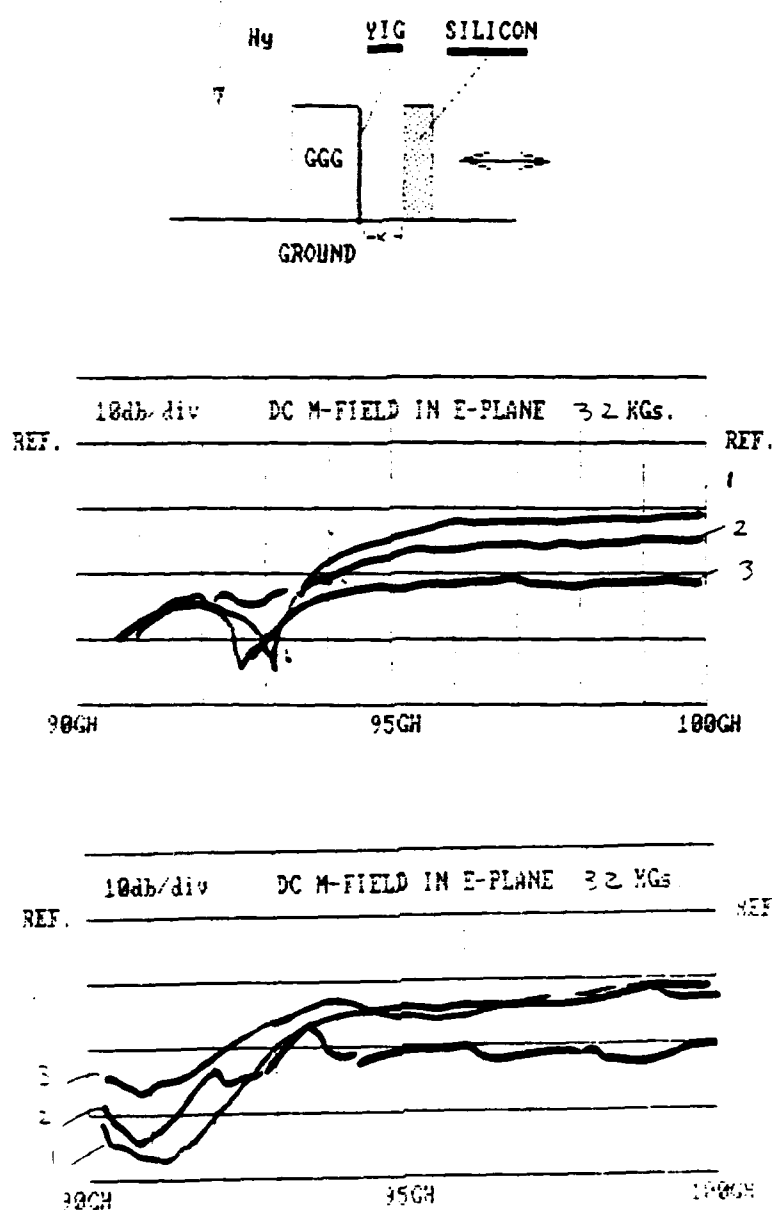


FIG. 12 THE EFFECT OF THE DISTANCE BETWEEN THE SAMPLE AND THE ABSORBER ON  $S_{21}$  AND  $S_{12}$ .

1.  $x = 0$  m
2.  $x = 0.3$  m
3.  $x = 0.5$  m

## CONCLUSIONS

The experimental results demonstrate that the YIG-GGG dielectric image line, whether the YIG film is in the E- or H-plane, has non-reciprocal characteristics for magnetic fields applied parallel to the YIG film surface. The non-reciprocal effect is significantly enhanced if an absorber of the proper resistivity and properly spaced from the YIG surface is added.

In all cases, the effect is at or near ferromagnetic resonance. For a practical W-band field displacement isolator it is desirable to operate the ferrite away from the ferromagnetic resonance. For YIG, with a saturation magnetization of  $\sim 2000$  Gauss, the DC magnetic field for the field displacement effect at 100GHz should be around 32,700 Oe with corresponding ferromagnetic resonance at 97GH. Thus, it is difficult to see a "pure" field displacement effect. More desirable is a ferrite material with 5000 Gauss saturation magnetization, and small linewidth. Then the DC field for 100GHz will be about 31,300 Oe which, corresponding to the resonance at 87.6GH, allowing a displacement dominated device. Thus low linewidth, high magnetization epitaxial ferrites are essential for MM wave isolators. Also, the bandwidth will increase with increasing magnetization. Finally, further optimization of the structures is required for performance improvements.

## 8.0 SUMMARY

Detailed theoretical and experimental investigation have been carried out on ion implanted oblique incidence magnetostatic reflective array filters. Correlation between theory and experiment has been good.

The principal application in which MSW ion implanted arrays offer some limited practical potential is oblique incidence compressive filters. Ground plane contouring is a preferred technique, characterized by 20 db insertion losses over 500 MHz bandwidths compared to insertion losses of 50 db over maximum bandwidths of 250 MHz for reflective arrays. Reflective arrays cannot compete with transducer arrays in the fabrication of low loss spectral weighted filters. In the context of oblique incidence compressive filters, implanted reflectors perform comparably to metal stripes without the conductive losses. Implanted reflective arrays, however, are characterized by relatively narrow bandwidths, small time-bandwidth products, and high insertion losses. Reflectivities are difficult to predict due to a considerable sensitivity to film surface quality. Although MSW RAFs promise little hope of ever equaling the performance of SAW devices, they have the advantage of operating in the 1-20 GHz frequency range and of magnetic tunability.

Theoretical and experimental studies of MM wave isolators based on field displacement in ferrite coated dielectric waveguides shows significant promise. Using a YIG on GGG structure an W-band isolator has been built and tested with isolation of  $> 20$  db and an insertion loss of 5 db. The bandwidth is narrow ( $< 1$  GHz) and bias field high ( $\sim 32$  KG). With higher magnetization materials superior devices are feasible and integration with other components in a dielectric waveguide format is possible.

## 9.0 PUBLICATIONS RESULTING FROM ARO SUPPORT

1. J. M. Owens, C. V. Smith, and R. L. Carter, "MSW Reflecting Array Filters," Proceedings of the 1981 RADC Microwave Magnetics Technology Workshop, RADC-TR-83-15, Rome Air Development Center, Griffis Air Force Base, NY 13441, pp. 106-116 (1983).
2. J. M. Owens and R. L. Carter, "Magnetostatics Advance: The Shape of Things To Come," Microwave System News, V. 13 No. 3, pp.103-111 (1983).
3. K. W. Reed, J. M. Owens, R. L. Carter and C. V. Smith, Jr., "An Oblique Incidence Ion Implanted MSFVW RAF with Linear Group Delay," 1983 IEEE MTT-S International Microwave, IEEE Cat. #82CH1871-3, pp. 259-261.
4. K. W. Reed, J. M. Owens and R. L. Carter, "Current Status of Magnetostatic Wave Reflective Array Filters." invited paper, Circuits, Systems and Signal Processing, Vol. 4, No. 1-2, 1985, pp. 157-211.
5. J. M. Owens, J. H. Collins and R. L. Carter, "System Applications of Magnetostatic Wave Devices," invited paper, Circuits, Systems and Signal Processing, Vol. 4, No. 1-2, 1985, pp. 317-335.
6. R. L. Carter, and J. M. Owens, "Magnetostatic Wave Devices and Their Application," MICROONDE, December 1985, pp. 7-22.
7. Y.J. Ataiiyan, J. M. Owens, K. W. Reed, R. L. Carter, and W. A. Davis, "MSSW Transversal Filters Based on Current Weighting in Narrow (10 Micron) Transducers," to be published, 1986 IEEE-S International Microwave Symposium Proceedings, June 1986.
8. L. R. Adkins, H. L. Glass, F. S. Stearns, Y. J. Ataiiyan, R. L. Carter, J. M. Owens, and D. D. Stancil, "New Time Delay Technologies for Phase Array Systems," Proceedings of "Phased Arrays '85," October 1985.

APPENDIX A  
WAVE IMPEDANCES

### A.1 MSFVW Characteristic Impedance

The wave impedance is defined as the ratio of transverse electric field to transverse magnetic field,

$$\tilde{Z}^{\pm} = \frac{\tilde{e}_z^{\pm}}{\tilde{h}_x^{\pm}} . \quad (\text{A.1.1})$$

Small letters are used to denote the time varying part of the total fields, with separable harmonic time dependence,

$$\exp\{j\omega t\}. \quad (\text{A.1.2})$$

Using the magnetostatic approximation, the spacial harmonics are separable in  $x$  and  $y$ , and neglecting  $z$  variation have the form,

$$(A\exp[\tilde{\gamma}x] + B\exp[-\tilde{\gamma}x]) \exp[\pm jk_y y] . \quad (\text{A.1.3})$$

Subject to these constraints, the two sides of Faraday's law are,

$$\text{curl}(\tilde{\mathbf{e}}) = \begin{bmatrix} \hat{x} & \hat{y} & \hat{z} \\ \frac{\partial}{\partial x} & \frac{\partial}{\partial y} & \frac{\partial}{\partial z} \\ 0 & 0 & \tilde{e}_z \end{bmatrix} = \begin{bmatrix} \pm jk_y \tilde{e}_z \\ -\frac{\partial \tilde{e}_z}{\partial x} \\ \frac{\partial \tilde{e}_z}{\partial y} - \frac{\partial \tilde{e}_x}{\partial y} \end{bmatrix} \quad (\text{A.1.4a})$$

and,

$$-j\omega\mu_0\tilde{\mathbf{u}}\tilde{\mathbf{h}} = -j\mu_0 \begin{bmatrix} 1 & 0 & 0 \\ 0 & \mu_1 - j\mu_2 \\ 0 & j\mu_2 & \mu_1 \end{bmatrix} \begin{bmatrix} \tilde{h}_x \\ \tilde{h}_y \\ \tilde{h}_z \end{bmatrix} = -j\omega\mu_0 \begin{bmatrix} \tilde{h}_x \\ \mu_1\tilde{h}_y - j\mu_2\tilde{h}_z \\ j\mu_2\tilde{h}_y + \mu_1\tilde{h}_z \end{bmatrix}$$

which combined yield,

$$\begin{bmatrix} \pm j k \tilde{e}_z \\ -\frac{\partial \tilde{e}_z}{\partial x} \\ \frac{\partial \tilde{e}_y}{\partial x} - \frac{\partial \tilde{e}_x}{\partial y} \end{bmatrix} = -j\omega\mu_0 \begin{bmatrix} \tilde{h}_x \\ \mu_1 \tilde{h}_y - j\mu_2 \tilde{h}_z \\ j\mu_2 \tilde{h}_y + \mu_1 \tilde{h}_z \end{bmatrix} \quad (\text{A.1.4b})$$

The characteristic impedance follows directly from the x-equation,

$$\tilde{Z}^{\pm} = \pm \frac{\omega\mu_0}{k} , \quad (\text{A.1.5})$$

and is the familiar form characteristic of uniform cross-section wave guides.

## A.2 MSSW Characteristic Impedance

The MSSW characteristic impedance can be calculated from Faraday's law,

$$\text{curl}(\tilde{\mathbf{e}}) = -\mu_0 \tilde{\mathbf{u}} \frac{\partial \tilde{\mathbf{h}}}{\partial t} \quad (\text{A.2.1})$$

and the known forms of the field solutions,

$$\begin{aligned} \tilde{h}_y^{\pm} &= \{C \exp[\tilde{\gamma} x] + D \exp[-\tilde{\gamma} x]\} \exp[\pm j k_{\pm} y] \\ \tilde{h}_x^{\pm} &= \{F \exp[\tilde{\gamma} x] + G \exp[-\tilde{\gamma} x]\} \exp[\pm j k_{\pm} y] . \end{aligned} \quad (\text{A.2.2a})$$

In the absence of a current density within the ferrite, and neglecting dielectric anisotropy, Ampere's law,

$$\text{curl}(\tilde{\mathbf{h}}) = \epsilon_0 \epsilon \frac{\partial \tilde{\mathbf{e}}}{\partial t} \quad (\text{A.2.3})$$



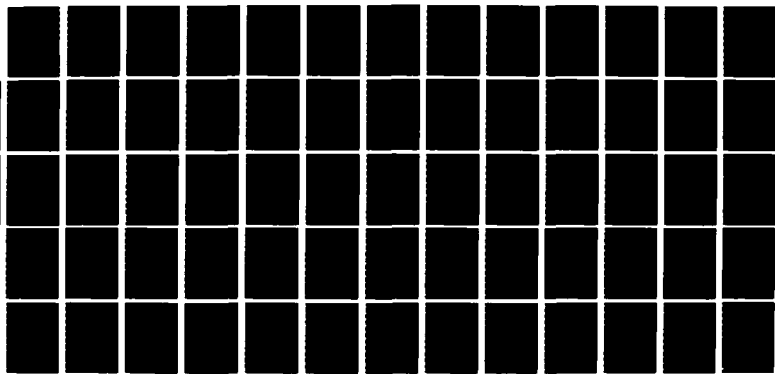
AD-A175 472

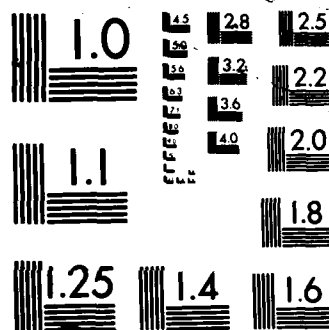
TUNABLE MICROWAVE TRANSVERSAL FILTERS AND DISPERSIVE  
DELAY LINES BASED ON (U) TEXAS UNIV AT ARLINGTON DEPT  
OF ELECTRICAL ENGINEERING J M OWENS ET AL 30 SEP 86  
ARO-17685 1-EL DRAG29-82-K-8873 F/G 9/5

3/3

UNCLASSIFIED

NL





PHOTOCOPY RESOLUTION TEST CHART

indicates that the time varying component of the electric field points in the z-direction,

$$\tilde{e}_z^{\pm} = \{A \exp[\tilde{\gamma}x] + B \exp[-\tilde{\gamma}x]\} \exp[\tilde{\gamma}jk_{\pm}y] \quad (\text{A.2.2b})$$

normal to the plane of incidence in which the time varying part of the magnetic field is located.

It is assumed that terms of like x-dependence independently satisfy the boundary conditions at the interfaces between reflector and land regions. Without this constraint, the boundary conditions would cause the x-dependence of field solutions in the reflector regions to appear in the solutions of the land regions, which is true only in close proximity to the interfaces between these regions. Detailed matching of the boundary conditions by like terms, is equivalent to neglecting the transition zone around the interface, modeling the fields as though they exhibit a small abrupt discontinuity there. Subject to these constraints, the components of Faraday's law are,

$$\text{curl}(\tilde{\mathbf{e}}) = \begin{vmatrix} \hat{x} & \hat{y} & \hat{z} \\ \frac{\partial}{\partial x} & \frac{\partial}{\partial y} & \frac{\partial}{\partial z} \\ 0 & 0 & \tilde{e}_z \end{vmatrix} = \frac{\partial \tilde{e}_z}{\partial y} \hat{x} - \frac{\partial \tilde{e}_z}{\partial x} \hat{y} = \begin{bmatrix} \tilde{\gamma}jk_{\pm} \\ \tilde{\gamma} \\ 0 \end{bmatrix} \tilde{e}_z$$

$$-\mu_0 \tilde{\mathbf{u}} \frac{\partial \tilde{\mathbf{h}}}{\partial t} = -j\omega\mu_0 \begin{bmatrix} \mu_1 & -j\mu_2 & 0 \\ j\mu_2 & \mu_1 & 0 \\ 0 & 0 & 0 \end{bmatrix} \begin{bmatrix} \tilde{h}_x \\ \tilde{h}_y \\ 0 \end{bmatrix} = -j\omega\mu_0 \begin{bmatrix} \mu_1 \tilde{h}_x - j\mu_2 \tilde{h}_y \\ \mu_1 \tilde{h}_y - j\mu_2 \tilde{h}_x \\ 0 \end{bmatrix}$$

yielding,

$$\begin{pmatrix} \mu_1 \tilde{h}_x - j\mu_2 \tilde{h}_y \\ \mu_1 \tilde{h}_x - j\mu_2 \tilde{h}_y \end{pmatrix} = \begin{pmatrix} \pm \tilde{k}_\pm / \omega \mu_0 \\ \pm \gamma / j\omega \mu_0 \end{pmatrix} \tilde{e}_z \quad (\text{A.2.4})$$

Referring to equation (A.2.2), it should be noted that + and - in front of  $\tilde{\gamma}$  refer to top and bottom surface waves, respectively, and in front of  $\tilde{k}$  forward and reverse waves, respectively. The subscript signs on  $\tilde{k}$  emphasize that the waves are anisotropic and should be the same as the sign in front of  $\tilde{k}$ . Solving this set of linear equations for the ratio of the transverse electric field,  $\tilde{e}_z$ , to the transverse magnetic field,  $\tilde{h}_x$ , gives the characteristic impedance,

$$\tilde{Z}^\pm = \frac{\tilde{e}_z}{\tilde{h}_x} = \frac{\omega \mu_0 (\mu_1^2 - \mu_2^2)}{\pm k_\pm \mu_1 \pm \gamma \mu_2} \quad (\text{A.2.5})$$

The various possible combinations of signs and their meaning are summarized in TABLE A.

TABLE A  
GENERALIZED MSSW CHARACTERISTIC IMPEDANCES

|                             | BOTTOM SURFACE $(-\gamma)$   | TOP SURFACE $(+\gamma)$  |
|-----------------------------|--|--|
| FORWARD<br>$(+\tilde{k}_+)$ | $\frac{\omega \mu_0 (\mu_1^2 - \mu_2^2)}{k_\pm \mu_1 - \gamma \mu_2}$  | $\frac{\omega \mu_0 (\mu_1^2 - \mu_2^2)}{k_\pm \mu_1 + \gamma \mu_2}$  |
| REVERSE<br>$(-\tilde{k}_-)$ | $-\frac{\omega \mu_0 (\mu_1^2 - \mu_2^2)}{k_\pm \mu_1 + \gamma \mu_2}$ | $-\frac{\omega \mu_0 (\mu_1^2 - \mu_2^2)}{k_\pm \mu_1 - \gamma \mu_2}$ |

The magnetostatic approximation implies that,

$$\text{curl}(\tilde{\mathbf{h}}) = 0, \quad (\text{A.2.6a})$$

which leads to,

$$\tilde{\mathbf{y}} = \tilde{\mathbf{k}}_{\pm}, \quad (\text{A.2.6b})$$

from which the values in TABLE 2.4 are obtained.

APPENDIX B  
REFLECTION AND TRANSMISSION COEFFICIENTS

The reflection and transmission coefficients at an interface are a direct consequence of matching the tangential boundary conditions there. Consider the wave in Figure B.1, impinging normally on the boundary between anisotropic regions " $\xi$ " and " $\zeta$ ", characterized by the forward (+) and reverse (-) wave impedances,  $\tilde{Z}_{\xi}^{+}$  and  $\tilde{Z}_{\zeta}^{+}$ , respectively.

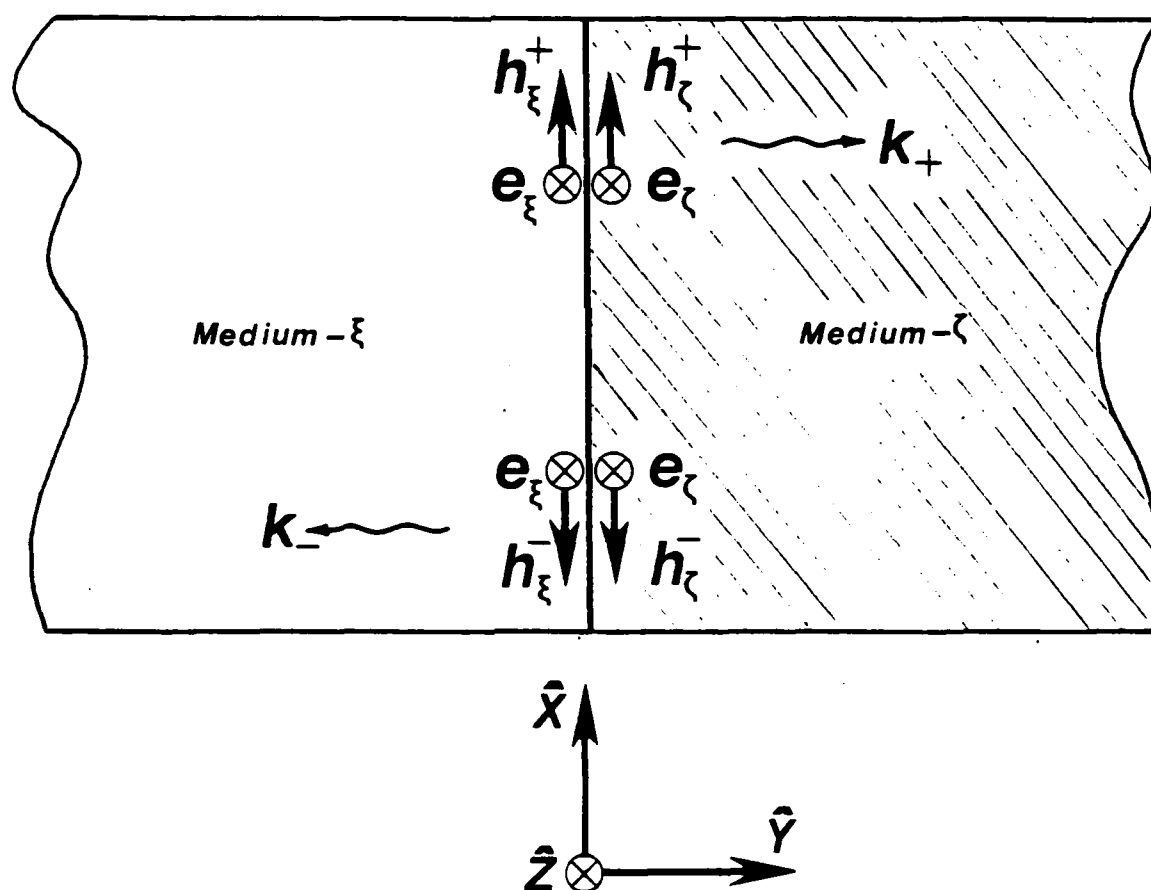


Figure B.1. Reflection and transmission at an interface.

Satisfaction of the tangential magnetic and electric boundary conditions in the absence of free charge or sheet currents at the interface yields,

$$\tilde{e}_{\xi}^{+} + \tilde{e}_{\xi}^{-} = \tilde{e}_{\zeta}^{+} + \tilde{e}_{\zeta}^{-} \quad (\text{B.1})$$

$$\tilde{h}_{\xi}^{+} + \tilde{h}_{\xi}^{-} = \tilde{h}_{\zeta}^{+} + \tilde{h}_{\zeta}^{-}$$

where, the transverse fields are used. The first equation is expressible in terms of the transverse magnetic field, via the characteristic impedance,

$$\tilde{Z}_v^{\pm} = + \frac{\tilde{e}_v^{+}}{\tilde{h}_v^{+}} = - \frac{\tilde{e}_v^{-}}{\tilde{h}_v^{-}} \quad , \quad (\text{B.2})$$

as follows,

$$\tilde{Z}_{\xi}^{+} \tilde{h}_{\xi}^{+} + \tilde{Z}_{\xi}^{-} \tilde{h}_{\xi}^{-} = \tilde{Z}_{\zeta}^{+} \tilde{h}_{\zeta}^{+} \quad . \quad (\text{B.3})$$

The equations (B.1) and (B.3) can be rewritten in accordance with  $\tilde{h}_{\xi}^{+}$  being the excitation and  $\tilde{h}_{\xi}^{-}$  and  $\tilde{h}_{\zeta}^{+}$  the unknown scattering products,

$$-\tilde{Z}_{\xi}^{-} \tilde{h}_{\xi}^{-} + \tilde{Z}_{\zeta}^{+} \tilde{h}_{\zeta}^{+} = \tilde{Z}_{\xi}^{+} \tilde{h}_{\xi}^{+} \quad (\text{B.4})$$

$$\tilde{h}_{\xi}^{-} + \tilde{h}_{\zeta}^{+} = \tilde{h}_{\xi}^{+}$$

and subsequently solved for the ratios of reflected and transmitted h-fields to the incident field, to obtain the reflection and transmission coefficients, respectively,



$$\Delta = \begin{vmatrix} -\tilde{Z}_\xi^- & \tilde{Z}_\zeta^+ \\ 1 & 1 \end{vmatrix} = -(\tilde{Z}_\xi^- + \tilde{Z}_\zeta^+)$$

$$\tilde{\rho}_{\xi\zeta}^+ = \frac{\tilde{h}_\xi^-}{\tilde{h}_\xi^+} = \frac{1}{\Delta} \begin{vmatrix} \tilde{Z}_\xi^+ & \tilde{Z}_\zeta^+ \\ 1 & 1 \end{vmatrix} = \frac{\tilde{Z}_\zeta^+ - \tilde{Z}_\xi^+}{\tilde{Z}_\xi^- + \tilde{Z}_\zeta^+} \quad (\text{B.5})$$

$$\tilde{\tau}_{\xi\zeta}^+ = \frac{\tilde{h}_\zeta^+}{\tilde{h}_\xi^+} = \frac{1}{\Delta} \begin{vmatrix} -\tilde{Z}_\xi^- & \tilde{Z}_\xi^+ \\ 1 & 1 \end{vmatrix} = \frac{\tilde{Z}_\xi^- + \tilde{Z}_\xi^+}{\tilde{Z}_\xi^- + \tilde{Z}_\zeta^+}$$

The reflection and transmission coefficients for the **electric field** can be obtained from these from the definition of the characteristic impedance, resulting in additional scale factors,

$$\tilde{\rho}_{\xi\zeta}^+ = \frac{\tilde{Z}_\xi^- \tilde{h}_\xi^-}{\tilde{Z}_\xi^+ \tilde{h}_\xi^+} = \frac{\tilde{Z}_\xi^-}{\tilde{Z}_\xi^+} \cdot \frac{1}{\Delta} \begin{vmatrix} \tilde{Z}_\xi^+ & \tilde{Z}_\zeta^+ \\ 1 & 1 \end{vmatrix} = \frac{\tilde{Z}_\xi^-}{\tilde{Z}_\xi^+} \cdot \frac{\tilde{Z}_\zeta^+ - \tilde{Z}_\xi^+}{\tilde{Z}_\xi^- + \tilde{Z}_\zeta^+}$$

$$\tilde{\tau}_{\xi\zeta}^+ = \frac{\tilde{Z}_\zeta^+ \tilde{h}_\zeta^+}{\tilde{Z}_\xi^+ \tilde{h}_\xi^+} = \frac{\tilde{Z}_\zeta^+}{\tilde{Z}_\xi^+} \cdot \frac{1}{\Delta} \begin{vmatrix} -\tilde{Z}_\xi^- & \tilde{Z}_\xi^+ \\ 1 & 1 \end{vmatrix} = \frac{\tilde{Z}_\zeta^+}{\tilde{Z}_\xi^+} \cdot \frac{\tilde{Z}_\xi^- + \tilde{Z}_\xi^+}{\tilde{Z}_\xi^- + \tilde{Z}_\zeta^+} \quad (\text{B.6})$$

The reflection and transmission coefficients for reverse propagating waves are obtained from the above by replacing  $\xi$  by  $\zeta$  and  $+$  by  $-$ .

APPENDIX C  
COMPUTER PROGRAMS

### C.1 Normal Incidence MSSW Array Analysis

The listing in this section represents the theory used to predict the normal incidence MSSW array responses, based on the characteristic impedances derived in APPENDIX A and superposition. The main program calculates the dispersion relation from the four layer model for both the implanted and the unimplanted sections, and then calls the array function program written by Brinlee {2.24} which performs the necessary matrix manipulations to generate the transmission and reflection responses. Ferrite losses are calculated in terms of the Gilbert loss model, resulting in a complex dispersion relationship,

$$\tilde{k} = \beta - j\alpha,$$

corresponding to assumed propagation of the form,

$$\exp\{j(\omega t - \tilde{k}y)\}.$$

The program is self contained and requires no other sources of data than that indicated by the "User Supplied Input" sections.

```

C-----
C  PROGRAM DESCRIPTION:
C
C      THIS PROGRAM CALCULATES THE COMPLEX DISPERSION RELATION FOR
C
C      1) ION IMPLANTED MSSW,
C
C      2) UNIMPLANTED MSSW.
C
C  THE ASSUMED FORM IS,
C
C       $\exp(J(WT-KY))$ ,
C
C  CORRESPONDING TO A DISPERSION FACTOR OF THE FORM,
C
C       $K = \text{BETA} - J \cdot \text{ALPHA}$ .
C-----
C
C  SET UP CONSTANTS AND DECLARE COMPLEX AND REAL-----
C      COMPLEX J,CHO,GAMFO,GAMFI,GAMRO,GAMRI,K1,K2,K3,K4,
C      1GAMMA,E2KU,E2KD,FOFKFO,FOFKRO,FOFKFI,FOFKRI,COSHKV,SINHKV
C      REAL MO
C      OPEN(UNIT=23,DEVICE='DSK',DIALOG)
C      PI=3.1415927
C      J=CMPLX(0.0,1.0)
C      GYRO=17.6E+06
C      MO=1760.0
C      ZERO=1.0E-04
C      FRACT=1.0E-04
C-----
C
C  USER SUPPLIED INPUTS
C-----
C
C  IMPLANT DEPTH (MICRONS)-----
C      TYIGIM=0.4
C
C  YIG THICKNESS (MICRONS)-----
C      TYIG=13.50
C
C  ALUMINA SUBSTRATE THICKNESS (MICRONS)-----
C      TAL203=250.0
C
C  MULTIPLIER FOR IMPLANTED MO (MOIMP/MOPURE)-----
C      STRAIN=0.5
C
C  INTERNAL BIAS FIELD (OERSTEDS)-----
C      H0=375.0

```

```

C
C GILBERT LOSS PARAMETERS (FO IN HERTZ AND DELTA-H MIN IN OERSTEDS)-
  FO=3.0E+09
  DHMIN=0.5
C
C DESIRED FREQUENCY INCREMENT IN OUTPUT DATA (MHZ)-----
  DELF=2.0
C
C DESIRED START AND STOP FREQUENCY IN OUTPUT (GHZ)-----
  FSTART=2.50
  FSTOP=3.50
  BOUND=-20.0
C
C -----
C
  TYIGIM=TYIGIM*1.0E-06
  TYIGPU=(TYIG*1.0E-06)-TYIGIM
  TAL203=TAL203*1.0E-06
  WSTART=FSTART*2.0E+09*PI
  WSTOP=FSTOP*2.0E+09*PI
  DELW=DELF*2.0E+06*PI
  W=WSTART-DELW
C
C MAKE AN INITIAL GUESS ON GAMMA-----
  GAMFO=CMPLX(0.0,0.0)
  GAMFI=GAMFO
  GAMRO=GAMFO
  GAMRI=GAMFO
  GLAST=-1000.0
11111 W=W+DELW
      F=W/(2.0*PI)
C
C CALCULATE GILBERT LOSS TERMS-----
  DELH=DHMIN*(FO/F+F/FO)/2.0
  CHO=CMPLX(HO,DELH/2.0)
C
C CALCULATE PERMITIVITY RELATED CONSTANTS FOR FORWARD PROPAGATION---
  K1=1.0 + STRAIN*MO/(CHO - W/GYRO)
  K2=1.0 + STRAIN*MO/(CHO + W/GYRO)
  K3=1.0 + MO/(CHO - W/GYRO)
  K4=1.0 + MO/(CHO + W/GYRO)
C
C INCREMENT NEWTON RAPHSON ON FORWARD UNIMPLANTED GAMMA-----
  DO2 IK2=1,200,1
    SINHKV=-J*CSIN(J*GAMFO*TAL203)
    COSHKV=CCOS(J*GAMFO*TAL203)
    E2KU=CEXP(2.0*GAMFO*TYIGIM)
    E2KD=CEXP(2.0*GAMFO*TYIGPU)
    FOPKF0=(K4+1.0)*(K3*COSHKV+SINHKV)*E2KU*E2KD
    1      -(K3-1.0)*(K4*COSHKV-SINHKV)

```

```

IF(CABS(FOFKFO).LE.ZERO) GO TO 1000
GAMFO=CLOG((K3-1.0)*(K4*COSHKV-SINHKV)
1 /((K4+1.0)*(K3*COSHKV+SINHKV)))/(2.0*(TYIGPU+TYIGIM))
CHRE=ABS(REAL(GAMMA-GAMFO))
CHIM=ABS(AIMAG(GAMMA-GAMFO))
OLDRE=ABS(REAL(GAMMA))
OLDIM=ABS(AIMAG(GAMMA))
IF(CHRE.GT.FRACT*OLDRE) GO TO 77
IF(CHIM.LT.FRACT*OLDIM) GO TO 1000
77 GAMMA=GAMFO
2 CONTINUE
WRITE(6,31) F,GAMFO,CHRE,CHIM
31 FORMAT(1X,'FREQ = ',1E10.3,5X,'GAMFO = ',2(E10.3,1X),4X,
1/,1X,'CHRE = ',1E10.3,5X,'CHIM = ',1E10.3)
STOP

```

C  
C INCREMENT NEWTON RAPHSON ON FORWARD IMPLANTED GAMMA-----

```

1000 DO3 IK3=1,200,1
SINHKB=-J*CSIN(J*GAMFI*TAL203)
COSHKV=CCOS(J*GAMFI*TAL203)
E2KU=CEXP(2.0*GAMFI*TYIGIM)
E2KD=CEXP(2.0*GAMFI*TYIGPU)
FOFKFI=(K4+1.0)*((K3-K1)*(K2*COSHKV-SINHKV)
1 +(K2+K3)*(K1*COSHKV+SINHKV)*E2KU)*E2KD
2 -(K3-1.0)*((K1+K4)*(K2*COSHKV-SINHKV)
3 +(K4-K2)*(K1*COSHKV+SINHKV)*E2KU)
IF(CABS(FOFKFI).LE.ZERO) GO TO 2000
GAMFI=CLOG((K3-1.0)*((K1+K4)*(K2*COSHKV-SINHKV)
1 +(K4-K2)*(K1*COSHKV+SINHKV)*E2KU)
2 /((K4+1.0)*((K3-K1)*(K2*COSHKV-SINHKV)
3 +(K2+K3)*(K1*COSHKV+SINHKV)*E2KU)))
4 /(2.0*TYIGPU)
CHRE=ABS(REAL(GAMMA-GAMFI))
CHIM=ABS(AIMAG(GAMMA-GAMFI))
OLDRE=ABS(REAL(GAMMA))
OLDIM=ABS(AIMAG(GAMMA))
IF(CHRE.GT.FRACT*OLDRE) GO TO 88
IF(CHIM.LT.FRACT*OLDIM) GO TO 2000
88 GAMMA=GAMFI
3 CONTINUE
WRITE(6,32) F,GAMFI,CHRE,CHIM
32 FORMAT(1X,'FREQ = ',1E10.3,5X,'GAMFI = ',2(E10.3,1X),4X,
1/,1X,'CHRE = ',1E10.3,5X,'CHIM = ',1E10.3)
STOP

```

C  
C REDEFINE PERMEABILITIES FOR REVERSE PROPAGATION-----

```

2000 K1=1.0 + STRAIN*M0/(CHO + W/GYRO)
K2=1.0 + STRAIN*M0/(CHO - W/GYRO)
K3=1.0 + M0/(CHO + W/GYRO)

```

K4=1.0 + M0/(CHO - W/GYRO)

```

C
C INCREMENT NEWTON RAPHSON ON REVERSE UNIMPLANTED GAMMA-----
DO4 IK4=1,200,1
  SINHKV=-J*CSIN(J*GAMRO*TAL203)
  COSHKV=CCOS(J*GAMRO*TAL203)
  E2KU=CEXP(2.0*GAMRO*TYIGIM)
  E2KD=CEXP(2.0*GAMRO*TYIGPU)
  FOFKRO=(K4+1.0)*(K3*COSHKV+SINHKV)*E2KU*E2KD
1  -(K3-1.0)*(K4*COSHKV-SINHKV)
  IF(CABS(FOFKRO).LE.ZERO) GO TO 3000
  GAMRO=CLOG((K3-1.0)*(K4*COSHKV-SINHKV)
1  /((K4+1.0)*(K3*COSHKV+SINHKV)))/(2.0*(TYIGPU+TYIGIM))
  CHRE=ABS(REAL(GAMMA-GAMRO))
  CHIM=ABS(AIMAG(GAMMA-GAMRO))
  OLDRE=ABS(REAL(GAMMA))
  OLDIM=ABS(AIMAG(GAMMA))
  IF(CHRE.GT.FRACT*OLDRE) GO TO 99
  IF(CHIM.LT.FRACT*OLDIM) GO TO 3000
99 GAMMA=GAMRO
4 CONTINUE
  WRITE(6,33) F,GAMRO,CHRE,CHIM
33 FORMAT(1X,'FREQ = ',1E10.3,5X,'GAMRO = ',2(E10.3,1X),4X,
1/,1X,'CHRE = ',1E10.3,5X,'CHIM = ',1E10.3)
  STOP

```

```

C
C INCREMENT NEWTON RAPHSON ON REVERSE IMPLANTED GAMMA-----
3000 DO5 IK5=1,200,1
  SINHKV=-J*CSIN(J*GAMRI*TAL203)
  COSHKV=CCOS(J*GAMRI*TAL203)
  E2KU=CEXP(2.0*GAMRI*TYIGIM)
  E2KD=CEXP(2.0*GAMRI*TYIGPU)
  FOFKRI=(K4+1.0)*((K3-K1)*(K2*COSHKV-SINHKV)
1  +(K2+K3)*(K1*COSHKV+SINHKV)*E2KU)*E2KD
2  -(K3-1.0)*((K1+K4)*(K2*COSHKV-SINHKV)
3  +(K4-K2)*(K1*COSHKV+SINHKV)*E2KU)
  IF(CABS(FOFKRI).LE.ZERO) GO TO 4000
  GAMRI=CLOG((K3-1.0)*((K1+K4)*(K2*COSHKV-SINHKV)
1  +(K4-K2)*(K1*COSHKV+SINHKV)*E2KU)
2  /((K4+1.0)*((K3-K1)*(K2*COSHKV-SINHKV)
3  +(K2+K3)*(K1*COSHKV+SINHKV)*E2KU)))
4  /(2.0*TYIGPU)
  CHRE=ABS(REAL(GAMMA-GAMRI))
  CHIM=ABS(AIMAG(GAMMA-GAMRI))
  OLDRE=ABS(REAL(GAMMA))
  OLDIM=ABS(AIMAG(GAMMA))
  IF(CHRE.GT.FRACT*OLDRE) GO TO 66
  IF(CHIM.LT.FRACT*OLDIM) GO TO 4000
66 GAMMA=GAMRI
5 CONTINUE

```

```

      WRITE(6,34) F,GAMRI,CHRE,CHIM
34  FORMAT(1X,'FREQ = ',1E10.3,5X,'GAMRI = ',2(E10.3,1X),4X,
      1/,1X,'CHRE = ',1E10.3,5X,'CHIM = ',1E10.3)
      STOP
4000 FREQ=F/1.0E+09
C   WRITE(6,101) FREQ,GAMFI,GAMRI,GAMFO,GAMRO
101  FORMAT(1X,1F6.3,4(5X,1F10.1,1X,1F10.1))
      X=ARRAY(FREQ,GAMFI,GAMRI,GAMFO,GAMRO)
      XYZ=20000.0
      IF(X.LE.BOUND) WRITE(23,103) XYZ
103  FORMAT(1X,1F9.1)
      IF(X.LE.BOUND) STOP
      WRITE(23,102) FREQ,X
102  FORMAT(1X,1F6.3,5X,1F10.3)
      IF(W.LT.WSTOP) GO TO 11111
      STOP
      END
      FUNCTION ARRAY(PRSNTF,GF1,GR1,GF2,GR2)
C-----
C   PROGRAM DESCRIPTION:
C
C       THIS PROGRAM CALCULATES THE RESPONSE OF A NORMAL INCIDENCE
C   MSSW ARRAY OF N IDENTICAL BAR/GAP SECTIONS.  THE OUTPUT IS
C   INSERTION LOSS IN DB VERSUS FREQUENCY.
C-----
C
C   COMPLEX GF1, GR1, GF2, GR2, J, ZF1, ZR1,ZF2, ZR2, TZ,
C   1TA, TB, TC, TD, ZW, TAUR, T1, T2, T3, T4, TZR, EIGNDF, EIGNN,
C   2RHOR, V1, V2, V3, V4, Z1, Z2, Z3, Z4, Z5, Z6, Z7, Z8,
C   4EIGN1, EIGN2, EIGNN1
C-----
C   USER DEFINED INPUT:
C-----
C   "WIDTH1" IS THE BAR WIDTH IN (MICRONS)-----
C   WIDTH1=100.0
C
C   "WIDTH2" IS THE GAP WIDTH IN (MICRONS)-----
C   WIDTH2=100.0
C
C   "N" IS THE NUMBER OF BAR/GAP SECTIONS-----
C   N=46
C-----
C
C   PI=3.1415926
C   M=59
C   IF=0

```



```

      ROFANG=0.0
      RORANG=0.0
      J=CMPLX(0.0,1.0)
      UM=PI*4.0E-03

C
C  DETERMINE STRUCTURE LENGTH-----
      GF1=J*GF1/100.0
      GR1=-J*GR1/100.0
      GF2=J*GF2/100.0
      GR2=-J*GR2/100.0
      F=PRSNTF*1000.0
      W=2.0*PI*F*1.0E+06
C  CALCULATE IMPEDANCES-----
C
      ZF1=J*UM*F/GF1
      ZF2=J*UM*F/GF2
      ZR1=J*UM*F/GR1
      ZR2=J*UM*F/GR2
C
C  SET UP TRANSMISSION MATRICES FOR TWO SECTIONS-----
C
      TZ=ZF1-ZR1
      V1=CEXP(GF1*WIDTH1*1.0E-04)
      V2=CEXP(GF2*WIDTH2*1.0E-04)
      V3=CEXP(GR1*WIDTH1*1.0E-04)
      V4=CEXP(GR2*WIDTH2*1.0E-04)
      Z1=(ZF1*V1-ZR1*V3)/TZ
      Z2=(ZF1*ZR1*(V3-V1))/TZ
      Z3=(V1-V3)/TZ
      Z4=(ZF1*V3-ZR1*V1)/TZ
      TZ=ZF2-ZR2
      Z5=(ZF2*V2-ZR2*V4)/TZ
      Z6=(ZF2*ZR2*(V4-V2))/TZ
      Z7=(V2-V4)/TZ
      Z8=(ZF2*V4-ZR2*V2)/TZ
C
C  CASCADE MATRICES TO OBTAIN ONE ARRAY SECTION-----
C
      T1=Z1*Z5+Z2*Z7
      T2=Z1*Z6+Z2*Z8
      T3=Z3*Z5+Z4*Z7
      T4=Z3*Z6+Z4*Z8
C
C  COMPUTATION OF EIGENVALUES OF MATRIX-----
C
      EIGN1=(T1+T4+CSQRT((T1+T4)**2-4.0*(T1*T4-T2*T3)))/2.0
      EIGN2=(T1+T4-CSQRT((T1+T4)**2-4.0*(T1*T4-T2*T3)))/2.0
      EIGNN1=EIGN1**(N+1)-EIGN2**(N+1)
      EIGNN=EIGN1**N-EIGN2**N
      EIGNDF=EIGN1-EIGN2

```

```

C
C  CALCULATION IF EIGENVALUES ARE APPROXIMATELY EQUAL-----
C
      IF(CABS(EIGNDF).GT.1.0E-06*CABS(EIGN1)) GO TO 5
      TA=(N+1)*EIGN1**N-N*T4*EIGN1**(N-1)
      TB=N*T2*EIGN1**(N-1)
      TC=N*T3*EIGN1**(N-1)
      TD=(N+1)*EIGN1**N-N*T1*EIGN1**(N-1)
      GO TO 51
C
C  RAISE MATRIX TO NTH POWER-----
C
      5  TA=(EIGNN1-EIGNN*T4)/EIGNDF
      TB=(EIGNN*T2)/EIGNDF
      TC=(EIGNN*T3)/EIGNDF
      TD=(EIGNN1-EIGNN*T1)/EIGNDF
C
C  INVERT ARRAY AND SPACING MATRICES-----
C
      51 TZR=TA*TD-TB*TC
      V1 =TD/TZR
      V2 =-TB/TZR
      V3 =-TC/TZR
      V4 =TA/TZR
C
C  DETERMINE TRANSMISSION AND REFLECTION COEFFICIENTS-----
C
      ZW=ZR2*V1+V2-ZF2*(V4+ZR2*V3)
      TAUR=(ZR2-ZF2)/ZW
      TAURMG=CABS(TAUR)
      IF(TAURMG.GT.1.0) TAURMG=1.0
      IF(TAURMG.LT.0.1) TAURMG=0.1
      ARRAY=20.0*ALOG10(TAURMG)
      RETURN
      END

```

## C.2 Normal Incidence MSFVW Array Analysis

This program is essentially the same as the one in section C.1, except that the main program calculates the MSFVW dispersion relation from the four layer model for implanted and unimplanted delay sections before calling the array function program written by Brinlee (2.24) that determines the array transmission response. The dispersion calculation includes the Gilbert loss term resulting in a complex propagation constant of the form,

$$\tilde{k} = \beta - j\alpha,$$

based on propagation in the y-direction of the form,

$$\exp\{j(\omega t - \tilde{k}y)\}.$$

This program is self contained and only requires the data indicated in the "User Supplied Input" sections.

```

C .....
C PROGRAM DESCRIPTION:
C   THIS PROGRAM CALCULATES THE LOSSY DISPERSION RELATION FOR
C   A FOUR-LAYER FLIPPED CONFIGURATION GEOMETRY (ALUMINA THICKNESS =
C   TAL203, TOTAL YIG LAYER THICKNESS = TYIG, DEPTH OF IMPLANTED YIG
C   LAYER = TIMP, MO(IMPLANTED YIG)/MO(UNIMPLANTED YIG) = RATIO).
C   THE DISPERSION IS CALCULATED FOR THE IMPLANTED CASE (GAMMAI) AND
C   FOR THE UNIMPLANTED CASE (GAMMAP)--BOTH WITH THE SAME TOTAL YIG
C   THICKNESS.
C .....
C DIMENSION COMPLEX AND REAL VARIABLES*****
C   COMPLEX J,ETAI,ETAP,GAMMAI,GAMMAP,CHO,FOFKI,FOFKP,DFDKI,DFDKP,
C   1SINHKB,COSHB,SINKX,COSKX,XP,DGAMAP,DGAMAI,GAMAPO,GAMAI0,CENTER,
C   2COSKD,SINKD,COSKU,SINKU,D,U,FF1,FF2,FF3,FF4,DFF1,DFF2,DFF3,DFF4
C   REAL MO
C
C SET UP FIXED ASSUNDRY PARAMETERS*****
C   DATA J,GYRO,MO/(0.0,1.0),2.8E+06,1760.0/
C   OPEN(UNIT=23,DEVICE='DSK',DIALOG)
C   LW=5
C
C .....
C USER SUPPLIED INPUT*****
C .....
C CONVERGENCE CRITERION*****
C   ZERO=1.0E-06
C   FRACT=1.0E-05
C   BOUND=-20.0
C
C FREQUENCY SCAN PARAMETERS*****
C   FSTEP=2.0E+06
C   FSTART=2.5E+09
C   FSTOP=3.50E+09
C   FDIV=1.00
C
C GEOMETRY PARAMETERS*****
C   TAL203=250.0E-06
C   TYIG=22.5E-06
C   TIMP=0.40E-06
C
C MATERIAL PARAMETERS*****
C   HO=880.0
C   DHMIN=0.5
C   RATIO=0.9
C   FO=HO*GYRO
C .....
C

```

```

C .....
C .....
C
C INITIALIZE FREQUENCY AND GAMMA-GUESS*****
  F=FSTART-FSTEP
  AP=0.876E+01
  BP=0.910E+03
  AI=AP
  BI=BP
  GAMMAP=CMPLX(BP,-AP)
  GAMMAI=CMPLX(BI,-AI)
  GAMAPO=GAMMAP
  GAMAIO=GAMMAI
  PLQT=FDIV-1.0
C
C START FREQUENCY DO-LOOP*****
  1 F=F+FSTEP
C
C LINEAR EXTRAPOLATION FOR CLOSER INITIAL GUESS*****
  DGAMAP=GAMMAP-GAMAPO
  DGAMAI=GAMMAI-GAMAIO
  GAMAPO=GAMMAP
  GAMAIO=GAMMAI
  GAMMAP=GAMMAP+DGAMAP
  GAMMAI=GAMMAI+DGAMAI
  AP=-AIMAG(GAMMAP)
  BP= REAL(GAMMAP)
  AI=-AIMAG(GAMMAI)
  BI= REAL(GAMMAI)
C
C CALCULATE GILBERT-LOSS AND GAMMA INDEPENDANT PARAMETERS*****
  DELH=DHMIN*(FO/F+F/FO)/2.0
  CHO=CMPLX(HO,DELH/2.0)
  ETAP=CSQRT((GYRO**2)*MO*CHO/(F**2-(GYRO*CHO)**2)-1.0)
  ETAI=CSQRT((GYRO**2)*MO*CHO*RATIO/(F**2-(GYRO*CHO)**2)-1.0)
  XP=ETAP*TYIG
  D=(TYIG-TIMP)*ETAP
  U=TIMP*ETAI
C
C INITIALIZE ORBIT DAMPER*****
  NORBIT=0
  CENTER=0.0
C
C GAMMA DO-LOOP FOR UNIMPALNTED REGION*****
  DO 2 I2=1,1000,1
C
C COMPLEX ROOT "ORBIT" DAMPER*****
  NORBIT=NORBIT+1
  CENTER=CENTER+GAMMAP/50.0
  IF(NORBIT.GE.50) GAMMAP=CENTER

```

```

      IF(NORBIT.GE.50) CENTER=CENTER/50.0
      IF(NORBIT.GE.50) NORBIT=1
C
C  CALCULATE GAMMA DEPENDENT FUNCTIONS USED IN F-OF-K & DF/DK*****
      SINHKV=-J*CSIN(J*GAMMAP*TAL203)
      COSHKV=CCOS(J*GAMMAP*TAL203)
      SINKX=CSIN(GAMMAP*XP)
      COSKX=CCOS(GAMMAP*XP)
C  CALCULATE F(K) AND DF/DK FOR NEWTON RAPHSON*****
      FOFKP=SINKX*((ETAP**2)*COSHKV-SINHKV)-COSKX*ETAP*(COSHKV+SINHKV)
      DFDKP=XP*COSKX*((ETAP**2)*COSHKV-SINHKV)
      1      +TAL203*SINKX*((ETAP**2)*SINHKV-COSHKV)
      2      +XP*ETAP*SINKX*(COSHKV+SINHKV)
      3      -TAL203*ETAP*COSKX*(COSHKV-SINHKV)
C  CALCULATE NEW ALPHA AND BETA BY NEWTON-RAPHSON*****
      UP=REAL(FOFKP)
      VP=AIMAG(FOFKP)
      IF(UP**2+VP**2.LE.ZERO) GO TO 5
      UXP=REAL(DFDKP)
      UYP=-AIMAG(DFDKP)
      DELAP=(VP*UXP+UP*UYP)/(UXP**2+UYP**2)
      DELBP=(VP*UYP-UP*UXP)/(UXP**2+UYP**2)
      AP=AP+DELAP
      BP=BP+DELBP
      GAMMAP=CMPLX(BP,-AP)
      IF(ABS(DELAP).GT.ABS(AP)*FRACT) GO TO 2
      IF(ABS(DELBP).LE.ABS(BP)*FRACT) GO TO 5
      2  CONTINUE
      WRITE(LW,31) F,GAMMAP,FOFKP,DFDKP
      31  FORMAT(1X,70(' '),//,1X,'DID NOT CONVERGE IN DO LOOP 2-CONTINUE:',
      1//,1X,'F',6X,'=',1X,1E10.3,/,1X,'GAMMAP',1X,'=',1X,2(1E10.3,5X),
      2/,1X,'FOFKP',2X,'=',1X,2(1E10.3,5X),/,1X,'DFDKP',2X,'=',1X,
      32(1E10.3,5X),//,1X,70(' '),//)
      STOP
C
C  INITIALIZE ORBIT DAMPER*****
      5  NORBIT=0
      CENTER=0.0
C
C  GAMMA DO-LOOP FOR IMPLANTED SECTION*****
      DO 8 I8=1,1000,1
C
C  COMPLEX ROOT "ORBIT" DAMPER*****
      NORBIT=NORBIT+1
      CENTER=CENTER+GAMMAI/50.0
      IF(NORBIT.GE.50) GAMMAI=CENTER
      IF(NORBIT.GE.50) CENTER=CENTER/50.0
      IF(NORBIT.GE.50) NORBIT=1
C
C  CALCULATE GAMMA DEPENDENT FUNCTIONS USED IN F(K) AND DF/DK*****

```

```

SINHKB=-J*CSIN(J*GAMMAI*TAL203)
COSHKB=CCOS(J*GAMMAI*TAL203)
COSKD=CCOS(GAMMAI*D)
SINKD=CSIN(GAMMAI*D)
COSKU=CCOS(GAMMAI*U)
SINKU=CSIN(GAMMAI*U)
C CALCULATE F(K) AND DF/DK FOR NEWTON RAPHSON*****
FF1=(ETAP*SINKD-COSKD)*ETAP
FF2=SINHKB*SINKU+ETAI*COSKU*COSHKB
FF3=ETAI*(SINKD+ETAP*COSKD)
FF4=SINHKB*COSKU-ETAI*SINKU*COSHKB
DFF1=D*ETAP*(ETAP*COSKD+SINKD)
DFF2=TAL203*(COSHKB*SINKU+ETAI*COSKU*SINHKB)+U*(SINHKB*COSKU
1-ETAI*SINKU*COSHKB)
DFF3=ETAI*D*(COSKD-ETAP*SINKD)
DFF4=TAL203*(COSHKB*COSKU-ETAI*SINKU*SINHKB)
1-U*(SINHKB*SINKU+ETAI*COSKU*COSHKB)
FOFKI=FF1*FF2-FF3*FF4
DFDKI=DFF1*FF2+FF1*DFF2-DFF3*FF4-FF3*DFF4
C CALCULATE NEW ALPHA AND NEW BETA BY NEWTON-RAPHSON*****
UI=REAL(FOFKI)
VI=AIMAG(FOFKI)
IF(UI**2+VI**2.LE.ZERO) GO TO 9
UXI=REAL(DFDKI)
UYI=-AIMAG(DFDKI)
DELAI=(VI*UXI+UI*UYI)/(UXI**2+UYI**2)
DELBI=(VI*UYI-UI*UXI)/(UXI**2+UYI**2)
AI=AI+DELAI
BI=BI+DELBI
GAMMAI=CMPLX(BI,-AI)
IF(ABS(DELAI).GT.ABS(AI)*FRACT) GO TO 8
IF(ABS(DELBI).LE.ABS(BI)*FRACT) GO TO 9
8 CONTINUE
WRITE(LW,32) F,GAMMAI,FOFKI,DFDKI
32 FORMAT(1X,70(' '),//,1X,'DID NOT CONVERGE IN DO LOOP 8-CONTINUE:',
1//,1X,'F',6X,'=',1E10.3,/,1X,'GAMMAI',1X,'=',1X,2(1E10.3,5X),
2//,1X,'FOFKI',2X,'=',1X,2(1E10.3,5X),/,1X,'DFDKI',2X,'=',1X,
32(1E10.3,5X),//,1X,70(' '),//)
STOP
C
C WRITE OUT DATA ON PAPER AND ON A FILE CALLED 'GAMMA'*****
9 FREQ=F/1.0E+09
Q2=REAL(GAMMAI)
Q3=AIMAG(GAMMAI)
Q4=REAL(GAMMAI)
Q5=AIMAG(GAMMAI)
C WRITE(LW,778) FREQ,Q2,Q3,Q4,Q5
C 778 FORMAT(2X,1F7.4,6X,4(1E10.3,5X))
X=ARRAY(FREQ,GAMMAI,GAMMAI,GAMMAI,GAMMAI)
IF(X.LT.BOUND) GO TO 707

```

```

      WRITE(23,102) FREQ, X
102  FORMAT(1X,1F6.3,5X,1F10.3)
      IF(F.LT.FSTOP) GO TO 1
707  XYZ=20000.0
      WRITE(23,708) XYZ
708  FORMAT(1X,1F8.1)
      STOP
      END
      FUNCTION ARRAY(PRSNTF,GF11,GR11,GF22,GR22)
C-----
C  PROGRAM DESCRIPTION:
C
C      THIS PROGRAM CALCULATES THE RESPONSE OF A NORMAL INCIDENCE
C  MSSW ARRAY OF N IDENTICAL BAR/GAP SECTIONS.  THE OUTPUT IS
C  INSERTION LOSS IN DB VERSUS FREQUENCY.
C-----
C
C      COMPLEX GF1, GR1, GF2, GR2, J, ZF1, ZR1,ZF2, ZR2, TZ,
C      1TA, TB, TC, TD, ZW, TAUR, T1, T2, T3, T4, TZR, EIGNDF, EIGNN,
C      2RHOR, V1, V2, V3, V4, Z1, Z2, Z3, Z4, Z5, Z6, Z7, Z8,
C      4EIGN1, EIGN2, EIGNN1,GF11,GR11,GF22,GR22
C-----
C  USER DEFINED INPUT:
C-----
C
C  "WIDTH1" IS THE BAR WIDTH IN (MICRONS)-----
C      WIDTH1=100.0
C
C  "WIDTH2" IS THE GAP WIDTH IN (MICRONS)-----
C      WIDTH2=100.0
C
C  "N" IS THE NUMBER OF BAR/GAP SECTIONS-----
C      N=46
C-----
C
C      PI=3.1415926
C      M=59
C      IF=0
C      ROFANG=0.0
C      RORANG=0.0
C      J=CMPLX(0.0,1.0)
C      UM=PI*4.0E-03
C
C  DETERMINE STRUCTURE LENGTH-----
C      GF1=J*GF11/100.0
C      GR1=-J*GR11/100.0
C      GF2=J*GF22/100.0

```



```

GR2=-J*GR22/100.0
F=PRSNIF*1000.0
W=2.0*PI*F*1.0E+06
C CALCULATE IMPEDANCES-----
C
ZF1=J*UM*F/GF1
ZF2=J*UM*F/GF2
ZR1=J*UM*F/GR1
ZR2=J*UM*F/GR2
C
C SET UP TRANSMISSION MATRICES FOR TWO SECTIONS-----
C
TZ=ZF1-ZR1
V1=CEXP(GF1*WIDTH1*1.0E-04)
V2=CEXP(GF2*WIDTH2*1.0E-04)
V3=CEXP(GR1*WIDTH1*1.0E-04)
V4=CEXP(GR2*WIDTH2*1.0E-04)
Z1=(ZF1*V1-ZR1*V3)/TZ
Z2=(ZF1*ZR1*(V3-V1))/TZ
Z3=(V1-V3)/TZ
Z4=(ZF1*V3-ZR1*V1)/TZ
TZ=ZF2-ZR2
Z5=(ZF2*V2-ZR2*V4)/TZ
Z6=(ZF2*ZR2*(V4-V2))/TZ
Z7=(V2-V4)/TZ
Z8=(ZF2*V4-ZR2*V2)/TZ
C
C CASCADE MATRICES TO OBTAIN ONE ARRAY SECTION-----
C
T1=Z1*Z5+Z2*Z7
T2=Z1*Z6+Z2*Z8
T3=Z3*Z5+Z4*Z7
T4=Z3*Z6+Z4*Z8
C
C COMPUTATION OF EIGENVALUES OF MATRIX-----
C
EIGN1=(T1+T4+CSQRT((T1+T4)**2-4.0*(T1*T4-T2*T3)))/2.0
EIGN2=(T1+T4-CSQRT((T1+T4)**2-4.0*(T1*T4-T2*T3)))/2.0
EIGNN1=EIGN1**(N+1)-EIGN2**(N+1)
EIGNN=EIGN1**N-EIGN2**N
EIGNDF=EIGN1-EIGN2
C
C CALCULATION IF EIGENVALUES ARE APPROXIMATELY EQUAL-----
C
IF(CABS(EIGNDF).GT.1.0E-06*CABS(EIGN1)) GO TO 5
TA=(N+1)*EIGN1**N-N*T4*EIGN1**(N-1)
TB=N*T2*EIGN1**(N-1)
TC=N*T3*EIGN1**(N-1)
TD=(N+1)*EIGN1**N-N*T1*EIGN1**(N-1)
GO TO 51

```

```

C
C RAISE MATRIX TO NTH POWER-----
C
  5 TA=(EIGNN1-EIGNN*T4)/EIGNDF
    TB=(EIGNN*T2)/EIGNDF
    TC=(EIGNN*T3)/EIGNDF
    TD=(EIGNN1-EIGNN*T1)/EIGNDF
C
C INVERT ARRAY AND SPACING MATRICES-----
C
  51 TZR=TA*TD-TB*TC
    V1 =TD/TZR
    V2 =-TB/TZR
    V3 =-TC/TZR
    V4 =TA/TZR
C
C DETERMINE TRANSMISSION AND REFLECTION COEFFICIENTS-----
C
    ZW=ZR2*V1+V2-ZF2*(V4+ZR2*V3)
    TAUR=(ZR2-ZF2)/ZW
    TAURMG=CABS(TAUR)
    IF(TAURMG.GT.1.0) TAURMG=1.0
    IF(TAURMG.LT.0.1) TAURMG=0.1
    ARRAY=20.0*ALOG10(TAURMG)
    RETURN
  END

```

e

### C.3 Oblique Incidence MSFVW Array Synthesis

Analysis and synthesis of the oblique incidence MSFVW arrays was done by three interacting programs that perform the following functions,

- (1) NEWTRY: Calculate the complex dispersion relation using the Gilbert loss model and the four layer structure for both implanted and unimplanted delay line sections. The form of the resultant dispersion relation is,

$$\tilde{k} = \beta - j\alpha$$

where,  $\alpha$  is the loss factor in Nepers/Meter and  $\beta$  is the wave number in Radians/Meter.

- (2) XDUCER: Calculate the frequency response contribution due to coupling of the microstrip transducers assuming a lossless ferrite (taken directly from Wu (2.1)).
- (3) DESIGNER: Synthesize the array using information from NEWTRY and XDUCER with the impulse model, and then analyze the design.

```

//NEWTRY   JOB B515-KWR,'KIM REED'
/*BOX      8546
/*TIME 2M
/*LINES 3K
//          EXEC FORNCX
C
C *****
C PROGRAM DESCRIPTION:
C   THIS PROGRAM CALCULATES THE LOSSY DISPERSION RELATION FOR
C   A FOUR-LAYER FLIPPED CONFIGURATION GEOMETRY (ALUMINA THICKNESS =
C   TAL203, TOTAL YIG LAYER THICKNESS = TYIG, DEPTH OF IMPLANTED YIG
C   LAYER = TIMP, MO(IMPLANTED YIG)/MO(UNIMPLANTED YIG) = RATIO).
C   THE DISPERSION IS CALCULATED FOR THE IMPLANTED CASE (GAMMAI) AND
C   FOR THE UNIMPLANTED CASE (GAMMAP)--BOTH WITH THE SAME TOTAL YIG
C   THICKNESS.
C *****
C
C DIMENSION COMPLEX AND REAL VARIABLES*****
C   COMPLEX J,ETAI,ETAP,GAMMAI,GAMMAP,CHO,FOFKI,FOFKP,DFDKI,DFDKP,
C   1SINHKB,COSHB,SINKX,COSKX,XP,DGAMAP,DGAMAI,GAMAP0,GAMAI0,CENTER,
C   2COSKD,SINKD,COSKU,SINKU,D,U,FF1,FF2,FF3,FF4,DFF1,DFF2,DFF3,DFF4
C   REAL MO
C
C SET UP FIXED ASSUNDRY PARAMETERS*****
C   DATA J,GYRO,MO/(0.0,1.0),2.8E+06,1760.0/
C   LR=5
C   LW=6
C   HEAD=0.0
C
C *****
C USER SUPPLIED INPUT*****
C *****
C
C CONVERGENCE CRITERION*****
C   ZERO=1.0E-06
C   FRACT=1.0E-05
C
C FREQUENCY SCAN PARAMETERS*****
C   FSTEP=1.0E+06
C   FSTART=2.5E+09
C   FSTOP=4.00E+09
C   FDIV=1.00
C
C GEOMETRY PARAMETERS*****
C   TAL203=250.0E-06
C   TYIG=25.0E-06
C   TIMP=0.40E-06
C
C MATERIAL PARAMETERS*****
C   HO=880.0
C
?
```

```

DHMIN=0.5
RATIO=0.5
FO=3.0E+09

```

```

C
C .....
C .....
C .....
C .....
C
C WRITE OUT ALL THE PERTINENT PARAMETERS FOR THIS RUN*****
  Q1=GYRO/1.0E+06
  Q2=FO/1.0E+09
  Q3=TYIG*1.0E+06
  Q4=TIMP*1.0E+06
  Q5=TAL203*1.0E+06
  Q6=FSTART/1.0E+09
  Q7=FSTOP/1.0E+09
  Q8=FSTEP/1.0E+06
  Q9=(FSTOP-FSTART)/FSTEP-3.0
  WRITE(1,777) Q6,Q7,Q8,Q9,H0
  WRITE(1,777) RATIO,TYIG,TIMP,TAL203,DHMIN
  WRITE(LW,102) Q1,M0,RATIO,DHMIN,Q2,Q3,Q4,Q5,Q6,
  1Q7,H0,Q8
102 FORMAT(1H1,44(' '),/,1X,'* MSFVW-PURE/IMPLANTED DISPERSION',
  1' SOLUTION ',/,1X,10(' '),* FLIPPED CONFIGURATION ',11(' '),/,1X,
  244(' '),/,1X,'* MATERIAL CONSTANTS:',/,2X,'GYROMAGNETIC RATIO',
  35X,'=',4X,1F5.2,' MHZ/OE',/,2X,'UNIMPLANTED M0',9X,'=',1X,1F8.2,
  41X,'OE',/,2X,'M0(IMP)/M0(PURE)',7X,'=',4X,1F5.2,/,/,
  51X,'* GILBERT-LOSS PARAMETERS:',/,2X,'DELTA-H',
  6' MIN',12X,'=',4X,1F5.2,1X,'OE',/,2X,'FO',21X,'=',4X,1F5.2,1X,
  7'GHZ',/,/,1X,'* GEOMETRY PARAMETERS:',/,2X,'YIG THICKNESS',10X,
  8'=',3X,1F6.2,1X,'MICRONS',/,2X,'IMPLANT DEPTH',10X,'=',4X,1F5.2,
  91X,'MICRONS',/,2X,'SUBSTRATE THICKNESS',4X,'=',2X,1F7.2,1X,
  1'MICRONS',/,/,1X,'* FREQUENCY PARAMETERS:',/,2X,'START FREQUENCY',
  28X,'=',4X,1F5.2,1X,'GHZ',/,2X,'STOP FREQUENCY',9X,'=',4X,1F5.2,
  31X,'GHZ',/,2X,'H0',21X,'=',2X,1F7.2,1X,'OE',/,2X,'FREQUENCY',
  4' STEP-SIZE',4X,'=',4X,1F5.2,1X,'MHZ',/,1X,44(' '),/,1H1,
  5'FREQUENCY',5X,'BETA(UNIMP)',3X,'-ALPHA(UNIMP)',3X,'BETA(IMPLT)',
  63X,
  7'-ALPHA(IMPLT)',/,3X,'(GHZ)',7X,'(RAD/METER)',4X,'(RAD/METER)',4X,
  8'(RAD/METER)',4X,'(RAD/METER)',/,)
C
C INITIALIZE FREQUENCY AND GAMMA-GUESS*****
  F=FSTART-FSTEP
  AP=0.876E+01
  BP=0.910E+03
  AI=AP
  BI=BP
  GAMMAP=CMPLX(BP,-AP)
  GAMMAI=CMPLX(BI,-AI)
  GAMAPO=GAMMAP
?
```

```

      GAMAIO=GAMMAI
      PLOT=FDIV-1.0
C
C  START FREQUENCY DO-LOOP*****
C  1 F=F+FSTEP
C
C  LINEAR EXTRAPOLATION FOR CLOSER INITIAL GUESS*****
      DGAMAP=GAMMAP-GAMMAPO
      DGAMAI=GAMMAI-GAMAIO
      GAMMAPO=GAMMAP
      GAMAIO=GAMMAI
      GAMMAP=GAMMAP+DGAMAP
      GAMMAI=GAMMAI+DGAMAI
      AP=-AIMAG(GAMMAP)
      BP= REAL(GAMMAP)
      AI=-AIMAG(GAMMAI)
      BI= REAL(GAMMAI)
C
C  CALCULATE GILBERT-LOSS AND GAMMA INDEPENDANT PARAMETERS*****
      DELH=DHMIN*(FO/F+F/FO)/2.0
      CHO=CMPLX(HO,DELH/2.0)
      ETAP=CSQRT((GYRO**2)*MO*CHO/(F**2-(GYRO*CHO)**2)-1.0)
      ETAI=CSQRT((GYRO**2)*MO*CHO*RATIO/(F**2-(GYRO*CHO)**2)-1.0)
      XP=ETAP*TYIG
      D=(TYIG-TIMP)*ETAP
      U=TIMP*ETAI
C
C  INITIALIZE ORBIT DAMPER*****
      NORBIT=0
      CENTER=0.0
C
C  GAMMA DO-LOOP FOR UNIMPALNTED REGION*****
      DO 2 I2=1,1000,1
C
C  COMPLEX ROOT "ORBIT" DAMPER*****
      NORBIT=NORBIT+1
      CENTER=CENTER+GAMMAP/50.0
      IF(NORBIT.GE.50) GAMMAP=CENTER
      IF(NORBIT.GE.50) CENTER=CENTER/50.0
      IF(NORBIT.GE.50) NORBIT=1
C
C  CALCULATE GAMMA DEPENDENT FUNCTIONS USED IN F-OF-K & DF/DK*****
      SINHKV=-J*CSIN(J*GAMMAP*TAL203)
      COSHKV=CCOS(J*GAMMAP*TAL203)
      SINKX=CSIN(GAMMAP*XP)
      COSKX=CCOS(GAMMAP*XP)
C  CALCULATE F(K) AND DF/DK FOR NEWTON RAPHSO*****
      FOFKP=SINKX*((ETAP**2)*COSHKV-SINHKV)-COSKX*ETAP*(COSHKV+SINHKV)
      DFDKP=XP*COSKX*((ETAP**2)*COSHKV-SINHKV)
      1 +TAL203*SINKX*((ETAP**2)*SINHKV-COSHKV)
?
```

```

      2      +XP*ETAP*SINKX*(COSHKV+SINHKV)
      3      -TAL203*ETAP*COSKX*(COSHKV+SINHKV)
C  CALCULATE NEW ALPHA AND BETA BY NEWTON-RAPHSON*****
      UP=REAL(FOFKP)
      VP=AIMAG(FOFKP)
      IF(UP**2+VP**2.LE.ZERO) GO TO 5
      UXP=REAL(DFDKP)
      UYP=-AIMAG(DFDKP)
      DELAP=(VP*UXP+UP*UYP)/(UXP**2+UYP**2)
      DELBP=(VP*UYP-UP*UXP)/(UXP**2+UYP**2)
      AP=AP+DELAP
      BP=BP+DELBP
      GAMMAP=CMPLX(BP,-AP)
      IF(ABS(DELAP).GT.ABS(AP)*FRACT) GO TO 2
      IF(ABS(DELBP).LE.ABS(BP)*FRACT) GO TO 5
      2 CONTINUE
      WRITE(LW,31) F,GAMMAP,FOFKP,DFDKP
      31 FORMAT(1X,70(' '),//,1X,'DID NOT CONVERGE IN DO LOOP 2-CONTINUE:',
      1//,1X,'F',6X,'=',1X,1E10.3,/,1X,'GAMMAP',1X,'=',1X,2(1E10.3,5X),
      2//,1X,'FOFKP',2X,'=',1X,2(1E10.3,5X),/,1X,'DFDKP',2X,'=',1X,
      32(1E10.3,5X),//,1X,70(' '),//)
      STOP

C
C  INITIALIZE ORBIT DAMPER*****
      5 NORBIT=0
      CENTER=0.0

C
C  GAMMA DO-LOOP FOR IMPLANTED SECTION*****
      DO 8 I8=1,1000,1

C
C  COMPLEX ROOT "ORBIT" DAMPER*****
      NORBIT=NORBIT+1
      CENTER=CENTER+GAMMAI/50.0
      IF(NORBIT.GE.50) GAMMAI=CENTER
      IF(NORBIT.GE.50) CENTER=CENTER/50.0
      IF(NORBIT.GE.50) NORBIT=1

C
C  CALCULATE GAMMA DEPENDENT FUNCTIONS USED IN F(K) AND DF/DK*****
      SINHKV=-J*CSIN(J*GAMMAI*TAL203)
      COSHKV=CCOS(J*GAMMAI*TAL203)
      COSKD=CCOS(GAMMAI*D)
      SINKD=CSIN(GAMMAI*D)
      COSKU=CCOS(GAMMAI*U)
      SINKU=CSIN(GAMMAI*U)

C  CALCULATE F(K) AND DF/DK FOR NEWTON RAPHSON*****
      FF1=(ETAP*SINKD-COSKD)*ETAP
      FF2=SINHKV*SINKU+ETAI*COSKU*COSHKV
      FF3=ETAI*(SINKD+ETAP*COSKD)
      FF4=SINHKV*COSKU-ETAI*SINKU*COSHKV
      DFF1=D*ETAP*(ETAP*COSKD+SINKD)

```

```

      DFF2=TAL203*(COSHKV*SINKU+ETAI*OSKU*SINHVK)+U*(SINHVK*OSKU
1-ETAI*SINKU*COSHKV)
      DFF3=ETAI*D*(COSKD-ETAP*SINKD)
      DFF4=TAL203*(COSHKV*OSKU-ETAI*SINKU*SINHVK)
1-U*(SINHVK*SINKU+ETAI*OSKU*COSHKV)
      FOFKI=FF1*FF2-FF3*FF4
      DFDKI=DFF1*FF2+FF1*DFF2-DFF3*FF4-FF3*DFF4
C  CALCULATE NEW ALPHA AND NEW BETA BY NEWTON-RAPHSON*****
      UI=REAL(FOFKI)
      VI=AIMAG(FOFKI)
      IF(UI**2+VI**2.LE.ZERO) GO TO 9
      UXI=REAL(DFDKI)
      UYI=-AIMAG(DFDKI)
      DELAI=(VI*UXI+UI*UYI)/(UXI**2+UYI**2)
      DELBI=(VI*UYI-UI*UXI)/(UXI**2+UYI**2)
      AI=AI+DELA
      BI=BI+DELB
      GAMMAI=CMPLX(BI,-AI)
      IF(ABS(DELA).GT.ABS(AI)*FRACT) GO TO 8
      IF(ABS(DELB).LE.ABS(BI)*FRACT) GO TO 9
      8 CONTINUE
      WRITE(LW,32) F,GAMMAI,FOFKI,DFDKI
32  FORMAT(1X,70(' '),//,1X,'DID NOT CONVERGE IN DO LOOP 8-CONTINUE:',
1//,1X,'F',6X,'=',1E10.3,/,1X,'GAMMAI',1X,'=',1X,2(1E10.3,5X),
2//,1X,'FOFKI',2X,'=',1X,2(1E10.3,5X),/,1X,'DFDKI',2X,'=',1X,
32(1E10.3,5X),//,1X,70(' '),//)
      STOP
C
C  WRITE OUT DATA ON PAPER AND ON A FILE CALLED 'GAMMA'*****
9  Q1=F/1.0E+09
      Q2=REAL(GAMMA)
      Q3=AIMAG(GAMMA)
      Q4=REAL(GAMMAI)
      Q5=AIMAG(GAMMAI)
      PLOT=PLOT+1.0
      IF(PLOT.EQ.FDIV) WRITE(1,777) Q1,Q2,Q3,Q4,Q5
      IF(PLOT.EQ.FDIV) PLOT=0.0
777  FORMAT(1F7.4,4E15.8)
      HEAD=HEAD+1.0
      IF(HEAD.EQ.59.0) WRITE(LW,779)
      IF(HEAD.EQ.59.0) HEAD=1.0
779  FORMAT(1X,'FREQUENCY',5X,'BETA(UNIMP)',3X,'-ALPHA(UNIMP)',3X,
1'BETA(IMPLT)',3X,'-ALPHA(IMPLT)',/,3X,'(GHZ)',7X,'(RAD/METER)',
24X,'(RAD/METER)',4X,'(RAD/METER)',4X,'(RAD/METER)',/)
      WRITE(LW,778) Q1,Q2,Q3,Q4,Q5
778  FORMAT(2X,1F7.4,6X,4(1E10.3,5X))
      IF(F.LT.FSTOP) GO TO 1
      STOP
      END
//X.FT01F001 DD DSN=B515.KWR.GAMMA20,
?
```



```
// DISP=(OLD,CATLG),UNIT=DISKA,  
// DCB=(LRECL=67,RECFM=FB,BLKSIZE=3350),  
// SPACE=(TRK,(10,10),RLSE)  
//X.SYSIN DD *  
//  
?
```

```
//XDUCER      JOB B515-KWR,'KIM REED'
/*BOX         8546
/*LINES       2K
/*TIME        2M
//           EXEC FORNCX,LPARM='SIZE=500K',XREGION=500K
```

```
C
C PROGRAM DESCRIPTION: *****
```

```
C
C THIS PROGRAM IS A COMPOSITE OF HENRY'S DISP, RAD, AND RESP
C PROGRAMS. IT GIVES A STRAIGHT FLIPPED CONFIGURATION MSFVW DELAY
C LINE RESPONSE WITH DIFFERENT INPUT AND OUTPUT TRANSDUCERS AND
C CREATES A FILE "CNVLOS" THAT IS USED IN PROGRAM "DESIGNER" TO
C SYNTHESIZE ION IMPLANTED OBLIQUE INCIDENCE FILTERS.
```

```
C
C NOTE: WHEN USED FOR "DESIGNER" THE VARIABLE
C "PATH" SHOULD BE SET TO ZERO.
```

```
C *****
```

```
C CHARACTER*4 PARA1,PARA2,AMEAN1,AMEAN2,PIE1,PIE2,ACON11,ACON12,
1ACON01,ACON02
REAL*8 FQ,PR,QF,QR,RMX,RMX1,TMD,XX,DO,TO,HI,BO,SO,TU,
1RLGH
COMMON FQ(152),PR(152,10),QF(305),QR(305,10),RMX(152),
1RMX1(152),TMD(152),XX(152),DO,TO,HI,BO,SO,TU
COMMON/KIM2/ JCONF,NMAX
COMMON/KIM3/ DELH,PATH,FSTART,DELF
COMMON/KIM4/ NMNM
COMMON/KIM5/ RLGH
DATA PARA1,PARA2,AMEAN1,AMEAN2,PIE1,PIE2/'PARA','LLEL',' MEA',
1'NDER',' P','I ' /
```

```
C *****
C USER SUPPLIED INPUT*****
C *****
```

```
C "HI" IS THE BIAS FIELD (OE)*****
HI=892.857
```

```
C "TU" IS THE YIG/TRANSDUCER AIR GAP (METERS)*****
TU=15.0E-06
```

```
C "PATH" IS THE DELAY PATHLENGTH (CM)*****
PATH=0.0
```

```
C "APATRI" IS THE INPUT TRANSDUCER APERTURE (METERS)*****
```

```
C "APATRO" IS THE OUTPUT TRANSDUCER APERTURE (METERS)*****
APATRI=3.0E-03
APATRO=19.0E-03
```

```
C
?
```

```

C "BI" IS THE INPUT TRANSDUCER FILIMENT WIDTH (METERS)*****
C "BO" IS THE OUTPUT TRANSDUCER FILIMENT WIDTH (METERS)*****
  BI=50.0E-06
  BO=50.0E-06
C
C "WI" IS SPACING BETWEEN INPUT FILIMENT CENTERS (METERS)***
C "WO" IS SPACING BETWEEN OUTPUT FILIMENT CENTERS (METERS)**
  WI=100.0E-06
  WO=100.0E-06
C
C "JCONF=" 1-SINGLE BAR, 2-PARALLEL ODD BARS, 3-PARALLEL****
C EVEN BARS, 4-MEANDER, 5-PI 0.5 CENTER SPACING, 6-PI 1.5****
C CENTER SPACING*****
  JCONFI=4
  JCONFO=1
C
C "NMAXI" IS THE STRIPE NUMBER IN THE INPUT TRANSDUCER*****
C "NMAXO" IS THE STRIPE NUMBER IN THE OUTPUT TRANSDUCER*****
  NMAXI=2
  NMAXO=1
C
C *****
C *****
C *****
C
  READ(1,111) FBEGIN,FEND,FSTEP,QNDAT,HO
  READ(1,111) FUDGE,DO,TIMP,TO,DELH
111 FORMAT(1F7.4,4E15.8)
  ACONI1=PARA1
  ACONI2=PARA2
  ACONO1=PARA1
  ACONO2=PARA2
  IF(JCONFI.GT.3) ACONI1=AMEAN1
  IF(JCONFI.GT.3) ACONI2=AMEAN2
  IF(JCONFO.GT.3) ACONO1=AMEAN1
  IF(JCONFO.GT.3) ACONO2=AMEAN2
  IF(JCONFI.GT.4) ACONI1=PIE1
  IF(JCONFI.GT.4) ACONI2=PIE2
  IF(JCONFO.GT.4) ACONO1=PIE1
  IF(JCONFO.GT.4) ACONO2=PIE2
  QI1=TU*1.0E+06
  QO1=TU*1.0E+06
  QI2=APATRI*1.0E+03
  QO2=APATRO*1.0E+03
  QI3=BI*1.0E+06
  QO3=BO*1.0E+06
  QI4=WI*1.0E+06
  QO4=WO*1.0E+06
333 FORMAT(//,1X,44(' '),/,1X,10(' '), ' TRANSDUCER INFORMATION ',
  110(' '),/,1X,44(' '),//,22X,' INPUT',10X,' OUTPUT',//,1X,

```

```

2'TRANSDUCER',9X,2A4,8X,2A4,/,1X,'CONFIGURATION',/,1X,
3'NUMBER OF',14X,1I3,13X,1I3,/,1X,'STRIPES',/,1X,
4'YIG/TRANSDUCER',6X,1F6.1,10X,1F6.1,/,1X,'AIR GAP (UM)',/,1X,
5'SIGNAL',14X,1F6.1,10X,1F6.1,/,1X,'APERTURE (MM)',/,1X,
6'FILAMENT',12X,1F6.1,10X,1F6.1,/,1X,'WIDTH (UM)',/,1X,
7'FILAMENT CTR',8X,1F6.1,10X,1F6.1,/,1X,'SPACING (UM)',/,1X,
8'INPUT-OUTPUT',8X,1F6.1,10X,1F6.1,/,1X,'PATH (CM)',/,1X,
944(' '))
QGYRO=2.8
QMO=1760.0
QFO=H0*QGYRO/1.0E+03
QTYIG=D0*1.0E+06
QTIMP=TIMP*1.0E+06
QAL203=T0*1.0E+06
WRITE(6,102) QGYRO,QMO,FUDGE,DELH,QFO,QTYIG,QTIMP,QAL203,FBEGIN,
1FEND,H0,FSTEP
WRITE(6,333) ACONI1,ACONI2,ACONO1,ACONO2,NMAXI,NMAXO,QI1,QO1,
1QI2,QO2,QI3,QO3,QI4,QO4,PATH
102 FORMAT(1H1,44(' '),/,1X,'* MSFVW-PURE/IMPLANTED DISPERSION',
1' SOLUTION ',/,1X,10(' '), ' FLIPPED CONFIGURATION ',11(' '),/,1X,
244(' '),/,1X,'*MATERIAL CONSTANTS:',/,2X,'GYROMAGNETIC RATIO',
35X,'=',4X,1F5.2,' MHZ/OE',/,2X,'UNIMPLANTED MO',9X,'=',1X,1F8.2,
41X,'OE',/,2X,'MO(IMP)/MO(PURE)',7X,'=',4X,1F5.2,/,/,
51X,'*GILBERT-LOSS PARAMETERS:',/,2X,'DELTA-H',
6' MIN',12X,'=',4X,1F5.2,1X,'OE',/,2X,'FO',21X,'=',4X,1F5.2,1X,
7'GHZ',/,/,1X,'*GEOMETRY PARAMETERS:',/,2X,'YIG THICKNESS',10X,
8'=',3X,1F6.2,1X,'MICRONS',/,2X,'IMPLANT DEPTH',10X,'=',4X,1F5.2,
91X,'MICRONS',/,2X,'SUBSTRATE THICKNESS',4X,'=',2X,1F7.2,1X,
1'MICRONS',/,/,1X,'*FREQUENCY PARAMETERS:',/,2X,'START FREQUENCY',
28X,'=',4X,1F5.2,1X,'GHZ',/,2X,'STOP FREQUENCY',9X,'=',4X,1F5.2,
31X,'GHZ',/,2X,'H0',21X,'=',2X,1F7.2,1X,'OE',/,2X,'FREQUENCY',
4' STEP-SIZE',4X,'=',4X,1F5.2,1X,'MHZ',/,1X,44(' '),/)
CONFI=JCONFI
CONFO=JCONFO
QMAXI=NMAXI
QMAXO=NMAXO
FSTART=FBEGIN
DELF=(FEND-FBEGIN)/200.0
WRITE(2,222) TU,TU
WRITE(2,222) APATRI,APATRO
WRITE(2,222) BI,BO
WRITE(2,222) WI,WO
WRITE(2,222) CONFI,CONFO
WRITE(2,222) QMAXI,QMAXO
222 FORMAT(2E11.4)
C CALL HENRYS PROGRAMS*****
SO=2.0*WI
BO=BI
RLGH=APATRI
JCONF=JCONFI

```

?

```

NMAX=NMAXI
NMNM=0
CALL DISP
CALL RAD
CALL RESP
SO=2.0*WO
BO=BO
RLGH=APATRO
JCONF=JCONFO
NMAX=NMAXO
CALL DISP
CALL RAD
CALL RESP
STOP
END
SUBROUTINE DISP
C MSFVW DISPERSION RELATION CALCULATES 152 W-K POINTS AND 305 W-K
C POINTS FOR HILBERT TRANSFORM INTEGRATION
C BOTH GEOMETRIES A/B, 10 MODES
C DIMENSION FN(10),RR(10),R(10),BL(10),B1(10)
REAL*8 DO,TO,T,HI,OMGH,FRQ1,FRQ2,DELTA,FRQ,F,OMGA,U1,ET1,BL,B1,AL,A
11,DL,D1,EL,E1,TDL,TD1,FDL,FD1,X,EX,TX,FX,B,G,C,DF,R,RR,PR,R1,V,S,T
,MD,QF,QR,FRQ3,FRQ4,RMX,RMX1,XX,FQ,BO,SO,TU
REAL*8 DSQRT,DSIN,DCOS,DTANH,DABS
COMMON FQ(152),PR(152,10),QF(305),QR(305,10),RMX(152),
1RMX1(152),TMD(152),XX(152),DO,TO,HI,BO,SO,TU
COMMON/KIM4/ NMNM
T=TO/DO
OMGH=HI/1750.0
FRQ3=OMGH*4.9E9
FRQ4=DSQRT(OMGH*(OMGH+1.))*4.9E9
FRQ1=2.54E9
FRQ2=4.26E9
C FREQUENCY SAMPLING 305 POINTS FOR HILBERT TRANSFORM
QF(1)=FRQ3
QF(3)=FRQ1
QF(2)=0.5*(FRQ3+FRQ1)
QF(103)=0.5*(FRQ2+FRQ1)
QF(305)=FRQ4
QF(303)=FRQ2
QF(304)=0.5*(FRQ2+FRQ4)
DF=(QF(103)-QF(3))/100.0
DO 100 I=1,99
RI=I
J=I+3
100 QF(J)=QF(3)+RI*DF
DO 101 I=1,199
RI=I
J=I+103
101 QF(J)=QF(103)+RI*DF*0.5
?
```

```

C      FREQUENCY SAMPLING 152 POINTS FOR DISPERSION RELATION
      FQ(1)=FRQ3+0.75*(FRQ1-FRQ3)
      FQ(2)=FRQ1+0.5*DF
      DO 102 I=1,49
      RI=I
      J=I+2
102    FQ(J)=FQ(2)+RI*DF*2.0
      IF(NMNM.EQ.1) GO TO 7777
      FQ(52)=QF(103)+DF*0.25
      DO 103 I=1,99
      RI=I
      J=52+I
103    FQ(J)=FQ(52)+RI*DF
      FQ(152)=FRQ2+0.25*(FRQ4-FRQ2)
C      WRITE (6,12)
C      12  FORMAT(2X,'N',FREQ,K0,K1,K2,K3,
C      1    ,K4,K5,K6,K7,K8,K9')
C      DISPERSION RELATION
      DO 130 M=1,152
      F=FQ(M)
      OMGA=F/4.9E9
      U1=OMGH/(OMGA*OMGA-OMGH*OMGH)-1.0
      ET1=DSQRT(U1)
      BL(1)=1.0E-9
      B1(1)=3.141592653
      DO 9101 I=1,9
      I1=I+1
      BL(I1)=BL(I)+3.141592654
      B1(I1)=B1(I)+3.141592654
9101    CONTINUE
      DO 50 K=1,10
      AL=BL(K)
      A1=B1(K)
      DL=AL/ET1
      D1=A1/ET1
C      REGI FALSI ITERATION TO FIND INITIAL GUESS FOR NEWTON ITERATION
      DO 20 I=1,1000
      EL=ET1*DL
      E1=ET1*D1
      TDL=DTANH(T*DL)
      TD1=DTANH(T*D1)
      FDL=DCOS(EL)*(1.+TDL)-DSIN(EL)*(ET1-TDL/ET1)
      FD1=DCOS(E1)*(1.+TD1)-DSIN(E1)*(ET1-TD1/ET1)
      X=(DL*FD1-D1*FDL)/(FD1-FDL)
      EX=ET1*X
      TX=DTANH(T*X)
      FX=DCOS(EX)*(1.+TX)-DSIN(EX)*(ET1-TX/ET1)
      IF(DABS(FX)-1.0E-6) 51,51,31
31      CLX=FX*FDL
      CUX=FX*FD1

```

?

```

        IF(CUX.GT.0.) D1=X
        IF(C LX.GT.0.) DL=X
20    CONTINUE
C    NEWTON ITERATION
51    DO 90 L=1,500
        EX=ET1*X
        TX=DTANH(T*X)
        B=T*(1.0000000000-TX**2)
        G=ET1-TX/ET1
        C=(U1+1.00000000)*(U1+1.00000000)/(ET1*OMGH*(-1))*OMGA
        FX=DCOS(EX)*(1.0+TX)-DSIN(EX)*G
        DF=DCOS(EX)*(B-ET1*G)+DSIN(EX)*(B/ET1-ET1*(1.0+TX))
        IF(DABS(FX)-1.0E-9) 92,92,91
91    X=X-FX/DF
90    CONTINUE
92    R(K)=X
        FN(K)=FX
        RR(K)=R(K)/DO
        PR(M,K)=RR(K)
50    CONTINUE
C    PHASE VELOCITY, GROUP VELOCITY AND DELAY TMD CALCULATION
        R1=R(1)
        EX=ET1*R1
        TX=DTANH(T*R1)
        B=T*(1.0000000000-TX**2)
        G=ET1-TX/ET1
        C=(U1+1.00000000)*(U1+1.00000000)/(ET1*OMGH*(-1))*OMGA
        V=B*DCOS(EX)*(DCOS(EX)+DSIN(EX)/ET1)-ET1*G
        S=(R1*G+DSIN(EX)*DCOS(EX)*(1.0+TX/U1))*C
        TMD(M)=3.248060E-13*S/(V*DO)
130   CONTINUE
C    HILBERT TRANSFORM W-K POINTS
DO 5130 M=2,304
        F=QF(M)
        OMGA=F/4.9E9
        U1=OMGH/(OMGA*OMGA-OMGH*OMGH)-1.0
        ET1=DSQRT(U1)
        BL(1)=1.0E-9
        B1(1)=3.141592653
        DO 5101 I=1,9
            I1=I+1
            BL(I1)=BL(I)+3.141592654
            B1(I1)=B1(I)+3.141592654
5101   CONTINUE
DO 550 K=1,10
        AL=BL(K)
        A1=B1(K)
        DL=AL/ET1
        D1=A1/ET1
C    REGI FALSI ITERATION TO FIND INITIAL GUESS FOR NEWTON ITERATION
?
```

```

DO 520 I=1,1000
EL=ET1*DL
E1=ET1*D1
TDL=DTANH(T*DL)
TD1=DTANH(T*D1)
FDL=DCOS(EL)*(1.+TDL)-DSIN(EL)*(ET1-TDL/ET1)
FD1=DCOS(E1)*(1.+TD1)-DSIN(E1)*(ET1-TD1/ET1)
X=(DL*FD1-D1*FDL)/(FD1-FDL)
EX=ET1*X
TX=DTANH(T*X)
FX=DCOS(EX)*(1.+TX)-DSIN(EX)*(ET1-TX/ET1)
IF(DABS(FX)-1.0E-6) 551,551,531
531 CLX=FX*FDL
CUX=FX*FD1
IF(CUX.GT.0.) D1=X
IF(CLX.GT.0.) DL=X
520 CONTINUE
C NEWTON ITERATION
551 DO 590 L=1,500
EX=ET1*X
TX=DTANH(T*X)
B=T*(1.0000000000-TX**2)
G=ET1-TX/ET1
C=(U1+1.00000000)*(U1+1.00000000)/(ET1*OMGH*(-1))*OMGA
FX=DCOS(EX)*(1.0+TX)-DSIN(EX)*G
DF=DCOS(EX)*(B-ET1*G)+DSIN(EX)*(B/ET1-ET1*(1.0+TX))
IF(DABS(FX)-1.0E-9) 592,592,591
591 X=X-FX/DF
590 CONTINUE
592 R(K)=X
FN(K)=FX
RR(K)=R(K)/DO
QR(M,K)=RR(K)
550 CONTINUE
5130 CONTINUE
74 FORMAT(1X,5D16.9)
71 FORMAT(1X,1I4,12E10.3)
79 FORMAT(1X,1I4,11E10.3)
7777 CONTINUE
RETURN
END
SUBROUTINE RAD
C MSFVW RADIATION IMPEDANCE RM AND XM/ RM AS A SUBPROGRAM, XM
C CALCULATED FROM HILBERT TRANSFORM OF XM BY USING 2ND ORDER CLOSED
C FORM SIMPSON RULE FOR INTEGRATION
DIMENSION QRM(305)
REAL*8 FRQ,PR,QF,QR,FRQ3,FRQ4,FRQ1,FRQ2,DF,XM,RFRQ,QRM,F,ZF,QK,RMX
1,RMX1,ARGUE,H1,H2,H3,SUM1,SUM2,SUM,SIMP2,RM,RM1,RN,RND,OMGH,HI,RML
12,XML2,RLGH,FQ,XX,TMD,DO,TO,BO,SO,TU
REAL*8 DLOG,DSQRT

```



```

COMMON/KIM/ F,QK(10),RM,RM1
COMMON/KIM5/ RLGH
COMMON FQ(152),PR(152,10),QF(305),QR(305,10),RMX(152),
1RMX1(152),TMD(152),XMX(152),DO,T0,HI,B0,S0,TU
74 FORMAT(5D16.9)
OMGH=HI/1750.0
FRQ3=OMGH*4.9E9
FRQ4=DSQRT(OMGH*(OMGH+1.))*4.9E9
FRQ1=2.54E9
FRQ2=4.26E9
DF=(FRQ2-FRQ1)/200.0
QF(1)=FRQ3
QF(305)=FRQ4
RFRQ=FRQ4/FRQ3
QRM(1)=0.
QRM(305)=0.
DO 200 I=2,304
F=QF(I)
DO 201 IK=1,10
201 QK(IK)=QR(I,IK)
CALL PGRM
QRM(I)=RM
QF(I)=QF(I)/FRQ3
200 CONTINUE
DO 400 I=1,152
F=FQ(I)
ZF=F/FRQ3
DO 491 IK=1,10
491 QK(IK)=PR(I,IK)
CALL PGRM
RMX(I)=RM
RMX1(I)=RM1
ARGUE=(ZF+1.)*(RFRQ-ZF)/((ZF-1.)*(RFRQ+ZF))
H1=(QRM(1)-RM)/(QF(1)*QF(1)-ZF*ZF)
H2=(QRM(2)-RM)/(QF(2)*QF(2)-ZF*ZF)
H3=(QRM(3)-RM)/(QF(3)*QF(3)-ZF*ZF)
SUM1=(FRQ1-FRQ3)*(H1+4.*H2+H3)/(6.*FRQ3)
H1=(QRM(303)-RM)/(QF(303)*QF(303)-ZF*ZF)
H2=(QRM(304)-RM)/(QF(304)*QF(304)-ZF*ZF)
H3=(QRM(305)-RM)/(QF(305)*QF(305)-ZF*ZF)
SUM2=(FRQ4-FRQ2)*(H1+4.*H2+H3)/(6.*FRQ3)
SUM=SUM1+SUM2
DO 401 K=1,50
JK=2*(K+1)
J1=JK-1
J2=JK+1
H1=(QRM(J1)-RM)/(QF(J1)*QF(J1)-ZF*ZF)
H2=(QRM(JK)-RM)/(QF(JK)*QF(JK)-ZF*ZF)
H3=(QRM(JK)-RM)/(QF(JK)*QF(JK)-ZF*ZF)
SIMP2=DF*(H1+4.*H2+H3)/(3.*FRQ3)

```

?

```

401 SUM=SUM+SIMP2
DO 402 K=51,150
C 2ND ORDER CLOSED FORM OF SIMPSON RULE FOR INTEGRATION
JK=2*(K+1)
J1=JK-1
J2=JK+1
H1=(QRM(J1)-RM)/(QF(J1)*QF(J1)-ZF*ZF)
H2=(QRM(JK)-RM)/(QF(JK)*QF(JK)-ZF*ZF)
H3=(QRM(JK)-RM)/(QF(JK)*QF(JK)-ZF*ZF)
SIMP2=DF*(H1+4.*H2+H3)*0.5/(3.*FRQ3)
402 SUM=SUM+SIMP2
XMX(I)=0.318098862*(RM*DLOG(ARGUE)+2.*ZF*SUM)
XML2=XMX(I)*RLGH*0.5
RML2=RMX(I)*RLGH*0.5
400 CONTINUE
C84 FORMAT(1X,5D16.9)
C 73 FORMAT(1X,1I4,6D14.7)
RETURN
END
SUBROUTINE PGRM
C RM SUBPROGRAM TO CALCULATE RADIATION RESISTANCE
REAL*8 DO,TO,BO,SO,T,HI,OMGH,F,QK,OMGA,RNMAX,RN,PN,U1,ET1,RK,RKD,R
1KS,TKD,RK1,BT,FT,DELT,EXT,A,B,C,D,PC,P1,P2,P3,P,PWR,RM1,RM,X,DET1,
1DET2,E,G,RTT,RTU,TT,TU
REAL*8 FQ,PR,QF,QR,RMX,RMX1,TMD,XMX
REAL*8 SSECH,SECH,DTANH,DSIN,DCOS,DSQRT,DABS
DIMENSION PWR(10)
COMMON/KIM/ F,QK(10),RM,RM1
COMMON/KIM2/ JCONF,NMAX
COMMON FQ(152),PR(152,10),QF(305),QR(305,10),RMX(152),
1RMX1(152),TMD(152),XMX(152),DO,TO,HI,BO,SO,TU
SSECH(X)=1.-DTANH(X)*DTANH(X)
SECH(X)=DSQRT(1.-DTANH(X)*DTANH(X))
U0=1.256637E-06
TT=TO+TU
C CONDITION JUMP ON TRANSDUCER CONFIGURATIONS ( 1 FOR SINGLE BAR, 2
C FOR PARALLEL ODD BARS, 3 FOR PARALLEL EVEN BARS, 4 FOR MEANDER
C STRIPS, 5 FOR PI 0.5 CENTER SPACING, 6 FOR PI 1.5 CENTER SPACING)
C NMAX IS THE STRIP NUMBER FOR MSW TRANSDUCERS
RN=NMAX
ND=NMAX/2
RND=ND
OMGH=HI/1750.0
OMGA=F/4.9E9
U1=OMGH/(OMGA*OMGA-OMGH*OMGH)-1.0
ET1=DSQRT(U1)
DO 100 I=1,10
RK=QK(I)
RKD=RK*DO
TKD=TO*RK

```

?

```

RK1=ET1*RKD
RKS=RK*SO
RTT=TT*RK
RTU=TU*RK
BT=DSIN(0.5*RK*BO)/(0.5*RK*BO)
C   CONDITION JUMP ON TRANSDUCER CONFIGURATIONS ( 1 FOR SINGLE BAR, 2
C   FOR PARALLEL ODD BARS, 3 FOR PARALLEL EVEN BARS, 4 FOR MEANDER
C   STRIPS, 5 FOR PI 0.5 CENTER SPACING, 6 FOR PI 1.5 CENTER SPACING)
C   NMAX IS THE STRIP NUMBER FOR MSW TRANSDUCERS
GO TO (91,92,93,94,95,96),JCONF
91 FT=1.
GO TO 99
92 FT=1.
DO 920 N=1,ND
PN=N
920 FT=FT+2.*DCOS(PN*RKS)
GO TO 99
93 FT=0.
DO 930 N=1,ND
PN=N
930 FT=FT+2.*DCOS((PN-0.5)*RKS)
GO TO 99
94 FT=0.
DO 940 N=1,ND
PN=N
940 FT=FT+2.*((-1.)**N)*DSIN((PN-0.5)*0.5*RKS)
GO TO 99
95 FT=0.
DO 950 N=1,ND
PN=N
950 FT=FT+2.*DSIN((PN-0.75)*RKS)
GO TO 99
96 FT=0.
DO 960 N=1,ND
PN=N
960 FT=FT+2.*DSIN((PN-0.25)*RKS)
99 DET1=ET1*DO*(U1-DTANH(RTT))/DCOS(RK1)-TT*SSECH(RTT)*(DSIN(RK1)+ET1
1*DCOS(RK1))
DET2=DSIN(RK1)*(U1-DTANH(RTT))-ET1*DCOS(RK1)*(DTANH(RTT)+1.)
DELT=(TO*SSECH(TKD)*DTANH(RTU)+TU*SSECH(RTU)*DTANH(TKD))*DET2+(1.+
1DTANH(TKD)*DTANH(RTU))*DET1
EXT=BT*FT/(DELT*RK)
A=(DSIN(RK1)*(U1-DTANH(RTU))-ET1*DCOS(RK1)*(DTANH(RTU)+1.))*EXT
B=-DTANH(TKD)*(ET1*DSIN(RK1)-DCOS(RK1))*EXT*SECH(RTU)
C=DTANH(TKD)*(ET1*DCOS(RK1)+DSIN(RK1))*EXT*SECH(RTU)
D=ET1*DTANH(TKD)*EXT*SECH(RTU)
E=-DTANH(TKD)*(ET1*DSIN(RK1)-DCOS(RK1))*EXT*ET1
G=DTANH(TKD)*(ET1*DCOS(RK1)+DSIN(RK1))*EXT
PC=6.283185307*U0*F*RK
P1=0.5*A*A*(DTANH(TKD)/RK-TO*SSECH(TKD))

```

?

```

      P2=U1*(0.5*D0*(B*B-C*C)+0.25*(B*B-C*C)*DSIN(2.*RK1)/(ET1*RK)+0.5*B
1  *C*(1.-DCOS(2.*RK1))/(ET1*RK))
      P3=0.5*D*D/RK
      P4=0.5*TU*(E*E-G*G)*SSECH(RTU)+0.5*(E*E+G*G)*DTANH(RTU)/RK+E*G*DTA
1 NH(RTU)*DTANH(RTU)/RK
      P=PC*(P1+P2+P3+P4)
100 PWR(I)=P
      RM1=2.*PWR(1)
      RM=RM1
      DO 101 I=2,10
101 RM=RM+2.*PWR(I)
      RETURN
      END
      SUBROUTINE RESP
C      MSFVW FREQUENCY RESPONSE PROGRAM TO CALCULATE TRANSMISSION
C      LINE PARAMETERS, CIRCUIT ELEMENTS, INPUT IMPEDANCE, AND INSERTION
C      LOSS
      REAL LOSS,LOSS1,LOSS2
      DIMENSION WV(152),ZIL(152),LOSS(51),FREQ(51),WAVE(51)
      REAL*8 FQ,TMD,RMX,XX,XX1,F,TM1,RM,XX,XX1,EK,RLGH,PXIN,ZC,BETA,AC
1 ,RML2,XML2,AR,AR1,ARI,CZC,CBT,CAC,CAR,CXM,ALPH,AL,BL,RIN,XIN,RI1,R
1 IC,XMIN,PT1,CL1,XL1,COMX,RN,RND,X,CST,QF,QR,PR,BO,DO,TO,
1 HI,SO,TU
      REAL*8 SECH,DTANH,DSIN,DCOS,DSQRT,DEXP,DLOG10
      COMMON/KIM2/ JCONF,NMAX
      COMMON/KIM3/ DELH,PATH,FSTART,DELF
      COMMON/KIM4/ NMNM
      COMMON/KIM5/ RLGH
      COMMON FQ(152),PR(152,10),QF(305),QR(305,10),RMX(152),
1 RMX1(152),TMD(152),XX(152),DO,TO,HI,BO,SO,TU
      SECH(X)=DSQRT(1.-DTANH(X)*DTANH(X))
      EK=6.0516
      PXIN=0.0
C      CONDITION JUMP ON TRANSDUCER CONFIGURATIONS ( 1 FOR SINGLE BAR, 2
C      FOR PARALLEL ODD BARS, 3 FOR PARALLEL EVEN BARS, 4 FOR MEANDER
C      STRIPS, 5 FOR PI 0.5 CENTER SPACING, 6 FOR PI 1.5 CENTER SPACING)
C      NMAX IS THE STRIP NUMBER FOR MSW TRANSDUCERS
      RN=NMAX
      ND=NMAX/2
      RND=ND
      CST=1.
      DO 105 J=1,152
      F=FQ(J)
      TM1=TMD(J)
      RM=RMX(J)
      XX=XX(J)
      RM1=RMX1(J)
      ZC=90.0
      BETA=3.636102608D-8*F
      AC=7.96D-7*DSQRT(F)/(BO*ZC)

```

```

RML2=RM*RLGH*0.5
XML2=XM*RLGH*0.5
AR=0.5*RM/ZC
AR1=0.5*RM1/ZC
ARI=0.5*XM/ZC
C  CONDITION JUMP ON TRANSDUCER CONFIGURATIONS ( 1 FOR SINGLE BAR, 2
C  FOR PARALLEL ODD BARS, 3 FOR PARALLEL EVEN BARS, 4 FOR MEANDER
C  STRIPS, 5 FOR PI 0.5 CENTER SPACING, 6 FOR PI 1.5 CENTER SPACING)
C  NMAX IS THE STRIP NUMBER FOR MSW TRANSDUCERS
GO TO (91,92,92,93,94,94),JCONF
91 CZC=1.
   CBT=1.
   CAC=1.
   CAR=1.
   CXM=1.
   GO TO 99
92 CZC=1./RN
   CBT=1.
   CAC=1.
   CAR=1./RN
   CXM=1./RN
   GO TO 99
93 CZC=1.
   CBT=RN
   CAC=RN
   CAR=1./RN
   CXM=1./RN
   GO TO 99
94 CZC=1./RND
   CBT=2.
   CAC=2.
   CAR=1./RN
   CXM=1./RN
C  TRANSMISSION LINE PARAMETER MODIFICATIONS FOR TRANSDUCER ARRAYS
99 ZC=CZC*ZC
   BETA=CBT*BETA
   AC=CAC*AC
   AR=CAR*AR
   AR1=CAR*AR1
   ARI=ARI*CXM
   ALPH=AR+AC
   BETA=BETA+ARI
   AL=2.*ALPH*RLGH
   BL=2.*BETA*RLGH
C  INPUT IMPEDANCE AND CIRCUIT ELEMENTS
   RIN=ZC*DTANH(AL)/(1.+DCOS(BL)*SECH(AL))
   XIN=ZC*DSIN(BL)*SECH(AL)/(1.+DCOS(BL)*SECH(AL))-PXIN
   QRIN=RIN/50.
   QXIN=XIN/50.
   RI1=RIN*ARI/ALPH
?
```

```

RIT=RIN*AR/ALPH
RIC=RIN*AC/ALPH
XMIN=XIN*ARI/BETA
C POWER RATIO, CONVERSION LOSS AND INSERTION LOSS
PT1=200.0*RI1/((RIN+50.0)**2.+XIN**2)
CL1=10.*DLOG10(PT1)
C
C THE THREE TERMS IN THE FOLLOWING LINE ARE CONVERSION LOSS
C PROPAGATION LOSS, AND BIDIRECTIONAL RADIATION LOSS *****
679 XL1=CL1+(-76.4E+6*TM1*DELH*PATH+10.*DLOG10(0.25D+00))/2.0
COMX=PXIN
IF(MNM.EQ.0) ZIL(J)=0.0
ZIL(J)=-XL1+ZIL(J)
IF(MNM.EQ.0) GO TO 105
FQ(J)=F/1.E9
WV(J)=(2.*3.14159/PR(J,1))*1.0E+06
105 CONTINUE
IF(MNM.EQ.0) GO TO 777
LOSS1=0.0
WAVE1=0.0
MM=0
JSTOP=5
FREQ1=FSTART
DO555 M=1,50,1
FREQ(M)=FREQ1
LOSS(M)=LOSS1
WAVE(M)=WAVE1
DO666 J=1,JSTOP,1
FREQ1=FREQ1+DELF
DO333 I=2,152,1
IF(FQ(I).GT.FREQ1) GO TO 444
333 CONTINUE
444 LOSS1=(ZIL(I)-ZIL(I-1))*(FREQ1-FQ(I-1))/(FQ(I)-FQ(I-1))+ZIL(I-1)
LOSS2=10.0**(-LOSS1/10.0)
WAVE1=(WV(I)-WV(I-1))*(FREQ1-FQ(I-1))/(FQ(I)-FQ(I-1))+WV(I-1)
WAVE2=WAVE1*1.0E-06
IF(MM.EQ.0) FREQ(1)=FREQ1
IF(MM.EQ.0) LOSS(1)=LOSS1
IF(MM.EQ.0) WAVE(1)=WAVE1
IF(MM.EQ.0) MM=1
WRITE(2,111) WAVE2,LOSS2
C WRITE(LW,111) WAVE2,LOSS2
111 FORMAT(2E11.4)
666 CONTINUE
JSTOP=4
555 CONTINUE
CALL GRFPLT(LOSS,FREQ,WAVE,M)
777 MNM=1
1 FORMAT(4F18.15)
3 FORMAT(4X,'RIN,XIN,RI1,RIC,XMIN',7E14.4)
?
```



```
      5 WRITE(6,103)
103  FORMAT(1H+,10X,'IG'//)
      GO TO 1000
      6 WRITE(6,104)
104  FORMAT(1H+,10X,'I',60X,'L'//)
1000 CONTINUE
      RETURN
      END
//X.FT01F001 DD DISP=SHR,DSN=B515.KWR.GAMMA20
//X.FT02F001 DD DSN=B515.KWR.CNVLOS,
//  DISP=(OLD,CATLG),UNIT=DISKA,
//  DCB=(LRECL=22,RECFM=FB,BLKSIZE=2200),
//  SPACE=(TRK,(10,10),RLSE)
//X.SYSIN DD *
?
```



```

//DESIGNER      JOB B515-KWR,'KIM REED'
/*BOX          8546
/*LINES 2K
/*REGION       256K
//            EXEC FORNCX,INDX='A500.LPLOT',LPARM='SIZE=500K',XREGION=500K
C
C PROGRAM DESCRIPTION: *****
C
C THIS PROGRAM DESIGNS AND ANALYZES OBLIQUE INCIDENCE ION.
C IMPLANTED MAGNETOSTATIC FILTER ARRAYS USING:
C
C (1) DISPERSION DATA FROM PROGRAM "NEWTRY"
C
C (2) TRANSDUCER RESPONSE DATA FROM PROGRAM "XDUCER"
C
C
C NOTE: BE SURE TO RUN PROGRAMS "NEWTRY" AND "XDUCER"
C WITH THE DESIRED PARAMETERS BEFORE RUNNING THIS
C ONE. ALSO, BE SURE THAT THE FILES CREATED BY
C NEWTRY AND XDUCER ARE THE SAME AS THOSE NAMED
C AT THE END OF THIS PROGRAM.
C
C *****
C
C DIMENSION SGAMAP(2000),SGAMAI(2000),SFREQ(2000),IL(1,600),
C 1TGROU(1,600),SY(500),SW(500),SL(500),PHASE(1,600),SF(500)
C 2,TXLOSS(202),WAVELN(202)
C
C CHARACTER*4 PARA1,PARA2,AMEAN1,AMEAN2,PIE1,PIE2,
C 1ACON11,ACON12,ACON01,ACON02
C REAL IL,L,ILO
C COMPLEX GAMMAP,GAMMAI,SGAMAP,SGAMAI,R,RHO,J
C
C DATA J,PI/(0.0,1.0),3.1415926/
C DATA PARA1,PARA2,AMEAN1,AMEAN2,PIE1,PIE2/'PARA','LLEL',' MEA',
C 1'NDER',' P','I '/
C
C *****
C USER SUPPLIED INPUT*****
C *****
C
C "YNOT" IS THE DISTANCE FROM THE CENTER OF THE INPUT TRANSDUCER TO
C THE LEADING EDGE OF THE FIRST ARRAY BAR (METERS). IT SHOULD BE
C ATLEAST 1.5MM SO THAT THE FIRST BAR DOESN'T OVERLAP THE INPUT
C TRANSDUCER. *****
C
C YNOT=2.0E-03
C
C
C "Z0" IS THE DISTANCE FROM THE ARRAY AXIS TO OUTPUT XDUCER (METERS)
C Z0=2.0E-03
C
C

```

```

      Z0=2.0E-03
C
C  "CO" IS THE SLOPE OF THE LINEAR GROUP DELAY (SEC/HZ)*****
      CO=-0.6E-15
C
C  "BAND" IS DESIRED (LOWER IF CO>0;UPPER IF CO<0) BANDEGE (GHZ)****
      BAND=3.5
C
C  "ARRAYLN" IS THE TOTAL ALLOWED LENGTH INCLUDING THE 1.5MM DUE TO**
C  BAR SLANT AND THE FREE PROPAGATION DISTANCE 'YNOT' (MILLIMETERS)**
      ARRAYLN=19.0
C
C  "RATIO" IS THE MAXIMUM ALLOWED RATIO OF THE LONGEST BAR LENGTH TO
C  THE MINIMUM BAR LENGTH*****
      RATIO=10.0
C
C  IF "NOWAIT" IS SET TO 1 THE WEIGHTING FUNCTION WILL BE IGNORED***
C  IF "NOWAIT" IS SET TO 0 THE WEIGHTING FUNCTION WILL BE USED*****
      NOWAIT=1
C
C  "PLTJMP" IS THE PLOT INTERVAL TO BE USED*****
      PLTJMP=0.005
C
C  *****
C  *****
C  *****
C
C  INITIALIZE CONSTANTS *****
      GRID=-60.0
      TGRID=300.0
      LW=6
      WO=0.0
      YO=0.0
      DY=0.0
      NN=1
      N=1000
      SKIP=0.5
      M=0
      SMIN=1.0E+08
      SMAX=0.0
      HEAD=0.0
      FA=3.0E+09
      TO=-CO*(BAND*1.0E+09-FA)
      KPLOT=0
      JI=1
      NXDAT=200-6
      IF(CO.LT.0.0) JI=NXDAT-1
C
C  READ PARAMETERS FROM PROGRAM "NEWTRY"*****
?

```

```

      READ(1,111) FBEGIN,FEND,DELF,QNDAT,H0
      NDAT=QNDAT
      READ(1,111) FUDGE,TYIG,TIMP,TAL203,DHMIN
C
C  READ PARAMETERS FROM PROGRAM "XDUCER"*****
      READ(2,333) TU,PATH
      READ(2,333) APATRI,APATRO
      READ(2,333) BI,BO
      READ(2,333) WI,WO
      READ(2,333) CONFI,CONFO
      READ(2,333) QMAXI,QMAXO
C
C  WRITE OUT ALL PERTINENT PARAMETERS FOR THIS DESIGN*****
      QI1=TU*1.0E+06
      QO1=TU*1.0E+06
      QI2=APATRI*1.0E+03
      QO2=APATRO*1.0E+03
      QI3=BI*1.0E+06
      QO3=BO*1.0E+06
      QI4=WI*1.0E+06
      QO4=WO*1.0E+06
      NMAXI=QMAXI
      NMAXO=QMAXO
      QGYRO=2.8
      QMO=1760.0
      QFO=H0*QGYRO/1.0E+03
      QTYIG=TYIG*1.0E+06
      QTIMP=TIMP*1.0E+06
      QAL203=TAL203*1.0E+06
      ACONI1=PARA1
      ACONI2=PARA2
      ACONO1=PARA1
      ACONO2=PARA2
      IF(CONFI.GT.3) ACONI1=AMEAN1
      IF(CONFI.GT.3) ACONI2=AMEAN2
      IF(CONFO.GT.3) ACONO1=AMEAN1
      IF(CONFO.GT.3) ACONO2=AMEAN2
      IF(CONFI.GT.4) ACONI1=PIE1
      IF(CONFI.GT.4) ACONI2=PIE2
      IF(CONFO.GT.4) ACONO1=PIE1
      IF(CONFO.GT.4) ACONO2=PIE2
      WRITE(6,102) QGYRO,QMO,FUDGE,DHMIN,QFO,QTYIG,QTIMP,QAL203,FBEGIN,
1 FEND,H0,DELF
      DELF=DELF/1.0E+03
      WRITE(6,313) ACONI1,ACONI2,ACONO1,ACONO2,NMAXI,NMAXO,QI1,QO1,
1 QI2,QO2,QI3,QO3,QI4,QO4,PATH
102 FORMAT(1H1,44(' '),/,1X,'* MSFVW-PURE/IMPLANTED DISPERSION',
1 ' SOLUTION ',/,1X,10(' '), ' FLIPPED CONFIGURATION ',11(' '),/,1X,
244(' '),/,1X,'* MATERIAL CONSTANTS:',/,2X,'GYROMAGNETIC RATIO',
35X,'=',4X,1F5.2, ' MHZ/OE',/,2X,'UNIMPLANTED MO',9X,'=',1X,1F8.2,
?
```

```

41X,'OE',/,2X,'MO(IMP)/MO(PURE)',7X,'=',4X,1F5.2,///,
51X,'*GILBERT-LOSS PARAMETERS:',/,2X,'DELTA-H',
6' MIN',12X,'=',4X,1F5.2,1X,'OE',/,2X,'FO',21X,'=',4X,1F5.2,1X,
7'GHZ',///,1X,'*GEOMETRY PARAMETERS:',/,2X,'YIG THICKNESS',10X,
8'=',3X,1F6.2,1X,'MICRONS',/,2X,'IMPLANT DEPTH',10X,'=',4X,1F5.2,
91X,'MICRONS',/,2X,'SUBSTRATE THICKNESS',4X,'=',2X,1F7.2,1X,
1'MICRONS',///,1X,'*FREQUENCY PARAMETERS:',/,2X,'START FREQUENCY',
28X,'=',4X,1F5.2,1X,'GHZ',/,2X,'STOP FREQUENCY',9X,'=',4X,1F5.2,
31X,'GHZ',/,2X,'HO',21X,'=',2X,1F7.2,1X,'OE',/,2X,'FREQUENCY',
4' STEP-SIZE',4X,'=',4X,1F5.2,1X,'MHZ',///,1X,44(' '),/)
333 FORMAT(//,1X,44(' '),/,1X,10(' '), ' TRANSDUCER INFORMATION ',
110(' '),/,1X,44(' '),/,22X,'INPUT',10X,'OUTPUT',/,1X,
2'TRANSUCER',9X,2A4,8X,2A4,/,1X,'CONFIGURATION',/,1X,
3'NUMBER OF',14X,1I3,13X,1I3,/,1X,'STRIPES',/,1X,
4'YIG/TRANSUCER',6X,1F6.1,10X,1F6.1,/,1X,'AIR GAP (UM)',/,1X,
5'SIGNAL',14X,1F6.1,10X,1F6.1,/,1X,'APERTURE (MM)',/,1X,
6'FILIMENT',12X,1F6.1,10X,1F6.1,/,1X,'WIDTH (UM)',/,1X,
7'FILIMENT CTR',8X,1F6.1,10X,1F6.1,/,1X,'SPACING (UM)',/,1X,
8'INPUT-OUTPUT',8X,1F6.1,10X,'-----',/,1X,'PATH (CM)',/,1X,
944(' '),/)

C
C READ DATA FROM NEWTRY *****
DO 2 INDEX=1,NDAT,1
READ(1,111) F1,GAMMAP,GAMMAI
SFREQ(INDEX)=F1
SGAMAP(INDEX)=GAMMAP
SGAMAI(INDEX)=GAMMAI
111 FORMAT(1F7.4,4E15.8)
2 CONTINUE

C
C READ DATA FROM XDUCER *****
DO 5 INDEX=1,NXDAT,1
READ(2,333) WAVELN(INDEX),TXLOSS(INDEX)
333 FORMAT(2E11.4)
5 CONTINUE

C
C SET UP SYNTHESIS DATA SWEEP-DIRECTION, BASED ON SIGN OF CO (BARS
C NEAREST INPUT MUST BE DESIGNED FIRST)*****
INDEX=1
IF(CO.LT.0.0) INDEX=NDAT
F1=SFREQ(INDEX)*1.0E+09
GAMMAP=SGAMAP(INDEX)
F=F1
BETA1=REAL(GAMMAP)
W=PI/BETA1
ISTOP=NDAT-1

C
C SYNTHESIS DATA SWEEP*****
DO1 I=1,ISTOP,1
FOO=F

```

```

      DY0=DY
      W00=W
      F0=F1
      BETA0=BETA1
      INDEX=I-1
      IF(CO.LT.0.0) INDEX=NDAT-I
C
C   ESTABLISH A VALUE OF K AND F *****
C   F1=SFREQ(INDEX)*1.0E+09
C   GAMMAP=SGAMAP(INDEX)
C   BETA1=REAL(GAMMAP)
C   F=(F0+F1)/2.0
C
C   CALCULATE REQUIRED BAR OR GAP WIDTH RELATIVE TO THE LAST CUT TO**
C   SATISFY
C       T=(DK/DW)(Z0+Y(I))=CO*F+T0
C
C   AND...   Y(I)=Y(I-1)+(W(I-1)/2
C
C       DY=(CO*(F-FA)+T0)*2.0*PI*(F1-F0)/(BETA1-BETA0) - (Z0+Y0+W0/2.0)
C
C   CALCULATE BAR OR GAP WIDTH THAT WILL COUPLE TO K BEING CONSIDERED*
C   (W=PI/K)*****
C       W=2.0*PI/(BETA0+BETA1)
C
C   DY MUST EQUAL W/2, SO KEEP MOVING THRU THE K(F) DATA UNTIL DY GOES
C   FROM LESS THAN W/2 TO GREATER THAN W/2. THEN USE LINEAR INTERPOLA-
C   TION TO CALCULATE WHERE DY=W/2.
C       IF(DY.LT.(W/2.0)) GO TO 1
C       W1=W
C       W=(W00*(DY-DY0)/(W1-W00)-DY0)/((DY-DY0)/(W1-W00)-0.5)
C       DY=W/2.0
C       Y=DY+Y0+W0/2.0
C       F=(F-F00)*(W-W00)/(W1-W00)+F00
C
C   START THE ARRAY WHEN THE FIRST CUT POSITION BECOMES POSITIVE *****
C       QCUT=Y-W/2.0
C       IF(QCUT.LT.YNOT) GO TO 1000
C
C   STOP THE ARRAY WHEN IT EXCEEDS ARAYLN *****
C       IF((Y+W/2.0).GT.((ARAYLN-1.5)*1.0E-03).AND.SKIP.LT.1.0) M=1
C
C   FIND TRANSDUCER LOSS AT WAVELENGTH=2W *****
C       4 DELW1=WAVELN(JI)-W*2.0
C       DELW2=W*2.0-WAVELN(JI+1)
C       IF(DELW1.LT.0.0) JI=JI-1
C       IF(DELW2.LT.0.0) JI=JI+1
C       IF(DELW1*DELW2.LT.0.0) GO TO 4
C       TXL=TXLOSS(JI)-DELW1*(TXLOSS(JI)-TXLOSS(JI+1))/(DELW1+DELW2)
C
C
C

```

```

C FIND PROPAGATION LOSS AT WAVELENGTH=2W*****
  PROPL=EXP(2.0*AIMAG(GAMMAP)*(Y+Z0))
C
C SPECIFY THE DESIRED AMPLITUDE WEIGHTING FUNCTION *****
  WEIGHT=1.0
C
C SCALE BAR LENGTH TO COMPENSATE FOR TRANSDUCER AND PROPAGATION LOSS
  SCALE=WEIGHT/(TXL*PROPL)
  IF(NOWAIT.EQ.1) SCALE=1.0
  IF(SCALE.GT.SMAX.AND.M.EQ.0.AND.SKIP.LT.1.0) SMAX=SCALE
  IF(SCALE.LT.SMIN.AND.M.EQ.0.AND.SKIP.LT.1.0) SMIN=SCALE
  IF(M.EQ.0) N=NN
C
C LOAD ANALYSIS ARRAYS WITH BAR CENTERS, WIDTHS, AND LENGTHS*****
  SKIP=1.0/SKIP
  IF(SKIP.LT.1.0) NN=NN+1
  SY(NN)=Y
  SW(NN)=W
  SL(NN)=SCALE
  SF(NN)=F
  IF(SMAX/SMIN.GT.RATIO) M=1
C
C UPDATE FREQUENCY, BAR POSITION, AND BAR WIDTH AND MOVE ON TO THE
C NEXT BAR *****
1000 Y0=Y
      W0=2.0*DY
      F=F1
      W=W1
      DY=0.0
      1 CONTINUE
C
C DESIGN COMPLETE, WRITE OUT APPROXIMATE T*BW PRODUCT*****
      TBW=ABS(C0*(SF(N)-SF(1))**2)
      WRITE(LW,323) TBW
323  FORMAT(1X,'APPROXIMATE TIME*BANDWIDTH = ',1F8.2,/,
1,13X,'BAR',8X,'BAR',5X,'1/2BAR',5X,'CUT1*',5X,'CUT2*',6X,'BAR',/
2,3X,'FREQ',5X,'CENTER',5X,'WIDTH',4X,'LENGTH',5X,2('0.71',6X),/
3,3X,'(GHZ)',5X,5(' (MM)',6X),/)
C
C WRITE OUT ARRAY DESIGN*****
      DO 3 I=1,N,1
        SL(I)=SL(I)/SMAX
        QY=SY(I)*1.0E+03
        QW=SW(I)*1.0E+03
        QCUT1=(QY-QW/2.0)/SQRT(2.0)
        QCUT2=(QY+QW/2.0)/SQRT(2.0)
        QF=SF(I)/1.0E+09
        QL=SL(I)*APATRI*0.5E+03
        WRITE(LW,109) QF,QY,QW,QL,QCUT1,QCUT2,I
109  FORMAT(1X,5('F7.3,3X'),3X,123)
      3

```

```

      3 CONTINUE
C
C *****
C ANALYZE THE DESIGN *****
C *****
C
      JI=1
      IF(CO.LT.0.0) JI=NXDAT-1
      FSTART=(SF(N)+SF(1))/2.0E+09-249.0*DELF
      IF(FSTART.LT.2.5) FSTART=2.5
      IF(FSTART.GT.3.5) FSTART=3.5
      FF=FSTART
      BW=ABS(SF(N)-SF(1))/1.0E+09
      FC=(SF(N)+SF(1))/2.0E+09
      WRITE(3,4444) FC,DELF
      WRITE(3,4444) BW,BW
      WRITE(LW,2000)
2000 FORMAT(1H1,'FREQUENCY',5X,'INSERTION',6X,'PHASE',8X
1,'GROUP DELAY',
26X,'REFLECTANCE',/,3X,'(GHZ)',7X,'LOSS (DB)',6X,'(RAD)',10X,
3'(NSEC)',8X,'MODULUS PHASE',/)
C
C
C SPACE UP TO FIRST FREQUENCY TO BE PLOTTED*****
C
      DO 33 INDEX=1,NDAT,1
      IF(SFREQ(INDEX).GE.FSTART) GO TO 555
33 CONTINUE
555 PHASE(1,1)=0.0
C
C FREQUENCY SCAN*****
      DO 11 I=1,500,1
C
C READ IMPLANTED AND UNIMPLANTED GAMMAS STORED IN "GAMMA" FROM NEWTRY*
      III=INDEX+I-1
      GAMMAP=SGAMAP(III)
      GAMMAI=SGAMAI(III)
      F=SFREQ(III)
C
C OBTAIN TRANSDUCER CONVERSION LOSS AT PRESENT WAVELENGTH *****
      QLAMDA=2.0*PI/REAL(GAMMAP)
44 DELW1=WAVELN(JI)-QLAMDA
      DELW2=QLAMDA-WAVELN(JI+1)
      IF(DELW1.LT.0.0) JI=JI-1
      IF(DELW2.LT.0.0) JI=JI+1
      IF(DELW1*DELW2.LT.0.0) GO TO 44
      TXL=TXLOSS(JI)-DELW1*(TXLOSS(JI)-TXLOSS(JI+1))/(DELW1+DELW2)
C
C CALCULATE REFLECTANCE OF A BAR AT THIS FREQUENCY*****
      RHO=(GAMMAP-GAMMAI)/(GAMMAP+GAMMAI)
      ?

```

```

      RHOMOD=SQRT(REAL(RHO)**2+AIMAG(RHO)**2)
      RHOANG=ATAN(AIMAG(RHO)/REAL(RHO))
C
C   ADD UP REFLECTIONS FROM EACH BAR*****
      R=0.0
      DO 22 II=1,N,1
      R=R+SQRT(SL(II))*CEXP(-J*GAMMAP*SY(II))*CSIN(GAMMAP*SW(II)/2.0)
22  CONTINUE
C
C   CALCULATE I.L.AND PHASE AT EACH FREQUENCY AND STORE FOR PLOTING****
      R=R*2.0*J*RHO*CEXP(-J*GAMMAP*ZO)
      AMODSQ=R*CONJG(R)
      PHASE(1,I)=ATAN(AIMAG(R)/REAL(R))
C
C   LOAD PLOTTING ARRAYS WITH DATA TO BE PLOTTED*****
      WRITE(3,4444) R
4444  FORMAT(2E15.8)
      QIL=10.0*ALOG10(AMODSQ*TXL)
      IF(QIL.LT.-80.0) QIL=-80.0
      QGROUP=(PHASE(1,I-1)-PHASE(1,I))/(2.0*PI*DELF)
      IF(QGROUP.LT.0.0) QGROUP=TLAST
      IF(QGROUP.GT.TGRID) QGROUP=TGRID
      TLAST=QGROUP
      HEAD=HEAD+1.0
      IF(HEAD.EQ.56.0) WRITE(LW,2000)
      IF(HEAD.EQ.56.0) HEAD=1.0
      WRITE(LW,3000) F,QIL,PHASE(1,I),QGROUP,RHOMOD,RHOANG
3000  FORMAT(2X,1F7.4,8X,1F5.1,8X,1F5.2,8X,1F8.2,7X,1F7.4,1X,1F7.4)
      IF(ABS(F-FF).GT.DELF) GO TO 11
      FF=FF+PLTJMP
      KPLOT=KPLOT+1
      IL(1,KPLOT)=QIL
      IF(QIL.LT.GRID) IL(1,KPLOT)=GRID
      TGROUP(1,KPLOT)=QGROUP
11  CONTINUE
      WRITE(6,222)
222  FORMAT(1H1)
C
C   PLOT THE I.L. AND PHASE OF THE REFLECTION COEFFICIENT*****
C
      IL(1,1)=0.0
      IL(1,100)=GRID
      TGROUP(1,1)=0.0
      CALL PLOTLP(FSTART,PLTJMP,IL,1,100,1)
      WRITE(6,222)
      CALL PLOTLP(FSTART,PLTJMP,TGROUP,1,100,1)
      STOP
      END
//X.FT01F001 DD DISP=SHR,DSN=8515.KWR.GAMMA20
//X.FT02F001 DD DISP=SHR,DSN=8515.KWR.CNVLOS
?
```



```
//X.FT03F001 DD DSN=B515.KWR.SDAT,  
//  DISP=(OLD,CATLG),UNIT=DISKA,  
//  DCB=(LRECL=30,RECFM=FB,BLKSIZE=3000),  
//  SPACE=(TRK,(10,10),RLSE)  
//X SYSIN DD *
```

## REFERENCES

- {2.1} H. J. Wu, Ph.D. Dissertation, The University of Texas at Arlington, Arlington Texas, (1978).
- {2.2} R. L. Carter, C. V. Smith, Jr. and J. M. Owens, "Magnetostatic Forward Volume Wave Spin Wave Conversion by Etched Grating in LPE-YIG," IEEE Trans. Mag., Mag. 16, No. 5, (September, 1980), pp. 1159-1162.
- {2.3} C. G. Sykes, J. D. Adam and J. H. Collins, "Magnetostatic Wave Propagation in a Periodic Structure," Applied Physics Letters, Vol. 29, No. 6, (September 15, 1976).
- {2.4} J. H. Collins, J. D. Adam and Z. M. Bardai, "One-Port Magnetostatic Wave Resonator," Proceedings of the IEEE, 65, (1977), pp. 1090-1092.
- {2.5} J. M. Owens, C. V. Smith, E. P. Snapka, and J. H. Collins, "Two-Port Magnetostatic Wave Resonators Utilizing Periodic Reflective Arrays," Proc. IEEE, CH1355-7/78/0000-0440, (1978), pp. 440-442.
- {2.6} J. P. Castera, G. Volluet and P. Hartemann, "New Configurations for Magnetostatic Wave Devices," Ultrasonics Symposium Proceedings, IEEE, Cat. 80CH1602-2, Vol. 1, (1980), pp. 514-517.
- {2.7} R. L. Carter, J. M. Owens, W. R. Brinlee, Y. W. Sam and C. V. Smith, Jr., "Tunable Magnetostatic Surface Wave Oscillator at 4 GHz," IEEE MTT-S International Microwave Symposium, (1981), pp. 383-385.
- {2.8} J. E. Mercereau and R. P. Feynman, "Physical Conditions for Ferromagnetic Resonance," Phys. Rev., 104, p. 63.

- {2.9} D. Polder, "On the Theory of Ferromagnetic Resonance," *Philos. Mag.*, **40**, (1949), p. 99.
- {2.10} M. S. Sodha and N. C. Srivastava, "Microwave Propagation in Ferrimagnetics," Plenum Press, New York, (1981).
- {2.11} D. Wagner, "Introduction to the Theory of Magnetism," Pergamon Press, Oxford, (1972).
- {2.12} R. M. White, "Quantum Theory of Magnetism," McGraw-Hill, New York, (1970).
- {2.13} B. Lax and K. J. Button, "Microwave Ferrites and Ferrimagnetics," McGraw-Hill, New York, (1962).
- {2.14} T. A. Gilbert, Armour Research Foundation Rept. No. 11, ARF, Chicago, Ill., (unpublished).
- {2.15} L. D. Landau and E. M. Lifshitz, "On the Theory of Dispersion of Magnetic Permeability in Ferrimagnetic Bodies," *Phys. Z. Sowjetunion*. (English), **8**, (1935), p. 153.
- {2.16} W. H. von Aulock, "Handbook of Microwave Ferrite Materials," Academic Press, New York, (1965).
- {2.17} R. Wolfe, J. C. North, R. L. Barns, M. Robinson and J. H. Levinstein, *Appl. Phys. Lett.*, **19**, (1971), p. 298.
- {2.18} C. H. Wilts and S. Prasad, *IEEE Trans. Mag.*, **17**, (1981), p. 2405.
- {2.19} H. A. Algra and J. M. Ropertson, "The Effects of Ion Implantation on La, Ga: YIG Films as Observed by Spin Wave Resonance," *J. Appl. Phys.*, **51**, 7, (July 1980), pp. 3821-3826.
- {2.20} B. E. MacNeal and V. S. Speriosu, "Modeling Strain Distributions in Ion-Implanted Magnetic Bubble Materials," *J. Appl. Phys.*, **52**, 6, (June 1981), pp. 3935-3940.
- {2.21} V. S. Speriosu, Private Communication, Stanford University, Palo Alto, California.
- {2.22} G. Hasnain, "Magnetostatic Wave Transducer Array Filters," MSEE Thesis, The University of Texas at Arlington, Arlington Texas, (1980).

- {2.23} S. Ramo, J. R. Whinnery and T. Van Duzer, "Fields and Waves in Communication Electronics," John Wiley and Sons, Inc., New York, (1965), pp. 344-346.
- {2.24} S. A. Schelkunoff, Bell Sys. Tech. J., 17, (Jan. 1938), pp. 17-48.
- {2.25} W. R. Brinlee, "MSSW Two-Port Metal Strip Array Resonators," MSEE Thesis, The University of Texas at Arlington, Arlington Texas, (October, 1980).
- {2.26} R. H. Tancrell and M. G. Holland, "Acoustic Surface Wave Filters," Proc. IEEE, Vol. 59, (Mar. 1971), pp.393-409.
- {2.27} N. D. Parikh, "Beam Steering Measurements for Magnetostatic Forward Volume Waves Using an Induction Probe," MSEE Thesis, The University of Texas at Arlington, Arlington Texas, (May, 1982), pp. 43-48 (on MSSW).
- {3.1} D. S. Humpherys, "The Analysis, Design, and Synthesis of Electrical Filters," Prentice-Hall, Inc., N. J., (1970), Chapter 6.
- {3.2} Y. Ataiyan, Private Communication, The University of Texas at Arlington, Arlington, Texas.
- {3.3} K. W. Chang, J. M. Owens and R. L. Carter, "Linearly Dispersive Time-Delay Control of Magnetostatic Surface Waves by Variable Ground-Plane Spacing," Electronics Letters, Vol. 19, No. 14, (July, 1983), pp. 546-547.
- {3.4} C. S. Hartmann, D. T. Bell, Jr. and R. C. Rosenfeld, "Impulse Model Design of Acoustic Surface-Wave Filters," IEEE MTT, Vol. MTT-21, No. 4, (April 1973), pp. 162-175.
- {3.5} T. L. Szabo, K. R. Laker and E. Cohen, "Interdigital Transducer Models: Their Impact on Filter Synthesis," IEEE Trans. on Sonics and Ultrasonics, Vol. SU-26, No. 5, (September 1979), pp. 321-333.
- {4.1} J. F. Gibbons, W. S. Johnson and S. W. Mylroie, "Projected Range Statistics: Semiconductors and Related Materials," Dowden, Hutchinson, and Ross, Inc., (1975), 2nd Edition.
- {4.2} K. W. Chang and W. Ishak, "The Effect of Width Modes on the Performance of MSSW Resonators," IEEE Ultrasonics Symposium Proc., (1985).

- {5.1} H. J. Wu, Ph.D. Dissertation, The University of Texas at Arlington, Arlington Texas, (1978).
- {5.2} G. Volluet, "Unidirectional Magnetostatic Forward Volume Wave Transducers," IEEE Trans. Mag., Vol. Mag-16, No. 5, (1980), pp. 1162-1164.
- {6.1} G. Volluet, "Magnetostatic Forward Volume Wave Reflective Dot Arrays," IEEE Trans. Mag., Vol. MAG.-7, No. 6, (November 1981), pp. 2964-2966.
- {6.2} G. Volluet and P. Hartemann, "Reflection of Magnetostatic Forward Volume Waves by Ion Implanted Gratings," IEEE Ultrasonics Symposium, Cat. 81CH1689-9, Vol. 1, (1981), pp. 394-397.
- {6.3} W. L. Bongianini and J. H. Dickerman, "Sidelobe Suppression in Surface Wave Acoustic Dispersive Delay Lines," IEEE G-MTT 1970 Int. Microwave Symp., Newport Beach, Calif, (May 11-17), pp. 319-322.
- {6.4} J. Burnswieg, E. H. Gregory and R. J. Wagner, "Surface Wave Device Applications and Component Developments," 1970 IEEE Int. Solid State Circuits Conf., Digest of Technical Papers, Philadelphia, Pa., (February 18-20), p. 132.
- {6.5} C. E. Cook and M. Bernfeld, "Radar Signals," New York, Academic Press Inc., (1967).
- {7.1.} Ved P. Nanda, "A New Form of Ferrite Device for Millimeter-Wave Integrated Circuits," IEEE Trans. MTT, pp. 876-879, Nov. 1976.
- {7.2.} R.M. Knox and P.P. Toullos, "Integrated Circuits for the Millimeter through Optical Frequency Range," Proc. Symp. Submillimeter Waves, New York, Mar. 31-Apr. 2, 198 .
- {7.3.} W.V. McLevige, Tatsuo Itoh, and Raj Mittra, "New Waveguide Structures for Millimeter-Wave and Optical Integrated Circuits," IEEE Trans. Microwave Theory Tech., vol. MTT-23, pp. 788-794, Oct. 1975.
- {7.4.} Klavs Solbach and Ingo Wolff, "The Electromagnetic Fields and the Phase Constants of Dielectric Image Lines," IEEE Trans. Microwave Theory Tech., vol. MTT, pp. 266-274, Apr. 1978.

## LIST OF SYMBOLS AND ABBREVIATIONS

|   |  |
|---|--|
| $\alpha$  | Propagation Loss Factor [Nepers/Meter]<br>(for propagation in y-direction)   |
| $a, b, c$   | a cyclic permutation of $x, y, z$  |
| $\beta$   | Propagation Phase Factor ( $2\pi/\lambda$ ) [Radians/Meter]<br>(for propagation in y-direction)  |
| $b$   | Small Signal Magnetic Induction Field Vector   |
| $\tilde{b}_1, \tilde{b}_2,$<br>$\tilde{b}_3, \tilde{b}_4$ | Spacial Harmonic of the Small Signal Induction<br>Field Vector at frequency, $f$ , in the region<br>{1,2,3,or4} indicated by the subscript<br>(see Figure 2.8) |
| $B$   | Total Magnetic Induction Vector  |
| <b>Bold</b>   | Indicates a Vector   |
| $c$   | Speed of Light in a Vacuum   |
| $C_N(f)$  | Chebyshev Polynomial of order $N$  |
| $\sim$  | Indicates a Complex Quantity when placed over<br>a symbol  |
| $*$   | Indicates the Complex Conjugate when used as<br>a superscript  |
| $d$   | YIG Thickness (see Figure 2.8)   |
| $d_n$   | Propagation Path between the $n$ th element of<br>a phased transducer array and the receiver<br>antenna  |
| $d$   | Small Signal Electric Flux Density Vector  |
| $\delta_{\text{step}}$                                    | Vectorial Magnitude of a Step in the Gradient<br>Search Method   |
| $\Delta$  | Defined as   |
| $e$   | Small Signal Electric Field Vector   |
| $e$   | Electronic Charge  |

|                         |   |
|-------------------------|---|
| $\tilde{e}_t^{\pm}$     | Magnitude of the Small Signal Electric Field that is normal to the propagation direction in the YIG (+/- → Forward/Reverse Propagating) |
| $E^2(\bar{x}, \bar{p})$ | Square Of The Error at a Point between a desired or target system response and a theoretical or model response                          |
| $E_{msq}(\bar{p})$      | Mean Squared Error as a function of system parameters, $\bar{p}$  |
| $E_{mab}(\bar{p})$      | Mean Absolute Error as a function of system parameters, $\bar{p}$   |
| $f$                     | Frequency [Hz]  |
| $f_m$                   | Frequency Associated with the Magnetization   |
| $f_{ma,b,c}$            | Frequency Associated with the Magnetization about the a-axis, the b-axis, or the c-axis, where a,b,c = a cyclic permutation of x,y,z    |
| $f_{min}$               | Frequency where linewidth is minimum ( $\Delta H = \Delta H_{min}$ ) (see Figure 2.5)   |
| $f_o$                   | Lamor Precessional Frequency [Hz]   |
| $f_{oa}$                | Lamor Precessional Frequency about the a-axis, where a = x, or y, or z  |
| $f_{ob}$                | Lamor Precessional Frequency about the b-axis, where b = x, or y, or z  |
| $f_{oc}$                | Lamor Precessional Frequency about the c-axis, where c = x, or y, or z  |
| $f_{oa,b,c}$            | Lossless Lamor Precessional Frequency about the a-axis, or the b-axis, or the c, axis, where a,b,c = a cyclic permutation of x,y,z      |
| $\tilde{f}_{oa,b,c}$    | Lossy Lamor Precessional Frequency about the a-axis, or the b-axis, or the c, axis, where a,b,c = a cyclic permutation of x,y,z         |
| $f_1$                   | Frequency of the Fundamental Field Harmonic   |
| $\tilde{F}(f)$          | Filter Transfer Function  |

|  |   |
|--|---|
| $\tilde{F}(\bar{x}, \bar{p})$                        | Generalized System Response or Transfer Function as a function of the state space, $\bar{x}$ , and the definable parameters, $\bar{p}$ (eg., $F(f, [R, L, C])$ would be the transfer function of a resistor, inductor, capacitor network as a function of the state or transform variable, frequency) |
| $\tilde{F}(\bar{x}_m, \bar{p})$                      | System Response of Transfer Function evaluated at a particular point in state space, $\bar{x}_m$ (eg., for the one-dimensional frequency <sup>m</sup> state space, this would be the transfer function at a particular frequency)   |
| $g$  | Lande g-factor  |
| $\tilde{G}_n(f)$                                     | Transfer Characteristic for the nth array element of a phased array assuming zero propagation path length   |
| $\gamma$   | Gyromagnetic Ratio  |
| $\text{grad}\{\}$                                    | Spacial gradient  |
| $\text{grad}_{\bar{p}}\{\}$                          | Gradient With Respect to $\bar{p}$ -Space   |
| $h$  | Small Signal Magnetic Field Vector  |
| $h_n$  | nth Harmonic of the Magnetic Field Vector   |
| $\tilde{h}_t^{\pm}$                                  | Magnitude of the Small Signal Magnetic Field that is normal to the propagation direction in the YIG (+/- $\rightarrow$ Forward/Reverse Propagating)   |
| $\tilde{h}_u^{\pm}, \tilde{h}_i^{\pm}$               | Magnitude of the Small Signal Magnetic Field that is normal to the propagation direction (+/- means Forward/Reverse, u/i means Unimplanted/Implanted transmission line section)   |
| $\tilde{h}_i(x, k, f)$                               | Spacial Harmonic of the Small Signal Magnetic Field Vector at frequency, $f$ , in the region indicated by the subscript, $i$ (see Figure 2.8)   |
| $\tilde{h}_1, \tilde{h}_2, \tilde{h}_3, \tilde{h}_4$ | Spacial Harmonic of the Small Signal Magnetic Field Vector at frequency, $f$ , in the region {1,2,3,or4} indicated by the subscript (see Figure 2.8)  |



|                                      |   |
|--------------------------------------|---|
| $H$                                  | Total Magnetic Field Vector   |
| $\tilde{H}$                          | Total Complex Magnetic Field  |
| $\tilde{H}_i(x,y,f)$                 | Spectral Harmonic of the Small Signal Magnetic Field Vector at the point $(x,y)$ , in the region indicated by the subscript, $i$ (see Figure 2.8) |
| $\Delta H$                           | Magnetic Linewidth  |
| $\Delta H_{\min}$                    | Minimum Linewidth used in Gilbert Loss (see Figure 2.5)   |
| $H_0$                                | Static Magnetic Bias Field Vector   |
| $H_{0a,b,c}$                         | Magnitude of the Magnetic Bias Field along the a-axis, or the b-axis, or the c-axis, where a,b,c = a cyclic permutation of x,y,z                  |
| $\bar{I}$                            | Identity Matrix   |
| $\text{Im}\{\}$                      | Imaginary Part of what is inside $\{\}$   |
| $\int$                               | Integration   |
| $J$                                  | Square root of $-1$   |
| $J$                                  | Small Signal Current Density  |
| $\tilde{k}$                          | Complex Dispersion Relation $(\beta - j\alpha)$ for MSFVW propagation along the y-axis  |
| $\tilde{k}_-$                        | Complex Dispersion Relation $(\beta - j\alpha)$ for MSSW propagation against the y-direction  |
| $\tilde{k}_+$                        | Complex Dispersion Relation $(\beta - j\alpha)$ for MSSW propagation in the y-direction   |
| $K_z(y)$                             | Sheet Current Density in the z-direction as a function of $y$   |
| $\tilde{\kappa}_+, \tilde{\kappa}_-$ | Constants used in the calculation of the reflection and transmission coefficients (see eqn. (2.35))   |
| $l_i$                                | Length of the $i$ th Reflector measured transverse to the array axis  |
| $l_t$                                | Aperture Length of the Input Transducer   |

|                    |   |
|--------------------|---|
| $[ ]_L$            | Transverse Field Vector on the Leading Edge of an Implanted Reflector Zone  |
| $m$                | Electron Magnetic Dipole Moment   |
| $m_n$              | Magnetic Moment of the nth Electron   |
| $\tilde{m}_n$      | nth Harmonic of the Magnetization Vector  |
| $m$                | Electronic Mass   |
| $M$                | Magnetization Vector  |
| $\tilde{M}$        | Complex Total Magnetization Vector  |
| $M_0$              | Saturation Magnetization Vector   |
| $M_{oa,b,c}$       | Magnitude of the Saturation Magnetization Vector along the a-axis, the b-axis, or the c-axis, where a,b,c = a cyclic permutation of x,y,z |
| $M_{imp}$          | Saturation Magnetization in the Implanted Layer   |
| $M_{pu}, M_{pure}$ | Saturation Magnetization in the Unimplanted YIG Regions   |
| MSBVW              | Magnetostatic Backward Volume Wave  |
| MSFVW              | Magnetostatic Forward Volume Wave   |
| MSQ                | Mean Squared  |
| MSSW               | Magnetostatic Surface Wave  |
| MSW                | Magnetostatic Wave  |
| $\mu_0$            | Permeability of a Vacuum  |
| $\tilde{\mu}$      | Complex Magnetic Permeability Tensor  |
| $\mu_1$            | Diagonal Element of the Lossless Permeability Tensor.   |
| $\tilde{\mu}_1$    | Diagonal Element of the Complex Lossy Permeability Tensor.  |
| $\mu_2$            | Magnitude of the Off Diagonal Element of the Lossless Permeability Tensor.  |

|   |  |
|---|--|
| $\tilde{\mu}_2$   | Off Diagonal Element of the Lossy Permeability Tensor  |
| $\mathbf{p}$  | Electron Angular Momentum Vector   |
| $\bar{\mathbf{p}}$  | Set of Designer Selectable Parameters that the system characteristic depends upon  |
| $\bar{\mathbf{p}}_0^i$  | The $i$ th Point in Parameter Space in an iterative solution of the mean squared error equations   |
| $\Delta \bar{\mathbf{p}}^i$   | The Increment of the Point in Parameter Space between the $(i-1)$ th and $i$ th iteration of the mean squared error equations  |
| $p_m$   | The $m$ th Component of the Vector $\bar{\mathbf{p}}$  |
| $\tilde{\psi}_i(x,y,t)$   | Complex Representation of the Time Signal that would be received at the point $(x,y)$  |
| $\pi$   | 3.1415926... [radians]   |
| $\tilde{R}_A(f)$  | Array Reflection Transfer Function   |
| RAF   | Reflective Array Filter  |
| $\tilde{\rho}(f)$   | Reflection Coefficient for an unimplanted to implanted zone interface  |
| $\tilde{\rho}_{\xi\zeta}^+$   | Reflection Coefficient for positive going (+y-direction) wave, on interface bounded by regions $\xi$ and $\zeta$ , with $\xi$ preceeding $\zeta$ (see eqn. (2.35), subscripts assume values $u$ for unimplanted and $i$ for implanted) |
| $\tilde{\rho}_{\xi\zeta}^-$   | Reflection Coefficient for negative going (-y-direction) wave, on interface bounded by regions $\xi$ and $\zeta$ , with $\zeta$ preceeding $\xi$ (see eqn. (2.35), subscripts assume values $u$ for unimplanted and $i$ for implanted) |
| Re, Re{ }   | Real Part of what follows or is inside { }   |
| RMS   | Root Mean Squared  |
| SAW   | Surface Acoustic Wave  |
| $\tilde{S}_{11}, \tilde{S}_{12},$<br>$\tilde{S}_{21}, \tilde{S}_{22}$ | Elements of the Scattering Matrix for Normal Incidence Arrays<br>(Scattering Parameters)   |

|  |  |
|--|--|
| $\Sigma$   | Summation Series   |
| $T$  | Torque on a magnetic dipole  |
| $\tilde{T}(\bar{x})$   | Target (Desired) System Response or Transfer Function as a function of the state or transform variables, $\bar{x}$   |
| $\tilde{T}(\bar{x}_m)$   | Target System Response evaluated at a specific state, $\bar{x}_m$ (eg., for the one-dimensional frequency state space, this would be the system transfer function evaluated at a particular frequency)                                       |
| $\tilde{T}_A(f)$   | Array Transfer Function (Unapodized)   |
| $\tilde{T}_A^n(f)$   | Transfer Function for the nth Subarray or Array Strip (Apodized)   |
| $T_1, T_2, \dots, T_N$   | Normal Incidence Array Section Transmission Matrices (Unapodized)  |
| $T_1^1, T_2^1, \dots, T_N^M$                                     | Normal Incidence Array Element Transmission Matrices (Apodized), where superscript indicates strip and subscript indicates array element (see Fig. 2.14)   |
| $\tilde{T}_{11}, \tilde{T}_{12}, \tilde{T}_{21}, \tilde{T}_{22}$ | Elements of the Transmission Matrix for Normal Incidence Arrays (Transmission Parameters)  |
| $[\tilde{T}_{M,N}]$  | Transmission Matrix that relates the transverse fields in the Mth array element to those in the Nth array element  |
| $\tilde{\tau}_{\xi\zeta}^+$                                      | Complex Transmission Coefficient for positive going (+y-direction) wave, on interface bounded by regions $\xi$ and $\zeta$ , with $\xi$ preceeding $\zeta$ (see eqn. (2.35), subscripts assume values u for unimplanted and i for implanted) |
| $\tilde{\tau}_{\xi\zeta}^-$                                      | Complex Transmission Coefficient for negative going (-y-direction) wave, on interface bounded by regions $\xi$ and $\zeta$ , with $\zeta$ preceeding $\xi$ (see eqn. (2.35), subscripts assume values u for unimplanted and i for implanted) |
| $[ ]_T$  | Transverse Field Vector on the Trailing Edge of an Implanted Reflector Zone  |

|   |   |
|---|---|
| $u$   | Thickness of Implanted Surface Layer  |
| $\hat{u}_n$   | Unit Vector Along the $p_n$ Coordinate Axis<br>in parameter space   |
| $v$   | Thickness of Alumina Microstrip Substrate   |
| $\tilde{V}_m$   | Scalar Magnetic Potential   |
| $\tilde{V}_{m1}, \tilde{V}_{m2},$<br>$\tilde{V}_{m3}, \tilde{V}_{m4}$ | Spacial Harmonic of the Magnetic Scalar<br>Potential at frequency, $f$ , in the region<br>indicated by the subscript (see Figure 2.8) |
| $\Delta V$  | Volume with maximum lineal dimension that is<br>small compared to a magnetostatic wavelength  |
| $w_i$   | Width of the $i$ th Reflector Zone measured along<br>the array axis   |
| $w(f)$  | Weighting Function used in the Mean Squared<br>Error to emphasize points where the fit is<br>more critical                            |
| $\omega_m$  | Radian Frequency associated with the<br>Saturation Magnetization  |
| $\omega_o$  | Lamor Precessional Frequency [rad/sec]  |
| $\tilde{v}_+, \tilde{v}_-$  | Constants used in calculation of the reflection<br>and transmission coefficients (eqn. (2.35))  |
| $\hat{x}$   | Unit Vector along the X-Coordinate Direction  |
| $\bar{\chi}$  | Complex Suseptibility Tensor  |
| $\tilde{\chi}_{ab}$   | Element of the Complex Suseptibility Tensor from<br>the $a$ th ROW and $b$ th COLUMN  |
| $\tilde{X}_1(f),$<br>$\tilde{X}_2(f)$                                 | Transducer<br>Transfer Function<br>(1/2 + Input/Output)   |
| $y_i$   | Distance from the Input Transducer to the<br>Center of the $i$ th Reflector, measured along<br>the array axis                         |
| $\hat{y}$   | Unit Vector along the Y-Coordinate Direction  |
| $\hat{z}$   | Unit Vector along the Z-Coordinate Direction  |

|                           |  |
|---------------------------|--|
| $\zeta$                   | Gilbert Loss Factor (empirically determined proportionality constant)  |
| $z_o$                     | Distance from the Array Axis to the Output Transducer, measured normal to the array axis   |
| $z_e(\bar{x}, \bar{p})$   | An Auxiliary Polynomial that has zeros at the extrema of the pointwise error function, $E(\bar{x}, \bar{p})$ (see eqn. (3.4))                |
| $z_\xi(\bar{x}, \bar{p})$ | An Auxiliary Polynomial that has zeros where the pointwise error function $E(\bar{x}, \bar{p})$ equals some constant, $\xi$ (see eqn. (3.3)) |
| $Z_\pm(y)$                | Wave Impedance for Forward/Reverse (+/-) Propagating Waves   |

END

2-87

DTIC